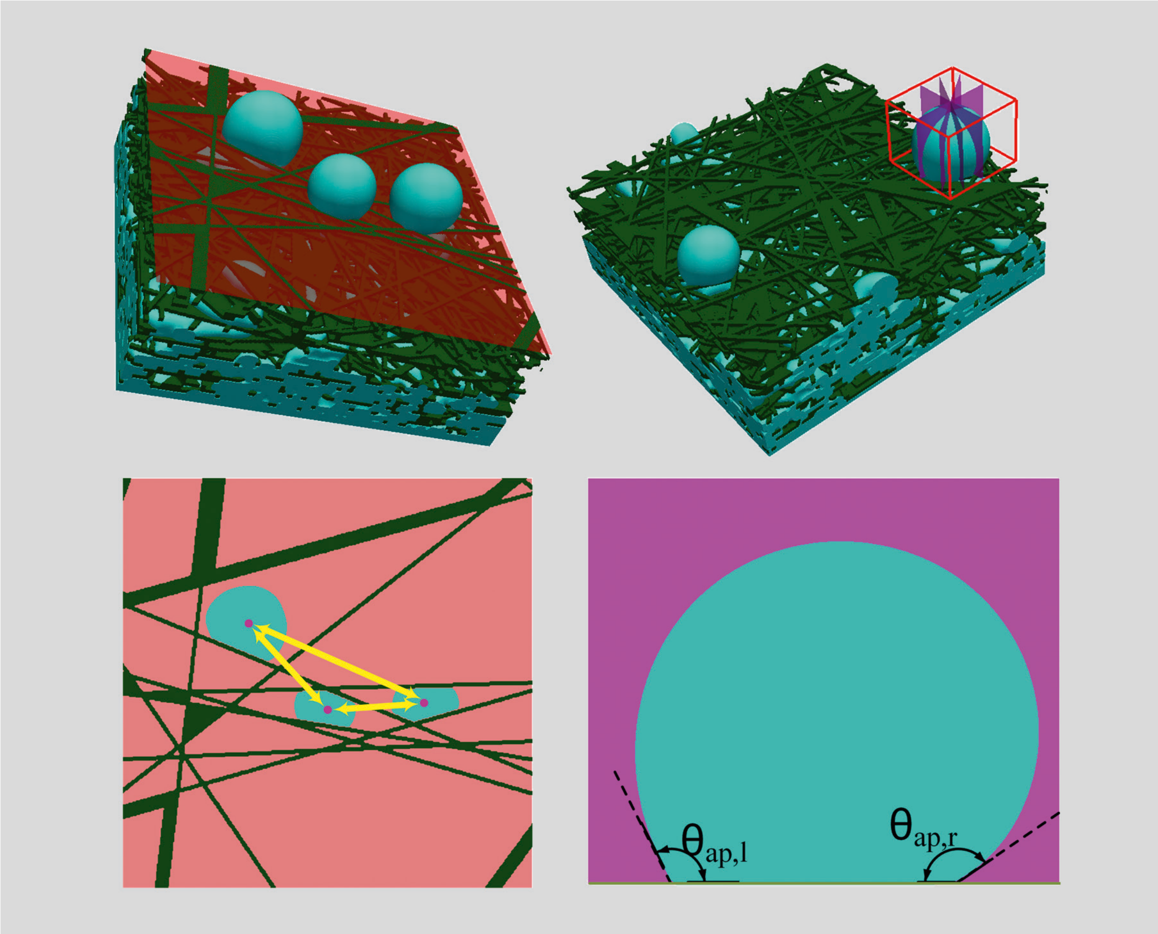

Lattice Boltzmann Simulation in Components of Polymer Electrolyte Fuel Cell

Junliang Yu

Energie & Umwelt / Energy & Environment
Band / Volume 438
ISBN 978-3-95806-360-0

Mitglied der Helmholtz-Gemeinschaft

JÜLICH
Forschungszentrum

Schriften des Forschungszentrums Jülich
Reihe Energie & Umwelt / Energy & Environment Band / Volume 438

Forschungszentrum Jülich GmbH
Institut für Energie- und Klimaforschung
Elektrochemische Verfahrenstechnik (IEK-3)

Lattice Boltzmann Simulation in Components of Polymer Electrolyte Fuel Cell

Junliang Yu

Schriften des Forschungszentrums Jülich
Reihe Energie & Umwelt / Energy & Environment Band / Volume 438

ISSN 1866-1793 ISBN 978-3-95806-360-0

Bibliografische Information der Deutschen Nationalbibliothek.
Die Deutsche Nationalbibliothek verzeichnet diese Publikation in der
Deutschen Nationalbibliografie; detaillierte Bibliografische Daten
sind im Internet über http://dnb.d-nb.de abrufbar.

Herausgeber und Vertrieb: Forschungszentrum Jülich GmbH
Zentralbibliothek, Verlag
52425 Jülich
Tel.: +49 2461 61-5368
Fax: +49 2461 61-6103
zb-publikation@fz-juelich.de
www.fz-juelich.de/zb

Umschlaggestaltung: Grafische Medien, Forschungszentrum Jülich GmbH

Druck: Grafische Medien, Forschungszentrum Jülich GmbH

Copyright: Forschungszentrum Jülich 2018

Schriften des Forschungszentrums Jülich
Reihe Energie & Umwelt / Energy & Environment, Band / Volume 438

D 82 (Diss., RWTH Aachen University, 2018)

ISSN 1866-1793
ISBN 978-3-95806-360-0

Vollständig frei verfügbar über das Publikationsportal des Forschungszentrums Jülich (JuSER)
unter www.fz-juelich.de/zb/openaccess.

This is an Open Access publication distributed under the terms of the Creative Commons Attribution License 4.0,
which permits unrestricted use, distribution, and reproduction in any medium, provided the original work is properly cited.

Lattice Boltzmann Simulation in Components of Polymer Electrolyte Fuel Cell

by Junliang Yu

Abstract

A polymer electrolyte fuel cell (PEFC) is a very promising energy conversion device that generates electricity from hydrogen. The gas diffusion layer (GDL) is one of the main components in PEFC. On the cathode side, the liquid water is produced under the operating temperature (around 70°C). The liquid water flows through the GDL and is removed in the gas channel by the gaseous reactant to ensure the fuel cell work continuously. The situation on the GDL surface when water breaking through the GDL is very important to be studied in detail. The liquid water flowing through GDL process is simulated by the lattice Boltzmann (LB) ShanChen model. Because it is a capillary force dominated process the density ratio and viscosity ratio between two phases can be negligible. The multiple-relaxation time (MRT) approach and exact difference method (EDM) force scheme are implemented on the present model.

The present LB ShanChen MRT-EDM two-phase model is validated by some tests. Different force schemes with single relaxation time (SRT) and MRT approach are compared in the external force driving Poiseuille flow test. Some model limitations, the lattice and relaxation time dependence are discussed in the flat interface test. The droplet test and contact angle test determine the model parameters to control the phase separation and material wettability. The open boundary condition is implemented on the outlet boundary for water flowing through the GDL simulations.

The model is applied on the water flowing through the GDL which is fully covered with hydrophic material. Some basic effects are studied including buffer space thickness, domain size, capillary number, geometry and wettability effects. It can be concluded that these factors have effects on the water flow behaviors. Under a specific capillary number condition, the results are consistent in quality with the theory of capillary force dominated process. Water will break through the GDL due to specified a velocity condition on inlet. The stochastic GDL geometries causes irregular water droplets are randomly formed on the GDL surface.

The apparent contact angles and breakthrough point distances (BPD) for the formed water droplets are analyzed statistically. For the local apparent contact angles, they vary with different view directions and positions along different geometries. They are different to the idealized contact angles by symmetric simplification. For the breakthrough point distances, they are analyzed statistically in two ways. The distribution of distances are evaluated statistically by the Lilliefors test. It is concluded that the BPD can be described by the normal distribution with certain statistic characteristics. Information of the apparent contact angle and the shortest neighbor breakthrough point distance can be the input modeling setups on the cell-scale simulations in the field of PEFC simulations.

Basic influences of polytetrafluoroethylene (PTFE) on the water flow are studied. Different PTFE content and PTFE distributions (along in-plane and through-plane directions in different sections) are applied on a GDL geometry. It is concluded that the PTFE content and its distribution have impact on the water flow behavior. The water is flowing preferably through the no-PTFE region. Different shapes of water saturation curves along the through-plane direction are observed on different PTFE distributions.

Lattice-Boltzmann-Simulation in Komponenten von Polymer-Elektrolyt-Brennstoffzellen

von Junliang Yu

Abstract

Eine Polymer-Elektrolyt-Brennstoffzelle (PEFC) ist ein sehr vielversprechendes Energieumwandlungsgerät, das Strom aus Wasserstoff erzeugt. Die Gasdiffusionsschicht (GDL) ist eine der wichtigsten Komponenten der PEFC. An der Kathode wird flüssiges Wasser bei einerr Betriebstemperatur von 70 °C produziert. Das flüssige Wasser fließt durch die GDL und es wird durch das Gasf im Brenngaskanal entfernt Damit wirdder kontinuierliche Betrieb der Brennstoffzelle gewährleistt. Es ist von großem Interesse, die GDL-Oberfläche detailliert zu untersuchen, wenn das Wasser die GDL verlässt. Der Transport des flüssigen Wassers durch die GDL wird durch das Lattice-Boltzmann (LB) ShanChen Modell simuliert. Der Transportprozess wird durch die Kapillarkraft dominiert, deshalb können die Verhältnisse der Dichte und der Viskosität der zwei Phasen vernachlässigt werden. Die Multi-Relaxation-Ttime-Diskretisierung (MRT) und Exact-Difference-Verfahren (EDM) wurden in dem vorliegenden Modell eingesetzt.

Das LB ShanChen MRT-EDM Zweiphasenmodell wurde durch Tests validiert. Unterschiedliche Kräfteschemata wurden mit der Single-Relaxation-Time-Diskretisierung (SRT) als auch MRT in dem durch externe Kraft getriebenen Poiseuille-Durchfluss-Test miteinander verglichen. Die Modelleinschränkungen, z.B. die Abhängigkeit des Gitters und der Relaxationszeit, wurden in den Grenzflächenest diskutiert. Der Tropfentest und der Kontaktwinkeltest können die Modellparameter bestimmen, die die Phasentrennung und die Material-Benetzbarkeit kontrollieren. Die offene Randbedingung wurde für den Ausgang verwendet, durch den das Wasser die GDL verlässt.

Das Modell für den Wassertransportw durch die GDL angewandt. Die GDL wurde als vollständig mit hydrophil angenommen. Die grundlegenden Effekte wurden untersucht, z.B. die Größe des Pufferbereichs, Größe der Dömane, Kapillarzahl, Geometrie und Benetzbarkeit. Diese Faktoren beeinflussen das Fließverhalten des Wassers . Unter der Bedingung einer spezifischen Kapillarzahl stimmen die Ergebnisse qualitativ mit der Theorie überein, dass der die Transportprozesse durch die Kapillarkraft dominiert werden. Mir einer fests Strömungsgeschwindigkeit am Eintritt wurde Wassertransport durch die GDL simuliert. Die stochastischen Geometrien der GDL verursachen unregelmäßig geformte Wassertropfen, die an zufälligverteilten Positionen der GDL-Oberfläche austreten.

Die Kontaktwinkel und die Abstände der Durchtrittspunkte (BPD) des erzeugten Wassers wurden statistisch analysiert. Die lokalen Kontaktwinkel variieren mit unterschiedlichen Projektionsebenen und Positionen bei verschiedenen Geometrien. Sie sind anders als die idealisierten Kontaktwinkel. Die Verteilung des Abstände wurde durch den Lilliefors-Test statistisch analysiert. Die BPD könnendurch eine Normalverteilung beschrieben werden kann. Die Kontaktwinkel und die BPD können Informationen für Zellsimulationen liefern.

Grundlegender Einfluss von Polytetrafluorethylen (PTFE) auf den Wassertransport wurde untersucht. Unterschiedliche PTFE-Gehalte und PTFE-Verteilungen (In-Plane und Through-Plane in verschiedenen Abschnitten der GDL) wurden untersucht. Der PTFE-Gehalt und seine Verteilung einen beeinflussen den Wassertransport. Das Wasser fließt bevorzugt durch Bereiche ohne PTFE. Unterschiedliche Wassersättigungskurven entlang der Through-Plane-Richtung wurden bei verschiedenen PTFE-Verteilungen beobachtet.

Contents

1.Introduction and literature review

Due to the growing concerns on the depletion of petroleum based energy resources and climate change, fuel cell technologies have received much attention in recent years owing to high efficiencies and low emissions[1][2]. Fuel cells are electrochemical devices that directly convert chemical energy from fuels such as hydrogen to electrical energy [3]. Polymer electrolyte fuel cell (PEFC) is the most commonly applied on portable, mobile and stationary areas, because of their noteworthy features including low operating temperature, high power density and easy scale-up [3]. There is a huge growing market for the PEFC today. It is very worthwhile to study PEFC deeper and understand more clearly the principle inside.

The PEFCs are constructed with polymer electrolyte membranes as proton conductor and platinum (Pt) based materials as catalyst. The detailed schematic graph of PEFC is shown in Fig. 1.1.

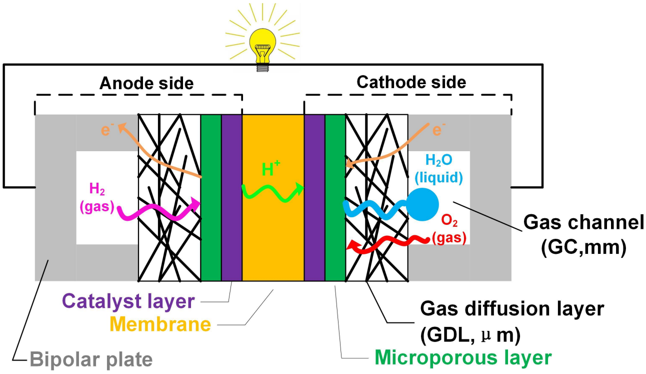

Figure 1.1.: Schematic graph of PEFC

Phenomena in working PEFCs are very complex, such as heat transfer, species and charge transport, multi-phase flows and electrochemical reactions are all involved. These phenomena are observed in components of PEFCs, namely the membrane electrode assembly (MEA) which consists of the catalyst layers (CL), membrane, gas diffusion layer (GDL) and micro-porous layer (MPL). The gas channel (GC) and bipolar plate (BiP) are added external side of MEA. Their geometry sizes are in different scales : the membrane, CL, MPL and GDL are in micrometer or even lower, while the GC and BiP are in millimeter or even larger. The membrane is located in the middle of the whole cell, while two electrodes are located on two sides of the membrane including anode side and cathode side. The anode side and cathode side consist of the same components such as CL, MPL and GDL. However, the chemical reactions happened in two electrodes are different. Their reactions are shown in Eq. (1.1) to Eq. (1.3).

$$\frac{1}{2}\mathrm{O}_2 + \mathrm{H}_2 \longrightarrow \mathrm{H}_2\mathrm{O} \qquad \text{(Overall reaction)} \tag{1.1}$$

$$\mathrm{H}_2 \longrightarrow 2\mathrm{H}^+ + 2\mathrm{e}^- \qquad \text{(Anode)} \tag{1.2}$$

$$\frac{1}{2}\mathrm{O}_2 + 2\mathrm{H}^+ + 2\mathrm{e}^- \longrightarrow \mathrm{H}_2\mathrm{O} \qquad \text{(Cathode)} \tag{1.3}$$

At the anode, the hydrogen oxidation reaction (HOR) happened, hydrogen is oxidized and forms protons and electrons. At the cathode, the oxygen reduction reaction (ORR) happened, oxygen is reduced with protons and electrons. The working process of reactants and products is graphically represented in Fig. 1.1. At the anode, gaseous hydrogen is forced to flow through GC. Part of hydrogen flows through two porous media (GDL and MPL) and diffuse to the CL. At the cathode, the reactant gaseous oxygen or air flows through the GDL and MPL to the CL. When the ORR is active, liquid water is produced continuously and transport through MPL and GDL to the GC. Liquid droplets emerge on the GDL-GC interface and they are removed by the reactant flow. In the membrane, the produced protons migrate and partial water is transported through the membrane from anode to cathode, while electrons are conducted by external circuits. It can be seen that all transport processes are in three dimensions and have anisotropy characteristics under practical current loads. Concerning the micro-scale two-phase flow in PEFC, the porous media - GDL plays an significant role and it contains some main primary functions below:

(i) Provide reactant transport to and product removal from the CL with a typical porosity.

(ii) Provide electron conduction to and from the CL.

(iii) Provide heat transfer from the CL to the current collector.

(iv) Provide mechanical support for the electrode structure preventing it from tenting into the GC of the bipolar plate [4].

There are mainly three styles of GDL, the carbon paper, the non-woven and the woven carbon cloth. The structure of GDL carbon paper is viewed by scanning electron microscopy (SEM) technology and shown in Fig. 1.2.

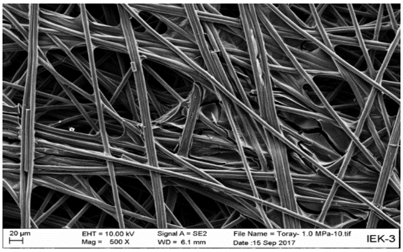

Figure 1.2.: SEM image of GDL carbon paper structure in Forschungszentrum Jülich. (Single fiber diameter is around 7 µm.)

GDL is assumed to be made of graphite. It is seen from Fig. 1.2 that straight carbon fibers are irregularly organized in GDL carbon paper. Straight carbon fibers are glued by binders and processed with hydrophobic materials. Usually, the carbon fibers of GDL are processed by covering polytetrafluoroethylene (PTFE) to improve hydrophobicity. It allows the produced water flowing through the GDL and emerging liquid droplets on the GDL-GC interface easier. The cell keeps running when the formed water droplets are removed by the gaseous reactant in the GC. The wettability of graphite in GDL is mildly hydrophobic and water contact angle is 90°. The water contact angle on PTFE surface θ_{PTFE} can be found from manufactures as approximately 110° [5][6]. It is necessary to have a deep understanding of water transport through the GDL from the micro-scale side.

1.1. Motivation and goal

There are two greatest barriers that decreased the world-wide commercialization of PEFC including durability and cost [7][8][9]. At present, breakthroughs in material development, acquisition of fundamental knowledge, and development of analytical models and experimental tools are the potential candidates to overcome these barriers and important for PEFC development. Particularly, the simulation or modeling method is an efficient tool to study the PEFC from all scales from micro-scale (micrometer or nanometer) to macro-scale (millimeter or larger). Before selecting a suitable simulation topic, the factors which affect the cell performance are analyzed to motivate this dissertation. The performance of PEFC is often represented by the polarization curve (output voltage versus the current density) [2] and shown in Fig. 1.3.

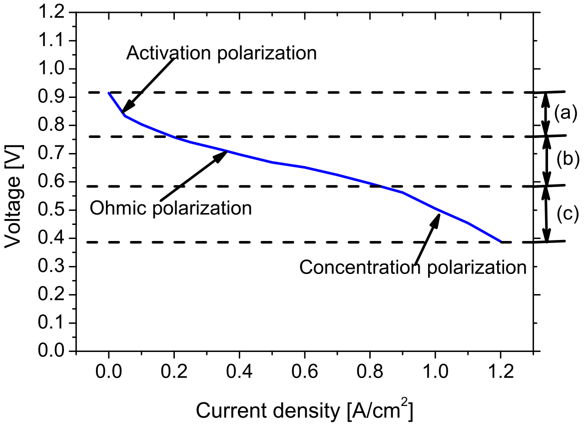

Figure 1.3.: Typical fuel cell polarization curve for a PEFC in Forschungszentrum Jülich. The voltage loss are dominated with (a) reaction rate losses; (b) Resistance losses; (c) Mass transfer losses, under different current range. (Operating condition: temperature T = 70°C, pressure P = 0.1 MPa, reaction area is 14.44 cm^2, stoichiometry number $\lambda = 2$ in anode and cathode, 5 parallel single square GC with width 1 mm, Toray090 GDL with single fiber diameter 7 µm).

In the linear region (region (b) in Fig. 1.3) an increasing current density leads to decreasing the voltage due to its ohmic nature. The ohmic loss becomes less significant at the low current level and this region (the region (a) in Fig. 1.3) is called activation polarization. At the very high current density the voltage fall down significantly (the region (c) in Fig. 1.3) because of the reduction of gas exchange efficiency. This region is called concentration polarization and it is controlled by mass transport overpotentials, with contributions from activation and ohmic overpotentials [10]. It was reported from literature that phenomena happened in the multi-scales of PEFC affect the cell performance [11][12]. Particularly, the liquid water transport through GDL in cathode side is the big issue for mass transport and the flooding in PEFC may happen. There are mainly two types of flooding including GDL flooding and GC flooding [13]. The inhomogeneous reactant distribution can also cause the easier locally flooding on the GDL and CL interface [14]. The GDL flooding is the situation when pores in the GDL are filled with water, the transport of oxygen to the CL gets blocked and the catalyst sites get covered. The GC flooding is the situation if the accumulation of water reaches a point when water flowing to the GC, gaseous reactant flow becomes blocked or clogged.

The GDL flooding increases the flow resistance of reactant and decreases the fuel cell performance when the complex interactions of several properties of GDL (porosity, morphology, thickness and the PTFE content) happened [15][16]. GDL flooding hinders the oxygen transport from the GC to the reaction site, and it covers electrochemically active sites with liquid water [17]. The mass transfer process can be studied and optimized in both macro and micro scales [18]. From the macro-scale side, the produced water should be removed continuously on the GC of cathode to avoid GC flooding. If the water removal rate in GC is lower than the water generation rate, excess water will accumulate. From the micro-scale side, the water through GDL process can be optimized to avoid the GDL flooding. The water flowing through the GDL in cathode side can be optimized and decrease GDL flooding risk. Particularly, the GDL flooding can be decreased by designing the GDLs carefully with an appropriate combination of hydrophobic and hydrophilic characteristics. The GDLs are typically wet proofed with PTFE to ensure that the whole GDL remains relatively hydrophobic to avoid GDL and GC flooding [19]. Therefore, the liquid water flowing through the GDL needs to be studied in details from the micro-scale side. With a better understanding the liquid flow behavior, the risk of GDL flooding can be decreased with optimizing the flow. The simulation approach is a good tool because of repeatability in the GDL structures and flexible simulation conditions. There are different types of GDL including the carbon paper and carbon cloth with woven and no-woven fibers. In this thesis, a previous thesis [20] is extended by features supporting two-phase flow in GDL. Brinkmann [20] showed the applicability of lattice Boltzmann method (LBM) on irregular GDL structures and the LBM framework is running in Jülich's supercomputer JURECA (formerly JUROPA). From the algorithms side, the LBM is preferred on simulating liquid water flowing through the GDL with three main benefits. The first is that LBM is suitable on the small dimension (in µm range) and irregular porous structures (such as GDL see Fig. 1.2) [21]. The second is that LBM can be implemented with parallel computing and the super computer is applied [22]. The third is the easy mesh process (mesh with voxel from structure images) and the real porous geometries (such as from X-ray) can be applied [23]. So in this thesis, the simulation approach is decided to study liquid water through the GDL and the carbon paper GDL is applied. The GC flooding risk can be decreased with optimizing the two-phase flow in GC from the macro-scale side. The cell-scale two-phase modeling and simulation in GC can be developed. From the multi-scale simulation theory, macro-scale simulations can be supported by the results from the micro-scale simulation. In a summary, four main goals below are expected to be achieved:

- A two-phase suitable LBM model is expected to simulate liquid water flowing through the GDL.
- Better understand the liquid water flow behaviors in GDL with some effects such as geometry structures, produced water flux and material wettability.
- Provide some detailed information to bridge the gap in the multi-scale simulations of PEFC. Analyze the characteristics of droplets at the GDL-GC interface with the statistical method.
- Understand the PTFE distribution effects on the liquid water flowing through the GDL.

1.2. Two-phase flow in GDL of PEFC

1.2.1. Two-phase flow mechanisms

According to the description in section 1.1, the two-phase flow in GDL has effect on mass transfer, and further on the cell performance. The liquid water is produced at the cathode. The amount of reactant consumption and produced water in cathode can be calculated with the Faraday's laws from Eq. (1.4) to Eq. (1.6) [24].

$$I = \dot{I} \cdot A_{\text{eff}} \tag{1.4}$$

$$\dot{m}_{\mathrm{O_2}} = \frac{I}{4F} \cdot M_{\mathrm{O_2}} \quad ; \quad \dot{V}_{\mathrm{O_2}} = \frac{\dot{m}_{\mathrm{O_2}}}{\rho_{\mathrm{O_2}}} \quad ; \quad \bar{\mathbf{u}}_{\mathrm{O_2}} = \frac{\dot{V}_{\mathrm{O_2}}}{A_{\text{trans}}} \tag{1.5}$$

$$\dot{m}_{\mathrm{H_2O}} = \frac{I}{2F} \cdot M_{\mathrm{H_2O}} \quad ; \quad \dot{V}_{\mathrm{H_2O}} = \frac{\dot{m}_{\mathrm{H_2O}}}{\rho_{\mathrm{H_2O}}} \quad ; \quad \bar{\mathbf{u}}_{\mathrm{H_2O}} = \frac{\dot{V}_{\mathrm{H_2O}}}{A_{\text{trans}}} \tag{1.6}$$

where I and $\dot{I}$ are the electric current and its current density with the unit Ampere (A) and A·cm^{-2}. The Faraday's constant F =96485 A · s · mol^{-1}. $\dot{m}_{\mathrm{H_2O}}$ and $\dot{V}_{\mathrm{H_2O}}$ are mass and volume flux separately. $\bar{\mathbf{u}}_{\mathrm{O_2}}$ is the average velocity of oxygen flow from GC to CL. $\bar{\mathbf{u}}_{\mathrm{H_2O}}$ is the average water produced velocity through the effective reaction area A_{eff}. M and ρ are molar mass and density. Properties of oxygen, water and air at 70°C, including ρ_r (density), M_r (molar mass), μ_r (dynamic viscosity) and ν_r (kinematic viscosity), are summarized in Table 1.1, with subscript r is 'O_2' for oxygen and 'H_2O' for water [25][26][27][28].

Table 1.1.: Properties of oxygen, water and air at 70°C

	Subscript r	ρ_r /kg · m^{-3}	M_r /kg · mol^{-1}	μ_r /kg · m^{-1} · s^{-1}	ν_r /m^2 · s^{-1}
Oxygen	'O_2'	1.11	0.032	2.33×10^{-5}	2.1×10^{-5}
Water	'H_2O'	975	0.018	3.50×10^{-4}	3.6×10^{-7}

Some salient dimensionless numbers are introduced to characterize the two-phase flow behavior in the GDL of PEFC, such as Reynolds number (*Re*), capillary number (*Ca*), Bond number (*Bo*) and Weber number (*We*). They are represented from Eq. (1.7) to Eq. (1.10).

$$Re = \frac{\text{inertia force}}{\text{viscous force}} = \frac{\rho_{\mathrm{H_2O}} \bar{\mathbf{u}}^2_{\mathrm{H_2O}} L^2_{\text{GDL}}}{\mu_{\mathrm{H_2O}} L_{\text{GDL}} \bar{\mathbf{u}}_{\mathrm{H_2O}}} = \frac{\rho_{\mathrm{H_2O}} \bar{\mathbf{u}}_{\mathrm{H_2O}} L_{\text{GDL}}}{\mu_{\mathrm{H_2O}}} = \frac{\bar{\mathbf{u}}_{\mathrm{H_2O}} L_{\text{GDL}}}{\nu_{\mathrm{H_2O}}} \tag{1.7}$$

$$Ca = \frac{\text{viscous force}}{\text{surface tension force}} = \frac{\mu_{\mathrm{H_2O}} L_{\text{GDL}} \bar{\mathbf{u}}_{\mathrm{H_2O}}}{\sigma_s L_{\text{GDL}}} = \frac{\mu_{\mathrm{H_2O}} \bar{\mathbf{u}}_{\mathrm{H_2O}}}{\sigma_s} = \frac{\nu_{\mathrm{H_2O}} \rho_{\mathrm{H_2O}} \bar{\mathbf{u}}_{\mathrm{H_2O}}}{\sigma_s} \tag{1.8}$$

$$Bo = \frac{\text{gravitational force}}{\text{surface tension force}} = \frac{\mathbf{g}(\rho_{\mathrm{H_2O}} - \rho_{\mathrm{O_2}}) L^3_{\text{GDL}}}{\sigma_s L_{\text{GDL}}} = \frac{\mathbf{g}(\rho_{\mathrm{H_2O}} - \rho_{\mathrm{O_2}}) L^2_{\text{GDL}}}{\sigma_s} \tag{1.9}$$

$$We = \frac{\text{inertial force}}{\text{surface tension force}} = Re \cdot Ca = \frac{\rho_{\mathrm{H_2O}} \bar{\mathbf{u}}^2_{\mathrm{H_2O}} L^2_{\text{GDL}}}{\sigma_s L_{\text{GDL}}} = \frac{\rho_{\mathrm{H_2O}} \bar{\mathbf{u}}^2_{\mathrm{H_2O}} L_{\text{GDL}}}{\sigma_s} \tag{1.10}$$

where ρ_r, μ_r, ν_r and $\bar{\mathbf{u}}_r$ are density, dynamic viscosity, kinematic viscosity and average velocity for species r separately (r is 'H_2O' for water and 'O_2' for oxygen). L_{GDL} is the characteristic length for fluids in GDL. g is the gravity acceleration and σ_s is the surface tension of water in air. The relations of main fluid related forces can be understood from these dimensionless numbers: *Re* defines the ratio of inertia force to viscous force; *Ca* represents the ratio of viscous force to surface tension force; *Bo* defines the ratio of gravitational force to surface tension force; *We* is the ratio of inertial force to surface tension force, which is the product of *Re* and *Ca*. The quantitative difference of these dimensionless numbers can present which forces dominate fluids flow and how to reproduce the main flow behaviors in different scenarios (such as different geometry sizes). The schematic graph of flow in the GDL is shown in Fig. 1.4.

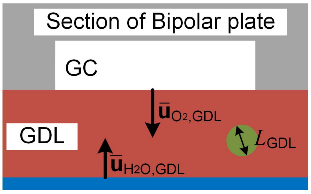

Figure 1.4.: Schematic graph of flow in the GDL. Blue: water; Red: GDL; Green: cross section of single fiber; Gray: section of Biplolar plate

It is seen from Fig. 1.4 that the oxygen (with velocity $\bar{\mathbf{u}}_{\mathrm{O_2,GDL}}$) and water (with velocity $\bar{\mathbf{u}}_{\mathrm{H_2O,GDL}}$) are counter flows in the GDL and under the GC. The flow parallel to the GDL surface (in-plane direction) and the compress of GDL are not considered. The L_{GDL} equals the diameter of single fiber [29]. All data and parameters to calculate dimensionless numbers in GDL are summarized in Table 1.2.

Table 1.2.: Conditions for calculating dimensionless numbers in GDL of the cathode side ($T = 70°\mathrm{C}$, $P = 0.1\ \mathrm{MPa} = 0.1\times10^6\ \mathrm{kg{\cdot}m^{-1}{\cdot}s^{-2}}$)

	Symbols	Values	Unit	Reference
Current density	$\dot{I}$	1.2	$\mathrm{A{\cdot}cm^{-2}}$	Maximum in Fig. 1.3
Stoichiometry number	λ	1	-	Operating condition
Faraday's constant	F	96485	$\mathrm{A{\cdot}s{\cdot}mol^{-1}}$	[24]
Gravity acceleration	$\mathbf{g}$	9.8	$\mathrm{m{\cdot}s^{-2}}$	[30]
Surface tension	σ_s	0.064	$\mathrm{kg{\cdot}s^{-2}}$	Parameter, [30]
Oxygen volume flux in GDL	$\dot{V}_{\mathrm{O_2}}$	1.3×10^{-6}	$\mathrm{m^3{\cdot}s^{-1}}$	Eq. (1.5), Table 1.1
Water volume flux in GDL	$\dot{V}_{\mathrm{H_2O}}$	1.7×10^{-9}	$\mathrm{m^3{\cdot}s^{-1}}$	Eq. (1.6), Table 1.1
Average oxygen velocity in GDL	$\bar{\mathbf{u}}_{\mathrm{O_2,GDL}}$	0.9×10^{-3}	$\mathrm{m{\cdot}s^{-1}}$	Eq. (1.5)
Average water velocity in GDL	$\bar{\mathbf{u}}_{\mathrm{H_2O,GDL}}$	1.1×10^{-6}	$\mathrm{m{\cdot}s^{-1}}$	Eq. (1.6)
Characteristic length in GDL	L_{GDL}	7	μm	Single fiber diameter in GDL of Fig. 1.2
Effective reaction area	A_{eff}	14.44	$\mathrm{cm^2}$	Condition of Fig. 1.3
Transport area in GDL	$A_{\mathrm{trans,GDL}}$	14.44	$\mathrm{cm^2}$	Same as effective area

The gaseous reactant (oxygen) is assumed flowing through the GDL after accessing the GC, and it has no influence on the liquid water transport in GDL [31]. The oxygen and water volume fluxes in GDL and volume flux are calculated from the Faraday's law in Eq. (1.5) and Eq. (1.6). The diameter of single fiber (7 μm) is chosen as the characteristic length in GDL L_{GDL}. The oxygen and water transport area $A_{\mathrm{trans,GDL}}$ is the same as the effective reaction area A_{eff} in GDL and equals 14.44 cm^2 in Table 1.2. Taking $\bar{\mathbf{u}}_{\mathrm{H_2O,GDL}}$, $\bar{\mathbf{u}}_{\mathrm{O_2,GDL}}$ (from Table 1.2) and properties (from Table 1.1) into Eq. (1.7) to Eq. (1.10), average dimensionless numbers in GDL can be calculated and summarized in Table 1.3.

Table 1.3.: Average dimensionless numbers in GDL of the cathode side

	Re	*Ca*	*Bo*	*We*
Gaseous oxygen (O_2)	3.0×10^{-4}	3.3×10^{-7}	1.2×10^{-5}	1.0×10^{-10}
Liquid water (H_2O)	2.2×10^{-5}	0.7×10^{-8}	1.2×10^{-5}	1.5×10^{-13}

The gas transport paths are suggested for the non-flooded pores because of $\mu_{\mathrm{H_2O}}$ is bigger than $\mu_{\mathrm{O_2}}$ (see Table 1.1) [31]. The process of oxygen transport through GDL is simplified to be a single phase flow process that assumes flooded pores are blocked and not be removed by oxygen. The *Re* makes more sense in the single phase process and it is clear that oxygen flow shows the laminar flow behavior ($Re \ll 2300$). The gravity force can be negligible in comparison with surface tension force for *Bo* number. The inertial force and viscous force are negligible when checking the definitions of *Ca* and *We* from Eq. (1.8) and Eq. (1.10) with their corresponding values in Table 1.3.

The process of liquid water flowing through GDL can be simplified as a two phase invasion (or immiscible fluids displacement) problem. According to the SEM bottom-up view image of GDL in Fig. 1.2 and the analysis from the statistician, e.g. Thiedmann [32], GDL is a porous media consists of stochastic fibers. For use in cell level simulation, the water through the GDL can be solved with the continuous approach. But when studying the water through the GDL from a top-down view, the process of liquid water through GDL can be discussed equivalently with a two-phase flows in porous media. In the two-phase flow in porous media problem, the dynamic viscosity ratio *M* are introduced and shown in Eq. (1.11).

$$M = \frac{\mu_{\mathrm{H_2O}}}{\mu_{\mathrm{O_2}}} \tag{1.11}$$

The water flowing through the porous media is studied, so dynamic viscosity ratio *M* is the dynamic viscosity of water divide that of oxygen shown in Eq. (1.11). A phase diagram including the relation of *Ca* and dynamic viscosity ratio *M*, was introduced by Lenormand et al. [33] to represent two-phase flow behaviors in porous media as shown in Fig. 1.5.

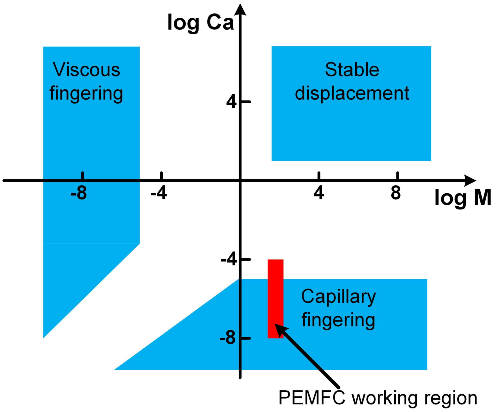

Figure 1.5.: Phase diagram of immiscible fluids displacement in porous media [33][34]. Red : liquid water transport through GDL of PEFC working region.

The phase diagram explains the flow behaviors of the injected fluid and the displaced fluid. In the water through GDL problem, water is the injected fluid and air is the displaced fluid. The phase diagram includes two parameters *Ca* and *M* in logarithm style, which consists of three regions including stable displacement, viscous fingering and capillary fingering. The dynamic viscosity ratio between water and air $M \approx 18$ using the viscosity data from Table 1.1. In the stable displacement region, the stable displacement front is observed. The principal force is due to the viscosity of the injected fluid, but capillary effects and pressure drop in the displaced fluid are negligible. In the viscous and capillary fingering regions, the 'finger' effect can be observed along the flow path. In viscous fingering region, fluid flow is dominated by the viscous force, the density ratio and viscosity ratio between two fluids are not negligible. In the capillary fingering region, the flow behavior is dominated by the surface tension force (or capillary force), the inertia force and viscous force can be negligible. In another word, the viscosity ratio and density ratio of two fluids can be negligible in the capillary fingering region. The red region in the phase diagram Fig. 1.5 shows the PEFC working region and the example calculation is in the red region (*Ca* in Table 1.3 and $M \approx 18$ from Table 1.1). However, it should be noticed that the local *Ca* (calculate by the local water velocity) can be bigger than the average *Ca* (calculate by the average water velocity) because of inhomogeneous ORR reactions and water are produced inhomogeneous.

In summary of discussions of two-phase flow mechanisms in GDL of PEFC, the liquid water flowing through GDL is a capillary force dominated process, which allows to neglect the density ratio and viscosity ratio of two liquids. In local positions of GDL, bigger local inject velocity (larger *Ca*) may happen during the fuel cell operation.

1.2.2. Two-phase flow simulations and experiments

From the macro point of view, some researchers did some reviews on the GDL from different application side. A. Weber et al. [35] reviewed the modeling of transport phenomena in the PEFC. J. Park et al. [36] did a review of GDL from the durability and degradation side. S. Park et al. [37] reviewed the GDL from the materials and application design side. A. Bazylak [38] reviewed the liquid water visualization in the PEFC. R. Anderson et al. [39] reviewed the two-phase flow in GDL and highlighted that this process will be highly affected by two-phase flow in GDL. M. Andersson et al. [40] reviewed the cell-scale two-phase flow modeling in PEFC and found some detailed information from the GDL were still missing. L. Chen et al. [41] reviewed the two-phase LB model application and emphasize its strong benefits on simulating two-phase flow in GDL. D. Wood et al. [42] reviewed the surface properties (particularly the wetting properties) of GDL. Besides these review work, some literature focus on the simulations and experiments to study two-phase flow in GDL. J. Park et al. [43][44] simulated a droplet passing through a quasi-GDL and compared with a simplified LB Stokes-Brinkman model. W. Tao's group [45][46] did some LBM simulations on water transport and distribution inside of GDL, which a 2D GDL was extracted from a 3D reconstructed GDL structures, and the influence of compressiblity, land wettability and *Ca* are discussed. X. Niu et al. [47] studied the relative permeability based on the partially saturated GDL. P. Zhou et al. [48] discussed the effects of fully wettability and spatial mixed-wettability on water configuration by LBM in an artificial random and regular structures. K. Kim [49] did LBM simulation of liquid water transport through MPL and GDL with randomly circle solid distributed porous medias. A 3D single component multi-phase LBM simulation was done by G. Molaeimanesh [50] for the cathode electrode in PEFC and a surface reaction model based on modified bounce back boundary condition was included in model. P. Cheng's group [51][52] were working on the water flowing through the reconstructed GDL and the water dynamic behavior in GC. Y. Tabe et al. [53] did the LBM simulations to elucidate the dynamic behavior of condensed water and gas flow in the PEFC and the two-phase flow with large density ratio in GDL are studied. T.

Koido et al. [54] did the LBM two-phase transport in the GDL with combining the capillary pressure which was measured by the porous diaphragm method and predicted by the PNM. The relative permeability was measured by the steady-state method and predicted by a combination of the single-phase and the two-phase LBM. Y. Gao et al. [55] investigated water flow in the GDL using a combination of the LBM and X-ray computed tomography at the micron scale. The water intrusion into initially dry GDL driven by a pressure gradient in attempts to understand the impact of hydrophobicity on water distribution in the GDL. D. Jeon and H. Kim [56] considered the compression of GDL on the water flow behavior with LBM two-phase model. B. Han and H. Meng [57] did LBM simulations on the interconnected horizontal and vertical pore combinations and discussed effect of the large perforated pores through the GDL. G. Molaeimanesh and M. Akbari [58] studied the water droplets dynamic behavior inside of GDL along the in-plane direction with the LBM. In a further step, the PTFE distribution effect on the water droplets inside of GDL are discussed as well [59]. Our group did some simulation works on LBM simulations in GDL. The Freudenberg GDL geometries are created with some stochastic algorithms by G. Gaiselmann et al. [60][61]. R. Thiedmann et al. [32] created stochastic carbon paper GDL geometries, all of them statistic equivalent to the real 3D structures as validated by the Helmholtz-Zentrum Berlin. The created GDL with stochastic method are applied on the micro-scale simulations (such as LBM simulations) [20][62][63][64][65]. Single component mass transfer was simulated by the LBM for the high-temperature PEFC and the results are analyzed from the stochastic way. Some other researchers were working on the stochastic reconstruction. N. Zamel et al. [66] applied the stochastic GDL geometries to study the species and heat transport properties. J. Hyman et al. [67] studied the heterogeneities of flow in stochastically generated porous media. P. Satjaritanun et al. [68] applied the X-ray computed tomography GDL to the liquid water breakthrough inside it and the effect of wettability on water breakthrough pressure are studied. P. Salaberri et al. [69] studied the effective diffusivity in partially-saturated (through-plane saturation distribution) GDL and applied to the cell-scale continuum models. From the situation of GDL-GC interface side, some literature proves the two-phase flow in GDL affect the two-phase situation in the GC. CZ. Qin [70] did the general simulations for two-phase flow in whole PEFC. X. Zhu et al. [71] simulated the water droplet dynamics in the GC and proved the water breakthrough area and wettability of GDL affect the droplet behaviors. P. Polverino et al. [72] did a ex-situ experimental validation of a lumped model of single droplet behaviors (deformation, oscillation and detachment) on the GDL-GC interface and found some simplifications of droplet lead some errors when comparing the model and experiment.

Some experiments studied the behavior of liquid water flowing through GDL to analyze the process in quantity. A. Bazylak et al. [73] visualize the droplet breakthrough GDL and its growth on the GDL-GC interface. H. Markötter et al. [74] investigate the 3D water transport paths in GDL by combining in-situ synchrotron X-ray radiography and tomography, and the large pores in GDL or cracks in the MPL could identify preferred water transport paths. N. Djilali's group [75] observed more than one water breakthrough path in different time steps. A new transport mechanism was introduced S. Litster et al. [76] (two-phase flow in GDL is dominated by capillary fingering and channeling and features numerous "dead ends") which is consistent with the experimental observations. J. Benziger et al. [77] measured the hydrostatic pressure of different carbon paper and cloth based GDL. A. Santamaria studied the effects of inject area and velocity on droplets formed on GDL interface by injecting water through GDL experiments, and analyzed the mechanisms behind that [78]. F. N. Büchi's group [79][80][81] were working on analyzing liquid saturation, Phosphoric acid electrolyte migration and evaporation in GDL by X-Ray tomographic microscopy. For the experiments checking water distribution through-plane direction in GDL, the very inhomogeneous water distribution along the through-plane direction (from CL to GC) were observed in experiments with high resolution X-Ray radiography [82][83]. Besides some experiments were done to study water flow through the GDL, some experiments were done to study the produced GDL such as PTFE distribution in GDL. T. Kitahara et al. did experiments with hydrophilic and hydrophobic double micro-porous layer coated GDL for enhancing fuel cell performance under no-humidification at the cathode [84]. B. Gao et al. [85] visualized the unstable water flow ('column flow') in different types of GDL. R. Fu et al. [86] used the high-resolution neutron radiography to detect the through-plane liquid water distribution in the GDL and the general tendency of water distribution along the through-plane direction was observed. M. Sabharwal et al. [87] developed a cluster based full morphology model to predict liquid water intrusion in GDL geometries which obtained from μ-CT.

AJ. Mendoza et al. [88] used the Raman spectroscopic mapping to describe the carbon and PTFE distribution in the GDL. W. Song et al. [89] studied the effect of PTFE distribution in the GDL on water flooding in PEFC and presented the uniform PTFE distribution benefited cell performance. A. Rofaiel et al. [90] was the first direct experimental investigation of the through-plane PTFE distribution for various commercially available GDLs. T. Reshetenko et al. [91] used a segmented cell system to study the impact of localized variations of GDL PTFE on the spatial and overall cell performance and the GDL with PTFE structures were studied by SEM. C. Tötzke et al. [92] did the X-ray tomographic study for the hydrophobic treatment on the structure of compressed GDLs and the relation between the PTFE content and porosity were presented. M. Mortazavi and K. Tajiri [93] observed different contact angles on the GDL surface with different PTFE content and the water droplets behaviors on the GDL were influenced by PTFE content and gas velocities in GC. E. Antolini et al. [94] studied the morphological characteristics of carbon/PTFE films deposited on porous carbon support and some physical properties (such as density) of carbon and PTFE are provided. A. Santamaria et al. [78] and BR. Friess et al. [95] did some experiments to study the wettability of GDL and PTFE material. The GDL is made of graphite and some experiments were to study the wettability of graphite material. A. Kozbial et al. [96] observed the contact angle on the polished graphite surface (minimize roughness effect) changes during putting the graphite sample in the ambient air, but the graphite surfaces are intrinsically mildly hydrophilic. C. Pike et al. [97] presented that the GDL is assumed the graphite sample which set in the ambient air longer than the critical time (roughly 20 min). The wettability of graphite was also presented by F. Taherian et al. [98], S. Wang et al. [99] and Rafiee et al. [100] that assume graphite is made of several graphene layers.

In a summary, the experiments for GDL present that the the flow 'fingers' were observed in two-phase flow through the GDL. Droplets formed on the GDL-GC interface and its dynamic process in GC are affected by the GDL surface. The strong relevance of the GDL-GC interface to the two-phase flow in GC were reviewed and clearly declared. The contact angle of the formed droplets is very important. The contact angle is highly affected by the GDL surface properties. It is quite necessary to calculate properties of the two-phase flow on GDL-GC interface from simulation of physical processes in the porous media (GDL). The detailed information on the GDL-GC interface are missing in multi-scale simulations, like the contact angles of droplets on GDL-GC interface and definition of breakthrough point distance. They can be supported by LBM two-phase flow simulations in GDL. Some side-work were done to study the wettability of GDL, but it is still lack of some modeling and simulations study on the two-phase flow in GDL with wettability effects. Moreover, some experiments with applying the GDL with different content or distribution of PTFE were discussed. It was observed the PTFE content and distribution have impact on the water flowing inside of GDL. Therefore, some simulation work for the two-phase flow with effect of PTFE are necessary to have a better understanding the theory behind that.

2. Methods

The LBM is a kinetic gas theory based simulation method [101]. It does not consider fluid particle (or molecule) behavior alone but behavior of collection of fluid particles as a unit. The property of the collected particles is presented by a distribution function and it has many advantages. It is suitable on complex geometries of domain and can be naturally adapted to parallel processing computing [102]. Furthermore, the lattice Boltzmann equation is equivalent with the Navier-Stokes (NS) equations at each time when the flow is assumed to be incompressible and continuum. However, it usually needs more computer memory (the LBM algorithm includes 'collision' and 'stream' steps, both steps needs computer memory) compared with macroscopic CFD solver, which is not a big constraint [103][104].

The LB equations (LBE) can be recovered to the macroscopic NS equations, which the continuity flow is assumed in the macroscopic approach. Under certain conditions, LBM is consistent with macroscopic approaches for continuity flow. The Knudsen (*Kn*) is a characteristic number to define if the flow can be assumed as continuity or not. *Kn* is presented as following formula

$$Kn = \frac{\lambda_f}{L_{\mathsf{GDL}}} \tag{2.1}$$

where λ_f is the mean free path length and L_{GDL} is the representative physical length scale for flow in the GDL. The incompressibility of fluid is also assumed when converting LBE to the NS equations. The correlated dimensionless number to define if the flow can be assumed as incompressible flow, is Mach (*Ma*) number defined in Eq. (2.2).

$$Ma = \frac{\bar{\mathbf{u}}_{\mathsf{H_2O,GDL}}}{c_s} \tag{2.2}$$

where $\bar{\mathbf{u}}_{\mathsf{H_2O,GDL}}$ is the average water velocity in GDL and c_s is the local sound velocity in liquid water. The data used to calculate *Kn* and *Ma* for water flow in GDL are summarized in Table 2.1.

Table 2.1.: Data to calculate *Kn* and *Ma* for water flow in GDL

	Symbols	Values	Unit	Reference
Mean free path length of water	λ_f	0.33	nm	[105]
Representative physical length scale	L_{GDL}	7	µm	Table 1.2
Average water velocity in GDL	$\bar{\mathbf{u}}_{\mathsf{H_2O,GDL}}$	1.1×10^{-6}	$\mathrm{m{\cdot}s^{-1}}$	Table 1.2
Sound velocity	c_s	1555	$\mathrm{m{\cdot}s^{-1}}$	[106]
Knudsen number	*Kn*	4.7×10^{-5}	-	Eq. (2.1)
Mach number	*Ma*	7.1×10^{-10}	-	Eq. (2.2)

The fluid can be assumed as continuity when *Kn* is small enough ($Kn < 10^{-2}$) [107], so the water flow in the GDL can be assumed as a continuous flow ($Kn = 4.7\times10^{-5}$ in Table 2.1).

Furthermore, the water through GDL can be simplified to incompressible flow (Ma=7.1×10^{-10} in Table 2.1) when $Ma < 0.3$ [107][108]. Therefore, the LBM can be applied to simulate water flow through the GDL and a suitable two-phase model should be chosen. There are some main two-phase LBM models including the Rothman-Keller (RK) model (proposed by Rothman and Keller in 1988 and the phase separation occurred by a "color gradient" [109]), the ShanChen pseudo-potential model (proposed by Shan and Chen in 1993 and phase separation is based on collaborating interactive body forces [110]), the free energy model (proposed by Swift et al. in 1995 and two phases are introduced directly to the 'collision' step [111]) and the He-Chen-Zhang (HCZ) model (introduced by He et al. in 1999 and two distribution functions are introduced to recover the incompressible NS equations [112]). Particularly, ShanChen model is the most commonly used two-phase model and it has two sub-models including ShanChen single-component multi-phase (SCMP) model and ShanChen multi-component multi-phase (MCMP) model [113].

In this work, ShanChen MCMP model is chosen to simulate two-phase flow in GDL with the following three main reasons:

(i) Some alternative force schemes (approach of collaborating interaction body force in LBM) were proposed in literature to improve numerical stability and accuracy.

(ii) The two-phase flow in GDL is a capillary force dominated process (see Fig. 1.5), the density ratio and viscosity ratio are negligible.

(iii) Simplification of isothermal condition and phase change (condensation or evaporation) are not considered. The water and gaseous oxygen are assumed two pure components.

However, ShanChen MCMP model also has some limitations such as the limited density ratio and viscosity ratio. They are observed in this work as well and the details are discussed in section 4.2.1 and 4.2.2.

2.1. ShanChen MCMP model

The LBM was firstly developed from the cellular automata, which were originally introduced by Stanislaw Ulam and John vor Neumann in the 1940s [114]. One of milestones for LBM development is the first paper which propose a lattice gas cellular automaton (LGCA) for the NS equations in 1986 by Frisch et al. [115]. The use of a triangular grid restored some of the symmetry required to simulate fluids. A major simplification was introduced by Qian et al. in 1992 [116], that the collision matrix is replaced by a single relaxation time (SRT), leading to the also socalled Bhatnagar, Gross, and Krook (BGK) model. Begining with the 21st century, LBM access a very fast development period. Wolf-Gladrow (2000) [117], Succi (2001) [107], Sukop and Thorne (2006) [118] and A.A. Mohamad [119] all provide instructive information on the model and the extensions. The ShanChen MCMP model was firstly introduced with SRT approach in 1993 [120]. Later in 2002, the ShanChen MCMP model with multiple relaxation time (MRT) approach was extended, which the single relaxation time is replaced by a collision matrix including more than one relaxation time [121].

2.1.1. ShanChen MCMP model with SRT approach

The LBM derived from BGK approximation is called Lattice-BGK (LBGK) method and the Boltzmann equation in a multi-component system is shown in Eq. (2.3) [122].

$$\frac{\partial f_\alpha(\mathbf{x},t)}{\partial t} + \nabla f_\alpha(\mathbf{x},t) + \mathbf{F}_\alpha(\mathbf{x},t) \cdot \nabla f_\alpha(\mathbf{x},t) = -\frac{f_\alpha(\mathbf{x},t) - f_\alpha^{eq}(\mathbf{x},t)}{\tau_\alpha} \tag{2.3}$$

where $f_\alpha(\mathbf{x},t)$ is the single particle distribution function in the phase space $(\mathbf{x},t)$ and $f^{eq}(\mathbf{x},t)$ is the Maxwell-Boltzmann distribution function for αth component, $\alpha = 1$ or 2 in two components system. Eq. (2.3) is solved for each component separately. $\mathbf{x}$ is the position vector and represented (x,y,z) in a 3 dimensional (3D) Cartesian coordinate system. $\mathbf{F}_\alpha(\mathbf{x},t)$ is a body force acting on the αth component, and τ_α is the relaxation time which determines the kinematic viscosity for the αth component. In the Eq. (2.3), there is only one relaxation time τ_α, so the LBGK method is also called LBM with single relaxation time (SRT) approach.

In the LBGK model, the Boltzmann equation (Eq. (2.3)) is discretized and satisfies the lattice Boltzmann equation (LBE) as Eq. (2.4):

$$f_{\alpha,i}(\mathbf{x} + \mathbf{e}_i\Delta t, t + \Delta t) - f_{\alpha,i}(\mathbf{x},t) = -\frac{1}{\tau_\alpha}\left(f_{\alpha,i}(\mathbf{x},t) - f_{\alpha,i}^{eq}(\mathbf{x},t)\right) + S_\alpha(\mathbf{x},t) \tag{2.4}$$

where $f_{\alpha,i}(\mathbf{x},t)$ is the density distribution function of the αth component related to the discrete velocity direction i. The left hand side of equal sign in Eq. (2.4) is called the 'stream' step, while the right hand side of equal sign in Eq. (2.4) is called the 'collision' step. i in Eq. (2.4) is ranging from 0 to 18 according to D3Q19 lattice scheme in 3D cases . The lattice scheme of D3Q19 in this work is shown in Fig. 2.1.

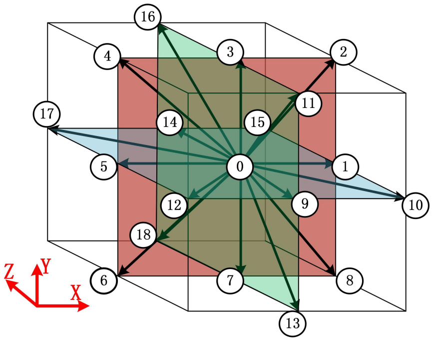

Figure 2.1.: Lattice scheme of D3Q19

The kinematic viscosity ν_α can be calculated from τ_α by Eq. (2.5).

$$\nu_\alpha = c_s^2(\tau_\alpha - \frac{1}{2})\Delta t \tag{2.5}$$

with c_s is the sound speed and set $c_s = 1/\sqrt{3}$ in lattice system. $f_{\alpha,i}^{eq}(\mathbf{x},t)$ are equilibrium distribution function and calculated as [123]

$$f_{\alpha,i}^{eq}(\mathbf{x},t) = \omega_i\rho_\alpha\Big[1 + \frac{\mathbf{e}_i \cdot \mathbf{u}_\alpha^{eq}}{c_s^2} + \frac{(\mathbf{e}_i \cdot \mathbf{u}_\alpha^{eq})^2}{2c_s^4} - \frac{\mathbf{u}_\alpha^{eq} \cdot \mathbf{u}_\alpha^{eq}}{2c_s^2}\Big] \tag{2.6}$$

where $\mathbf{e}_i$ are discrete velocities and summarized in Eq. (2.7). The ω_i are weight factors and shown in Eq. (2.8)

$$\text{D3Q19}: \quad \left[\mathbf{e}_0, \mathbf{e}_1, \mathbf{e}_2, \mathbf{e}_3, \mathbf{e}_4, \mathbf{e}_5, \mathbf{e}_6, \mathbf{e}_7, \mathbf{e}_8, \mathbf{e}_9, \mathbf{e}_{10}, \mathbf{e}_{11}, \mathbf{e}_{12}, \mathbf{e}_{13}, \mathbf{e}_{14}, \mathbf{e}_{15}, \mathbf{e}_{16}, \mathbf{e}_{17}, \mathbf{e}_{18}\right]$$
$$= \begin{bmatrix} 0 & 1 & 1 & 0 & -1 & -1 & -1 & 0 & 1 & 0 & 1 & 0 & -1 & 0 & 0 & 1 & 0 & -1 & 0 \\ 0 & 0 & 1 & 1 & 1 & 0 & -1 & -1 & -1 & 0 & 0 & 1 & 0 & -1 & 0 & 0 & 1 & 0 & -1 \\ 0 & 0 & 0 & 0 & 0 & 0 & 0 & 0 & 0 & -1 & -1 & -1 & -1 & -1 & 1 & 1 & 1 & 1 & 1 \end{bmatrix} \tag{2.7}$$

$$\text{D3Q19}: \qquad \omega_i = \begin{cases} \frac{1}{3} & i = 0 \\ \frac{1}{18} & i = 1{,}3{,}5{,}7{,}9{,}14 \\ \frac{1}{36} & i = 2{,}4{,}6{,}8{,}10{,}11{,}12{,}13{,}15{,}16{,}17{,}18 \end{cases} \tag{2.8}$$

In ShanChen model, different force schemes are chosen when physical effects (such as interaction body forces) are included. In Eq. (2.4), $S_\alpha(\mathbf{x},t)$ is the source term and $\mathbf{u}_\alpha^{eq}$ is equilibrium velocity which have different forms according to force schemes, and they are summarized in Table 2.2 of section 2.2. The fluid density ρ_α and velocity $\mathbf{u}_\alpha$ can be obtained from Eq. (2.9).

$$\rho_\alpha = \sum_{i=0}^{18} f_{\alpha,i} \quad ; \quad \rho_\alpha \mathbf{u}_\alpha = \sum_{i=0}^{18} \mathbf{e}_i f_{\alpha,i} + \frac{1}{2}\mathbf{F}_\alpha \tag{2.9}$$

The total density ρ and velocity of whole components $\mathbf{u}$ are calculated by Eq. (2.10).

$$\rho = \sum_{\alpha=1}^{2} \rho_\alpha \quad ; \quad \rho\mathbf{u} = \sum_{\alpha=1}^{2}\sum_{i=0}^{18} \mathbf{e}_i f_{\alpha,i} + \frac{1}{2}\sum_{\alpha=1}^{2} \mathbf{F}_\alpha \tag{2.10}$$

In ShanChen pseudopotential model, the pseudopotential is presented as the body force $\mathbf{F}_\alpha$ acting on the αth component shown in Eq. (2.11), which includes fluid-fluid cohesion $\mathbf{F}_{\text{coh},\alpha}$, fluid-solid adhesion $\mathbf{F}_{\text{adh},\alpha}$ and external body force $\mathbf{F}_{\text{ext},\alpha}$. Their formulas are presented from Eq. (2.12) to Eq. (2.14).

$$\mathbf{F}_\alpha(\mathbf{x},t) = \mathbf{F}_{\text{coh},\alpha}(\mathbf{x},t) + \mathbf{F}_{\text{adh},\alpha}(\mathbf{x},t) + \mathbf{F}_{\text{ext},\alpha}(\mathbf{x},t) \tag{2.11}$$

$$\mathbf{F}_{\text{coh},\alpha}(\mathbf{x},t) = -G_{\text{coh}}\psi_\alpha(\mathbf{x},t)\sum_{i=0}^{18} w_i\psi_\alpha(\mathbf{x}+\mathbf{e}_i\Delta t,t)\mathbf{e}_i \tag{2.12}$$

$$\mathbf{F}_{\text{adh},\alpha}(\mathbf{x},t) = -G_{\text{adh},\alpha}\psi_\alpha(\mathbf{x},t)\sum_{i=0}^{18} \psi_\alpha(\mathbf{x}+\mathbf{e}_i\Delta t,t)\mathbf{e}_i \tag{2.13}$$

$$\mathbf{F}_{\text{ext},\alpha}(\mathbf{x},t) = \rho_\alpha\mathbf{g}_\alpha \tag{2.14}$$

where ψ_α is called the "effective number density" or interaction potential, and it is defined as a function of $\mathbf{x}$ through its dependency on the local density $\psi_\alpha = \psi_\alpha(\rho_\alpha)$. The interaction potential is special in that its "... behavior is consistent with that of an isothermal process ..." [124][125]. It can have different forms, such as $\psi_\alpha = \rho_\alpha$ [126], $\psi_\alpha = \psi_0\exp(\frac{-\rho_0}{\rho_\alpha})$ [118], $\psi_\alpha = \rho_0\left[1 - \exp(\frac{-\rho_\alpha}{\rho_0})\right]$ [120] and follow different equation of state (EOS) [127]. The ψ_0 and ρ_0 are constants and details can be found in the corresponding literature [23]. In this work,

$\psi_\alpha = \rho_\alpha$ as suggested by Pan et al. [126], because the lattice spacing is usually much larger than the molecule size (a condition necessary for ensemble average) and it completely ignores the effects of the repulsive core. Without a balancing repulsive core, this choice inevitably leads to "mass collapse"– a phenomenon in which particle density approaches the big unrealistic value [110]. Furthermore, Shan et.al (one of inventors of ShanChen model) [128] suggested that $\psi_\alpha = \rho_\alpha$ when the external forces (such as gravity) are not considered. The gravity is negligible from the water transport algorithm in GDL (it is a surface tension force dominated process and gravity can be negligible, see *Bo* in Table 1.3). Moreover, there were some literature of two phase flow simulations in GDL which did the same choice of ψ_α as well [29][55].
G_{coh} in Eq. (2.12) is a parameter that controls the strength of fluid-fluid cohesion [123]. The immiscible phenomena happen when G_{coh} is larger than its critical value $G_{\text{coh,crit}}$ [129]. The $G_{\text{coh,crit}}$ is presented in the form of Eq. (2.15) and was suggested by Huang et al. [129] in D3Q19 ShanChen model.

$$G_{\text{coh,crit}} = \frac{1}{18(\rho_1 + \rho_2)} \tag{2.15}$$

where $\rho_1 + \rho_2$ is the total densities of component 1 and 2 on the same lattice. $G_{\text{adh},\alpha}$ in Eq. (2.13) is the parameter to control the fluid-solid adhesion. In two components system, different contact angles can be achieved by adjusting this parameter and it satisfies the relation $G_{\text{adh},1} = -G_{\text{adh},2}$. In the water transport through GDL simulations of section 5, the value of model parameters $G_{\text{adh},1}$ and G_{coh} are summarized in the Table 5.1 with $G_{\text{coh}} = 0.06$ for immiscible phenomena and $G_{\text{adh},1} = -0.005$ for the contact angle 110°. The $\mathbf{g}_\alpha$ in Eq. (2.14) is the acceleration of external body force such as gravity ($\mathbf{g}_1 = \mathbf{g}_2 = 9.8$ m·s^{-2} [130]). For the simulation of liquid water transfer through the GDL, the gravity is negligible in comparison with the surface tension force (see *Bo* in Table 1.3), so $\mathbf{g}_\alpha$ is not considered in this dissertation. The pressure P of the whole fluid can be computed from the ρ_σ according to Eq. (2.16).

$$P(\mathbf{x}) = c_s^2 \sum_{\alpha=1}^{2} \rho_\alpha(\mathbf{x},t) + 6G_{\text{coh}}\psi_1(\mathbf{x},t)\psi_2(\mathbf{x},t) \tag{2.16}$$

This can also be considered as the EOS of a non-ideal fluid, which makes the separation of liquid and gas phase possible in the SCMP model [127].
There are some limitations on the ShanChen model which use the nearest-neighbor and the next nearest-neighbor interaction model to approximate the effect of the intermolecular potential (Eq. (2.12) and Eq. (2.13)). It was resolved by choosing a ψ_α that is proportional to ρ_α for small ρ_α and tends be to a constant for large ρ_α. However, any choice of ψ_α other than $\psi_\alpha \propto \rho_\alpha$ appears to lead to thermodynamic inconsistencies which is one of main limitations of ShanChen model [125][23]. The Eq. (2.12) behaves the same way as the surface tension and its strength is fixed after choosing G_{coh}. It creates application difficulties in which an adjustable surface tension is required.

2.1.2. ShanChen MCMP model with MRT approach

For the LBM, the generalized hydrodynamics (the wave vector dependence of the transport coefficient) of a generalized LBE is studied. The generalized LBE (is also called LBM with MRT approach) is constructed in the momentum space rather than in the discrete velocity space. The generalized LBM has a maximum number of adjustable parameters for the given set of discrete velocities [131]. In order to improve numerical stability and reduce some side effects by tuning the adjustable relaxation parameters, Dominique et al. [121] derived the MRT collision operator to LBM, and this model is so-called lattice MRT model in 2002. The MRT collision operator is an important extension of the relaxation LB method proposed by Higuera et al. [132]. The standard LB-MRT equation was summarized by d'Humieres et al. [133]. The evolution equation of the LBM (Eq. (2.4)) with MRT collision operator for ShanChen MCMP model can be written in a more general form as Eq. (2.17) [134].

$$f_{\alpha,i}(\mathbf{x}+\mathbf{e}_i\Delta t,t+\Delta t) = f_{\alpha,i}(\mathbf{x},t) - \mathbf{M}^{-1}\Lambda_\alpha(\mathbf{m}_\alpha(\mathbf{x},t) - \mathbf{m}^{eq}_\alpha(\mathbf{x},t)) + S_\alpha(\mathbf{x},t) \tag{2.17}$$

where the transformation matrix $\mathbf{M}$ for D3Q19 in this work are shown in the Appendix A.1. In comparison with the formula of model with SRT approach in Eq. (2.4), the distribution function $f_{\alpha,i}(\mathbf{x},t)$ are replaced by that in the momentum space $\mathbf{m}_\alpha(\mathbf{x},t)$ and the single relaxation time τ_α is replaced by a diagonal matrix Λ_α. With the transformation matrix $\mathbf{M}$, the density distribution function $f_{\alpha,i}$ and its equilibrium distribution $f^{eq}_{\alpha,i}$ can be projected on to the momentum space through the matrix calculation $\mathbf{m}_\alpha = \mathbf{M}f_{\alpha,i}$ and $\mathbf{m}^{eq}_\alpha = \mathbf{M}f^{eq}_{\alpha,i}$. Λ_α in Eq.(2.17) is a diagonal matrix given by

$$\begin{aligned}\Lambda_\alpha = \mathrm{diag}(&s_{0,\alpha},s_{1,\alpha},s_{2,\alpha},s_{3,\alpha},s_{4,\alpha},s_{5,\alpha},s_{6,\alpha},s_{7,\alpha},s_{8,\alpha},s_{9,\alpha},\\ &s_{10,\alpha},s_{11,\alpha},s_{12,\alpha},s_{13,\alpha},s_{14,\alpha},s_{15,\alpha},s_{16,\alpha},s_{17,\alpha},s_{18,\alpha})\end{aligned} \tag{2.18}$$

whose elements represent the inverse of the relaxation time for the transformed distribution function $\mathbf{m}_\alpha$ as it is relaxed to the equilibrium distribution function $\mathbf{m}^{eq}_\alpha$ in the momentum space. Elements in Λ_α follows relations that $s_{0,\alpha} = s_{3,\alpha} = s_{5,\alpha} = s_{7,\alpha}$, $s_{4,\alpha} = s_{6,\alpha} = s_{8,\alpha}$, $s_{10,\alpha} = s_{12,\alpha}$, $s_{16,\alpha} = s_{17,\alpha} = s_{18,\alpha}$ and $s_{9,\alpha} = s_{11,\alpha} = s_{13,\alpha} = s_{14,\alpha} = s_{15,\alpha}$ [121]. The bulk viscosity ζ_α and the kinematic viscosity ν_α of αth component in MRT model is shown in Eq. (2.19) and Eq. (2.20)

$$\zeta_\alpha = \frac{2}{9}(\frac{1}{s_{1,\alpha}} - \frac{1}{2}) \tag{2.19}$$

$$\nu_\alpha = \frac{1}{3}(\frac{1}{s_{9,\alpha}} - \frac{1}{2}) \tag{2.20}$$

In our simulations, $s_{0,\alpha} = 1$ because of consistent with the macroscopic hydrodynamic equation [135][136]. $s_{9,\alpha}$ can be derived by given kinematic viscosity ν_α in Eq. (2.20) in lattice system, and $s_{9,\alpha}$ is equivalent with τ_α in LBGK. Beside $s_{0,\alpha}$ and $s_{9,\alpha}$, some elements remain to be unknown and independently adjustable, and they can be used to tune the stability of the MRT model [121]. In the section 4.2.1 (Fig. 4.10), 4.3 (Fig. 4.16) and 4.4 (Fig. 4.35), the relaxation time dependency are analyzed. Finally, $s_{9,\alpha} = 1.67$ ($\tau_\alpha = 0.6$ see Eq. (2.5)) is used in all water through GDL simulations in section 6 and 7.

According to the theory of ShanChen MCMP model, the MRT approach can overcome some drawbacks (such as relaxation time dependence) with SRT approaches [121]. But the ShanChen MCMP model with MRT approach still has some intrinsic restrictions such as the viscosity ratio and density ratio are limited to one [103] and the details are discussed in section 4.2.1 and 4.2.2. In the simulations of chapter 5 and 7 concerning water flowing through the GDL, it can be concluded this process is dominated by the capillary force (see Table 1.3 and Fig. 1.5), the density ratio and viscosity ratio are all allowed to set as one.

2.2. Force schemes in ShanChen MCMP model

In the ShanChen pseudopotential model, the interaction potential was introduced with forms of interaction force $\mathbf{F}_\alpha$ in Eq. (2.11). Some force schemes were developed to couple the interaction force in the ShanChen model and they all can be implemented independently in

SRT or MRT approach. The algorithms of three main force schemes including shift velocity (SV) scheme [110], Guo scheme [137] and Exact difference method (EDM) scheme [138], are presented in this part.

- **Shift velocity (SV) scheme**

  This force scheme was from the original paper that introduced the pseudopotential multi-phase / multi-component LBM model [120]. The source term $S_\alpha(\mathbf{x},t)$ in Eq. (2.4) is zero. The equilibrium velocity $\mathbf{u}_\alpha^{eq}$ from Eq. (2.6) is computed as:

  $$\mathbf{u}_\alpha^{eq} = \mathbf{u}' + \frac{\tau_\alpha \mathbf{F}_\alpha}{\rho_\alpha} \tag{2.21}$$

  where $\mathbf{u}'$ is the velocity common to the various components and defined as:

  $$\mathbf{u}' = \frac{\sum_{\alpha=1}^{2}(\sum_{i=0}^{18} \frac{f_{\alpha,i}\mathbf{e}_i}{\tau_{\alpha=1}^2})}{\sum_{\alpha=1}^{2} \frac{\rho_\alpha}{\tau_\alpha}} \tag{2.22}$$

  It is seen from Eq. (2.21) that $\mathbf{u}_\alpha^{eq}$ depends on relaxation time τ_α. According to the theory of LBM, that $1/\tau_\alpha$ should locate between 0 and 2. The more instability raises when $1/\tau_\alpha$ is close to 0 and 2 [118].

- **Guo scheme**

  This force scheme was proposed by Guo et al. [137]. The source term $S_\alpha(\mathbf{x},t)$ in Eq. (2.4) takes the following form

  $$S_\alpha = (1 - \frac{1}{2\tau_\alpha})w_i[\frac{\mathbf{e}_i - \mathbf{u}'}{c_s^2} + \frac{\mathbf{e}_i \cdot \mathbf{u}'}{c_s^4}\mathbf{e}_i] \cdot \mathbf{F}_\alpha \tag{2.23}$$

  where $\mathbf{u}'$ is the same as Eq. (2.22). The equilibrium velocity $\mathbf{u}_\alpha^{eq}$ from Eq. (2.6) in Guo scheme is computed as:

  $$\rho_\alpha \mathbf{u}_\alpha^{eq} = \sum_{i=0}^{18} f_{\alpha,i}\mathbf{e}_i + \frac{\mathbf{F}_\alpha \Delta t}{2} \tag{2.24}$$

  Guo scheme can recover the exact NS equations and has no discrete lattice effects [137]. Therefore, Guo scheme will reproduce the original mechanical stability condition of the ShanChen pseudopotential model and it makes the simulation independent of the relaxation time τ_α in MRT approach [139]. In comparison with the SV scheme, it can be seen they are using different way to calculate the equilibrium velocity $\mathbf{u}_\alpha^{eq}$ in Eq. (2.21) and Eq. (2.24). The SV scheme is related with the relaxation time τ_α, but Guo scheme use the body force $\mathbf{F}_\alpha$ directly and is independent of the relaxation time.

- **Exact difference method (EDM) scheme**

  In 2009, Kupershtokh et al. [138] introduced the EDM, which is directly derived from the Boltzmann equation. The source term in Eq. (2.4) is outlined below:

  $$S_\alpha = f_{\alpha,i}^{eq}(\rho_\alpha,\mathbf{u}_\alpha^{eq} + \Delta\mathbf{u}_\alpha) - f_{\alpha,i}^{eq}(\rho_\alpha,\mathbf{u}_\alpha^{eq}) \tag{2.25}$$

  with

  $$\Delta\mathbf{u}_\alpha = \frac{\mathbf{F}_\alpha \Delta t}{\rho_\alpha} \tag{2.26}$$

This source term can be understood as the difference in the equilibrium distribution functions corresponding to the mass velocity before and after the action of a body force during time step at constant density ρ_α. Therefore, the equilibrium velocity is the same as the standard LBE without body force and is computed as follows:

$$\rho_\alpha \mathbf{u}_\alpha^{eq} = \sum_{i=0}^{18} f_{\alpha,i}\mathbf{e}_i \tag{2.27}$$

According to the Chapman-Enskog analysis of LBE with EDM scheme, this force scheme suffer from the discrete lattice effects and therefore cannot recover the correct macroscopic equations [23]. It was observed in the numerical stability investigation of SCMP model that EDM scheme can always simulate the largest achievable density ratio in comparison with SV and Guo scheme [139]. Therefore, it can be concluded that EDM scheme has higher order of numerical stability.

The equilibrium velocity $\mathbf{u}_\alpha^{eq}$ and the source term S_α are listed in Table 2.2 by summary all equations above in this part.

Table 2.2.: $\mathbf{u}_\alpha^{eq}$ and S_α for force schemes

Scheme	Equilibrium velocity $\mathbf{u}_\alpha^{eq}$	Source term S_α
SV	$\frac{\sum_{\alpha=1}^{2}\left(\sum_{i=0}^{18}\frac{f_{\alpha,i}\mathbf{e}_i}{\tau_\alpha}\right)}{\sum_{\alpha=1}^{2}\frac{\rho_\alpha}{\tau_\alpha}} + \frac{\tau_\alpha \mathbf{F}_\alpha}{\rho_\alpha}$	0
Guo	$\frac{\sum_{i=0}^{18} f_{\alpha,i}\mathbf{e}_i}{\rho_\alpha} + \frac{\mathbf{F}_\alpha}{2\rho_\alpha}$	$(1-\frac{1}{2\tau_\alpha})w_i[\frac{\mathbf{e}_i - \mathbf{u}'}{c_s^2} + \frac{\mathbf{e}_i \cdot \mathbf{u}'}{c_s^4}\mathbf{e}_\alpha] \cdot \mathbf{F}_\alpha$
EDM	$\frac{\sum_{i=0}^{18} f_{\alpha,i}\mathbf{e}_i}{\rho_\alpha}$	$f_{\alpha,i}^{eq}(\rho_\alpha,\mathbf{u}_\alpha^{eq}+\Delta\mathbf{u}_\alpha)-f_{\alpha,i}^{eq}(\rho_\alpha,\mathbf{u}_\alpha^{eq})$

In the present model, three force schemes are all implemented. The possibility of the force schemes implementation are proved in the external force driving Poiseuille flow test in section 4.1. Then the accuracy of the three force schemes with SRT and MRT approaches are discussed in the steady flad interface test of section 4.2.1 and it is concluded that the MRT-EDM (the EDM scheme is coupled in the MRT approach) model is the most accurate (the least viscosity dependence) model. Finally, the MRT-EDM model is chosen in all water flowing through the GDL simulations (chapter 5 to 7).

2.3. Open boundary condition

In the present model, the open boundary condition is implemented for the situation in outlet boundary to make the outlet boundary more close to the reality [20]. The open boundary condition is the condition to make the mass flux not change at outlet [140]. When simulating water through the GDL, the situation in the outlet is not specific (e.g. not sure when liquid droplets go out of domain). The situation in outlet boundary is neither the fixed velocity nor the fixed pressure (density), therefore a more general boundary condition in outlet - open boundary condition, is necessary. Some of previous work done by Gao et al. [55] and Mukherjee et al. [29] simplified the outlet boundary with a fixed pressure boundary conditions. The open boundary condition assumes the pressure gradient between the last two grid layers on the outlet

boundary is zero. The flow profile does not change at the outlet boundary and fluid can flow out in arbitrary directions.
The open boundary condition is based on the specific finite difference scheme of the kinetic equation for the discrete velocity distribution function, and a simple extrapolation of the distribution functions on the boundary is applied [141]. The discrete velocity schemes of open boundary lattice on outlet and the grid next to the outlet are shown in Fig. 2.2.

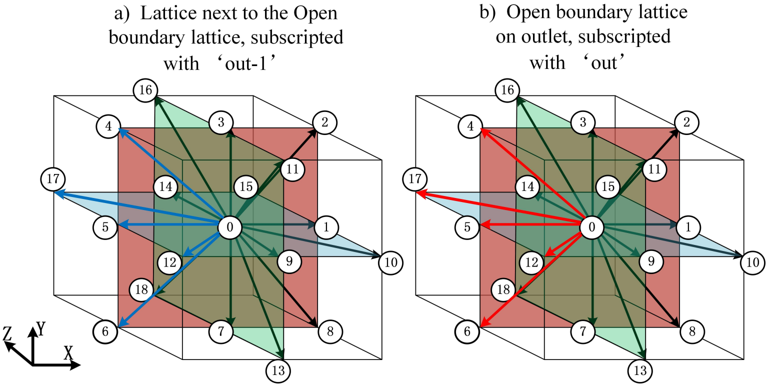

Figure 2.2.: a) Discrete velocities scheme on the lattice next to the open boundary lattices (outlet layer). b) Discrete velocities scheme on the open boundary lattices. Flow is along $\mathbf{X}$ direction. Red discrete velocities are unknown and blue discrete velocities are known after the 'collision' step.

The distribution function on the open boundary lattice (outlet layer) are subscript with 'out' and the lattice next to the outlet are subscript with 'out-1'. Assume fluid flow along X direction, after collision and stream steps, the distribution functions $f_{\alpha,4,\text{out}}$, $f_{\alpha,5,\text{out}}$, $f_{\alpha,6,\text{out}}$, $f_{\alpha,12,\text{out}}$ and $f_{\alpha,17,\text{out}}$ of outlet boundary lattices are unknown (see the red discrete velocity directions in open boundary lattice in Fig. 2.2. In the open boundary condition, they equal to the distribution function from the lattice next to the outlet (see blue discrete velocities on the next open boundary lattice in Fig. 2.2, and formulas are shown in Eq. (2.28):

$$\begin{aligned} f_{\alpha,4,\text{out}} = f_{\alpha,4,\text{out-1}} \quad ; \quad f_{\alpha,5,\text{out}} = f_{\alpha,5,\text{out-1}} \quad ; \quad f_{\alpha,6,\text{out}} = f_{\alpha,6,\text{out-1}} \\ f_{\alpha,12,\text{out}} = f_{\alpha,12,\text{out-1}} \quad ; \quad f_{\alpha,17,\text{out}} = f_{\alpha,17,\text{out-1}} \end{aligned} \tag{2.28}$$

It is seen that this scheme does need some information from the inside flow regions so that at each boundary node, and it is different from the bounce-back condition where each calculation is strictly local. In order to validate the open boundary condition, two numerical tests are done in section 4.5. The behavior of this boundary condition is illustrated in Fig. 4.42 where a droplet can leave the simulation domain without prescribing particular conditions on either phase.

2.4. Unit conversion

In the LBM model, the simulation variables are in the lattice units (LU). In order to connect the lattice system and physical system (with International System of Units (SI)), the unit conversion is needed to convert between LU and SI. The reference variables subscripted by 'r' are used in this conversion, including reference length l_r, reference time t_r and reference mass

m_r. Physical variables with SI (subscripted by 'p') includes length l_p, time t_p and mass m_p, while these variables with LU (subscripted by 'l') include length l_l, time t_l and mass m_l. The conversions of some commonly used variables are shown in Table 2.3

Table 2.3.: Unit conversion between SI and LU

variables	LU	SI	Conversion
Length	l_l	l_p /m	$l_p = l_l l_r$
Time	t_l	t_p /s	$t_p = t_l t_r$
Mass	m_l	m_p /kg	$m_p = m_l m_r$
Density	$\boldsymbol{\rho}_l$	$\boldsymbol{\rho}_p$ $/\mathrm{kg} \cdot \mathrm{m}^{-3}$	$\boldsymbol{\rho}_p = \boldsymbol{\rho}_l \frac{m_r}{l_r^3}$
Kinematic viscosity	$\boldsymbol{\nu}_l$	$\boldsymbol{\nu}_p$ $/\mathrm{m}^2 \cdot \mathrm{s}^{-1}$	$\boldsymbol{\nu}_p = \boldsymbol{\nu}_l \frac{l_r^2}{t_r}$
Velocity	$\mathbf{u}_l$	$\mathbf{u}_p$ $/\mathrm{m} \cdot \mathrm{s}^{-1}$	$\mathbf{u}_p = \mathbf{u}_l \frac{l_r}{t_r}$
Surface tension	$\boldsymbol{\sigma}_{s,l}$	$\boldsymbol{\sigma}_{s,p}$ $/\mathrm{kg} \cdot \mathrm{s}^{-2}$	$\boldsymbol{\sigma}_{s,p} = \boldsymbol{\sigma}_{s,l} \frac{m_r}{t_r^2}$
Force	F_l	F_p $/\mathrm{kg} \cdot \mathrm{m} \cdot \mathrm{s}^{-2}$	$F_p = F_l \frac{m_r \cdot l_r}{t_r^2}$
Pressure	P_l	P_p $/\mathrm{kg} \cdot \mathrm{m}^{-1} \cdot \mathrm{s}^{-2}$	$P_p = P_l \frac{m_r}{l_r \cdot t_r^2} = P_l \boldsymbol{\rho}_r (\frac{l_r}{t_r})^2$

The detailed conversion procedures are below:

(i) Compute the reference length l_r. The physical characteristic length l_p and its equivalent lattice nodes l_l are known. The reference length l_l can be calculated by $l_r = l_p / l_l$ according to the Table 2.3.

(ii) Compute the reference time t_r. It is computed from kinematic viscosity $\boldsymbol{\nu}_p$ and $\boldsymbol{\nu}_l$ of the injected fluid in two-phase simulations (e.g. liquid water is the injected fluid to simulate liquid water flowing through GDL). $\boldsymbol{\nu}_p$ is given from tables of physical properties in the textbook from Lienhard IV and Lienhard V [26]. $\boldsymbol{\nu}_l$ can be calculated from the relaxation time τ_α (Eq. (2.5)) in LBM model with SRT approach, or from elements of diagonal matrix Λ (Eq. (2.20)) in LBM model with MRT approach. The kinematic viscosity of the studied fluid (such as liquid water) is known. According to the Table 2.3, the reference time can be computed with Eq. (2.29).

$$t_r = \frac{\boldsymbol{\nu}_l l_r^2}{\boldsymbol{\nu}_p} \tag{2.29}$$

(iii) Compute the reference mass m_r. It is computed from $\boldsymbol{\sigma}_{s,l}$ and $\boldsymbol{\sigma}_{s,p}$. ShanChen pseudopotential model is a phenomenally based model and momentum is not conserved locally [124]. Therefore, $\boldsymbol{\sigma}_{s,l}$ can be obtained from numerical experiments of Laplace law (static droplet test) by ShanChen model [55]. $\boldsymbol{\sigma}_{s,p}$ between two immiscible fluids can be found from surface science literature [142]. According to the Table 2.3, the reference mass m_r can be computed by Eq. (2.30).

$$m_r = \frac{\boldsymbol{\sigma}_{s,p} t_r^2}{\boldsymbol{\sigma}_{s,l}} \tag{2.30}$$

An detailed example of unit conversion, which is used in all water flowing through the GDL simulations from chapter 5 to 7, is shown in Appendix A.2.

2.5. Apparent contact angle on rough surface

When simulating liquid water through the GDL (and also the in-situ experimental observations of two-phase flow process through GDL on the running PEFC), droplets are formed on the GDL surface. The GDL surface is very rough and irregularly consists of carbon fibers shown in Fig. 1.2. Therefore, how to calculate the apparent contact angle on the rough surface are discussed in this part. Moreover, the information of apparent contact angle can bridge the gap in the multi-scale simulations of PEFC (as motivated in section 1.1).

When analyzing the droplet shape on the solid surface, some physical principles are behind. The droplet shape (the shape of the liquid-vapor interface) on the solid surface will be formed based on the thermodynamic equilibrium between three phases: the liquid phase (L), the solid phase (S) and the gas or vapor phase (G) with Young-Laplace equation in Eq. (2.31) [143].

$$\gamma_{\mathsf{SG}} - \gamma_{\mathsf{SL}} - \gamma_{\mathsf{LG}}\cos\theta = 0 \tag{2.31}$$

with the solid-vapor interfacial energy is denoted by γ_{SG}, the solid-liquid interfacial energy by γ_{SL}, the liquid-vapor interfacial energy (is also called the surface tension) by γ_{LG} and the local contact angle θ. The γ_{SG}, γ_{SL} and γ_{LG} are values with unit kg·s^{-2}. In some cases (such as images of droplet on a solid surface), these three interfacial energy are unknown. Therefore, a post-process method is proposed to analyze asymmetric droplet shapes (contact angles).

For the PEFC application, after liquid water breaks through GDL, droplets are formed on the GDL-GC interface. According to the description in section 1.2.2, contact angles of the formed droplets can be an input parameter of two-phase droplets simulations in GC. It was observed that the formed droplets shapes are asymmetric on the irregular surface [144]. The droplet shape can reflect the GDL surface irregularity. Capturing the drop profile and establishing the baseline are very important to perform accurate drop shape analysis. A clear and sharp liquid-solid interface, high-quality sessile drop image with sharp and focused boundary, will reduce errors in assigning the baseline and fitting the drop profile. In typical practices, these can be proceeded by hardware and software of measuring devices [145].

The contact angle can be calculated after the drop shape profile is captured and handled by curve-fitting software in most of the commercial goniometers. There are several mathematical methods to calculate contact angles including tangential method, circle method, ellipse method, Young-Laplace method, polynomial method, sub-pixel polynomial fitting (SPPF) method and B-spline snakes method. Some of them are limited to symmetric droplets, such as tangential method, circle method and Young-Laplace method. The ellipse method can be applied on the slightly asymmetrical drop, while the polynomial and SPPF method have no limitation on droplet shape.

These methods have advantages and disadvantages. The tangential method is to take the tangent at the contact point after digitize a 2D cross section of the droplet. It may have large errors from disturbance of drop shape. Ellipse method is similar with circle method, but instead of an assumed ideal circle by a ellipse which is more generic. Ellipse fitting method is using mathematical algorithm to process the geometry information and it may lead small deviation (more accurate) for large droplets with large contact angles (the droplet shape with large contact angle is more asymmetric for bigger droplet and the gravity may not be negligible). Young-Laplace method is also called axisymmetric drop shape analysis (ADSA). The drop shape is axisymmetric under the surface tension and the gravity. It is often used if the drops are highly axisymmetric. In this work, circle method and SPPF method are applied on symmetric and asymmetric droplet shape analysis separately. They are introduced in details below:

- **Circle method**

  The principle of circle method assumes the liquid drop on the holder surface is part of ideal sphere without influence of gravity when drop volumes are very small. Therefore, this method is only valid for the symmetric droplet. It is the most simple method for the symmetric droplet with higher accuracy. The schematic graph of a cross-section of an symmetric (idealized) droplet is shown in Fig. 2.3.

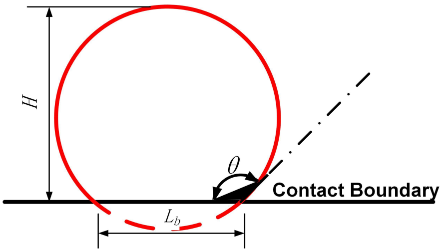

Figure 2.3.: Schematic graph of circle method. Solid red line: droplet shape profile; dash red line: spurious circle droplet boundary; solid black line: contact boundary

  The shape profile of the idealized droplet is symmetric with line vertical to contact boundary and through the center of contact length [146]. The contact length is L_b and the droplet height is H. According to the symmetric geometry analysis, the idealized contact angle θ_{idl} is simplified as twice of arctan$(H/(\frac{L_b}{2}))$ and computed as

$$\theta_{\text{idl}} = 2 \times \text{arctan}\left(\frac{2H}{L_b}\right) \tag{2.32}$$

  In order to describe the observations of contact angles in experiments or simulations, an apparent contact angle θ_{ap} is introduced. The θ_{ap} is the contact angle on the cross section of droplet which is vertical to the contact base and through the geometry center of the contact area. For the symmetric droplet, the contact angle fulfilled the relation in Eq. (2.33).

$$\theta_{\text{idl}} \equiv \theta_{\text{ap}} \tag{2.33}$$

- **SPPF method**

  In this work, SPPF method will be applied on asymmetric droplet shape analysis. It fits the captured drop profile near the three phase point and the contact angle is calculated using the slope of the polynomial at the contact point which is selected by a spurious sub-pixel on the contact boundary [147]. Therefore, the apparent contact angle θ_{ap} can be analyzed locally. The local θ_{ap} are the same for the symmetric droplets but different for the asymmetric ones. It mainly consists of three steps.

  (i) Detecting the droplet boundary. The threshold value is defined on one scaled field of domain (density field in our simulations). The droplet boundary points can be found as red grids in Fig. 2.4 a).

(ii) Finding the contact point. The three-phase (water, air and solid) points (contact point, yellow grid in Fig. 2.4 b)) can be found by the 1st order polynomial curve fitting (blue curve in Fig. 2.4 b)) [148]. In theory, there are two contact points (because of two three-phase point) on the cross section of the droplet, but only one contact point is shown in Fig. 2.4 b). The SPPF finds the exact location of the contact point by extrapolating the drop boundary points and intersecting it with the contact line. A 1st order polynomial (blue line in Fig. 2.4 b)) is used for extrapolation and the contact line selects the solid-neighbor layer in the fluid-solid interface. Such improved precision, can avoid the problem when one deals with very high contact angles [147]. It is difficult to encounter when trying to detect the full drop profile for contact angle measurement, the macroscopic weave of the textile fibers and the flexibility of the fabric will hinder a discerning of the substrate baseline [148].

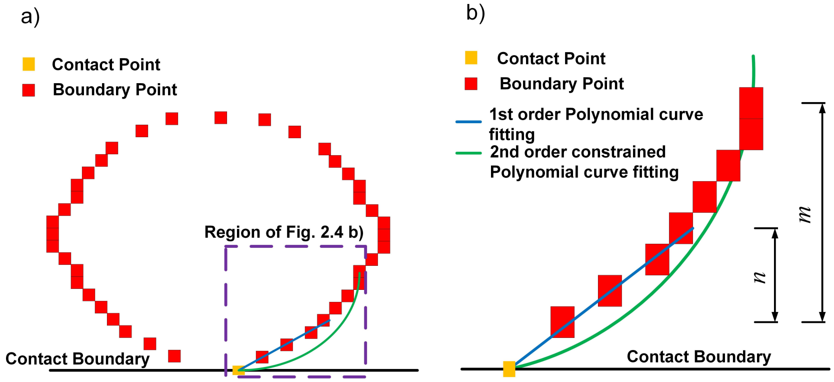

Figure 2.4.: a) Schematic graph of SPPF; b) Zoomed schematic graph of SPPF [149]

The certain amount of available drop boundary points (n) close to contact point are chosen to be fitted to generate the 1st order polynomial curve fitting. The n should be bounded to be smaller than 9% of the available drop boundary points (points along the droplet height direction in hydrophobic cases) [147].

(iii) Contact angle calculation. Contact angle is found from the slope of the 2nd order constrained fitted polynomial (green curve in Fig. 2.4b)) through the contact point. The number of pixels required for the 2nd order constrained polynomial curve fitting is m. In the last step, m should be adjusted to fit the 2nd order polynomial to the drop boundary with the constraint of the contact point [147]. The selections of n and m will be discussed later in section 4.4.

All postprocess of results were done in Paraview 5.0 and calculation of curve fittings were done by in-house program in MATLAB R2009b. The details of how to procedure SPPF method in MATLAB can be seen in Appendix A.3.

3.Simulation framework

All of 3D simulations are based on an in-house LB solver - Julabos. It was developed by J. Brinkmann from the institute of energy and climate research (IEK-3), Forschungszentrum Jülich [20]. The whole solver was implemented in Fortran90. It is capable to simulate single phase, multi-phase and multi-components problems by LBM concerning applications of HT-PEFC or PEFC.

3.1. Simulation process

The working flow chart of Julabos is shown in Fig. 3.1.

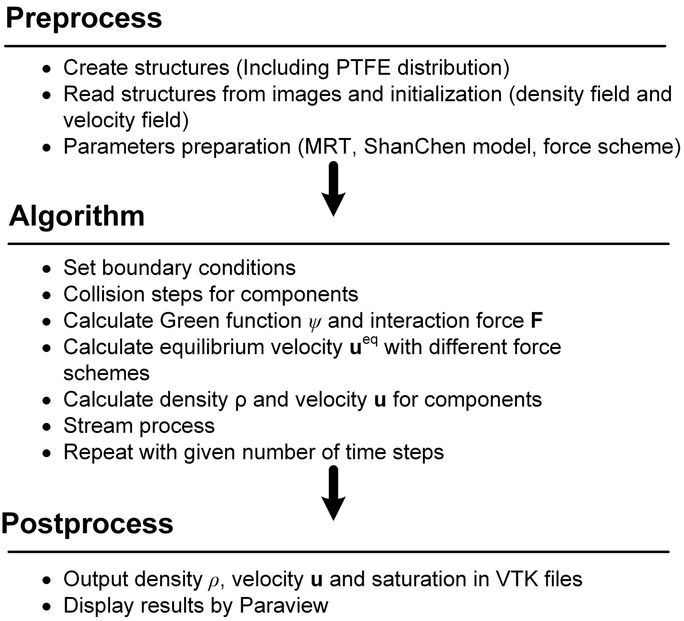

Preprocess

- Create structures (Including PTFE distribution)
- Read structures from images and initialization (density field and velocity field)
- Parameters preparation (MRT, ShanChen model, force scheme)

Algorithm

- Set boundary conditions
- Collision steps for components
- Calculate Green function ψ and interaction force **F**
- Calculate equilibrium velocity $\mathbf{u}^{eq}$ with different force schemes
- Calculate density ρ and velocity **u** for components
- Stream process
- Repeat with given number of time steps

Postprocess

- Output density ρ, velocity **u** and saturation in VTK files
- Display results by Paraview

Figure 3.1.: Working flow chart of Julabos

It is seen from Fig. 3.1 that some specific features concerning PEFC applications and algorithms are included in this LBM solver.The Julabos consists of three main steps including preprocess, algorithm and postprocess. In preprocess, the stochastic GDL geometries which are equivalent to the real GDL geometries are used and the details of the geometry are introduced in section 3.2. After reading geometries, domain field initialization are done as well including density and velocity fields. Some switch functions are defined to select single-phase or multi-phase, MRT or SRT, force schemes (including SV, Guo and EDM schemes) and forms of interaction potential ψ_α (including $\psi_\alpha = \rho_\alpha$, $\psi_\alpha = 1 - \exp(-\rho_\alpha)$, Peng-Robinson (P-R) EOS and Carnahan-Starling (C-S) EOS [127]).

Then jump to the algorithm step that follows the usual calculation procedures of LBM model. Boundary conditions on inlet and outlet are checked in every loop and some boundary condition types are available which includes pressure, velocity, open and periodic boundary conditions.

Density and velocity fields on pressure or velocity boundaries are updated by Zouhe method [150]. The open boundary condition is only valid on the outlet boundary in Julabos [141]. Periodic boundary means the system is closed by the edges being treated as if they are attached to the opposite edges [118]. When simulating the water flowing through the GDL and applying the periodic condition around the GDL structures, the periodic condition has effect on the flow near the periodic boundaries. Because the periodic condition is only valid for the fluid grid but not for the solid grid, the fluid can flow with periodic situation, but the GDL structures are not periodic. The fully periodic boundaries are also useful for simplifies an infinite domain of multi-phase or multi-components validation cases [151]. The solid grids are divided to the inner solid grid and solid surface grid by checking if any solid neighbor grids are fluid grids. All boundary conditions are applied on the fluid grids. For example the standard bounce-back conditions is applied on the fluid-solid interface grids, and it is particularly simple and play a major role in making LBM popular on flows in porous media [107]. In the LBM, two main steps in the algorithm part are 'collision' and 'stream' steps. These two steps are processed in every loop of the simulation. In the two-phase LBM simulations, the interaction force, the equilibrium velocity are calculated according to the force scheme defined in the preprocess step. Then the density and velocity in whole fluid field are calculated in every loop. In the postprocess, the VTK format files are output which can be read by the postprocess software Paraview. The density and velocity distribution can be visualized in Paraview 5.0.
The algorithm of parallel computing is using IntelMPI package [152]. The computation speed t_{cal} (time for one iteration) of a test case (10^6 total grids) against number of CPUs is shown in Fig. 3.2 a) for single component and two components with SRT and MRT approaches. The dimensionless calculation time t^* are also shown in Fig. 3.2 b) and the dimensionless time t^* are computed with Eq. (3.1).

$$t^* = \frac{t_{\text{cal}}}{t_{\text{cal,min}}} \tag{3.1}$$

with $t_{\text{cal,min}}$ is the minimum calculation time and it equals computation speed when CPU amount is 240.

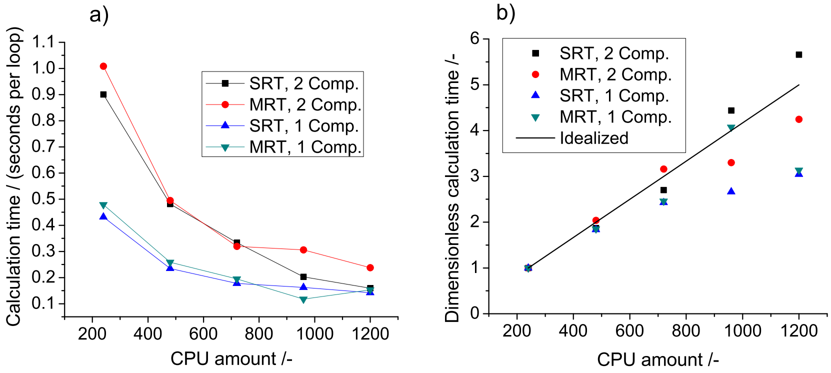

Figure 3.2.: a) Computation time of MRT and SRT with single and two components. b) Dimensionless computation time of MRT and SRT with single and two components in comparison with the idealized case

It is seen from Fig. 3.2 a), the whole tendency that the computation time is decreasing with more CPU, and calculation for 1 component is almost half of that for 2 components (2 components means roughly proceeds whole simulation of 1 component twice). MRT and

SRT consumed almost the same time but SRT is a little bit faster than MRT ($\approx 5\%$) when CPU amount $\leqslant$ 720. Concerning this issue, it is valuable to use MRT if we can achieve a higher stability or accuracy. When CPU amount $>$ 720, the decrease of computation time is not obvious and even have some fluctuation (e.g. the 1200 CPU consumed more time in comparison with 1200 and 960 CPU in MRT). Moreover, the case with MRT consumed less time than that with SRT (see Fig. 3.2 a), 1 component in SRT and MRT with 960 CPU). It means the parallel computation is efficient in a certain range ($\leqslant$720 CPU in this case) and the parallel is not strongly efficient afterward. It is possible to get the same conclusion from Fig. 3.2 b) more directly when comparing with the idealized speed optimization curve. When CPU amount increases, the t^* have further distance away the idealized curve. It also proves the parallel computation is less efficient when increasing CPU numbers. Due to the theory of MPI algorithms, the computation speed does not only depend on CPU amounts but also CPUs distribution (communication time is necessary between CPUs and more communication time is needed in a worse CPUs distribution).

3.2. Geometry introduction

In preprocess, 3D structures are created externally and read from a serious of 2D images with portable graymap (PGM) format along the flow direction as shown in Fig. 3.4. In the simulations, the GDL structures were created by Thiedmann et al. [32]. Some assumptions and simplifications were made in the geometry model including only straight fibers, binders, negligible fibers oriented to the direction of the GDL thickness and distributing intersecting carbon fibers randomly in the in-plane direction. The introduction of the geometry model are presented in Fig. 3.3

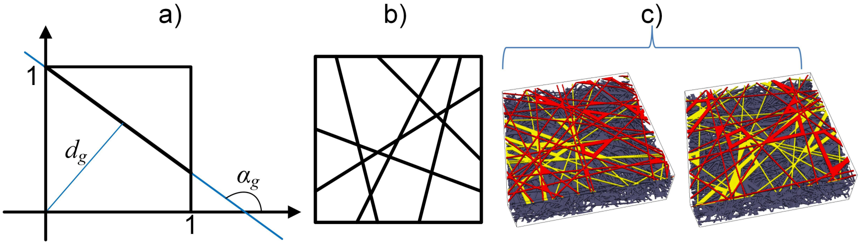

Figure 3.3.: a) Algorithm of setting a single fiber in a certain region. b) Several single fibers are set on one layer. c) Two realized 3D GDL geometries (red: fibers on the 1st layer of GDL; yellow: fibers on the 2nd layer of GDL)

The fibers within a given thin section are seen as mutually penetrating cylinders. The random line tessellations are done with the Poisson line tessellations (PLT) (planar random line tessellations as a modeling element for the fibers within the individual thin sections). It is seen from Fig. 3.3 a), a single fiber is distributed on a certain region (e.g. a unit square) with two random variables d_g and α_g. The values of the signed distance d_g can be arbitrary real numbers, whereas the random directions α_g take values between 0 and π. After that how often the single fibers connecting to each other are defined according to the experiment observation of actual carbon paper GDL structures. The single fiber is dilated to the defined fiber diameter (7 µm). Then some single fibers are distributed on layers of whole domain. After that the fibers are dilatated until the total domain volume is covered by fibers related to intensity of the PLT (as shown in Fig. 3.3 b)). Finally, some 2D layers are assembled toward flow direction to

create a 3D structures (shown in Fig. 3.3 c)). In this work, 22 GDL realizations were used on simulations. In Fig. 3.3 c), two of them are shown and it is clear the structures of the top two layers of GDL are different but these two geometries are all statistically equivalent to the real GDL structures. The present GDL geometries have the same porosity (0.8) [32]. The same geometries had been applied on some of our previous works [62][64][65].
After creating the GDL structures. the hydrophobic material PTFE can be distributed on the structures. Some regions with PTFE can be arranged randomly in every image (e.g. In Fig. 3.4, red is PTFE; black is carbon solid). The coverage fraction of PTFE in GDL can be defined by an in-house Java program.

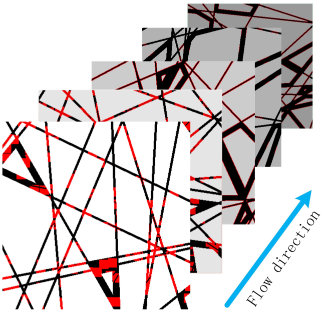

Figure 3.4.: 3D geometry is built with a series of 2D images along the flow direction. Red: PTFE; Black: carbon

The PTFE only has opportunities to distribute on the solid surface grids. The PTFE distribution is done by a in-house Java program. The PTFE distribution process is a separate independent image postprocess and it is based on a certain random algorithm. The working flow chart is shown in Fig. 3.5

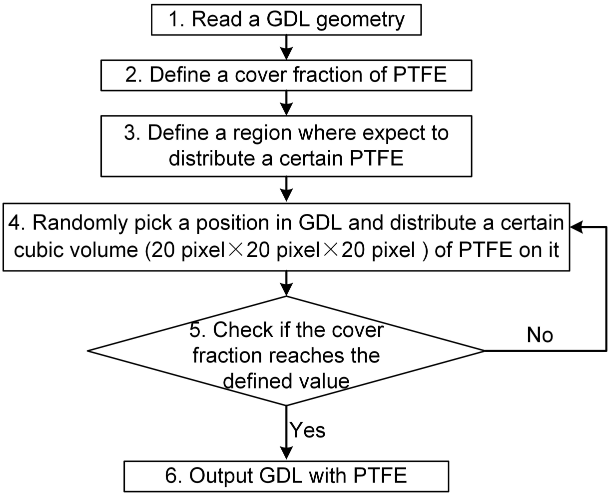

Figure 3.5.: Working flow chart of PTFE distribution on the GDL geometries.

As shown in Fig. 3.5, the working flow chart of PTFE distribution includes six steps. A fresh GDL (cover fraction of PTFE is zero) is read in the first step and then an expected PTFE cover fraction is defined in the second step. In the third step, a specific region of GDL is chosen to distribute the defined PTFE cover fraction on it. In the fourth and fifth step, the PTFE is distributed randomly with cubic region (20 pixel × 20 pixel × 20 pixel) to the GDL geometry until the expected coverage fraction of all fibers is achieved. Finally, outputting a GDL geometry with PTFE which can be read in Julabos. With covering PTFE on carbon fiber solids, only the carbon fiber surface grids (next to the fluid grids) convert to the PTFE grids. As discussed in detail in section 7.1, the PTFE distribution in postprocess does not change the porosity in our simulations. The size of the single cubic region can be varied, 20 pixel side length is selected in this work because of the corresponding local roughly estimated PTFE region area is around 30 µm × 30 µm from GDL SEM images [153]. In this dissertation, the GDL geometries are applied on the two-phase flow simulation through the GDL. The GDL geometries can be characterized with different local hydrophobicity (with PTFE or without PTFE).

4. Model validation

In this section, five tests were done to check the model validation, including external force driving Poiseuille flow test, flat interface test, droplet test, contact angle test (CAT) and open boundary condition test. Separately, different test can validate different specific features. The external force driving Poiseuille flow test validate the implementation of force schemes (introduced in section 2.2) in the ShanChen model and compared these force schemes with SRT approach. The flat interface test is to validate the model capability of simulating two immiscible components in the most idealized case (flat interface between two phases) with a steady flat interface test (without external force). Comparisons between SRT and MRT approach are presented in an external force driving layered Poiseuille flow test. In the droplet test, the more complex two-phase situation (interface between two phases are not flat but a droplet) are validated including single droplet test, cubic initialization test and coalescence test. In the two-phase flow transport inside of complex geometries, the non-flat two-phase interface are commonly seen and more realistic. In the contact angle test, the selection of input parameter $G_{\text{adh},\alpha}$ is discussed and the SPPF method (introduced in section 2.5) is validated. In the last open boundary condition test, the validation of implemented open boundary condition (introduced in section 2.3) is performed.

4.1. External force driving Poiseuille flow test

In this section, a poiseuille flow between two parallel plates, which is driven by the constant external body force $\mathbf{F}_{\text{ext},1}$ (see Eq. (2.14)), is simulated in D3Q19 ShanChen single component model with SRT approach. The following goals are expected to be achieved in the external force driving Poiseuille flow test:

(i) Check if the different force schemes can be implemented in LB single phase model (the most fundamental LB model).

(ii) Check the accuracy of the force schemes in LB single phase model.

The total force $\mathbf{F}_1 = \mathbf{F}_{\text{ext},1}$ because cohesive force and adhesive force are not included ($\mathbf{F}_{\text{coh},1} = \mathbf{F}_{\text{adh},1} = 0$, see Eq. (2.12) and Eq. (2.13)). The three force schemes (SV scheme, Guo scheme and EDM scheme, introduced in section 2.2) are validated and compared. Because of symmetry this case, a 2D ($\mathbb{Z}$ coordinate is neglected) schematic graph of the external force driving Poiseuille flow test is shown in Fig. 4.1.

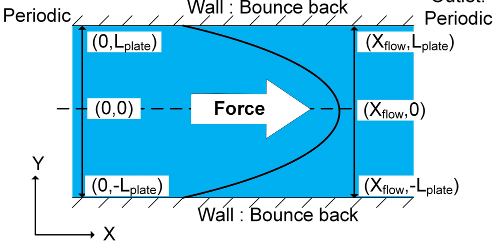

Figure 4.1.: Graphic description of Poiseuille flow between parallel plates driven by constant external force ($\mathbb{Z}$ coordinate is neglected because of symmetry and periodic condition)

$\mathbf{F}_1$ towards fluid flow direction (X direction). Top and bottom are solid walls and bounce back non-slip boundary conditions are applied. The periodic conditions are applied on all other boundaries. The fluid region is initialized with the uniform density (ρ_1) and zero velocity. For the Poiseuille flow between infinite plates, the dimensionless number *Re* is to present the fluid flow behaviors and defined as Eq. (1.7). With $\mathbf{u} = \mathbf{u}_1$ is the main (average) velocity of the field, the characteristic length L equals $2L_{\text{plate}}$, which is the distance between two plates. The kinematic viscosity ν_1 with lattice unit can be calculated by Eq. (2.5). In this validation case, all simulations are done with *Re*=300 concerning the actual gaseous reactant flow in GC under some certain operating conditions [154]. When the laminar flow between plates achieve the equilibrium state, the velocity profile along the flow direction will be the parabolic shape (see Fig. 4.1). In this case, $\mathbf{F}_1$ can be equivalent to the pressure gradient and represented as:

$$\mathbf{F}_1 = \mathbf{F}_{\text{ext},1} = (P_{\text{inlet}} - P_{\text{outlet}})/\mathrm{X}_{\text{flow}} \tag{4.1}$$

where P_{inlet} and P_{outlet} are pressure of inlet and outlet separately, and X_{flow} is the straight distance between inlet and outlet along the flow direction. The analytical velocity $\mathbf{u}_{\text{anal}}$ in any cross section which is vertical to the flow direction and independent of position along flow direction, is shown in Eq. (4.2).

$$\mathbf{u}_{\text{anal}}(x,y,z) = \frac{\mathbf{F}_1}{2\rho_1\nu_1}(L_{\text{plate}}^2 - y^2) \tag{4.2}$$

The average analytical velocity $\mathbf{u}_{\text{anal,aver}}$ in this case is computed with Eq. (4.3) [118].

$$\mathbf{u}_{\text{anal,aver}} = \frac{2}{3}\mathbf{u}_{\text{anal,max}} = \frac{\mathbf{F}_1 L_{\text{plate}}^3}{3\rho_1\nu_1^2} \tag{4.3}$$

where $\mathbf{u}_{\text{anal,max}}$ is the analytical maximum velocity which will be in the center-line along the flow direction ($y = 0$). L_{plate} is the distance from center-line along the flow direction to one of plates ($y = L_{\text{plate}}$ or $y = -L_{\text{plate}}$). Then the *Re* in this case can be calculated by combining Eq. (4.3) and Eq. (1.7) to the Eq. (4.4).

$$Re = \frac{\mathbf{u}_{\text{anal,aver}}(2L_{\text{plate}})}{\nu_1} = \frac{2\mathbf{F}_1 L_{\text{plate}}^3}{3\rho_1\nu_1^2} \tag{4.4}$$

The dimensionless analytical velocity $\mathbf{u}_{\text{anal}}^*$, dimensionless numerical velocity $\mathbf{u}^*$ (simulation result) and dimensionless position y^* along Y direction, where in the middle of domain ($x = \mathrm{X}_{\text{flow}}/2$) are normalized according to Eq. (4.5).

$$\mathbf{u}_{\text{anal}}^* = \mathbf{u}_{\text{anal}}/\mathbf{u}_{\text{anal,max}} \quad ; \quad \mathbf{u}^* = \mathbf{u}/\mathbf{u}_{\text{anal,max}} \quad ; \quad y^* = y/(2L_{\text{plate}}) \tag{4.5}$$

Then $\mathbf{u}_{\text{anal}}^*$ and $\mathbf{u}^*$ are involved to calculate the relative error ε_r by Eq. (4.6).

$$\varepsilon_r = \frac{\sqrt{(\mathbf{u}^* - \mathbf{u}_{\text{anal}}^*)^2}}{\mathbf{u}_{\text{anal}}^*} \tag{4.6}$$

The accuracy and validation of the force schemes is checked by ε_r.

It is seen from Eq. (4.4) that *Re* is affected by L_{plate}, ν_1 and $\mathbf{F}_1$ while ρ_1 is fixed. The following results shows ε_r of different L_{plate}, ν_1 and external body force $\mathbf{F}_1$.

Fig. 4.2 shows one of simulation results with $\mathbf{F}_1 = 5 \times 10^{-5}$ l.u., $\tau_1 = 1$ ($\nu_1 = 0.17$ l.u. from Eq. (2.5)) and *Re*=300.

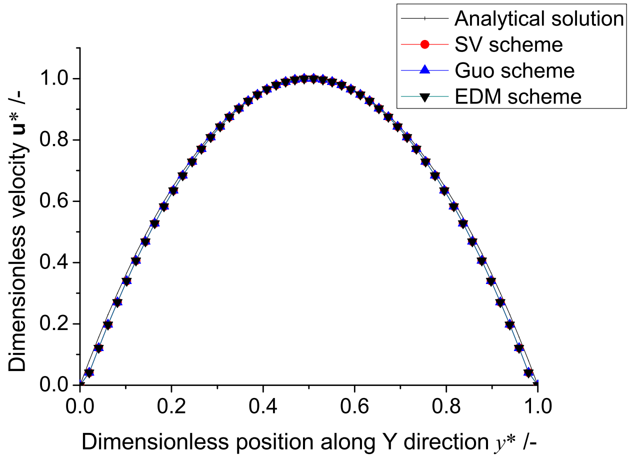

Figure 4.2.: Dimensionless velocity $\mathbf{u}^*$ against dimensionless position y^* along flow direction. $\mathbf{F}_1 = 5 \times 10^{-5}$ l.u., $\tau_1 = 1$ and *Re*=300.

It is seen that three force schemes agreed well with the analytical solution. The results of three force schemes are the same within the numerical deviation. So it is concluded that these three force schemes show the same effects and are equivalent in this validation case. The following results of this validation case are shown with one of schemes (SV scheme) and the other two schemes gave the same results as SV scheme in our simulations. All results shown in this validation case are all in l.u..

- **Lattice dependence analysis**

  The lattice dependence is analyzed under this item. The channel width $2L_{\text{plate}}$ varies from 10 l.u. to 190 l.u.. The lattice dependency with varying *Re* is discussed and the result is shown in Fig. 4.3

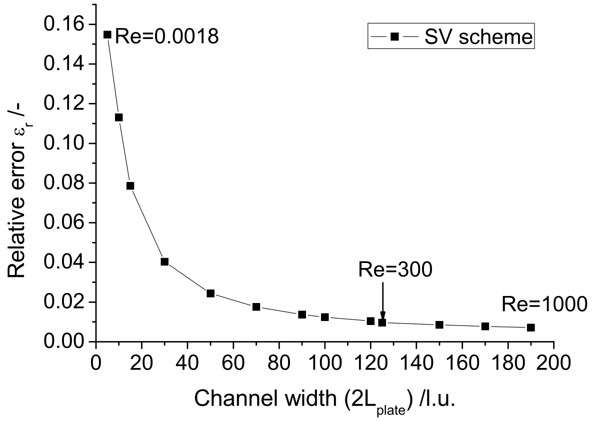

Figure 4.3.: Error dependence of varying channel width $2L_{\text{plate}}$. $\mathbf{F}_1 = 5 \times 10^{-5}$ l.u., $\tau_1 = 1$ ($\nu_1 = 0.17$ l.u. see Eq. (2.5)). Guo scheme and EDM scheme shows the same result. The point of *Re*=300 shows the case in Fig. 4.2

It is seen the *Re* increases with bigger L_{plate} when $\mathbf{F}_1$ and τ_1 is fixed (Eq. (4.4)). It can also be concluded that the errors increase when the fluid flowing in the situation which the characteristic length is small (such as 30 l.u. with roughly $\varepsilon_r = 0.04$ in Fig. 4.3). The error decreases with bigger L_{plate} but with different *Re*. The Fig. 4.4 studied how the L_{plate} affects the error with the fixed $Re = 300$. The $\mathbf{F}_1$ is adjusted by Eq. (4.7) to ensure the same *Re*.

$$\mathbf{F}_1 = \frac{\rho_1 \text{Re}(\tau_1 - 0.5)^2}{6L^3_{\text{plate}}} \tag{4.7}$$

The Eq. (4.7) can be derived by combining Eq. (2.5) and Eq. (4.4).

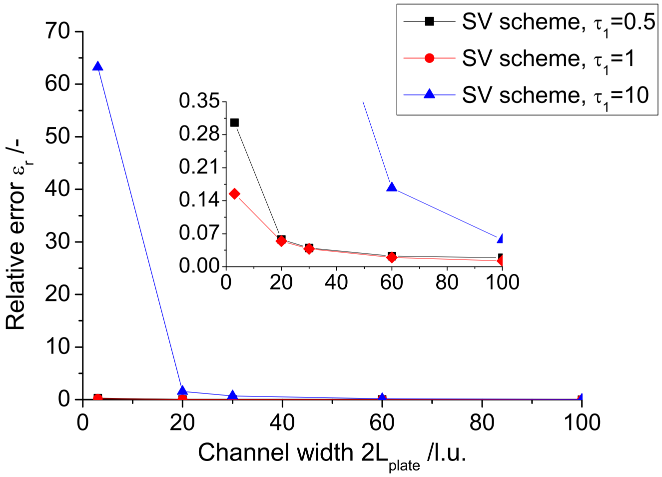

Figure 4.4.: Error dependence of varying channel width $2L_{\text{plate}}$ when *Re*=300. Force $\mathbf{F}_1$ is adjusted according to Eq. (4.7). Guo scheme and EDM scheme shows the same result.

It is seen that the error increases with rough grids for L_{plate}. The τ_1 has impact on the error as well and the error is in the similar order of magnitude when grids in L_{plate} is fine. when $\tau_1 = 10$, the errors have a sharp increase beyond our usual acceptable order of magnitude ($O(10^{-2})$) and the smallest error is represented with $\tau_1 = 1$.

- **Relaxation time dependence analysis**

The influence of the relaxation time τ_1 on error is discussed in this item. The SRT approach is applied on this validation case, τ_1 should have effects on the result in theory of LBM [107][20]. Fig. 4.5 shows the relative error against the relaxation time τ_1 with $2L_{\text{plate}} = 100$ l.u. and $Re = 300$. Force $\mathbf{F}_1$ is adjusted by Eq. (4.7) to ensure the same *Re*.

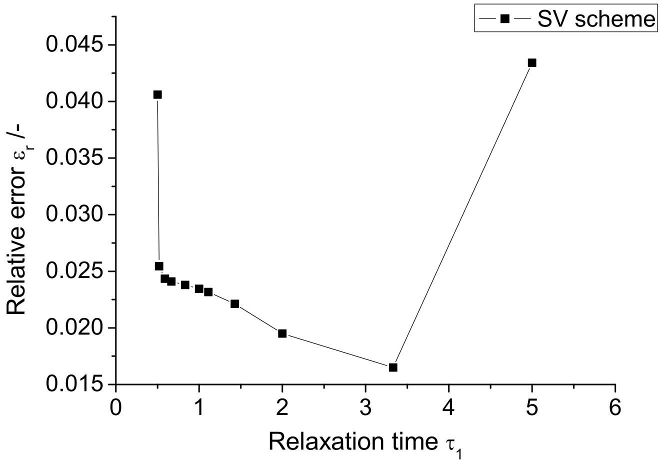

Figure 4.5.: Error dependence of varying relaxation time τ_1 when *Re*=300. Force $\mathbf{F}_1$ is adjusted according to Eq. (4.7) and $2L_{\text{plate}} = 100$ l.u.. Guo scheme and EDM scheme shows the same result.

It is seen that the relative errors are in the order of magnitude ($O(10^{-2})$) when 0.503$\leqslant \tau_1 \leqslant$5. In the range of $1.5\times10^{-2} \leqslant \varepsilon_r \leqslant$ 2.5 $\times$ 10^{-2}, the relative error decreases with bigger τ_1. When τ_1 is close to the two limits ($\tau_{1,\text{upl}} = \infty$ and $\tau_{1,\text{lowl}}$ =0.5), the errors increase very sharply. Moreover, the kinematic viscosity will become nonphysical (zero or very large, see Eq. (2.5)). It is consistent with the observations on some other LBM simulations of PEMFC like the work from Jan P. Brinkmann et al. [62].

- **Force dependence analysis**

The error from magnitude of force $\mathbf{F}_1$ is analyzed in this item. *Re* is fixed to 300 and $\mathbf{F}_1$ is varied. The relaxation time τ_1 is adjusted by reorganizing Eq. (2.5) and Eq. (4.4) to Eq. (4.8) and ensure the fixed *Re*.

$$\tau_1 = 0.5 + \sqrt{\frac{6\mathbf{F}_1 L_{\text{plate}}^3}{\rho_1 Re}} \tag{4.8}$$

Fig. 4.6 shows the result of the relative error against a series of $\mathbf{F}_1$. The corresponding *Re* is varied. $2L_{\text{plate}} = 100$ l.u..

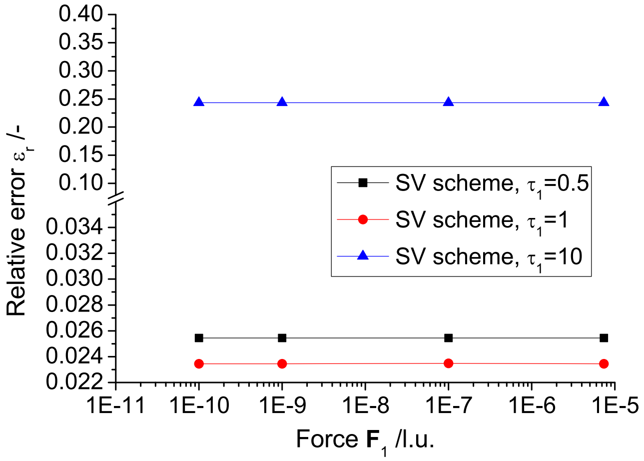

Figure 4.6.: Error dependence of varying force $\mathbf{F}_1$ when relaxation time τ_1 is fixed to $0.5, 1$ and 10. $2L_{\text{plate}} = 100$ l.u.. Guo scheme and EDM scheme shows the same result.

It is seen that the individual variation of $\mathbf{F}_1$ has no effects on relative error ε_r when τ_1 is fixed. The ε_r is lower when $\tau_1 = 1$ than another two cases ($\tau_1 = 0.5$ and $\tau_1 = 10$). Especially, the error of $\tau_1 = 10$ is very large and around ten times larger than that with τ_1 =1. This is also observed in Fig. 4.5 and consistent with the conclusion from relaxation time dependence analysis.

- **Convergence speed analysis**

  Convergence speed is an important criterion for the efficiency of a simulation. It is checked by the Cauchy convergence criterion as Eq. (4.9)

$$\left| \frac{\max\{\mathbf{u}_{it-g} : \mathbf{u}_{it}\} - \min\{\mathbf{u}_{it-g} : \mathbf{u}_{it}\}}{\max\{\mathbf{u}_{it-g} : \mathbf{u}_{it}\}} \right| < \varepsilon_{\text{limit}} \tag{4.9}$$

  where it is the iteration steps and g =1000 is the range of values along time steps here. $\varepsilon_{\text{limit}}$ is the criterion for accuracy. The monitored velocity **u** is the average value in whole domain. Results are converged when Eq. (4.9) is fulfilled and $\varepsilon_{\text{limit}}$ is set to 10^{-6}. The convergence speed of three force schemes when $Re = 300$ is shown in Table 4.1.

Table 4.1.: Convergence time steps of $Re = 300$ for different force schemes

τ_1	$\mathbf{F}_1$	SV scheme	Guo scheme	EDM scheme
10	0.289	1589	1589	1589
1	8×10^{-4}	17404	17404	17404
0.527	2.22×10^{-6}	226275	226275	226275

$\mathbf{F}_1$ is adjusted according to Eq. (4.7) by reorganizing Eq. (4.8) to ensure *Re* is fixed to 300. It is observed that convergence speed is independent of force scheme. The simulations are converged faster with increasing τ_1. This observation is consistent with the theory that the bigger kinematic viscosity fluid will converge faster (see Eq. (2.5)) [118].

In a summary, we can get some following conclusions from this validation case. The SV, Guo and EDM force schemes can be implemented in the LB model and compared by using Poiseuille flow between parallel plates. They have the exactly the same accuracy in the single component system. The lattice dependence test shows that the results are more accurate on finer grids. In SRT-LB model, the results are relaxation time dependent. Error arises when the relaxation time is close to the numerical limits. In the force dependence analysis, the accuracy is independent of force strength in the single component system. In the convergence speed analysis, it is observed that convergence speed increases when a bigger relaxation time is applied. In the next section, force schemes will be included in the MRT-LB model, the SRT and MRT approaches are compared.

4.2. Flat interface test

The capability of simulating two immiscible phases are validated by some cases having flat interfaces in this section. Firstly, the steady flat interface case without external force is discussed. Then a two phase displacement test with proper boundary conditions are discussed. Finally, an external force driving layered Poiseuille flow is checked that force acting on direction parallel to the flat interface. In this section, the SRT and MRT approaches are compared and one of them is fitted on the afterward simulations.

4.2.1. Steady flat interface test

In this section, the steady flat interface test (SFIT) is done with the lattice unit. It is the most simple case to check the possibility to simulate the two-phase problem. The SRT model with SV force scheme (SRT-SV), SRT model with EDM force scheme (SRT-EDM) and MRT model with EDM force scheme (MRT-EDM) are evaluated in this case. Because the SRT-SV model was most commonly used in LB ShanChen model before the appearance of EDM force scheme and MRT approach [113]. In the ShanChen MCMP model with MRT approach, the EDM force scheme does not affect the collision operator and can be implemented independently [155]. Moreover, the model parameter G_{coh} (see Eq. (2.12)) which controls the fluid-fluid strength is necessary to be defined as the model input parameter. Therefore, two following goals are expected to be validated in SFIT.

(i) Comparison of the force schemes with SRT and MRT approaches. Especially the SRT-SV, SRT-EDM and MRT-EDM are compared. A fixed $G_{\text{coh}} = 0.06$ is chosen for force scheme comparison.

(ii) Determine a proper model parameter G_{coh} for water flowing through the GDL simulations. After decision of a force scheme with SRT or MRT approach, a proper G_{coh} is determined for the afterward water flowing through GDL simulations in chapter 5 to 7. In order to achieve this goal, five different G_{coh} ($G_{\text{coh}} = 0.03, 0.04, 0.05, 0.06$ and 0.08) are discussed.

The 3D schematic of SFIT is shown in Fig. 4.7.

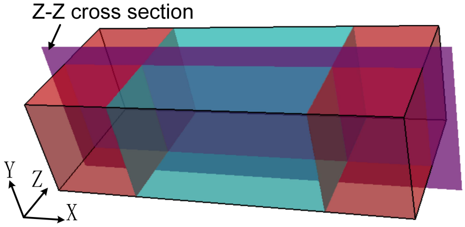

Figure 4.7.: 3D schematic graph of the SFIT test. (Blue: component 1; Red: component 2; Purple: Z-Z cross section)

The domain size is 100 l.u. × 50 l.u. × 50 l.u. in X, Y and Z coordinate.The component 1 is located in the center region of whole domain while the component 2 located on the two sides of domain. The periodic conditions are applied on all boundaries and initial interface thickness between two components is zero. The initialization of domain is based on the LB model studies on PEMFC by Chen et al. [45]. The center component 1 region is initialized with $\rho_{1,\text{init}} = 2$ l.u. and $\rho_{2,\text{init}} = 10^{-5}$ l.u., while the component 2 region is initialized with $\rho_{1,\text{init}} = 10^{-5}$ l.u. and $\rho_{2,\text{init}} = 2$ l.u.. Therefore, $G_{\text{coh,crit}} = \frac{1}{36}$ according to Eq. (2.15). $G_{\text{coh}} = 0.06$, which is approximately twice of $G_{\text{coh,crit}}$, is chosen to ensure two components are immiscible. The plots of density and velocity distribution of SFIT (Fig. 4.8 and Fig. 4.9) are based on this $G_{\text{coh}} = 0.06$ as well.

In theory of immiscible components, the interface thickness between two components should be the same as initialization because of periodic conditions and mass conservation. There is no two-phase interface thickness when initializing the domain. Because the interface is in the molecular or nanometer range, which is much lower than the scales of simulated domain (micrometer and mesoscopic method)[156]. In this test case, the viscosity ratio between two components is set to one with the same relaxation time ($\tau_1 = \tau_2$, see Eq. (2.5)). Fig. 4.8 and Fig. 4.9 shows the average density and velocity distribution on the Z-Z cross section for one of results ($\tau_1 = \tau_2 = 0.6$, $G_{\text{coh}} = 0.06$).

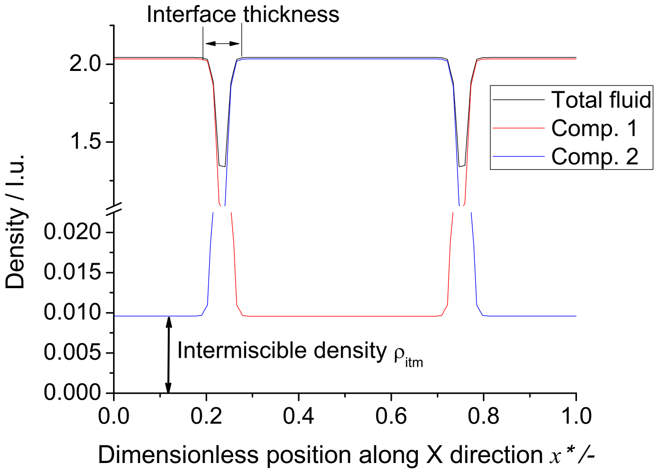

Figure 4.8.: Density distribution of components (according to Eq. (2.9)) and total fluid (according to Eq. (2.10)) on the cross section Z-Z. $\tau_1 = \tau_2 = 0.6$, $G_{\text{coh}} = 0.06$

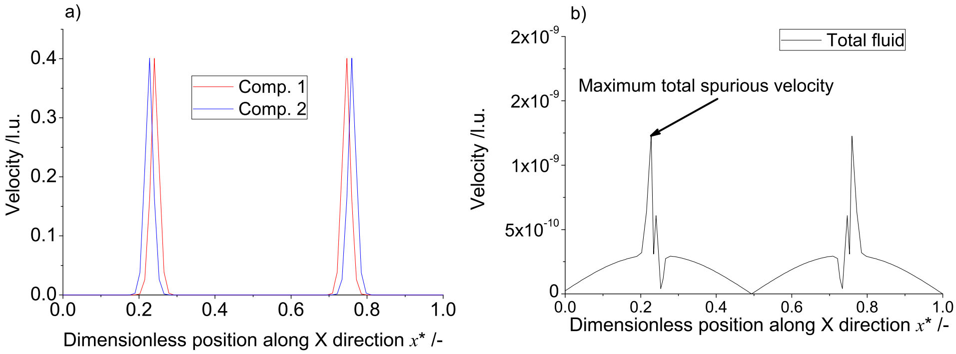

Figure 4.9.: a) Velocity distribution of components (according to Eq. (2.9)) on the Z-Z cross section; b) Velocity distribution of total fluid (according to Eq. (2.10)) on the Z-Z cross section. (Parameters are set $\tau_1 = \tau_2 = 0.6$, $G_{\mathsf{coh}} = 0.06$)

It is seen from Fig. 4.8 that immiscible components are distributed in different regions with the same density value (density ratio between two components is one). The density of total fluid is lower than that of separate component on the interface region between two components. The region where the total fluid density is different from initial values, is defined as the interface in Fig. 4.8. It is seen that the interface (thickness) is different from initialization (interface thickness is zero). The minimum density of component 2 in the component 1 region is not zero and it is the density dissolved in another components. This dissolved density is called intermiscible density ρ_{itm}. In our simulations, two phases are assumed two exactly immiscible components, therefore the dissolved density should be zero. Then the intermiscible density is one of error sources in simulation. The interface is located at the position where the density equals $(\rho_{1,\mathsf{init}} + \rho_{2,\mathsf{init}})/2$. The scaled intermiscible density $\rho_{\mathsf{itm}}{}^*$ is introduced to normalize the density with lattice units. The $\rho_{\mathsf{itm}}{}^*$ is defined with the ratio between intermiscible density ρ_{itm} and the initial density of whole fluids ($\rho_{\mathsf{init}} = \rho_{1,\mathsf{init}} + \rho_{2,\mathsf{init}} = 2 + 10^{-5}$ l.u.).

From the velocity distribution in Fig. 4.9, velocity of two components separately $\mathbf{u}_1$, $\mathbf{u}_2$ and total fluid velocity $\mathbf{u}$ are all located on the interface region. In theory, when SFIT is in the equilibrium state, $\mathbf{u}$ should be zero. However, the total fluid density is not zero, the $\mathbf{u}$ is called the total spurious velocity $\mathbf{u}_{\mathsf{spu}}$. The maximum total spurious velocity $\mathbf{u}_{\mathsf{spu,max}}$ are much smaller than the maximum spurious velocity of two components $\mathbf{u}_{1,\mathsf{spu,max}}$ and $\mathbf{u}_{2,\mathsf{spu,max}}$.

- **Relaxation time dependence analysis**

  The impact of τ_1 $(= \tau_2)$ on intermiscible density and maximum total spurious velocity are shown in Fig. 4.10 and Fig. 4.11 with $G_{\mathsf{coh}} = 0.06$.

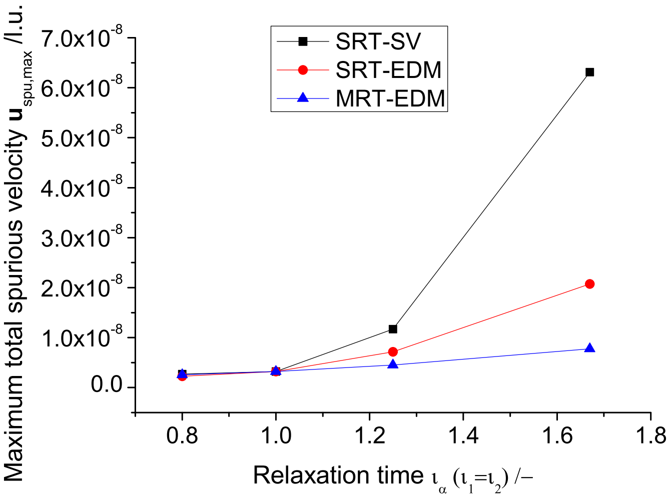

Figure 4.10.: Relaxation time τ_α $(\tau_1 = \tau_2)$ against maximum total spurious velocity $\mathbf{u}_{\mathsf{spu,max}}$ for different models $(G_{\mathsf{coh}} = 0.06)$.

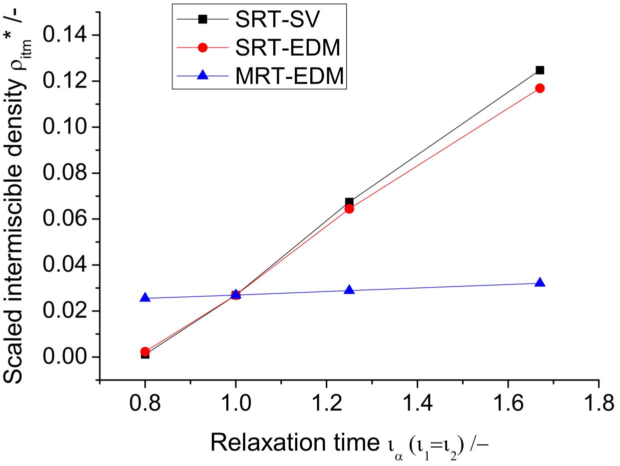

Figure 4.11.: Relaxation time τ_α $(\tau_1 = \tau_2)$ against scaled intermiscible density $\rho_{\mathsf{itm}}{}^*$ for different models $(G_{\mathsf{coh}} = 0.06)$.

In comparision with these three models, MRT-EDM is the most relaxation time independent model and it improves the accuracy and numerical stability of the model [121]. When relaxation time $\tau_\alpha = 1$, the results from these three cases are the same and it is consistent with the conclusion from Sun et al. [157] that SV scheme is identical to the EDM scheme when the $\tau_\alpha = 1$. In the SRT-SV and SRT-EDM, both are relaxation time dependent, the $\mathbf{u}_{\mathsf{spu,max}}$ and $\rho_{\mathsf{itm}}{}^*$ are larger with bigger relaxation time. In another words, the algorithm error in MRT-EDM is independent of relaxation time while that in

SRT-SV and SRT-EDM are affected by relaxation time. Therefore, the MRT-EDM is chosen to apply on all the afterward simulations.

- **Parameter G_{coh} dependence analysis**

  As description of cohesive force $\mathbf{F}_{\text{coh},\alpha}$ in Eq. (2.12), it is correlated with the parameter G_{coh} to directly control the strength of $\mathbf{F}_{\text{coh},\alpha}$. In the following part, the effect of G_{coh} on the $\mathbf{u}_{\text{spu,max}}$ and ${\rho_{\text{itm}}}^*$ are discussed.

  The density distribution of component 1 with different G_{coh} is shown in Fig. 4.12. In order to ensure the phase separation happens, the relation $G_{\text{coh}}(\rho_{1,\text{init}} + \rho_{2,\text{init}}) > 1/18$ has to be fulfilled [129], and $G_{\text{coh}} > 0.028$ with $\rho_{1,\text{init}} + \rho_{2,\text{init}} = 2$ l.u. in this work. Therefore, G_{coh} range from 0.03 to 0.08 are discussed in Fig. 4.12.

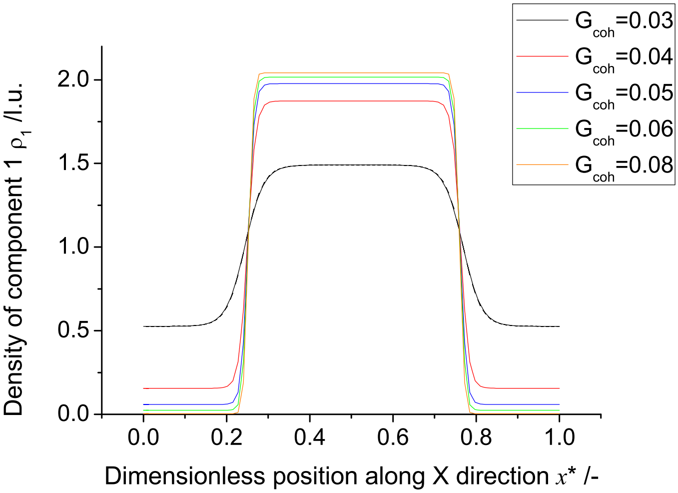

Figure 4.12.: Density distribution of component 1 in the Z-Z interface with different G_{coh} $(\tau_1 = \tau_2 = 0.6)$

It is seen that with G_{coh} increase, the ρ_{itm} decrease. The interface thickness locate the density transition region from the minimum to the maximum (see Fig. 4.8). For example when G_{coh} =0.03, the density transition region (ρ_1 from approximate 0.5 to 1.5) is from x^* ≈0.18 to x^* ≈0.3 and the total domain length along X direction is 100 l.u., so the interface thickness can be calculated from the definition of $x*$ and the interface thickness is 100 × (0.3-0.18)=12 l.u.. Use the same principle, the interface thickness can be analyzed from Fig. 4.12 and summarized in Table 4.2

Table 4.2.: Interface thickness with different G_{coh}. ($\tau_1 = \tau_2$ =0.6)

G_{coh}	Interface thickness /l.u.	G_{coh}	Interface thickness /l.u.
0.03	12	0.04	6
0.05	4	0.06	3
0.08	3	-	-

The interface thickness decreases with bigger G_{coh} (when $G_{\text{coh}} = 0.03$, interface thickness occupy roughly 10% of total length along X direction in this case). Then the results of $\rho_{\text{itm}}{}^*$ and the maximum total spurious velocity $\mathbf{u}_{\text{spu,max}}$ with different G_{coh} are shown in Fig. 4.13 and Fig. 4.14

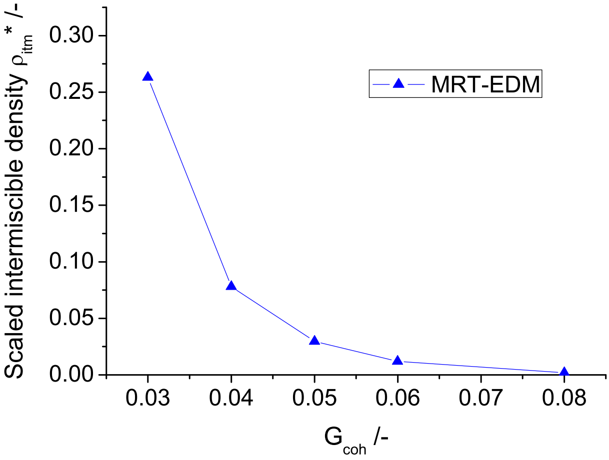

Figure 4.13.: Scaled intermiscible density $\rho_{\text{itm}}{}^*$ changes with different G_{coh}. $(\tau_1 = \tau_2 = 0.6)$

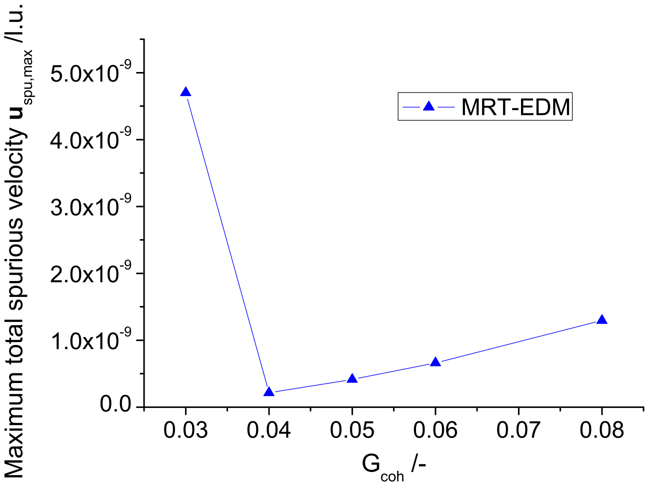

Figure 4.14.: Maximum total spurious velocity $\mathbf{u}_{\text{spu,max}}$ changes with different G_{coh}. $(\tau_1 = \tau_2 = 0.6)$

It is seen from Fig. 4.13 that $\rho_{\text{itm}}{}^*$ decreases with larger G_{coh}. When $G_{\text{coh}} = 0.08$, $\rho_{\text{itm}}{}^*$ is small and very close to zero. When $G_{\text{coh}} > 0.08$, the negative density may produce and the program is easily crashed. In Fig. 4.14, the $\mathbf{u}_{\text{spu,max}}$ increases with bigger G_{coh}

when $0.04 < G_{\text{coh}} < 0.08$. The $\mathbf{u}_{\text{spu,max}}$ raised very sharply when $G_{\text{coh}} = 0.03$, but its $\mathbf{u}_{\text{spu,max}}$ is in the same order with that of other G_{coh}. In summary, it can be concluded that variation of G_{coh} will cause different algorithm errors ($\rho_{\text{itm}}{}^{*}$ and $\mathbf{u}_{\text{spu,max}}$). In this disseration, the scaled intermiscible density $\rho^{*}_{\text{itm}} < 0.025$ and the maximum total spurious velocity $\mathbf{u}_{\text{spu,max}} < 10^{-9}$ are assumed in the SFIT. $G_{\text{coh}} = 0.06$ is chosen for all the afterward validation tests and water flowing through the GDL applications.

In summary, the interface thickness between two fluids and total spurious velocity should be very small and can be neglected from mesoscopic scale[158]. These two features are the main error source of the algorithm. However, the LBM algorithm cause some error in the interface region, such as interface thickness and spurious velocity. The ShanChen MCMP model with MRT and SRT approaches are compared. The SRT approach is relaxation time dependent. For MRT approach, the relaxation time τ_α have less effect on the spurious velocity and intermiscible density than that with SRT approach. When $\tau_1 = \tau_2 = 1$, both SRT and MRT approaches performed the same result within a certain accuracy. Therefore, the ShanChen MCMP model with MRT approach is preferred when $\tau_1 = \tau_2 \neq 1$. The parameter G_{coh} also has impact on the accuracy of model. $G_{\text{coh}} = 0.06$ is chosen to balance the intermiscible density and the spurious velocity.

4.2.2. External force driving layered Poiseuille flow

In this section, an external force driving layered Poiseuille flow between two parallel plates is simulated. It is to validate the capability of simulating immiscible components with different viscosity. The following goals are expected to be achieved within the external force driving layered Poiseuille flow:

(i) Check if the MRT-EDM ShanChen model is possible to simulate two-phase flow with different viscosity.

(ii) Check the accuracy of simulating two-phase flow when the viscosity of two phases are not the same.

As discussed in section 4.2.1, the MRT-EDM model is more independent of the relaxation time τ_α in the SFIT test. Therefore, MRT-EDM is chosen to applied in this layered Poiseuille flow test. The 3D schematic graph of this validation case is shown in Fig. 4.15 a) and the situation on Z-Z cross section is shown in Fig. 4.15 b). The density and velocity field are initialized the same way as that in the SFIT test. The boundary conditions are the same as that in no-layered Poiseuille flow between plates of section 4.1 (solid walls are set on the $y = \text{L}_{\text{plate}}$ and $y = -\text{L}_{\text{plate}}$ boundaries, and the periodic conditions are applied on other boundaries). The two components interface position fulfilled the relation $\text{L}_{\text{plate}} = 2\text{L}_{\text{wet}}$. An external force is acting on the direction parallel to the X-Z plate. The domain is arranged with 100 l.u. × 50 l.u. × 50 l.u. in X, Y and Z directions, which is the same as domain size in the SFIT of section 4.2.1

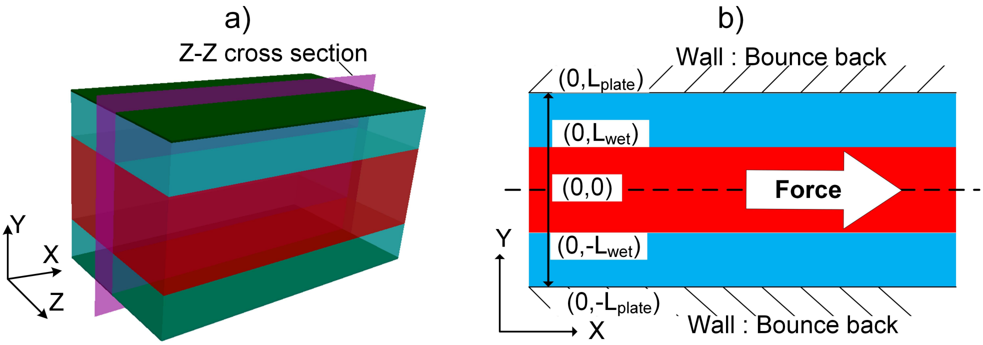

Figure 4.15.: a) 3D schematic graph of the external force driving layered Poiseuillr flow. b) 2D Schematic graph of external force driving layered Poiseuille flow between plates on the cross section in Fig. 4.15 a) (Red: component 1 and wet phase region; Blue: component 2 and non-wet phase region; Green: solid plate wall; Purple: cross section)

Here the layered Poiseuille flow between the parallel plates is assumed to be the laminar and fully developed flow. Its analytical velocity profile in the Z-Z cross section can be calculated by Eq. (4.10) and Eq. (4.11) [159]

$$\mathbf{u}_{\mathsf{anal}}(x,y,z) = \frac{\mathbf{F}_\alpha}{2\rho_2\nu_2}(\mathsf{L}_{\mathsf{plate}}^2 - y^2) \tag{4.10}$$

in the component 2 region where $\mathsf{L}_{\mathsf{wet}} \leqslant |y| \leqslant \mathsf{L}_{\mathsf{plate}}$, and

$$\mathbf{u}_{\mathsf{anal}}(x,y,z) = \frac{\mathbf{F}_\alpha}{2\rho_2\nu_2}(\mathsf{L}_{\mathsf{plate}}^2 - \mathsf{L}_{\mathsf{wet}}^2) + \frac{\mathbf{F}_\alpha}{2\rho_1\nu_1}(\mathsf{L}_{\mathsf{wet}}^2 - y^2) \tag{4.11}$$

in the component 1 region where $0 \leqslant |y| \leqslant \mathsf{L}_{\mathsf{wet}}$. $\mathbf{F}_\alpha$ is the body force for αth component and follows $\mathbf{F}_1 = \mathbf{F}_2$. In this layered Poiseuille flow, $\mathbf{F}_\alpha$ considered the $\mathbf{F}_{\mathsf{coh},\alpha}$ (see Eq. (2.12)) and $\mathbf{F}_{\mathsf{ext},\alpha}$ (see Eq. (2.14)). As the results in section 4.2.1, $\mathbf{F}_{\mathsf{coh},\alpha}$ is affected by G_{coh}, and $G_{\mathsf{coh}} = 0.06$ is chosen for this external force driving layered Poiseuille flow and make two components immiscible. $\mathbf{F}_{\mathsf{ext},\alpha}$ is chosen a value which was used in no-layered Poiseuille flow in section 4.2.1 to ensure the flow is laminar flow. The dimensionless analytical velocity $\mathbf{u}^*_{\mathsf{anal}}$ and dimensionless numerical velocity $\mathbf{u}^*$ can be computed by Eq. (4.5). The $\mathbf{u}_{\mathsf{anal,max}}$ is in the position with $y = 0$ (see Fig. 4.15) and calculated by Eq. (4.11). As discussion in section 4.2.1, the accuracy of no-layered Poiseuille flow is independent of $\mathbf{F}_\alpha$

- **Relaxation time dependence analysis**

  In this part, the relaxation time dependence is analyzed based on viscosity ratio between two components equals one ($\tau_1 = \tau_2$ and $\nu_1 = \nu_2$, see Eq. 2.5 and Eq. 2.20). The velocity profile on the Z-Z cross section (see Fig. 4.15 a)) is shown in Fig. 4.16

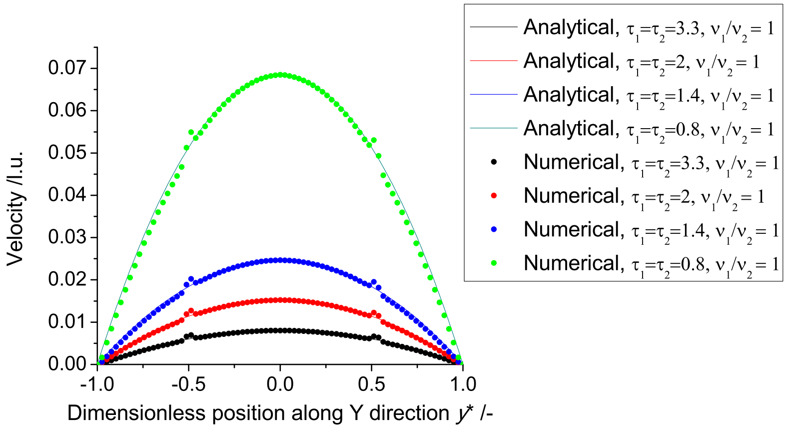

Figure 4.16.: Velocity profile of viscosity ratio equals one and relaxation time dependence

It is seen from Fig. 4.16 that when the relaxation time of two components are the same (viscosity ratio between two components is one), the results of velocity agree well with the analytical solutions. The obvious errors are observed on the region of $y^* = -0.5$ and $y^* = 0.5$ where are the initial two components interface locations. The errors on the two components interface are larger than other regions. Then the relative error ε_r is calculated by Eq. (4.6) to compare analytical solutions (according to Eq. (4.10) and Eq. (4.11)) and numerical solutions in Fig. 4.16. The ε_r with different relaxation time from Fig. 4.16 are summarized in Table 4.3

Table 4.3.: Relative error ε_r with different relaxation time in the external force driving layered Poiseuille flow ($\nu_1 = \nu_2$)

	$\tau_1 = \tau_2 = 3.3$	$\tau_1 = \tau_2 = 2$	$\tau_1 = \tau_2 = 1.4$	$\tau_1 = \tau_2 = 0.8$
ε_r	0.028	0.028	0.029	0.031

It is seen that the external force driving layered Poiseuille flow with MRT-EDM approach is very relaxation time independent. When relaxation time τ_1 and τ_2 decrease (from 3.3 to 0.8), the relative error ε_r slightly increases (from 0.028 to 0.031). The velocity profile when viscosity ratio equals one, agrees very well with the analytical solution within a certain accuracy ($0.028 \leqslant \varepsilon_r \leqslant 0.031$, see Table 4.3). It is consistent with the conclusions in SFIT in section 4.2.1.

- **Viscosity ratio dependence analysis**

  Four different non-unit viscosity ratios between two components ($\nu_1/\nu_2 = 1/5, 1/10,$ $5/1, 10/1$) are discussed. The simulation setups are the same as that in the relaxation time dependence analysis part above. The initial two components interface are on the $y^* = -0.5$ and 0.5. When viscosity ratio between wet and non-wet phase are less than one, such as $\nu_1/\nu_2 = 1/5$ and $1/10$. The velocity profiles of two different viscosity ratios (smaller than one) on the Z-Z cross section (Fig. 4.15 a)) are shown in Fig. 4.17 and Fig. 4.18

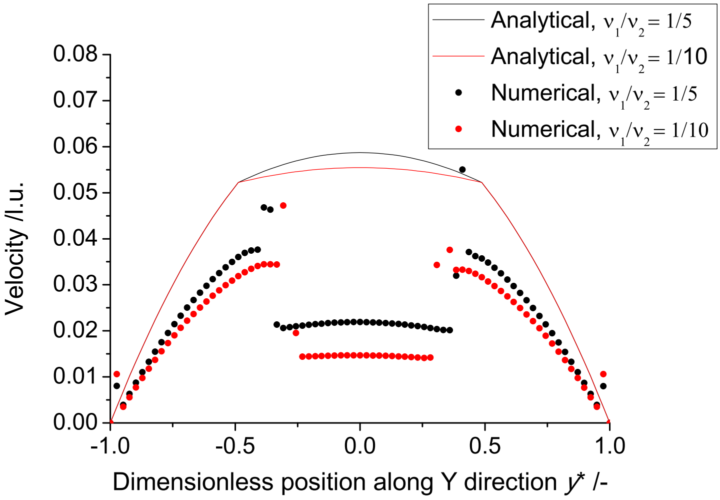

Figure 4.17.: Velocity profiles of different viscosity ratios which are smaller than one including $\nu_1/\nu_2 = 1/5$ and $1/10$ on the Z-Z cross section (see Fig. 4.15).

When the viscosity ratio between two components are larger than one such as $\nu_1/\nu_2 = 5/1$ and $10/1$, the results of velocities are shown in Fig. 4.18 and compared with the analytical solutions (Eq. (4.10) and Eq. (4.11)).

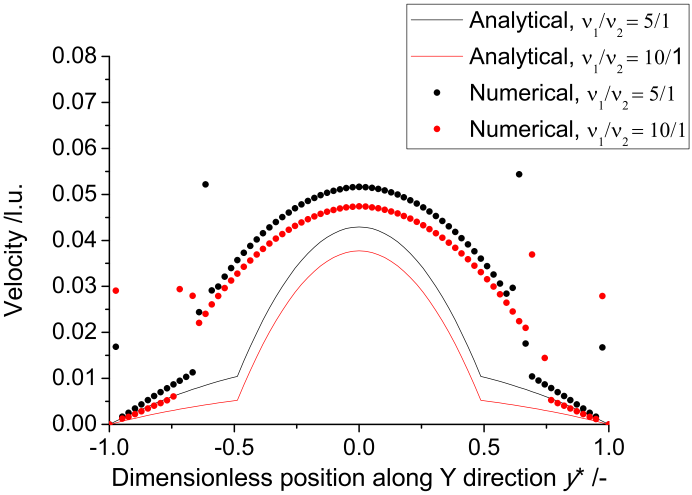

Figure 4.18.: Velocity profiles of different viscosity ratios which are bigger than one including $\nu_1/\nu_2 = 5/1$ and $10/1$ on the Z.Z cross section (see Fig. 4.15).

It can be concluded that the viscosity ratio has an very clear effect on the velocity, especially on the two components interface region and the solid surface region. The velocities fluctuations are observed on the two components interface and the solid surface region. Moreover, the two components interface position is different from the initial position ($y^* = -0.5$ and 0.5) and shifted some distances (around 4 or 5 lattices) towards the larger viscosity component area.

In summary, it is concluded from the external force driving layered Poiseuille flow between plates that the current model is possible to simulate the immiscible fluids with different viscosity ratios. But the error is very big (more than 50%). When the viscosity ratio equals one, the smallest errors were observed in comparison with the case of non-unit viscosity ratios. The ShanChen MCMP model cannot simulate the large viscosity ratio two-phases and it is one of important restriction on this model. This conclusion is consistent with previous ShanChen model literature [110][113]. Therefore, in the afterward simulations, the viscosity ratio is chosen to be one with the least algorithm errors. From the description of liquid water through GDL, it is allowed to set viscosity ratio as one because of the flow can be described with 'capillary fingering' and it is dominated by the capillary force (Ca$<10^{-4}$ in section 1.2.1).

4.3. Droplet test

According to the discussions in section 4.2, the MRT approach with EDM force scheme has the most accurate results and independent of fluid viscosity (relaxation time). Therefore, the ShanChen MRT-EDM model is applied on all simulations for the droplet test in this section.

4.3.1. Single ideal droplet test

In this section, the single ideal droplet test (SIDT) will be done to validate the capability of modeling the two phase flow behaviors with non-flat two phases interface [160]. Moreover, the ShanChen model is a phenomenally based model and the momentum is not conserved locally and one key two-phase parameters like surface tension has to be estimated by the single ideal droplet test [124][55]. Therefore, the following goals are expected to be achieved within the SIDT:

(i) Check the MRT-EDM model is possible to simulate two-phase flow with the no-flat two phase interface.

(ii) Evaluate the surface tension in the present MRT-EDM model.

(iii) Estimate the accuracy of simulating no-flat two phase interface (single ideal droplet) problems.

The 3D schematic of the single ideal droplet test is shown in Fig. 4.19 a). A Z-Z cross section is chosen to check the density and velocity in Fig. 4.20 a) and b).

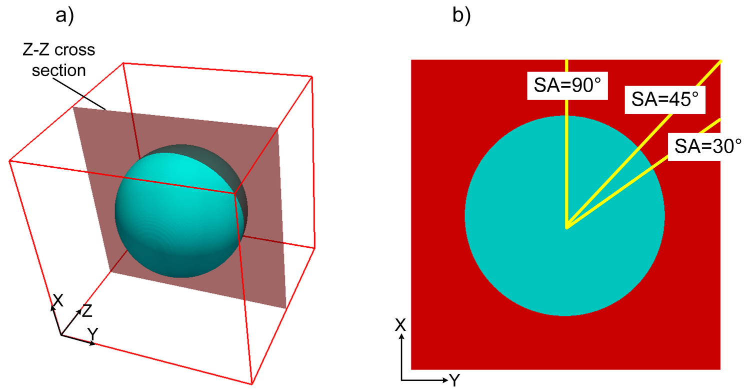

Figure 4.19.: a) 3D schematic graph of the single ideal droplet test. b) Three sample angles (SA) on the Z-Z cross section. Red: air; blue: water

An ideal sphere droplet is located in the center of domain without any external body force. The simulation domain size is 200 l.u. × 200 l.u. × 200 l.u.. Initially, the velocity field is set to be zero, the densities inside the droplet are set $\rho_{1,\text{init}} = 2$ l.u. and $\rho_{2,\text{init}} = 10^{-5}$ l.u., and outside of the droplet are set $\rho_{2,\text{init}} = 2$ l.u. and $\rho_{1,\text{init}} = 10^{-5}$ l.u. The periodic boundary conditions are applied on all boundaries. The cohesive force parameter G_{coh} in Eq. (2.12) is chosen to be 0.06 according to the G_{coh} dependence analysis in section 4.2.1. When the ideal sphere droplet achieves the equilibrium state, the relation between the pressure jump ΔP across the interface and the r_0 follows the Laplace's law (is also called Young-Laplace equation [161]) as Eq. (4.12) [162] :

$$\Delta P = P_{\text{inside}} - P_{\text{outside}} = \frac{2\sigma_s}{R} = \sigma_s(2/R) \tag{4.12}$$

where P_{inside} and P_{outside} are the pressure of inside and outside of droplet separately and can be calculated by the Eq. (2.16). R is the radius of the ideal sphere droplet and σ_s is the surface tension between two components. The same as the results of SFIT, the density and velocity on the Z-Z cross section are shown in Fig. 4.20 a) and b).

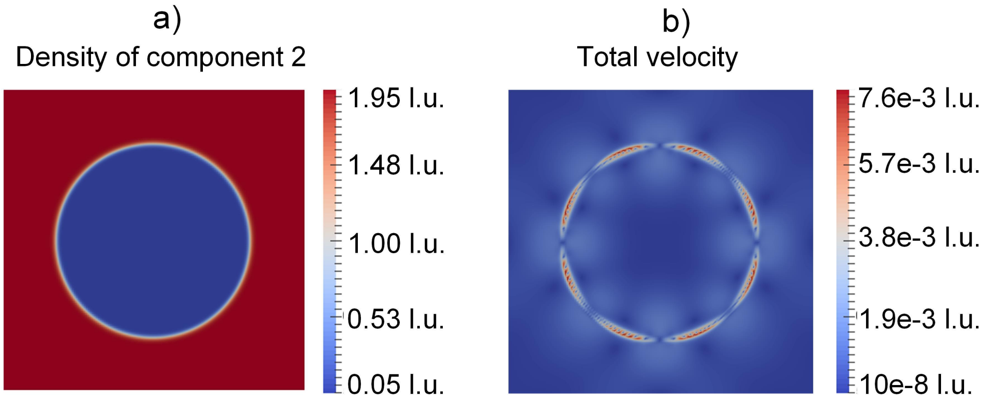

Figure 4.20.: a) Density distribution of component 2 on the Z-Z cross section (Fig. 4.19 a)). b) Total velocity distribution on the Z-Z cross section (Fig. 4.19 a)).

It is seen that the minimum density of component 1 is not zero which is called intermiscible density ρ_{itm} (introduced in section 4.2.1). The intermiscible density ρ_{itm} of component 1 locate inside of droplet while that of component 2 locate outside of the droplet. The maximum total velocity is observed on the interface region as well. The maximum total velocity is bigger than the analytical value (zero) and it is so called maximum spurious velocity $\mathbf{u}_{\text{spu,max}}$ (introduced in section 4.2.1). Positions of the $\mathbf{u}_{\text{spu,max}}$ are different on the two-phase interface but with symmetric distribution. Moreover, the lattice dependence, Laplace's law consistence and relaxation time dependence are discussed afterwards.

- **Lattice dependence analysis**

As shown in Fig. 4.19 b) that the radius of sphere are analyzed in three different sample angles (SA) including $30°$, $45°$ and $90°$. The surface tension σ_s is calculated by Eq. (4.12) that radius R is obtained from simulation result in different SA.

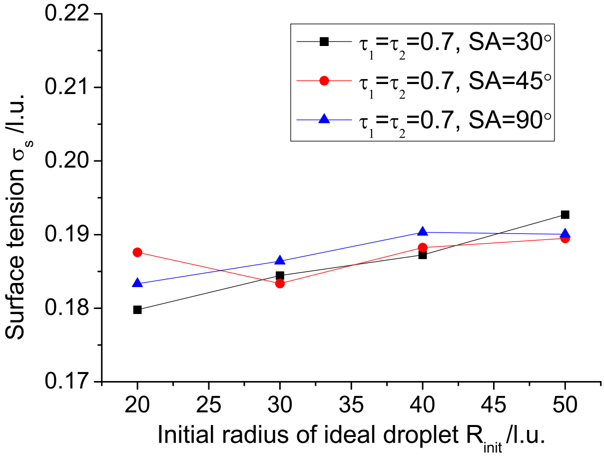

Figure 4.21.: Lattice dependence of the single ideal droplet test

It is seen that as bigger droplet sizes (or finer grids), the σ_s tends to a certain value. When the lattice is coarse (like $R_{\text{init}} = 20$), the maximum error is bigger than that of other cases. The error of lattice dependence analysis is mainly from the lattice setups. Then a relationship between the $\mathbf{u}_{\text{spu,max}}$ and initial radius of ideal droplet R_{init} is shown in Fig. 4.22

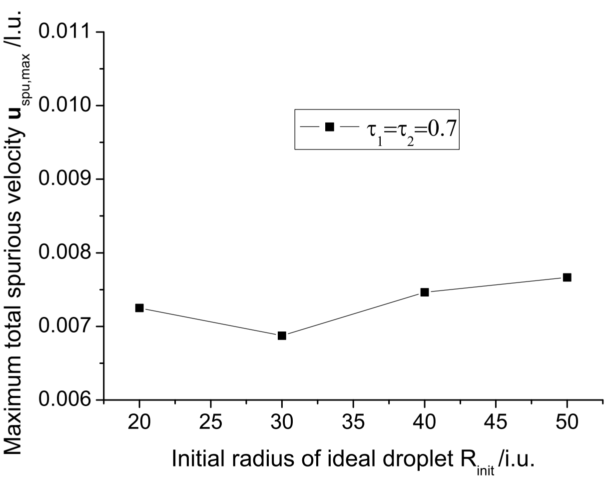

Figure 4.22.: The maximum spurious velocity $\mathbf{u}_{\text{spu,max}}$ in different initial radius of single ideal droplet R_{init} in the SIDT

It is seen from Fig. 4.22 that the radius of the initial ideal droplet have slight effect on the maximum total spurious velocity $\mathbf{u}_{\text{spu,max}}$ in the SIDT (less than 10% fluctuation). But it is observed that $\mathbf{u}_{\text{spu,max}}$ of SIDE is much larger ($O(10^5)$ higher) than that in the SFIT (see Fig. 4.10). It can be explained by the Laplace law of Eq. (4.12) and the velocity is bigger with higher pressure difference ΔP. When $R \rightarrow \infty$, the SFIT is more close to the section of SIDT on the two components interface, and the pressure difference $\Delta P \rightarrow 0$. Therefore, pressure difference ΔP (with order of $O(10^{-8})$) is very small and close to the zero in SFIT and much bigger in the SIDT (with order of $O(10^{-3})$).

- **Laplace law consistence**

As description of the SIDT and Eq. (4.12), the result of SIDT should follow the Laplace law and it can be seen from a ΔP - $2/R$ plot (the intersection on the ΔP coordinate should be zero). The relation between ΔP and $2/R$ is shown in Fig. 4.23 of $\tau_\alpha = 0.7$.

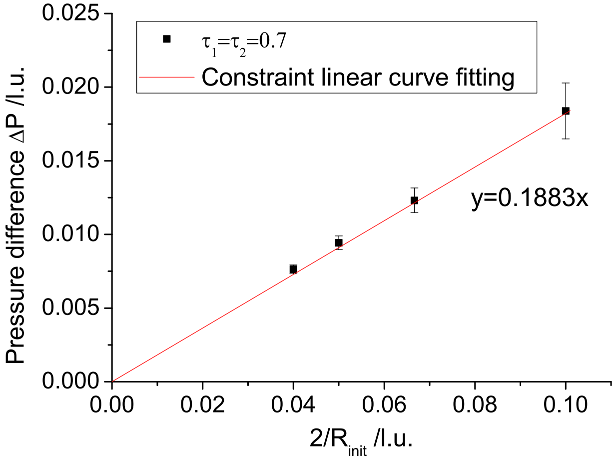

Figure 4.23.: Laplace consistence of the ideal droplet test

It is seen that this model can describe correctly the physical behavior of an ideal droplet. It means the results of this model can consistent with the Laplace law. The error of the Laplace law consistence are the same in different $2/R_{\text{init}}$ because of the same two phase interface thickness (4 l.u., see Table 4.2). It should be care that σ_s may be different in different ShanChen MCMP model and it depends on the fluids [129]. For example, $\rho_{1,\text{init}} + \rho_{2,\text{init}} = 2$ l.u. $+ 10^{-5}$ l.u. in initialization of the component 1 field.

- **Relaxation time dependence analysis**

  In this part, the surface tension σ_s is presented in Fig. 4.24 with different relaxation time in different initial radius of ideal droplet R_{init}.

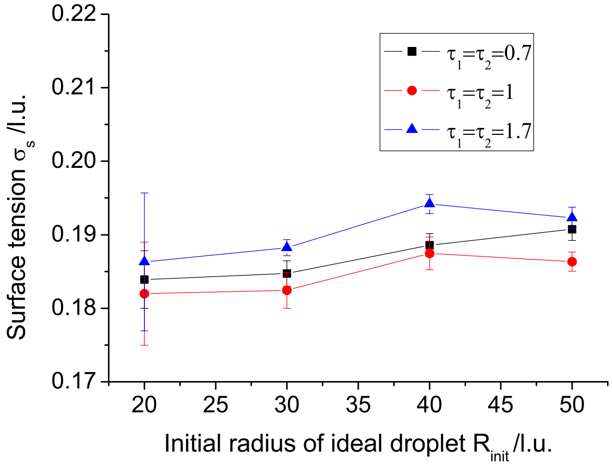

Figure 4.24.: Relaxation time τ_α dependence of the ideal droplet test

It is seen from Fig. 4.24 that σ_s tends to a certain value with the bigger R_{init}. The standard deviation is bigger when R_{init} is smaller because of the rougher grids. σ_s is not exactly the independent of the relaxation time. The similar results are also observed in SFIT for the relaxation time dependence on $\mathbf{u}_{\text{spu,max}}$ and ρ^*_{itm} in section 4.2.1 (see Fig. 4.10 and Fig. 4.11). The difference is caused by the relaxation time from the LB algorithm.

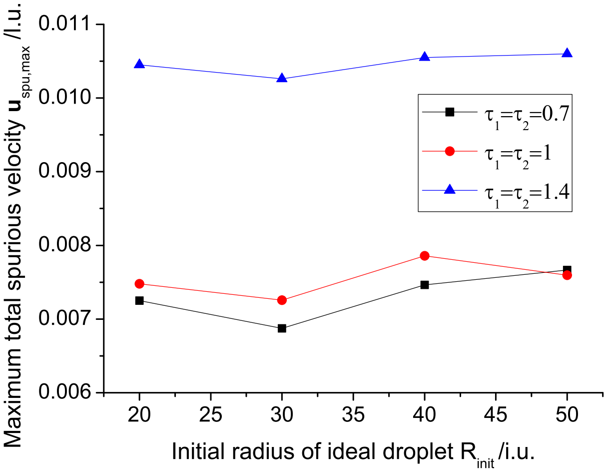

Figure 4.25.: Relaxation time τ_α dependence of the maximum spurious velocity $\mathbf{u}_{\text{spur,max}}$

The relaxation time impact on the $\mathbf{u}_{\text{spu,max}}$ with different R_{init} are presented in Fig. 4.25. The similar conclusion with that from Fig. 4.24 are got, that the result $\mathbf{u}_{\text{spu,max}}$ is independent of relaxation time within a certain deviation. By the way, there are slightly fluctuation ($\approx 5\%$ for every relaxation time) of $\mathbf{u}_{\text{spu,max}}$ when varying the R_{init}. Therefore, $\mathbf{u}_{\text{spu,max}}$ is independent of R_{init}.

In a summary, the SIDT is more complex than SFIT that the two-phase interface is not flat and more realistic for the two-phase flow in GDL. The total spurious velocity and intermiscible densities are also observed in SIDT. The surface tension σ_s is lattice and relaxation time independent in the MRT-EDM ShanChen MCMP model. This model is consistent with the Laplace law. It can be concluded that the ShanChen MCMP model is a phenomenally based model and the surface tension can be estimated by the SIDT.

4.3.2. Cubic initialization test

In this section, the physical effects of the surface tension is checked. In theory, the surface tension is the elastic tendency of a fluid surface which minimize its surface area. It is also the reason why the ideal (no external force) single droplet forms the ideal sphere shape not others. Therefore, the following goals are expected to be fulfilled in the cubic initialization test:

(i) Check the mass conservation of the present MRT-EDM model.

(ii) Check the effect of surface tension force (mimic the two phase interface area).

(iii) Check the effect of the relaxation time (viscosity).

In this test, a certain size (25 l.u. × 25 l.u. × 25 l.u.) cubic droplet is set in the center of the whole domain (50 l.u. × 50 l.u. × 50 l.u.). The initial density field, initial velocity field, parameter G_{coh} and boundary conditions are the same as that in SIDT of section 4.3.1. The 3D schematic graph is shown in Fig. 4.26.

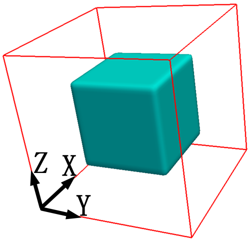

Figure 4.26.: 3D schematic of the cubic initialization test

As description above, the droplet shape is transformed from cubic to the ideal sphere when it reaches the equilibrium state due to the surface tension. The droplet shape evolution process with different relaxation time τ_α in start period are shown in Fig. 4.27

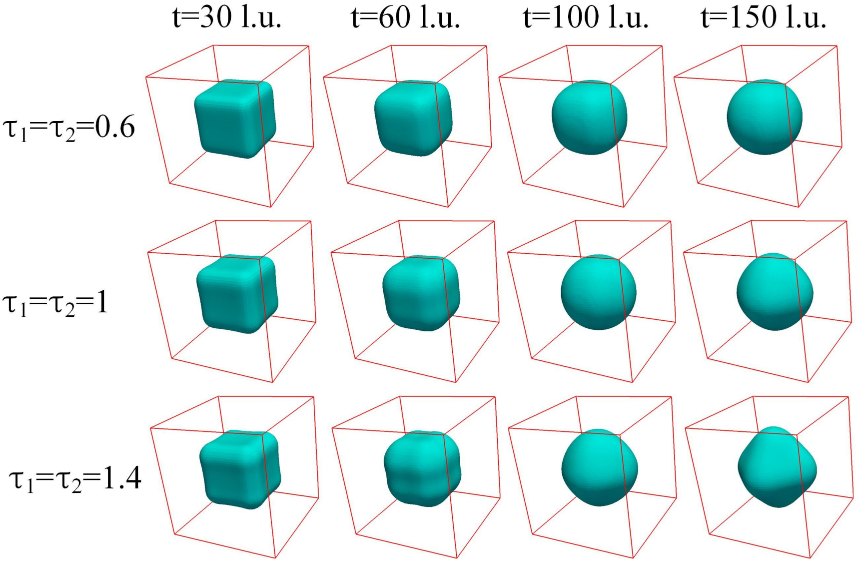

Figure 4.27.: Droplet shape evolution with different relaxation time ($\tau_1 = \tau_2 = 0.6$, $\tau_1 = \tau_2 = 1.0$ and $\tau_1 = \tau_2 = 1.4$) in different time steps ($t = 30$ l.u., $t = 60$ l.u., $t = 100$ l.u. and $t = 150$ l.u.)

It is seen that the cubic droplet is developing to the sphere droplet shape. As time goes by, the droplet shape are developed to the ideal sphere shape but with different evolution speed. In $t = 150$ l.u., droplet shape of $\tau_1 = \tau_2 = 0.6$ is already quite close the ideal sphere, while $\tau_1 = \tau_2 = 1$ and $\tau_1 = \tau_2 = 1.4$ are keeping evolution. Then the droplet fraction of droplet are checked during the evolution time. The analytical volume fraction of droplet S_{anal} and volume fraction of droplet in simulation S are computed by Eq.4.13

$$S_{\text{anal}} = \frac{V_{\text{liquid,init}}}{V_{\text{tot}}} \quad ; \quad S = \frac{V_{\text{liquid}}}{V_{\text{tot}}} \tag{4.13}$$

where $V_{\text{liquid,init}}$ and V_{tot} are the initial volumes of the liquid droplet and empty region in whole domain separately. V_{liquid} is the volume of the liquid droplet from the simulation results. The S with three relaxation time $\tau_1 = \tau_2$ $(0.6,1,1.4)$ against time steps and in comparison with the analytical solution shown in Fig. 4.28.

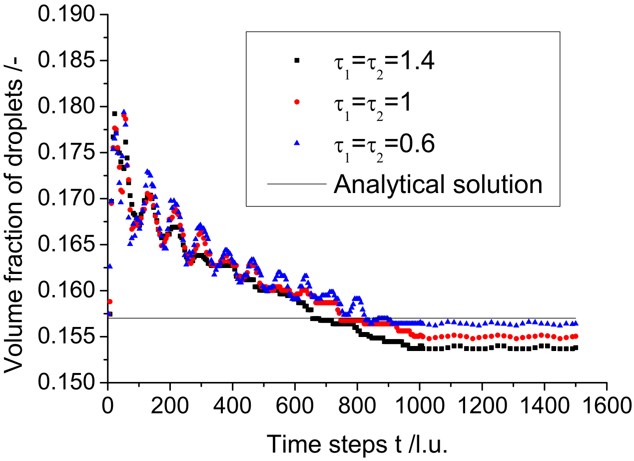

Figure 4.28.: Volume fraction of droplets against time steps for different relaxation time ($\tau_1 = \tau_2 = 0.6$, $\tau_1 = \tau_2 = 1$ and $\tau_1 = \tau_2 = 1.4$) and in comparison with the analytical solution for cubic initialization test

It is seen that S is very close to the S_{anal} and there are some error between them. In theory, S_{drop} equals to the $S_{\text{drop,anal}}$ when the system achieve the equilibrium state. These error are caused by the intermiscible density and interface between two phases (see section 4.2) and it is consistent with bigger errors raises when τ_1 $(= \tau_2)$ is close to the $\tau_{1,\text{lowl}} = \tau_{2,\text{lowl}} = 0.5$ in section 4.1.

In a summary from the cubic initialization test, the current model can simulate correctly the single droplet with surface tension effects from the physical side. The relaxation time affects the accuracy of simulation results. According to the discussed relaxation time cases, $\tau_1 = \tau_2 = 0.6$ have the smallest error. Therefore, in the afterward simulation in the GDL in section 5 and section 7.1, $\tau_1 = \tau_2 = 0.6$ are chosen for the simulations.

4.3.3. Coalescence test

In this section, the coalescence process is validated. In theory, the coalescence behavior happen when two or more droplets merge during contact to form a single daughter droplet. When simulating the liquid water through irregular porous media (like GDL), the liquid droplets with differnt sizes may be distributed inside and the coalescence will happen when they are neighbors.

Therefore, it is necessary to validate the capability of simulating the coalescence process. The following goals are expected to be achieved within the coalescence test:

(i) Check if the coalescence process can be simulated with the present MRT-EDM model.

(ii) Check the mass conservation and effect of the relaxation time (viscosity).

The 3D schematic graph of coalescence initialization is shown in Fig. 4.29.

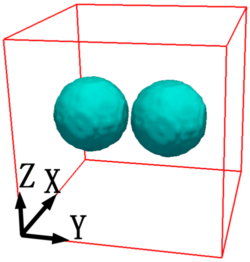

Figure 4.29.: 3D schematic of the coalescence initialization

Two ideal droplets with certain sizes (radius is 10 l.u.) locate neighborly in the center of whole domain (domain size is 50 l.u. × 50 l.u. × 50 l.u.) without any external body forces. The density and velocity field of droplets and outside of that are initialized the same as that in SIDT validation in section 4.3.1. The periodic conditions are applied on all boundaries. Parameter $G_{\text{coh}} = 0.06$ is the same as SIDT also. Fig. 4.30 shows the coalescence of two droplets with three different relaxation time ($\tau_1 = \tau_2 = 0.6$, $\tau_1 = \tau_2 = 1$ and $\tau_1 = \tau_2 = 1.4$).

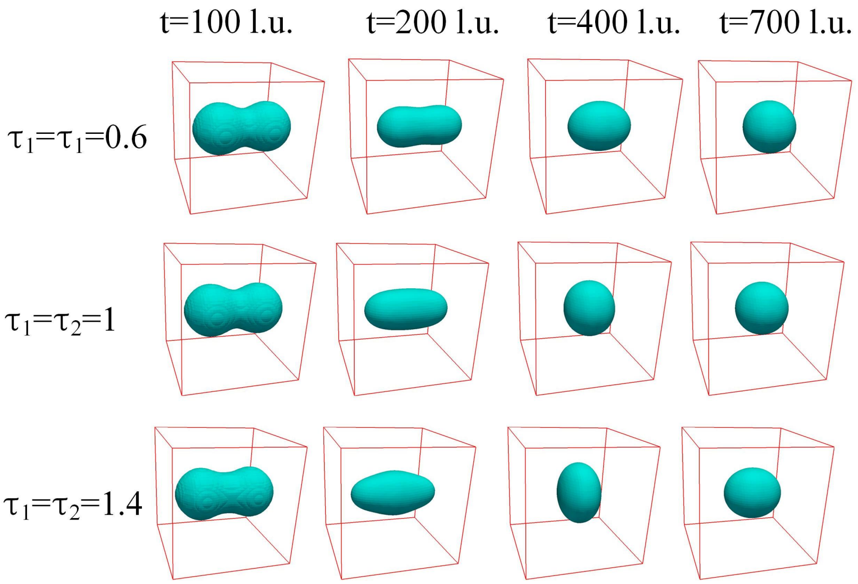

Figure 4.30.: Two droplets coalescence with different relaxation time ($\tau_1 = \tau_2 = 0.6$, $\tau_1 = \tau_2 = 1$ and $\tau_1 = \tau_2 = 1.4$) in different time steps ($t = 100$ l.u., $t = 200$ l.u., $t = 400$ l.u. and $t = 700$ l.u.)

It is observed that two individual small droplets are formed to be a bigger droplet. The time to achieve the equilibrium state are different. On the beginning period (t=100 l.u. and t=200 l.u.), the droplet shapes are different with different τ_1 ($=\tau_2$). The cases with $\tau_1 = \tau_2 = 0.6$ and $\tau_1 = \tau_2 = 1$ reach the equilibrium state faster than that with $\tau_\alpha = 1.4$ (when t=700 l.u., single ideal droplet is formed for $\tau_1 = \tau_2 = 0.6$ and $\tau_1 = \tau_2 = 1$, but $\tau_1 = \tau_2 = 1.4$ does not). The droplet of $\tau_1 = \tau_2 = 1.4$ at t =700 l.u. is irregular (close to ellipse from the present camera direction), and it means this case does not achieve the equilibrium state while another two cases already achieve the equilibrium state. The volume fraction of liquid are compared with analytical value under different τ_α in Fig. 4.31

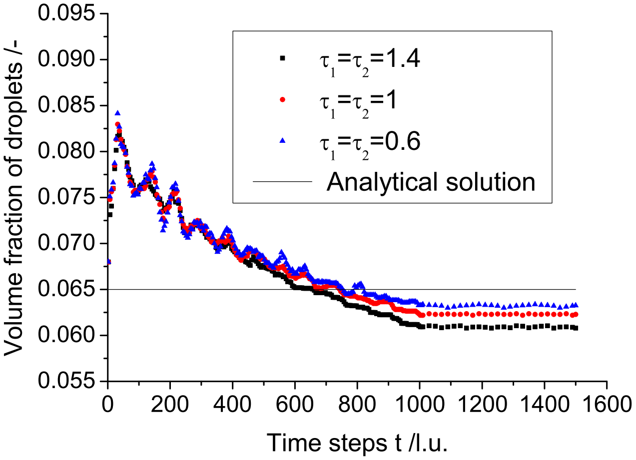

Figure 4.31.: Volume fraction of droplets against time steps for different relaxation time ($\tau_\alpha = 0.6$, $\tau_\alpha = 1$ and $\tau_\alpha = 1.4$) and in comparison with the analytical solution for coalescence test

When the simulations are converged, the results fitted well with the analytical solution but there is still slightly difference ($\leqslant 10\%$) between the results and the analytical solution. The error is from the interface thickness and intermiscible density of the algorithm which are discussed in section 4.2. With different relaxation time $\tau_1 = \tau_2$, their converged simulation results are slightly different (5% between $\tau_1 = \tau_2 = 1.4$ and $\tau_1 = \tau_2 = 0.6$). It is also seen that the volume fraction of droplets are different in different time steps before convergence and it means the shape of droplet are different, which are consistent with droplets coalescence shown in Fig. 4.30.

In a summary of the coalescence test, the droplets coalescence process can be simulated correctly from the physical aspect. With different relaxation time, the development of coalescence process to the equilibrium state are slightly different. When the process achieve the equilibrium state, the case with the smaller relaxation time is more close to the analytical solution within a certain range of error. This conclusion is consistent with that from the cubic initialization test and it proves availability of choosing $\tau_1 = \tau_2 = 0.6$ for afterwards water in GDL simulations.

4.4. Contact angle test

As the conclusion in section 4.2, the MRT-EDM is the most accurate and the least viscosity (relaxation time) dependent model. Therefore, the MRT-EDM is applied all simulations in the contact angle test in this section. According to the algorithm description in section 2.1.1 and 2.5, this ShanChen MCMP model is able to simulate the solid surface with different wettability (from $0°$ to $180°$) by varying parameter $G_{\text{adh},1}$ (see Eq. (2.13)). The circle method is suitable for the symmetric droplet, while SPPF does not have strict limitations on droplet shape. Therefore, two following goals are expected to be validated with contact angle test (CAT).

(i) The lattice dependence and relaxation time (viscosity) dependence analysis for the MRT-EDM ShanChen model. The model parameter $G_{\text{adh},1} = -0.005$ (see Fig. 4.36) is fixed with different initial droplet sizes for this analysis.

(ii) Capability of simulating different wettability. The MRT-EDM is checked to be able to simulate different contact angles. The model parameter $G_{\text{coh},1}$ is varied from -0.0125 to 0.0125 and the corresponding contact angles are discussed.

(iii) The validation of SPPF method. Comparison with contact angles of the symmetric droplet with the circle method and SPPF method.

(iv) Determine proper model parameters $G_{\text{adh},\alpha}$ to ensure the contact angle on the carbon material θ_{carbon} and the contact angle on the PTFE material θ_{PTFE}. Afterward, θ_{carbon} and θ_{PTFE} are assumed the material properties for the water flowing through GDL simulations in chapter 5 to 7.

The circle method and SPPF method will be validated by this contact angle test (CAT). The schematic graph of CAT is shown in Fig. 4.32a) with domain size 100 l.u. × 100 l.u. × 100 l.u., while the top view is shown in Fig. 4.32b)

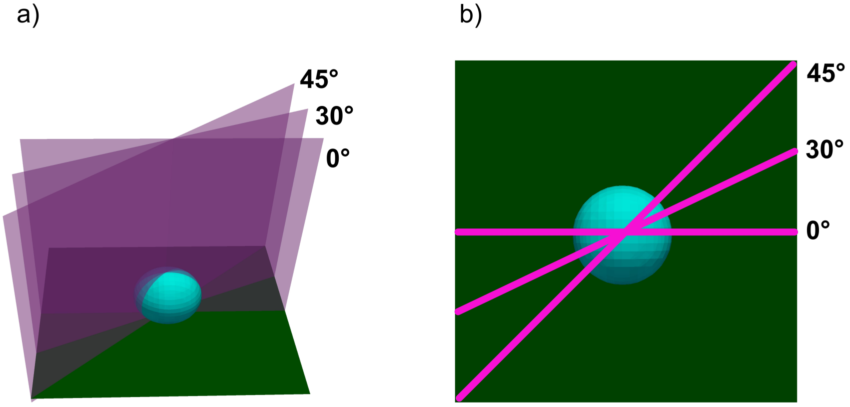

Figure 4.32.: a) Schematic graph of CAT ; b) Top view of CAT. Droplet (blue), solid surface (green), cutting plane of view angles (pink) [149]

Initially, a half-sphere droplet with a certain radius R_{init} is put on the solid surface without external force. The periodic conditions are applied on all boundaries. Density and velocity field in droplet and out of it are initialized the same as that in SIDT in section 4.3.1. The volume of semi-sphere droplet is computed with $V_{\text{init}} = 2\pi R_{\text{init}}^3/3$. Three view angles (VA) (VA=0°, 30° and 45°) are chosen to get the apparent contact angle θ_{ap}. The CAT consists of three parts. Firstly, the lattice dependence that the fixed cohesive force parameter $G_{\text{coh},\alpha}$ with different R_{init} are studied. Then effects of VA on the fixed R_{init} are analyzed and its effects on θ_{ap} are presented. Finally, the SPPF method are validated.

- **Lattice dependence analysis**

  As description the Eq. 2.13, $G_{\text{adh},1}$ $(= -G_{\text{adh},2})$ is the parameter to control the strength between solid and fluid, and different wettabilities can be achieved by adjusting it. In this lattice dependence analysis, a fixed $G_{\text{adh},1} = -0.005$ (because of the contact angle approximation on the smooth flat surface (around 110°) proposed by Huang et al. [129]) is set to check the contact angles. The relationship between $G_{\text{adh},1}$ and the contact angle is shown in Fig. 4.36.

  In theory, a droplet without external force on the smooth surface will be an exactly symmetric droplet and the contact angle from different VA will be the same as well. The contact angle of the ideal symmetric droplet is also called the idealized contact angle θ_{idl}. Therefore, the circle method in Eq. 2.32 and Eq. 2.33 can be applied to calculate apparent contact angle θ_{ap} and it is fulfilled the relation $\theta_{\text{idl}} \equiv \theta_{\text{ap}}$ for the ideal symmetric droplet in the CAT. Fig. 4.33 shows the θ_{idl} with a series of R_{init} from 13 l.u. to 50 l.u. in different VAs.

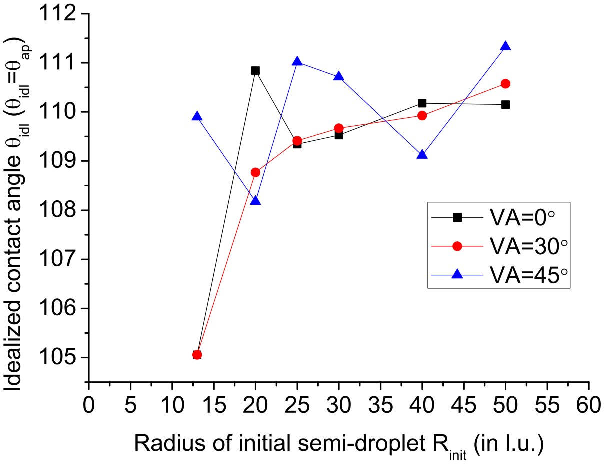

Figure 4.33.: Idealized contact angles of different initial half-sphere droplet radius R_{init}. $(G_{\text{adh},1} = -0.005,\ \tau_1 = \tau_2 = 0.6)$. [149]

It is seen that θ_{idl} varies in different VAs. The θ_{idl} with VAs are different because of the LB algorithm (discritized method) and these errors are from grids effects. θ_{idl} under different VAs are closer with bigger R_{init}. The maximum absolute error ϵ_{max} is defined in Eq.(4.14)

$$\epsilon_{\text{max}} = \frac{\theta_{\text{idl,max}} - \theta_{\text{idl,min}}}{2} \tag{4.14}$$

where $\theta_{\text{idl,max}}$ and $\theta_{\text{idl,min}}$ are the maximum and minimum θ_{idl} with the same R_{init} in different VAs. The error from the lattices are analyzed with different R_{init} and the plot of ϵ_{max} against R_{init} are shown in Fig. 4.34

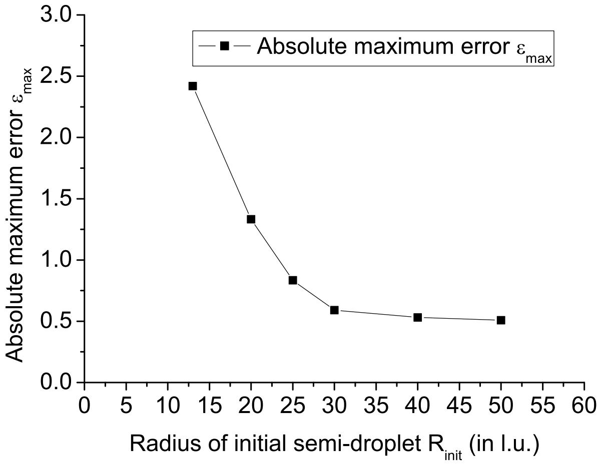

Figure 4.34.: The maximum absolute error ϵ_{max} of different initial half-sphere droplet radius R_{init} ($G_{\text{adh,1}} = -0.005$, $\tau_1 = \tau_2 = 0.6$). [149]

It is clear that ϵ_{max} is smaller with bigger droplet (larger R_{init}). When $R_{\text{init}} \leqslant 30$ i.u., ϵ_{max} decreased sharply and the error from lattice dominate it. The $\epsilon_{\text{max}} \approx 0.5°$ with $R_{\text{init}} = 50$ l.u. is acceptable in this work.

- **Relaxation time dependence analysis**

The relaxation time impact on the contact angles are studied under this subsection. The simulation setups are the same as that when analyzing lattice dependence. Model parameter $G_{\text{adh,1}} = -0.005$ is fixed (because of the contact angle approximation proposed by Huang et al.[129]) and contact angles from three different relaxation time ($\tau_1 = \tau_2 = 0.6, 1, 1.4$) are discussed. The droplet with $R_{\text{init}} = 50$ l.u. is chosen for the initial droplet in the relaxation time dependence analysis because of the least ϵ_{max} from the lattice error (see Fig. 4.34). The idealized contact angle θ_{idl} ($\theta_{\text{idl}} \equiv \theta_{\text{ap}}$ for the symmetry droplet) with three relaxation time in different VAs are presented in Fig. 4.35.

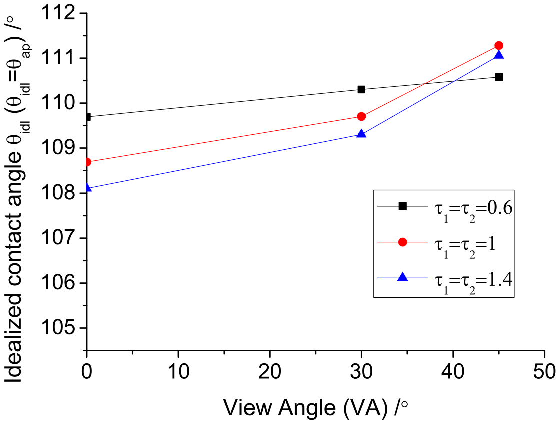

Figure 4.35.: The idealized contact angle θ_{idl} dependence of relaxation time τ_1 $(= \tau_2)$ in different VAs. $(G_{\text{adh},1} = -0.005$ and $R_{\text{init}} = 50$ l.u.)

It is seen from Fig. 4.35 that the contact angles are fluctuated in different VAs with the fixed relaxation time, and it is consistent with the conclusions from Fig. 4.33. When $\tau_1 = \tau_2 = 0.6$, the least view angle dependence (close to the theoretical droplet shape and view angle independent) is observed. This conclusion is consistent with the relaxation time dependence analysis in last three validation sections (see section 4.1, 4.2 and 4.3).

- **Wettability simulation**

According to the result in Fig. 4.34, the case with $R_{\text{init}} = 50$ l.u. has the least $\epsilon_{\max}$ and $R_{\text{init}} = 50$ l.u. is chosen in this wettability simulation part. The θ_{idl} of different VAs against $G_{\text{adh},1}$ are shown in Fig. 4.36

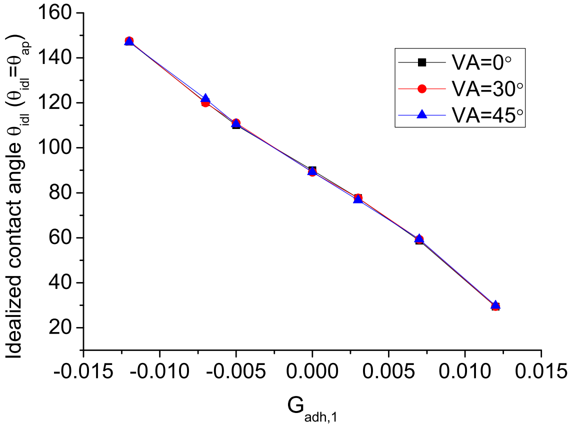

Figure 4.36.: θ_{idl} against a series of $G_{\text{adh},1}$ in the CAT. $(R_{\text{init}} = 50$ l.u., $\tau_1 = \tau_2 = 0.6$ and is calculated by circle method in Eq. 2.32 and Eq. 2.33) [149]

When $G_{\text{adh},1}$ varies from 0.012 to -0.013, the solid wettability changes from hydrophilic ($\theta_{\text{idl}} \approx 30^\circ$) to hydrophobic ($\theta_{\text{idl}} \approx 150^\circ$). The limited values ($\theta_{\text{idl}} = 0^\circ$ and $\theta_{\text{idl}} = 180^\circ$) are not checked here because of the difficulty to achieve accurately these critical values with the density-based fluid-solid interactions (see Eq. (2.13)) [163]. The θ_{idl} under three different VAs are almost the same with $\epsilon_{\text{max}} \approx 0.5^\circ$ for all tested $G_{\text{adh},1}$.

Concerning the application of the two-phase flow through the GDL, two material properties are needed including the contact angle on the carbon material θ_{carbon} and contact angle on the PTFE material θ_{PTFE}. The GDL properties are roughly described in the chapter 1, the values of material properties $\theta_{\text{carbon}} = 90^\circ$ and $\theta_{\text{PTFE}} = 110^\circ$ can be found from the GDL manufactures [98][5][6]. According to the Fig. 4.36, the corresponding model parameter $G_{\text{adh},1}$ $(= -G_{\text{adh},2}$ in Eq. (2.13)) can be derived for θ_{carbon} and θ_{PTFE}. It is found that $G_{\text{adh},1} = -0.005$ for $\theta_{\text{PTFE}} = \theta_{\text{idl}} \approx 110^\circ$ and $G_{\text{adh},1} = 0$ for $\theta_{\text{carbon}} = \theta_{\text{idl}} \approx 90^\circ$.

The details of density and velocity plots with three different wettabilities ($\theta_{\text{ap}} \approx 120^\circ$, 90° and 30°) are shown in Fig. 4.37. The density and velocity of the three-phase region (region with water, air and the solid, yellow frame region in Fig. 4.37) are zoomed and presented in Fig. 4.37. It is seen from Fig. 4.37 that the interface with certain thickness are observed between two phases. This is consistent with the conclusion of SFIT in Table 4.2 for the two-phase interface thickness. From the density plot on the zoom region, it is seen that the water-solid interface thickness increases with the contact angle increases. The large velocities (spurious velocities) are observed on the water-air interface and three-phase region. But no large velocities are observed on the water-solid and air-solid interface.

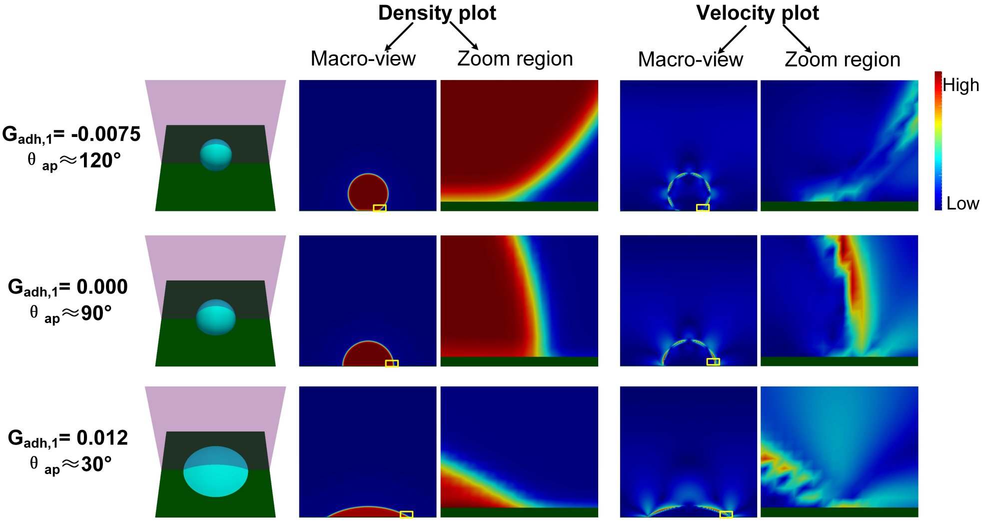

Figure 4.37.: The macro-view and zoom region of density and velocity plot on the cross section (purple surface) vertical to the solid surface and through the center of droplets with three different wettabilities ($\theta_{\text{ap}} \approx 120^\circ$, 90° and 30°). Green: solid; Blue: liquid. Yellow frame: zoom region.

It can be concluded that the present model is possible to simulate different wettabilities (contact angles) with varying model parameter $G_{\text{adh},1}$. The large spurious velocities are observed on the water-are interface and three-phase region. The water-solid interface thickness is smaller when contact angle decreases. The spurious velocity on water-solid interface are not oberved. The interface and spurious velocity on three-phae region cause the error when the simulations are related with two-phase flow on the solid surfaces.

- **SPPF method validation**

  The SPPF method will be validated in this part. In theory, θ_{ap} from circle method and SPPF method should be the same for symmetric droplet shape. Therefore, the result of θ_{idl} from both methods are compared. According to the description of SPPF method in section 2.5, two parameters n (grids amount for the 1st order polynomial curve fitting) and m (grids amount for the 2nd order polynomial curve fitting) are needed to determine the contact point and calculate the contact angle. Parameter $n = 4$ is smaller than 9% of available drop boundary length points (≈ 70 l.u. when $R_{\text{init}} = 50$ l.u.) [147]. The optimum parameter m can be selected when θ_{ap} from the circle method and the SPPF method are the most close. According to the result of lattice dependence in Fig. 4.21, $\theta_{\text{idl}} \approx 110°$ ($R_{\text{init}} = 50$ l.u. and $G_{\text{adh},1} = -0.005$) is chosen as the true value and compared with results from SPPF method. The comparison between two methods with attempting different m are shown in Fig. 4.38.

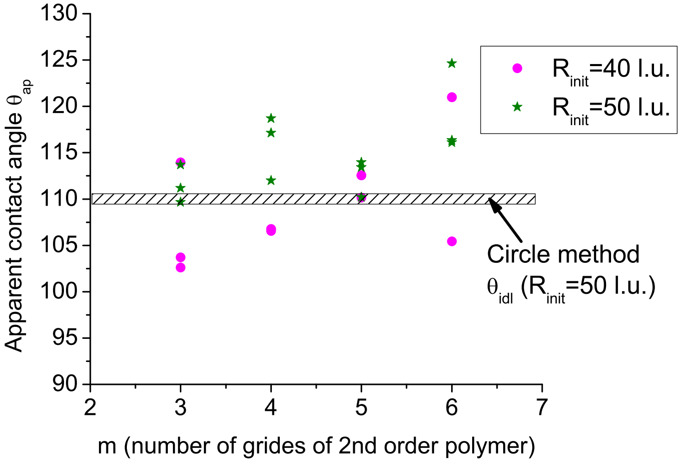

Figure 4.38.: Apparent contact angles θ_{ap} of VAs against m for two R_{init} done by SPPF method ($n = 4$) [149]

It is seen that θ_{ap} varies with different m. The variance is caused by the mathematical algorithms used for 2nd order polynomial curve fitting. It is seen that when $m = 5$, the results from $R_{\text{init}} = 40$ l.u. and $R_{\text{init}} = 50$ l.u. are close to the true value. Therefore, it is validated that SPPF can be used to calculate the apparent contact angle when the optimum m is chosen and $m = 5$ in this work.

In a summary of the contact angle test, the lattice dependence analysis results are consistent with that in the external force driving Poiseuille flow between plates in section 4.1. The absolute error is bigger with the rougher lattices. The contact angle is relaxation time independent and the most stable result within three VAs are observed when $\tau_1 = \tau_2 = 0.6$ (is also used in the afterward two-phase in GDL simulations). The current model is capable to simulate a range of wettabilities ($30^\circ \leqslant \theta_{\text{idl}} \leqslant 150^\circ$) with adjusting $G_{\text{adh},1}$ ($= -G_{\text{adh},2}$). Concerning the wettability of GDL, $G_{\text{adh},1} = -0.005$ ($\theta_{\text{idl}} \approx 110^\circ$) is chosen for the GDL with PTFE and $G_{\text{adh},1} = 0.000$ ($\theta_{\text{idl}} \approx 90^\circ$) is chosen for the fresh GDL without PTFE. These $G_{\text{adh},1}$ are applied for the water transport in GDL in section 5 and 7.1. The contact angles processed by SPPF method are validated by comparing with the result from the circle method. An optimum set of polynomial parameter $m = 5$ and $n = 4$ are found and applied on the shape of asymmetric liquid droplet on GDL surface analysis in section 6.1.

4.5. Open boundary condition test

In this section, a dynamic case is validated that component two is replaced by component one when component one is injected to this two immiscible components system. The MRT-EDM model is applied on simulations in the open boundary condition test. The 3D schematic graph of this flat two-phase interface system is shown in Fig. 4.39.

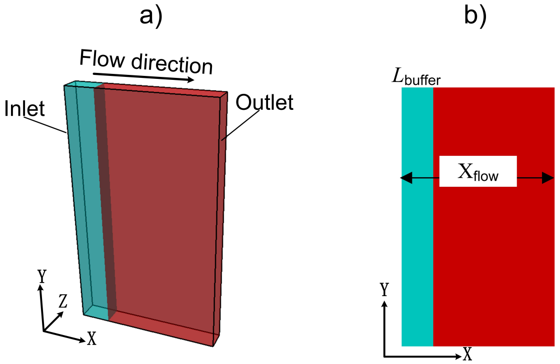

Figure 4.39.: a) 3D schematic plot of the open boundary condition validation. b) 2D schematic plot on the X-Y surface. Blue: buffer region occupied by water; red: air

The domain size is 50 l.u.×50 l.u. ×10 l.u. in X, Y and Z directions. The periodic conditions are applied on the Y and Z directions. The velocity condition is adopted to achieve the given velocity by Zouhe method [150] in inlet (x=0) towards X direction. And the open boundary condition is applied on the outlet ($x = \text{X}_{\text{flow}}$). Initially, as shown in Fig. 4.39, a buffer region (thickness is 5 l.u. in this part) near the inlet is occupied by liquid water ($\rho_{1,\text{init}} = 2$ l.u. and $\rho_{2,\text{init}} = 10^{-4}$ l.u. in buffer region) while the rest region is filled by air ($\rho_{1,\text{init}} = 10^{-4}$ l.u. and $\rho_{2,\text{init}} = 2$ l.u. in other region). In the displacement region, the air will be replaced by the liquid water as time goes on. The analytical saturation of domain S_{anal} can be calculated by Eq.(4.15)

$$S_{\text{anal}} = \frac{V_{\text{liquid}}}{V_{\text{tot}}} \tag{4.15}$$

$$\text{with} \qquad V_{\text{liquid}} = A_{\text{inlet}} L_{\text{buffer}} + A_{\text{inlet}} \mathbf{u}_{\text{inlet}} t \quad ; \quad V_{\text{total}} = A_{\text{inlet}} \text{X}_{\text{flow}} \tag{4.16}$$

$$S_{\text{anal}} = \frac{L_{\text{buffer}}}{\text{X}_{\text{flow}}} + \frac{\mathbf{u}_{\text{inlet}}}{\text{X}_{\text{flow}}} t \tag{4.17}$$

where V_{liquid} and V_{tot} are volume of liquid and total domain separately, and they are calculated by Eq. (4.16) . A_{inlet} is the inlet area, L_{buffer} is the buffer region length along the flow direction (see Fig. 4.39 b)), $\mathbf{u}_{\text{inlet}}$ is the inlet velocity and t is the time steps. The volume V_{liquid} is the sum of the volume of buffer region $A_{\text{inlet}}L_{\text{buffer}}$ and the inject liquid volume $A_{\text{inlet}}\mathbf{u}_{\text{inlet}}t$. The total domain volume V_{total} is calculated by Eq. (4.16) and X_{flow} is the total domain length along the flow direction (see Fig. 4.39 b)). Finally, combined the Eq. (4.15) and Eq. (4.16), the analytical solution of liquid saturation can be calculated by Eq. (4.17). In the following parts, the relaxation time dependence, inlet velocity effects are analyzed. The open boundary condition is compared with the pressure boundary condition. Finally, a single droplet with no-flat two-phase interface is checked with the open boundary condition.

- **Relaxation time dependence analysis**

The results of open boundary validation with three different relaxation time $\tau_1 = \tau_2 = 0.7, 1, 1.4$ are shown in Fig. 4.40 and $\mathbf{u}_{\text{inlet}}$ are the same and equals 0.001 l.u. ($Ca = 10^{-4}$ according to Eq. (1.8)).

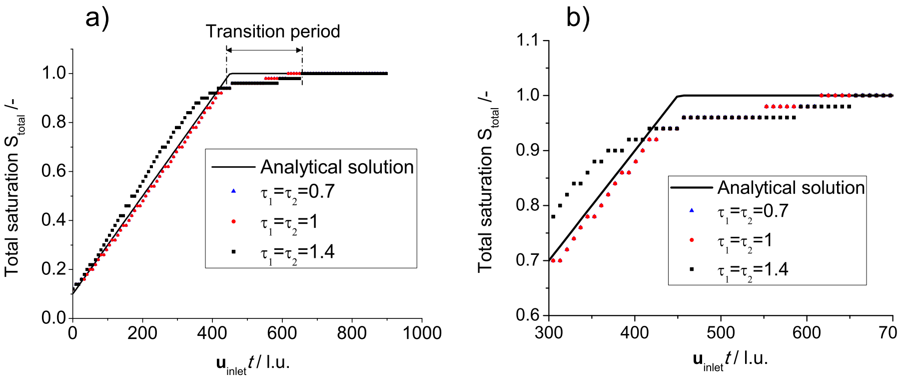

Figure 4.40.: a) Total saturation S_{total} against the $\mathbf{u}_{\text{inlet}}t$ of different relaxation time τ_1 $(= \tau_2)$ and in comparison with the analytical solution ($\mathbf{u}_{\text{inlet}} = 0.001$ l.u. and $Ca = 10^{-4}$). b) Zoom of transient period in Fig. 4.40 a).

The start value of S_{total} is 0.1 because of the buffer region is taken into account to the total saturation. The $S_{\text{total}} = 1$ in the final stage because the whole domain are fully filled with the water and this result can be achieved by all τ_α. It validates the open boundary condition can correctly simulate the extreme case (domain is fully filled with water). The relative error ε_r are calculated by Eq. (4.6) but the $\mathbf{u}$ is instead by S_{total} as shown in Eq. (4.18).

$$\varepsilon_r = \frac{\sqrt{(S_{\text{total}} - S_{\text{total,anal}})^2}}{S_{\text{total,anal}}} \tag{4.18}$$

where $S_{\text{total,anal}}$ is the analytical solution of total saturation. The results of ε_r for different relaxation time $\tau_1 = \tau_2$ are summarized in Table 4.4

Table 4.4.: Relative error ε_r with different relaxation time in the open boundary condition validation (summarized from Fig. 4.40 with $\mathbf{u}_{\text{inlet}} = 0.001$ l.u.)

ε_r /%	$\tau_1 = \tau_2 = 0.7$	$\tau_1 = \tau_2 = 1$	$\tau_1 = \tau_2 = 1.4$
Total	1.70	1.70	1.72
Before $S_{\text{anal}} = 1$	2.81	2.81	7.08
After $S_{\text{anal}} = 1$	1.09	1.09	1.45

It is also observed from Fig. 4.40 that the cases $\tau_1 = \tau_2 = 0.7$ and $\tau_1 = \tau_2 = 1$ agree very well with the analytical solution at the beginning period (0 l.u. $< \mathbf{u}_{\text{inlet}} t < 450$ l.u.). It is seen from the Table 4.4 that the case with $\tau_1 = \tau_2 = 1.4$ has the bigger error than that with another two relaxation times. In the last period before $S_{\text{total}} = 1$ (450 l.u. $< \mathbf{u}_{\text{inlet}} t < 750$ l.u.) which can be called the 'transient period' (critical point of $S_{\text{total}} = 1$ is involved) in Fig. 4.40, errors are observed for all relaxation time in this period. It means the open boundary condition has a restriction on the 'transient period'.

- **Inlet velocity effect**

In this part, different inlet velocities $\mathbf{u}_{\text{inlet}}$ under the same relaxation time $\tau_\alpha = 0.7$ are tested and the results are shown in Fig. 4.41.

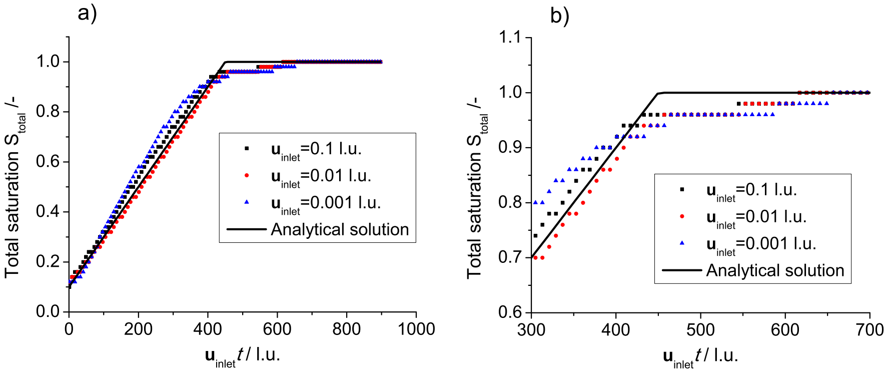

Figure 4.41.: a) Total saturation S_{total} against the $\mathbf{u}_{\text{inlet}} t$ of different inlet velocities $\mathbf{u}_{\text{inlet}}$ and in comparison with the analytical solution ($\tau_1 = \tau_2 = 0.7$). b) Zoom of transient period region in Fig. 4.41 a)

The cases with three $\mathbf{u}_{\text{inlet}}$ all agree well with the analytical solution. It means the open boundary condition validation is independent of $\mathbf{u}_{\text{inlet}}$ but with some errors. The 'transient period' are also observed in the Fig. 4.41. The relative error ε_r with different $\mathbf{u}_{\text{inlet}} t$ are summarized in Table 4.5

Table 4.5.: Relative error ε_r with different inlet velocity $\mathbf{u}_{\mathsf{inlet}}$ in the open boundary condition validation (summarized from Fig. 4.41 with $\tau_1 = \tau_2 = 0.7$)

ε_r /%	$\tau_1 = \tau_2 = 0.7$	$\tau_1 = \tau_2 = 1$	$\tau_1 = \tau_2 = 1.4$
Total	0.93	1.73	1.45
Before $S_{\mathsf{anal}} = 1$	4.30	2.81	6.40
After $S_{\mathsf{anal}} = 1$	1.05	1.09	1.45

The $\mathbf{u}_{\mathsf{inlet}}$ has influence on the accuracy of open boundary condition validation. When $\mathbf{u}_{\mathsf{inlet}}$ is smaller (like $\mathbf{u}_{\mathsf{inlet}} = 0.001$ l.u.), the bigger error are observed and the error sources are the spurious velocity $\mathbf{u}_{\mathsf{spu}}$ (introduced in section 4.2).

- **Compare with pressure condition**

According to the relaxation time dependence analysis above, $\tau_1 = \tau_2 = 0.6$ is chosen in this part. The inlet velocity $\mathbf{u}_{\mathsf{inlet}} = 10^{-3}$ l.u. (*Ca* $= 10^{-4}$) is chosen to save computation time. The results of open boundary and pressure boundary conditions on outlet are compared. The pressure boundary is achieved by the Zouhe method [150]. The ρ_1 and ρ_2 are fixed on the outlet ($\rho_1 = 2$ l.u. and $\rho_2 = 10^{-5}$ l.u. or $\rho_1 = 10^{-5}$ l.u. and $\rho_2 = 2$ l.u.). The pressure in outlet can be calculated by the Eq. (2.16). It is observed the cases with pressure boundary are more likely crashed when the two-phase moves close to the outlet boundary. However, the cases with open boundary conditions have the results shown in Fig. 4.40 and Fig. 4.41. Therefore, it is possible to conclude that open boundary condition is numerically more stable than the pressure boundary condition.

- **No-flat two-phase interface effect**

In this section, a suspended single droplet moves out of domain is simulated to check the influence of no-flat two-phase interface on open boundary condition. The simulation initialization is the same as that of SIDT in section 4.3.1. But the velocity boundary condition is adopted on the inlet layer (x=0 l.u.) by the Zouhe method [150]. And the open boundary condition is applied on the outlet boundary ($x = \mathrm{X}_{\mathsf{max}}$). Other boundaries are applied with the periodic condition. In order to compare the cases with different inlet velocities $\mathbf{u}_{\mathsf{inlet}}$, the snapshots with the same $\mathbf{u}_{\mathsf{inlet}}t$ are shown in Fig. 4.42

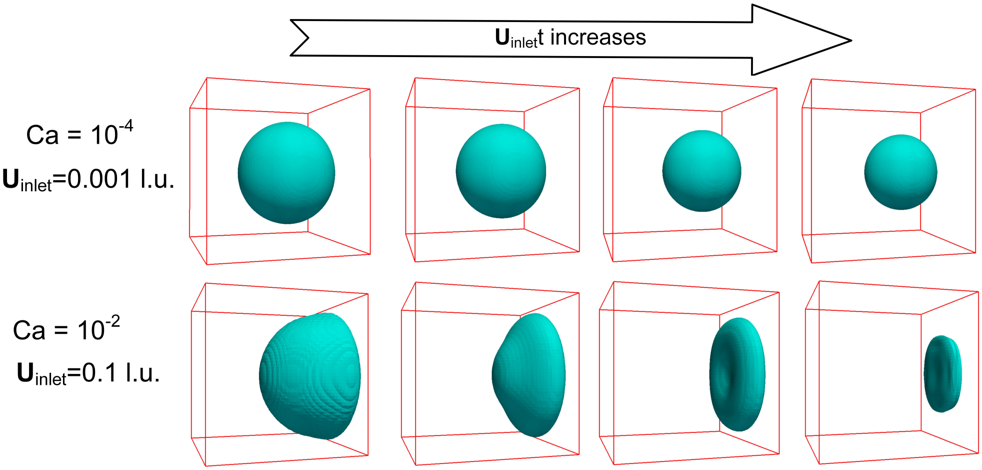

Figure 4.42.: Single droplet goes out of domain with different velocities to outlet with open boundary condition

When the inlet velocity $\mathbf{u}_{\text{inlet}}$ is relatively small, the liquid droplet will keep the sphere shape near the outlet area and becomes smaller (because liquid is pushed out of domain). When the $\mathbf{u}_{\text{inlet}}$ increases, the droplet shape is irregular when it touches the outlet boundary. As time goes on, the liquid volume is smaller, but the droplet shape still irregular. Because when the droplet moves out of the domain, the surface tension of the outer part cannot be considered. Therefore, the remaining surface will change (because no complete droplet anymore). Another reason of no-flat two-phase interface cannot be correctly simulated is that the open boundary condition is assumed the flow in outlet is fully developed which is not the case of no-flat two-phase interface.

4.6. Summary

In a short summary of this chapter, some main conclusions from validation tests are below.

(i) **External force driving Poiseuille flow test.** Three force schemes (SV, Guo and EDM schemes) can be implemented in the LB single-phase model and they have the same accuracy in the LB single-phase model.

(ii) **Flat interface test.** The LB ShanChen model with MRT approach is more relaxation time (viscosity) independent than that with SRT approach. The EDM scheme is more accurate than SV scheme. The MRT-EDM ShanChen model with the model parameter $G_{\text{coh}} = 0.06$ (in Eq. (2.12) are chosen for the afterward simulations because of interface thickness accuracy.

(iii) **Droplet test.** The model can work in the no-flat interface two-phase flow and the surface tension $\sigma_{s,l} = 0.1883$ l.u. which is independent of the relaxation time (viscosity). The model can simulate the surface tension force effect and the coalescence process.

(iv) **Contact angle test.** A series of contact angles can be simulated with varying the model parameter $G_{\text{adh},1}$. The different contact angles have different errors on the three-phase boundary (Fig. 4.37). The model parameter $G_{\text{adh},1} = -0.005$ to ensure $\theta_{\text{PTFE}} = 110°$, and $G_{\text{adh},1} = 0$ to ensure $\theta_{\text{carbon}} = 90°$. The SPPF method is valid with the symmetric droplet on the smooth solid surface and the method parameters $m = 5$ and $n = 4$ are applied on the afterward apparent contact angle analysis in chapter 6.1.

(v) **Open boundary condition test.** The open boundary can work in the present MRT-EDM model. In comparison with pressure boundary condition, the cases with open boundary condition are numerically more stable.

The model parameters determined from model validation are summarized in Table 4.6 and applied on all the afterward water flowing through the GDL simulations from chapter 5 to 7.

Table 4.6.: Model parameters determined by model validation of chapter 4

	Formula	Value	Reference	Section
Cohesive force parameter	G_{coh}	0.06	Eq. (2.12)	4.2.1
Relaxation time	$\tau_1 (= \tau_2)$	0.6	Eq. (2.20)	4.2.2
Surface tension	$\sigma_{s,l}$	0.1883 l.u.	Fig. 4.23 †	4.3.1
Adhesive force parameter for PTFE	$G_{\text{adh},1} (= -G_{\text{adh},2})$	-0.005	Eq. (2.13)	4.4
Contact angle on PTFE	θ_{PTFE}	110°	Manufacture [5][6]	4.4
Adhesive force parameter for carbon	$G_{\text{adh},1} (= -G_{\text{adh},2})$	0.0	Eq. (2.13)	4.4
Contact angle on carbon	θ_{carbon}	90°	Literature [98][164]	4.4
Pixel number for the 1st order polynomial curve fitting in SPPF	n	4	Literature [147]	4.4
Pixel number for the 2nd order polynomial curve fitting in SPPF	m	5	Fig. 4.38	4.4

In the Table 4.6, the contact angle on materials θ_{PTFE} and θ_{carbon} are all under the temperature 70°C. When temperature increases, the contact angle on the carbon θ_{carbon} is the same as that under the ambient temperature [164]. The contact angle is related with the surface tension (γ_{LG}, see Eq. (2.5)), the surface tension decreases with bigger temperature [30].

---

† The slope of the constraint linear curve fitting in Fig. 4.23 and it is 0.1883 l.u..

5. Simulation of liquid water through GDL

As described in section 1.2, the GDL plays a significant role for water management which maintains the balance between water removal and membrane hydration [16]. In this chapter, the liquid water flowing through GDL is simulated. The gaseous reactant in the GC which removes the formed droplets on the GDL surface is not considered. It is assumed that the steady apparent contact angle is not affected by the components in GC. It is also assumed that the liquid water and gaseous reactant have nearly no influence on water transport in GDL [31]. The effects of some basic factors on the water flowing through the GDL are discussed including the buffer space thickness effect, the domain size effect, the capillary number effect, the geometry effect and the wettability effect.

5.1. Simulation setups and conditions

From the model side, the MRT-EDM model is applied on the all simulations of liquid water flowing through the GDL in this chapter. The schematic simulation setup of apparent contact angles is shown in Fig. 5.1a). The simulation setup consists of three main regions including free space, GDL and buffer space. The thickness of the free space is big enough to see the situation after water breaking through GDL (such as formed water droplets on the GDL surface) and it equals the GDL thickness. The GDL material (carbon) itself is almost neutral hydrophobic (contact angle is around 90°) and treated with some hydrophobic agent (like PTFE) to enhance water removal [42]. The contact angle on the PTFE surface is approximate 110° measured by some GDL manufactures [6][5]. In the section 5 and 6, GDL is assumed to be fully covered with PTFE, model parameter $G_{\mathrm{adh},1} = -0.005$ and material property (contact angle on the PTFE material) $\theta_{\mathrm{PTFE}} = \theta_{\mathrm{idl}} \approx 110^{\circ}$ (see Fig. 4.36), except the section 5.6 mentioned the different wettability.

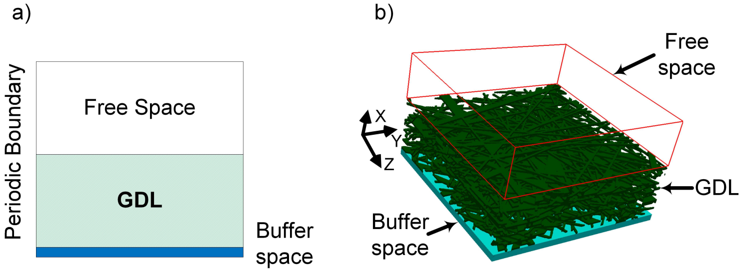

Figure 5.1.: a) Schematic simulation setup ; b) 3D simulation setup and initialization of the density field. Water is flowing along X direction [149].

The simulation initialization is shown in Fig. 5.1 b). The buffer space is initially fully occupied with water ($\rho_1 = 2$ l.u. and $\rho_2 = 10^{-5}$ l.u.) while other spaces (GDL and free space) are occupied with air ($\rho_2 = 10^{-5}$ l.u. and $\rho_1 = 2$ l.u.) which are based on the work by Chen et al. [45]. It is independent of mass unit conversion by m_r because m_r is calculated from surface tension σ_s as section 2.4. The inlet boundary is set on the bottom of buffer space ($x = 0$). The velocity condition is adopted to the inlet boundary and the given velocity is achieved by

the Zouhe method [150]. The outlet boundary locates on the top of free space ($x = \mathrm{X}_{\text{max}}$) and the open boundary condition (introduced in section 2.3) is adopted on that. The periodic boundary are applied in the span-wise directions to keep the formed droplets in the region above the GDL intact [29]. On the solid surface of GDL, the non-slip bounce-back condition is applied [141][102]. The velocity in inlet is set to 10^{-3} l.u. to ensure the *Ca* $\approx 10^{-4}$ which may happen on a small simulation domain area (0.36×10^{-2} cm^2) in comparison of whole active area (14.44 cm^2) of PEFC (introduced in section 1.2.1).
In the following water flowing through GDL simulation, the SI unit are used and converted from LU system according to the description in section 2.4, except for the specific topic the LU system are reminded. The reference variables and parameters in lattice unit are summarized in the Table 5.1. The corresponding model parameters (G_{coh}, $G_{\text{adh},1}$ and τ_1) are summarized in Table 4.6.

Table 5.1.: Variables and parameters used in the water flow in GDL (*Ca* $\approx 10^{-4}$)

	Formula	Value	Unit	Reference
Parameters in lattice unit				
Surface tension	$\sigma_{s,l}$	0.1883	l.u.	Table 4.6
kinematic viscosity	$\nu_1\ (= \nu_2)$	0.033	l.u.	Eq. (2.5)
Time	t_l	1	l.u.	Iteration loop
Inlet velocity	$\mathbf{u}_{\text{inlet},l}$	10^{-3}	l.u.	Input
Parameters in SI unit				
Surface tension	$\sigma_{s,p}$	0.064	kg·s^{-2}	Table 1.2
Kinematic viscosity (water)	ν_1	3.6×10^{-7}	m$^2 \cdot$ s^{-1}	Table 1.1
Inlet velocity	$\mathbf{u}_{\text{inlet},p}$	† 6×10^{-3}	m·s^{-1}	Table 2.3
Contact angle on PTFE	θ_{PTFE}	110	°	Table 4.6
Contact angle on carbon	θ_{carbon}	90	°	Table 4.6
Simulation GDL area	A_{sim}	0.36×10^{-2}	cm^2	GDL size
Simulation GDL thickness	$L_{\text{sim,GDL}}$	0.195	mm	GDL thickness
Current density	$\dot{I}$	6.3×10^3	A·cm^{-2}	Eq. (1.6)
Reference parameters				
Reference length	l_r	1.5×10^{-6}	m	Image resolution
Reference time	t_r	2.06×10^{-7}	s	Eq. (2.29)
Reference mass	m_r	8.6×10^{-13}	kg	Eq. (2.30)

It should be noticed that the elements in the diagonal matrix Λ_α, the $s_{9,1} = s_{9,2} = 1.64$ is calculated according to Eq. (2.20) with relaxation time $\tau_1\ (= \tau_2)$ in Table 5.1. In comparison with the current density data in Fig. 1.3 and $\dot{I}$ in Table 5.1, it is seen that $\dot{I}$ in simulation is already beyond and roughly thousand times larger than the current density up-limit of general operated PEFC. However, it is still comparable our simulation results and operated PEFC, because the main dimensionless number *Ca* $\approx 10^{-4}$ which is consistent with the situation in the actual running fuel cell (see section 1.2.1). But *Ca* $\approx 10^{-4}$ is still higher than the averaged value *Ca* $= 0.7 \times 10^{-8}$ (see Table 1.3). This big difference between simulation setup and actual

---

† The $\mathbf{u}_{\text{inlet},p}$ is converted from $\mathbf{u}_{\text{inlet},l}$ (10^{-3} l.u. in Table 5.1) by the unit conversion for velocity in Table 2.3.

operating condition due to the discrete effects (chemical reaction happens in-homogeneous) in the running PEFC [73] and the computation time (3 hour for 50000 loops of 30 million grids with 1200 CPU). The liquid flowing breakthrough the GDL will be slower with lower velocity, the computation time is proportional to the water inlet velocity. Therefore, if the real water velocity (from the experiments) are applied, the ages of time will be consumed by only one simulation. As the description of *Ca* in GDL in the Table 1.3 and Fig. 1.5, $Ca \approx 10^{-4}$ is possible in the operated fuel cell. According to the general description for components of PEFC as shown in Fig. 1.1, there is usually a MPL between the CL and the GDL. The function of MPL is to make the produced water more homogeneously before the water flowing through the GDL [31]. In the actual running fuel cell, it was observed that the produced water prefer to flow through the bigger pore regions [78]. The small cracks on the MPL and GDL were also observed during in-situ experiments by Markotter et al. [74] and a crack in the MPL and a GDL pore align to build up a transport path. Finally, these cracks have a localized effect on water transport property that may be magnified at a bigger inject fluid velocity (the bigger *Ca*) [165]. According to the geometry introduction in section 3.2, the GDL geometry with 400 l.u.×400 l.u.×130 l.u. (0.6 mm×0.6 mm×0.195 mm) are created. The GDL area in simulation is 0.36×10^{-2} cm^2 (0.6 mm×0.6 mm) and it is significant smaller than the actual effective area (A_{eff} =14.44 cm^2, see Table 1.2), which has four orders of magnitude difference. Moreover, the inhomogeneous chemical reaction happened on the CL. The droplet growth seed position will be randomly produced on the CL surface and the droplet size will be different in different timesteps and operation conditions. They were observed in some in-situ experiments by Zhang et al. [165]. From the computation time side, if the $Ca = 10^{-8}$ was used instead of $Ca \approx 10^{-4}$, the water inlet velocity $\mathbf{u}_{\text{inlet}}$ (see Eq. (1.8)) will be $O(10^{-4})$ lower. In order to observe water flowing through the GDL, there will be $O(10^4)$ times more time for one simulation case and the computation time will be much larger ($O(10^4)$) than that in the present case. Therefore, a compromise solution $Ca \approx 10^{-4}$ is chosen for afterward simulations, except the section 5.4 mentioned the different capillary numbers.

The MPL and the chemical reaction in the CL (see Fig. 1.1) are not considered in the model, the GDL surface on the CL side (buffer space in Fig. 5.1 a)) is set the inlet boundary and assumed to be fully flooded by water. This assumption is allowed because Eikerling's group work proved that the interface region between CL and GDL can be assumed to be a film which is fully flooded with produced water [166]. The counter flowed reactant Oxygen is diffused through the water film and chemical reaction happens by touching catalyst particles [167].

5.2. Buffer space thickness effect

In order to decrease the influence of velocity boundary layer and first GDL layer on the inlet side, there should be more than one layer arranged in the buffer space. If the buffer space consists of only one layer where the velocity boundary is defined on the same layer, and the first layer of GDL where may include some solid grids, the conflict of boundary conditions will raise (velocity boundary for inlet and bounce back for the solid neighbor grids) [150]. Considering the interface thickness (introduced in 4.2.1), the flow in the buffer space is even more inaccurate. Therefore, the influence of the buffer space thickness is checked in this section. One of geometries (geometry 5) is applied the simulations in this section. The setup of buffer space thickness effects is shown in Fig. 5.2. The GDL is assumed to be fully covered with PTFE and the material property (contact angle on the PTFE $\theta_{\text{PTFE}} \approx 110^{\circ}$ according to Table 4.6) is fixed.

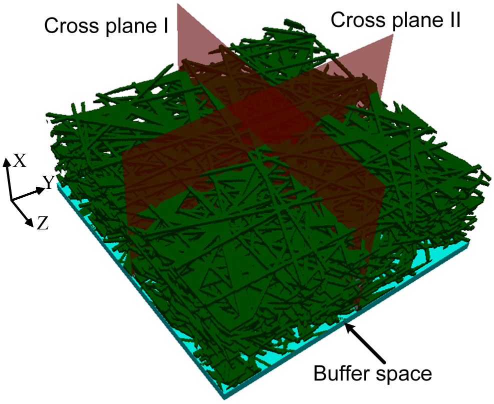

Figure 5.2.: 3D simulation setup of buffer space thickness (Geometry 5)

The density and velocity fields are initialized as description in section 5.1. The simulation results for checking buffer space thickness independence are presented when $t = 5$ ms (time is converted from time steps in lattice system to the SI unit according to description in section 5.1) before water breaks through GDL to save computation cost. The water distribution on cross plane I and II (see Fig. 5.2) with different buffer space thickness at $t = 5$ ms are shown in Fig. 5.3

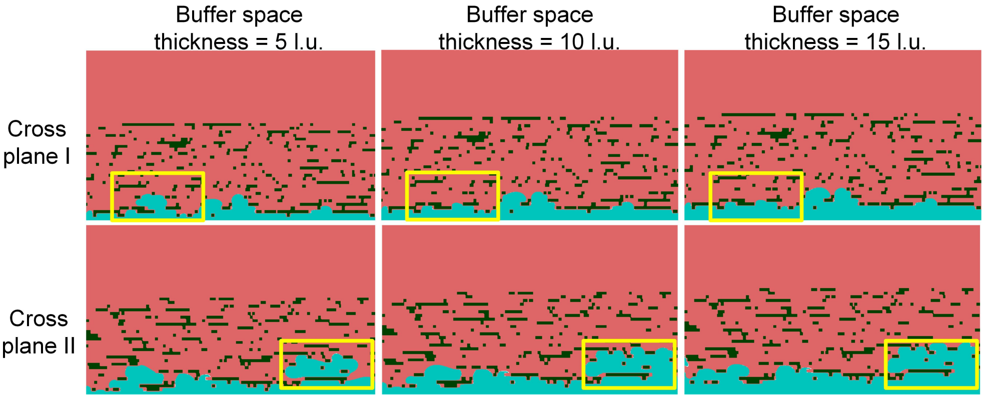

Figure 5.3.: Water distribution on cross plane I and II (see Fig. 5.2) with different buffer space thickness at $t = 5$ ms. yellow fram: potential 'finger' region. (Geometry 5) Green: PTFE; blue: water; red:air.

The potential 'finger' region is defined the region where may observe the flow 'fingers' on the certain cross plane in Fig. 5.3. From the water distribution on cross plane I and II in Fig. 5.3, the flows with buffer space thickness 10 l.u. and 15 l.u. are quite similar from the macro point of view. But the case with buffer thickness 5 l.u. is different from them especially in the potential 'finger' region (yellow frame region in Fig. 5.3). It means the simulation with buffer space thickness 5 l.u. is influenced more than another two cases. From the 3D view, the elevation plot of the liquid water are presented in Fig. 5.4. The water front is shown in the images (such as Fig. 5.4) colored by the elevation. The elevation of a location is its height above a fixed lowest reference point, while a fixed highest reference point where presenting the up-limit of elevation is also defined. In the Fig. 5.4, the lowest reference point is the geometry center of the inlet layer and the highest reference point is the geometry center of the layer in the middle of GDL along the through-plane direction.

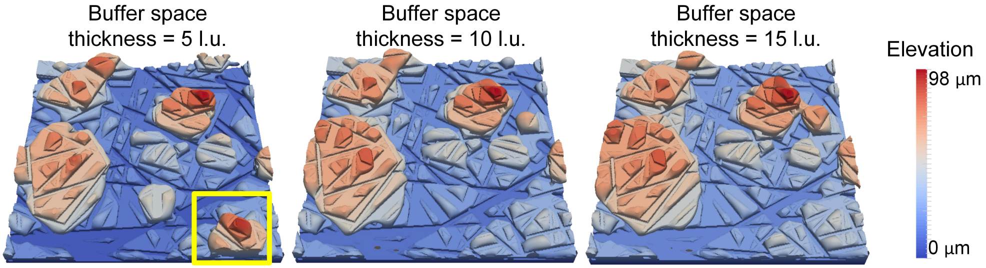

Figure 5.4.: Elevation plot of water distribution with different buffer space thickness at $t = 5$ ms. Yellow frame region is the mainly different region. (Geometry 5)

The local saturation S_{local} and total saturation S_{total} can be computed by Eq. (4.13) while V is the volume of empty pores in every layer and in whole GDL separately. The dynamic saturation curves of different buffer space thickness at the begin period ($\leqslant 5$ ms) are shown in Fig. 5.5

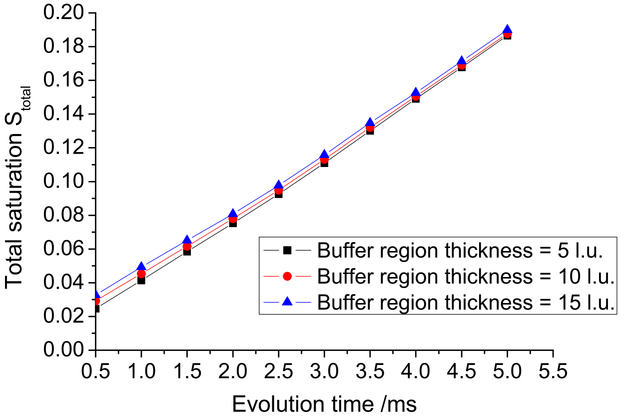

Figure 5.5.: Dynamic saturation curves of different buffer space thickness (5 l.u., 10 l.u. and 15 l.u) (Geometry 5)

It is seen from Fig. 5.5 that dynamic saturation curves with different buffer region thickness are not exactly the same. In the theory of mass balance, the total saturation curves should be exactly the same because of the same water volume flux are input in the domain. But the total saturation difference are mainly from the algorithm and the complex GDL structures. The algorithm errors are from the two-phase interface thickness (3 l.u. with $G_{\text{coh}} = 0.06$ in Fig. 4.2). Particularly, when water flows through the pore region which is locally equal or smaller than the interface thickness, it is hard to distinguish accurately whether the pore is saturated or not. Besides the algorithm error, this small difference ($\approx 5\%$) are reasonable due to the density and velocity field initialization. It is seen from Fig. 5.5 that the dynamic saturation curve is higher with bigger buffer region thickness. It is related with the interface thickness (3 l.u. when $G_{\text{coh}} = 0.06$, see Table 4.2). Because when the buffer region thickness is smaller, the error from two-phase interface thickness is bigger (interface thickness is close to the buffer region thickness) and it cause less grids in are taken into account to the water (the less water means the lower saturation) in the simulation results. The buffer space is fully initialized with the homogeneous density and zero velocity. Therefore, when simulation starts to run with a input velocity from the inlet boundary, several time steps are necessary to update the density and velocity field and move the whole water from the buffer space to the GDL area. It will redistribute the velocity field on the GDL surface and be more close to the realistic condition. If the buffer space is small (like 5 l.u.), the flow have less time to redistribute the flow and some extra flow behavior may happen (see yellow frame region in Fig. 5.4). In order to check the water details inside of GDL, the saturation along the through-plane direction for different buffer space thickness (t =5 ms) is shown in Fig. 5.6.

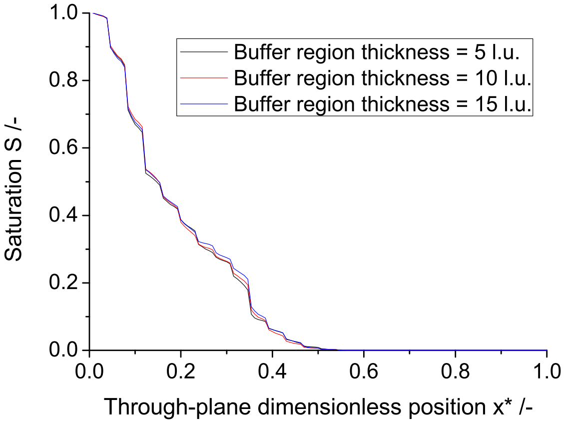

Figure 5.6.: Local saturation along the through-plane direction at $t = 5$ ms for different buffer space thickness (5 l.u., 10 l.u. and 15 l.u.) (Geometry 5)

The through-plane dimensionless position x^* is defined according to the Eq. (5.1).

$$x^* = x/L_{\text{sim,GDL}} \tag{5.1}$$

Where x is the position along the flow direction (X direction) through the GDL and $L_{\text{sim,GDL}}$ is the simulated GDL thickness (195 μm). The maximum total saturation difference ΔS_{total} and saturation difference ΔS for buffer space thickness 5 l.u. and 10 l.u., 10 l.u. and 15 l.u.. are summarized from data in Fig. 5.5 and Fig. 5.6 to the Table 5.2

Table 5.2.: Maximum total saturation difference $\Delta S_{\text{total,max}}$ and saturation difference ΔS_{max} between different buffer space thickness (Geometry 5)

Between which two buffer space thickness	$\Delta S_{\text{total,max}}$ /%	ΔS_{max} /%
5 l.u. and 10 l.u.	0.46	1.65
10 l.u. and 15 l.u.	0.39	1.68

It is seen from Fig. 5.6 and Table 5.2 that the local saturation with different buffer space thickness are slightly different ($\approx 5\%$). From $\Delta S_{\text{total,max}}$, it is seen that the bigger buffer space thickness have less effects on total flow behavior. Because further distance between inlet boundary and the first layer of GDL and the velocity condition in inlet has less effect on flow behavior. The ΔS_{max} is stable as increasing buffer space thickness cases but with a certain maximum difference ($\Delta S_{\text{max}} \approx 1.68\%$). The density field on the cross plane II (see Fig. 5.2) of buffer space thickness = 15 l.u. of geometry 4 at $t = 5$ ms is shown in Fig. 5.7.

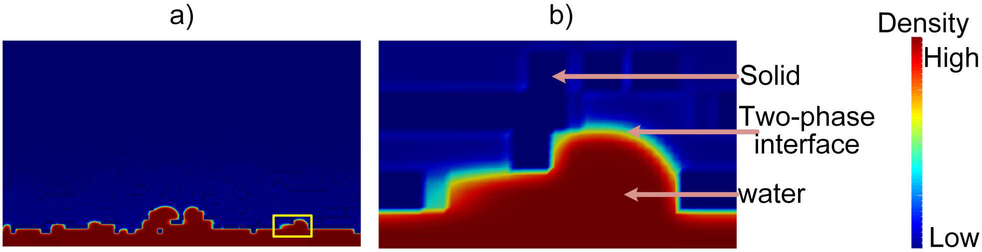

Figure 5.7.: a) Density field without image postprocess on the cross plane II (see Fig. 5.2) of buffer space thickness = 15 l.u. at $t = 5$ ms (Geometry 5). b) Zoom of yellow frame region in Fig. 5.7 a).

The Fig. 5.7 a) is also presented in the Fig. 5.3 (buffer space thickness = 15 l.u. of cross plane II) with a image postprocess to omit the two-phase interface. It is seen from the original density field in Fig. 5.7 b), the clear two-phase interface with a certain thickness (≈ 4 l.u., see Table 4.2) are observed and it is consistent with conclusion from Fig. 4.12. The interface thickness is close to the diameter of single solid fiber (5 l.u.), therefore some errors due to interface thickness raises and it is one of explanations why the local saturation are different in Fig. 5.6. Moreover, the total saturation difference in Table 5.2 is smaller than the relative error $\varepsilon_r \approx 11\%$ when the characteristic length is 8 l.u in Fig. 4.3. It proves the local water distribution difference is dominated by the local meshes and the algorithm (interface thickness). But it is clearly seen macro water flow behavior is highly affected by buffer space thickness and the extra 'flow fingers' are generated (see Fig. 5.4). The bigger buffer space thickness makes simulation more expensive and time consuming according to the results in Fig. 3.2.

In a conclusion, the buffer space thickness has effect on the water flow through the GDL. The small buffer space thickness cause the extra flow behaviors (e.g. the extra flow 'fingers'). The buffer space thickness of 10 l.u. is chosen for all the afterward simulations to balance the time consuming and accuracy.

5.3. Domain size effect

In this section the general domain size effect on the water flowing the GDL behavior is studied. The simulation setup and boundary conditions (in section 5.1) are the same with that in buffer space thickness effect of section 5.2. One of 22 GDL geometries (geometry 4) is chosen with different subdomains sizes. The subdomains (300 l.u. × 300 l.u., 200 l.u. × 200 l.u. and 100 l.u. × 100 l.u.) are cut off from the biggest domain (400 l.u. × 400 l.u.) shown in Fig. 5.8. The domain structures are assumed to be fully covered with PTFE and the material property (contact angle on the PTFE $\theta_{\text{PTFE}} \approx 110^\circ$ in Table 4.6) is fixed.

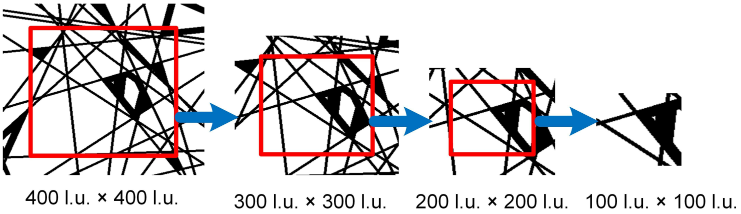

Figure 5.8.: The subdomains (300 l.u. × 300 l.u., 200 l.u. × 200 l.u. and 100 l.u. × 100 l.u.) are cut off from the biggest domain (400 l.u. × 400 l.u.). (Geometry 4)

The porosities of the subdomains are summarized in Table 5.3.

Table 5.3.: Porosity of different subdomains in geometry 4

	100 l.u.×100 l.u.	200 l.u.×200 l.u.	300 l.u.×300 l.u.	400 l.u.×400 l.u.
Porosity /-	0.798	0.791	0.796	0.801

It is seen that the porosities of these subdomains are slightly different but the difference is less than 1%. Therefore, it can be assumed that the porosity difference has a negligible impact on the transport simulation. The simulation setup and fields initialization are the same as buffer space thickness independence in section 5.2 but different domain sizes. The dynamic saturation curves with different domain sizes are shown in Fig. 5.9 a).

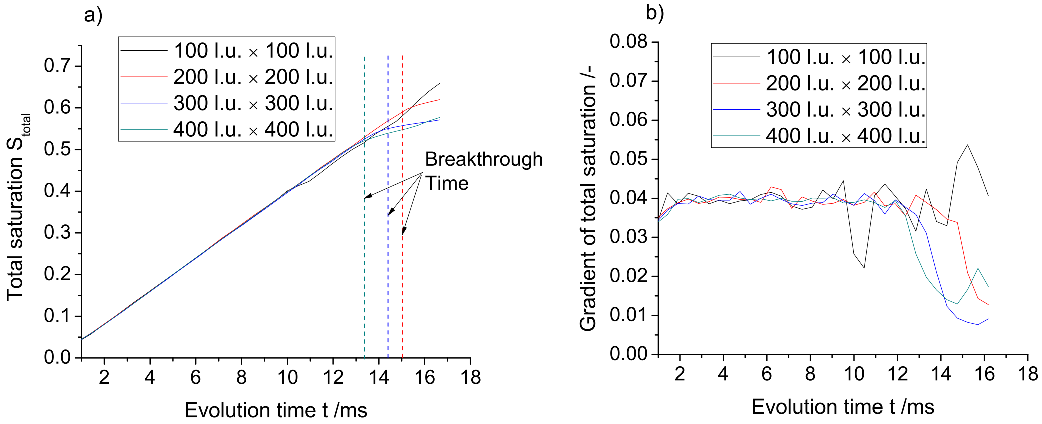

Figure 5.9.: a) Dynamic saturation curves of different domain sizes. b) Gradient of total saturation of different domain sizes (100 l.u. × 100 l.u., 200 l.u. × 200 l.u., 300 l.u. × 300 l.u. and 400 l.u. × 400 l.u.). (Geometry 4)

Different domain sizes have the quite similar dynamic saturation curve at the beginning period ($t \leqslant 10$ ms). Afterward (at $t \approx 11$ ms), the smallest domain (100 l.u. × 100 l.u.) is slightly different from others and the S_{total} keeps growing. In the theory of mass balance, the total saturation curves should be the same before water flowing breakthrough the GDL. It is observed that the slope of the dynamic saturation curve decreases due to water breaking through the

GDL. Then the breakthrough time t_{break} is defined when the slope starts to decrease. The breakthrough time for three domains with side length (200 l.u., 300 l.u. and 400 l.u.) are shown in Fig. 5.9 a) while the domain with side length 100 l.u. did not achieve breakthrough time. The gradient of total saturation of different cutoff sizes are shown in Fig. 5.9 b). It is observed that the case with 100 l.u.× 100 l.u. fluctuated more than another three cases. The gradient of total saturation starts continuously decrease after around 12 ms when subdomain sizes are bigger than 100 l.u.× 100 l.u.. It is clear that the liquid flowing through the domain with 100 l.u. × 100 l.u. is different from that in other subdomain sizes. It can be explained by the mean pore size (≈ 100 µm which is 70 l.u.) of this GDL geometries presented by Thiedmann et al. [168]. The mean pore size is very close to the smallest case of domain size (100 l.u.) and some mean pores have a higher possibility to be cut off from the original domain size. Due to the application of periodic condition around the geometries, it makes the GDL structure are different (the GDL structures are not periodic) from the original case and the water flow will be affected more from the periodic boundary. Due to the periodic condition, the empty pores on boundaries are connected. The empty pores may connect with themselves when they are large. The water can get a completely different 3D flow behaviors through the large empty pores instead of some small empty pores, and it causes the fluctuation at $t \approx 10$ ms for 100 l.u. × 100 l.u. in Fig. 5.9. Besides the geometry structure effect, water is also affected by the water inside of GDL. The formed droplets on GDL have effect back to the water inside of GDL due to the surface tension force. When the droplets (sphere-like) on the GDL surface keeps growing, finally the droplets are irregular and reformed because of the surface tension mimic the two-phase area (shown in geometry 4 in Fig. 5.19 and Fig. 5.25). The droplet coalescence with water happened close to the GDL surface. In another way, the two-phase interface also cause this fluctuation which are shown in Fig. 5.7 b). In this certain range of domain sizes, the bigger domain needs the shorter breakthrough time. In a snapshot time $t_{\text{snap}} = 14.3$ ms, the liquid situations are shown in Fig. 5.10

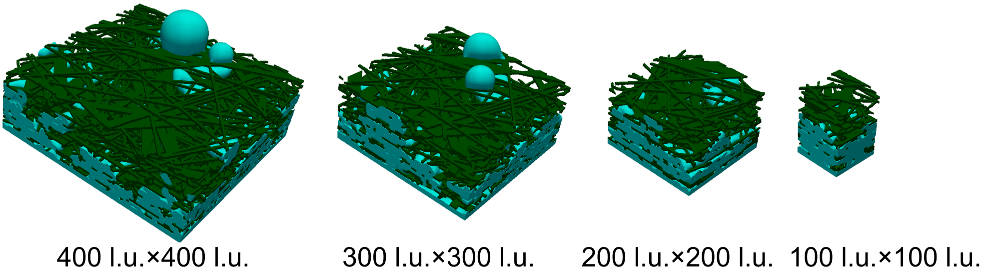

Figure 5.10.: Results of snapshot for different domain sizes (400 l.u. × 400 l.u., 300 l.u. × 300 l.u., 200 l.u. × 200 l.u. and 100 l.u. × 100 l.u.) at t_{snap} =14.3 ms. (Geometry 4)

The snapshot time is quite close to the breakthrough time of domain with side length 200 l.u., therefore liquid water looks 'almost' breaking through the GDL. For the two bigger domains (300 l.u. × 300 l.u. and 400 l.u. × 400 l.u.), the same amount of droplets are formed, but the sizes of the biggest droplet on geometries are different. The droplets sizes are different at the snapshot time because the water flow inside of two subdomains are different and they have different breakthrough time. For the case with earlier breakthrough time, the water have more chance to form bigger droplets on the GDL surface and less water are left inside of GDL. It can be concluded that the domain sizes have influence on the flow behavior. The local saturation of different domain sizes on the through-plane direction when $t = 15$ ms are shown in Fig. 5.11

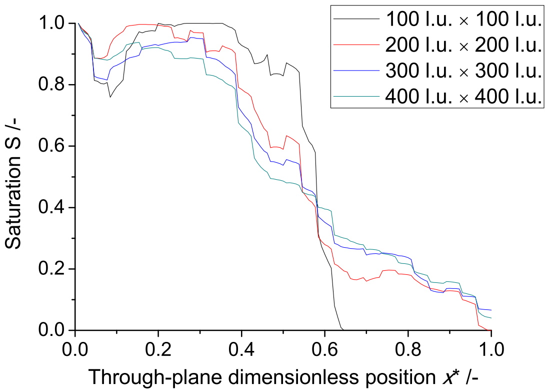

Figure 5.11.: Local saturation along the through-plane direction at $t_{\text{snap}} = 14.3$ ms for different domain sizes (400 l.u. × 400 l.u., 300 l.u. × 300 l.u., 200 l.u. × 200 l.u. and 100 l.u. × 100 l.u.) (Geometry 4)

It is seen from Fig. 5.11 that local saturation of 100 l.u.× 100 l.u. is largely different from other cases at $t_{\text{snap}} = 14.3$ ms. As time goes on, this local saturation along the through-plane direction are different due to water is continuously input. It is clear the case 100 l.u.× 100 l.u. are different from other cases at this time. It can be concluded that the case 100 l.u.× 100 l.u. is not big enough to represent the water flow through the GDL. The flow of 300 l.u.× 300 l.u. and 400 l.u.× 400 l.u. are more close than the cases with the smaller domain sizes. At $t_{\text{snap}} = 14.3$ ms, the flows on 100 l.u.× 100 l.u. and 200 l.u.× 200 l.u. are still not breaking through the GDL (local saturation on $x^* = 1.0$ are zero). It is also seen from Fig. 5.11 that the saturation of 100 l.u.× 100 l.u. is still zero after $x^* \approx 0.65$. On the region $0.2 < x^* < 0.4$, the local saturation of 100 l.u. × 100 l.u. is close to 1 while other cases are all lower than 1. It means the flow in 100 l.u.× 100 l.u. has a higher flooding (local saturation is 1) risk in the fuel cell.

- **Conclusion**

  The amount of formed droplets or breakthrough points are affected by the cut-off domain sizes. In the chosen case (geometry 4), the smaller cut-off domain sizes have rare opportunities to observe breakthrough points when some breakthrough points are already formed on the bigger cut-off domains. According to the pore size distribution of the created GDL geometries described by Thiedmann et al. [168], geometry 4 is one realization of that ensemble. Applying these GDL geometries on the simulations, the simulation domain should not be smaller than 300 l.u. × 300 l.u. within the present geometry resolution of 1.5 µm.

5.4. Capillary number effect

In this section, the capillary number effect on the water flowing through the GDL is discussed. The simulation setup is the same as before and described in section 5.1. One of geometries (geometry 5) is applied on simulations with different *Ca*. The GDL is assumed to be fully covered with PTFE and the material property (contact angle on the PTFE $\theta_{\text{PTFE}} \approx 110°$ according to Table 4.6) is fixed. The different water inlet velocities $\mathbf{u}_{\text{inlet}}$ are applied to ensure different *Ca* (Eq. (1.8)). In this section, four reference layers (ordered from R.L.1 to R.L. 4 along the flow direction and R.L.4 is on the top of GDL) are set which divides GDL into four equal parts shown in Fig. 5.12. The positions of them are $X = 48$ µm for R.L.1, $X = 96$ µm for R.L.2, $X = 144$ µm for R.L.3 and $X = 195$ µm for R.L.4.

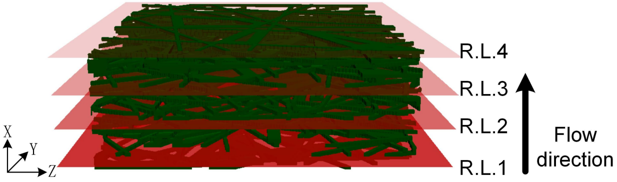

Figure 5.12.: Four reference layers (R.L.1 to R.L.4) are averagely set in GDL along the flow direction and R.L.4 is the top layer of GDL. (Geometry 5)

The simulation initialization and setup are described in section 5.1. The situations of different *Ca* are studied. According to the definition of *Ca* in Eq. (1.8), *Ca* is related with kinematic viscosity, velocity and surface tension. In this part, kinematic viscosity ν_2 and surface tension σ_s are given as section 5.1 ($\nu_2 = 0.037$ l.u. and $\sigma_s = 0.1883$ l.u.), inlet velocity $\mathbf{u}_{\text{inlet}}$ is adjusted to ensure a certain *Ca*. *Ca* is studied from 10^{-4} to 10^{-2}. As time goes on, water are input through the GDL and breaking through reference layers. The dynamic saturation curves with different *Ca* are shown in Fig. 5.13. In order to present the results of different *Ca* in Fig. 5.13, the $\mathbf{u}_{\text{inlet}}t$ is used on the horizontal coordinate. Four different specific snapshot positions $\mathbf{u}_{\text{inlet}}t = 30, 43, 73, 90$ µm are chosen for four reference layers from R.L.1 to R.L.4.

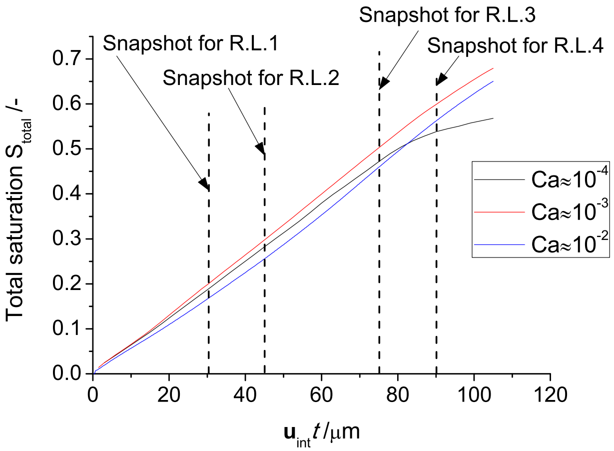

Figure 5.13.: Dynamic saturation curves of different *Ca* (10^{-4}, 10^{-3} and 10^{-2}). (Geometry 5)

It is seen from Fig. 5.13 that the case with *Ca* $\approx 10^{-4}$ shows the most clear that the slope of total dynamic saturation curve decreasing (happened on $\mathbf{u}_{\text{int}}t \approx 80$ µm). At different $\mathbf{u}_{\text{int}}t$, three dynamic saturation curves are different but not in a systematic way. The differences can be explained by the theory of two-phase in porous media (see Fig. 1.5) and the algorithm error. With the bigger *Ca*, the flow are more close to the stable displacement region in Fig. 1.5. It means the water flow through other routes to break through the GDL. The water front will be more complex (more flow fingers, see Fig. 5.14) with more flow path, and the two-phase

interface are formed on these water front positions (see Fig. 5.7 b)). Therefore, it will cause the bigger errors with the bigger *Ca*.
In order to compare the cases under different *Ca* (*Ca*≈ 10^{-4}, 10^{-3}, 10^{-2}), the water flow behavior with the different $\mathbf{u}_{\mathrm{int}}t$ and breaking through a certain reference layer are compared in Fig. 5.14. The inlet velocity and time used to present situations on four reference layers in Fig. 5.14 are summarized in Table 5.4

Table 5.4.: The inlet velocity $\mathbf{u}_{\mathrm{inlet}}$ and time used in Fig. 5.14

Ca	$\mathbf{u}_{\mathrm{inlet}}$ / m·s^{-1}	t for R.L.1 / ms	t for R.L.2 / ms	t for R.L.3 / ms	t for R.L.4 / ms
10^{-4}	0.0075	4.2	6.2	10.3	12.4
10^{-3}	0.075	0.42	0.62	1.03	1.24
10^{-2}	0.385	0.08	0.12	0.21	0.25

In order to compared the situations at different *Ca*, the $\mathbf{u}_{\mathrm{inlet}}t$ are the same for a specific reference layer (for example, $\mathbf{u}_{\mathrm{inlet}}t$ =30 µm for R.L.1 in Fig. 5.14).

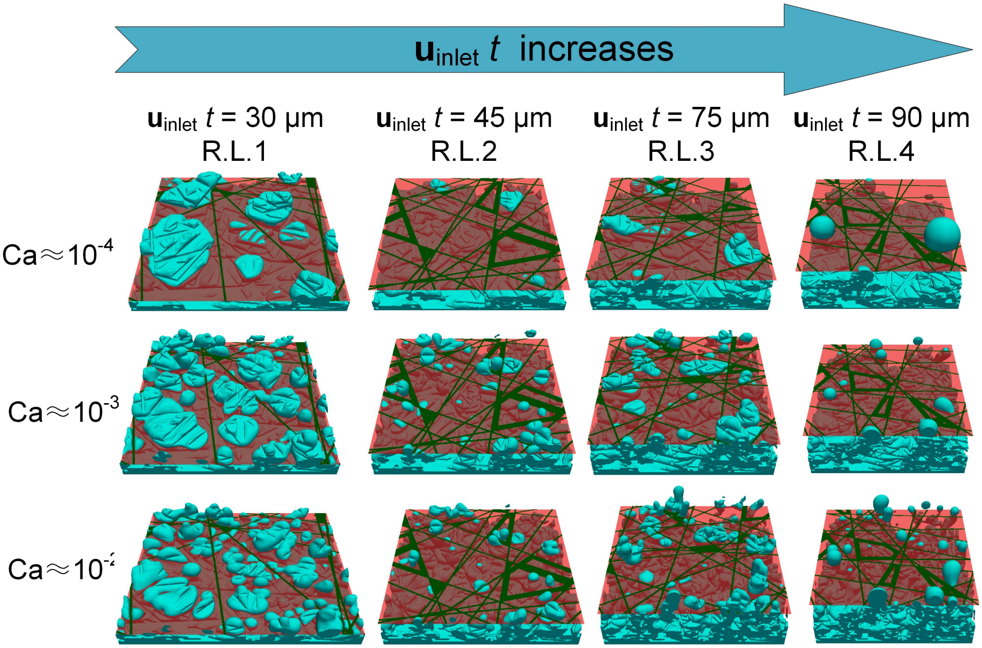

Figure 5.14.: Different *Ca* with different $\mathbf{u}_{\mathrm{inlet}}t$ when water breaking through the certain reference layer (Geometry 5). Red plane: reference layers; Blue: water; Green: carbon solid. R.L.4 is the top layer of GDL.

More droplets are formed on the R.L.4 when *Ca* is bigger. The formed droplets have different sizes and the smaller *Ca* have more opportunities to form the main bigger droplet. On the R.L.4, when the bigger *Ca*, some new breakthrough points and droplets are observed (the breakthrough point positions on R.L.4 when *Ca* $\approx 10^{-4}$ are also observed when *Ca* $\approx 10^{-3}$ and *Ca* $\approx 10^{-2}$). When checking the situation on the R.L.1, the clear amount of breakthrough points on R.L.1 can be seen and water front are 'finger-shape'. But much more breakthrough points are observed for *Ca* $\approx 10^{-3}$ and *Ca* $\approx 10^{-2}$. The water front is close to a irregular 'stable-displacement'. It is consist with the experiments observation that more droplets are formed with the bigger *Ca*, and the capillary effects are related with the GDL structures and the injection area [78]. Moreover, it is seen from Fig. 5.14 that with lower *Ca*, the more clear 'finger' can be seen and it means the 'finger dominated' process can be successfully simulated. The elevation plot of *Ca* $\approx 10^{-4}$ in different time t are shown in Fig. 5.15. In the elevation plot of Fig. 5.15, the lowest reference point for elevation is the geometry center of the inlet layer and the highest reference point is the geometry center of the GDL surface layer on the outlet side.

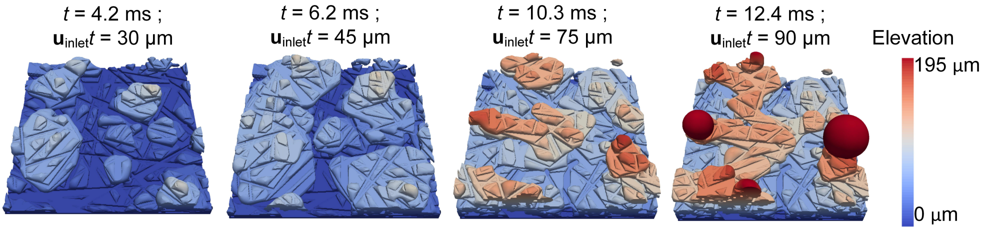

Figure 5.15.: Elevation plot of water distribution with *Ca*$\approx 10^{-4}$ at different time t (4.2 ms, 6.2 ms, 10.3 ms and 12.4 ms). (Geometry 5)

It validates *Ca* $\approx 10^{-4}$ can describe the 'capillary fingers' of water flowing through GDL (see section 1.2.1). It is also consistent with the conclusion from the two-phase flow behavior in porous media that the smaller *Ca* number, the more clear 'fingers' can be observed [34][33]. The local saturation along through-plane direction with different *Ca* when $\mathbf{u}_{\text{inlet}}t = 90$ µm are shown in Fig. 5.16.

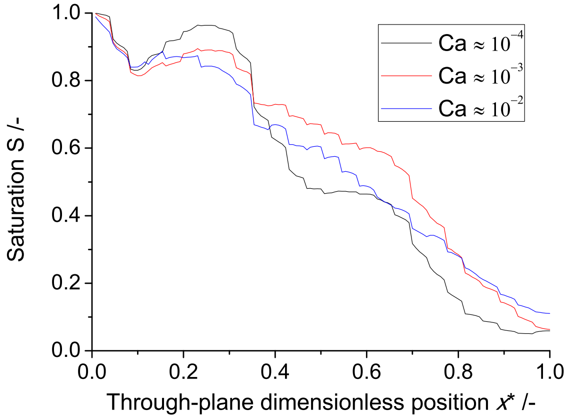

Figure 5.16.: Local saturation along the through-plane direction with different *Ca* (the same $\mathbf{u}_{\text{init}}t = 90$ µm, t =12.4 ms for *Ca* $\approx 10^{-4}$, t = 1.24 ms for *Ca* $\approx 10^{-3}$ and t = 0.25 ms for *Ca* $\approx 10^{-2}$)). (Geometry 5)

It is seen from Fig. 5.16 that the saturation with three *Ca* near the inlet region ($0 < x^* < 0.1$) are very close each other. After the inlet region ($0.1 < x^* < 1$), the saturation are not systematically related with the *Ca*. On the GDL surface ($x^* = 1$) of the outlet side, the *Ca* $\approx 10^{-2}$ has the bigger saturation than another two cases and it has the bigger breakthrough areas. The local saturation curves are tend to decrease along the through-plane direction and are consistent with the result from the PNM model and the continuum modeling [169][170]. The similar water saturation tendency through the GDL along through-plane direction from CL to GC were also observed in high-resolution neutron experiments [86].

- **Conclusion**

  Different *Ca* numbers are achieved by adjusting the inlet velocity $\mathbf{u}_{\text{inlet}}$. With the bigger *Ca* number, the less 'capillary effect' (more capillary 'fingers') can be observed. This observation is consistent with the experiments observations in phase diagram of two-phase flow behavior in porous media (Fig. 1.5) [33][34]. The local water saturation along the through-plane direction of GDL are different with different *Ca* numbers. In the operating fuel cell, when the *Ca* is calculated with the average velocity (*Ca* $\approx 10^{-8} \sim 10^{-5}$ in Table 1.3 and Fig. 1.5), the more clear capillary dominated process will happen and less fingers are observed. Therefore, the *Ca* $\approx 10^{-4}$ are used in the afterward water through GDL simulations because it is the most close case to the up-limit (*Ca* $\approx 10^{-5}$) of capillary dominated process in two-phase flow diagram (Fig. 1.5). The simulation time with *Ca* $\approx 10^{-4}$ (3 hours for 50 throusand time steps of 30 million grids with 1200 CPU) is acceptable in this thesis. The flow with *Ca* $\approx 10^{-2}$ is different from that with smaller *Ca* in GDL (see Fig. 5.14). It can also be concluded that the present model can only work properly (capillary fingering) on the water flowing through the GDL.

5.5. Geometry effect

As described in section 3.2, 25 different realized GDL geometries are created by the stochastic method with the similar porosity (≈ 0.8) and binder thickness (18 µm). In this part, 10 of 25 GDL geometries are applied on the water transport through GDL simulations. The porosity of these 10 GDL geometries are shown in Fig. 5.17. The effects of different geometry structures are studied.

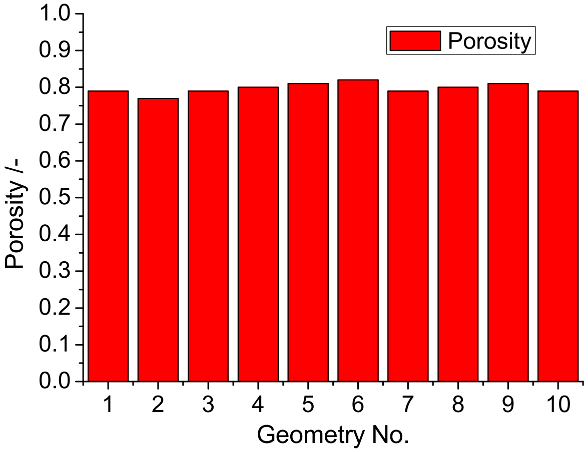

Figure 5.17.: Porosity of 10 GDL geometries.

Water flowing through 10 stochastic geometries which are statistical equivalent to the real structures. The simulation setups and conditions were described in section 5.1 with $Ca \approx 10^{-4}$ are simulated. The GDLs are assumed to be fully covered with PTFE and the contact angle on the PTFE $\theta_{\text{PTFE}} \approx 110^{\circ}$ is chosen according to the Table 4.6. The dynamic saturation curves of these 10 geometries are shown in Fig. 5.18

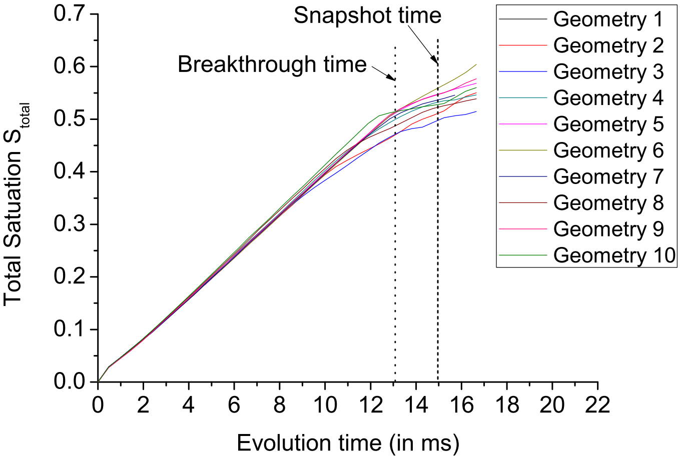

Figure 5.18.: Dynamic saturation curves of 10 different geometries. ($\theta_{\text{PTFE}} \approx 110^{\circ}$ with $G_{\text{adh},1} = -0.005$) [149].

It is seen from Fig. 5.18 that water flowing through 10 different GDL geometries have the quite similar dynamic saturation curves. They are not exactly the same because of slightly different porosity (see Fig. 5.17). There will be different total saturation S_{total} with different empty fluid grids in whole domain (according to definition of S_{total} in Eq. (4.13)). In comparison with the dynamic saturation curves in Fig. 5.13, the curves almost the same before the slope decrease. It means the errors from the geometries is smaller than that from different flow paths (water front). The breakthrough time t_{break} is defined when most of them (7 of 10 geometries) starts to decrease the slopes of dynamic saturation curves (due to liquid water breaking through the GDL) and it is around 13 ms. A same snapshot time $t_{\text{snap}} =$ 14.3 ms (2 ms later than t_{break}) is defined to catch the situation of droplets on the GDL surface. The snapshot time is taken during a non-steady state of droplet evolution. The chosen snapshot time ensures the biggest droplet in every geometry is large enough to allow the further detailed analysis (like apparent contact in section 6.1) The results of 10 geometries on the snapshot time ($t_{\text{snap}} =$ 14.3 ms) are shown in Fig. 5.19

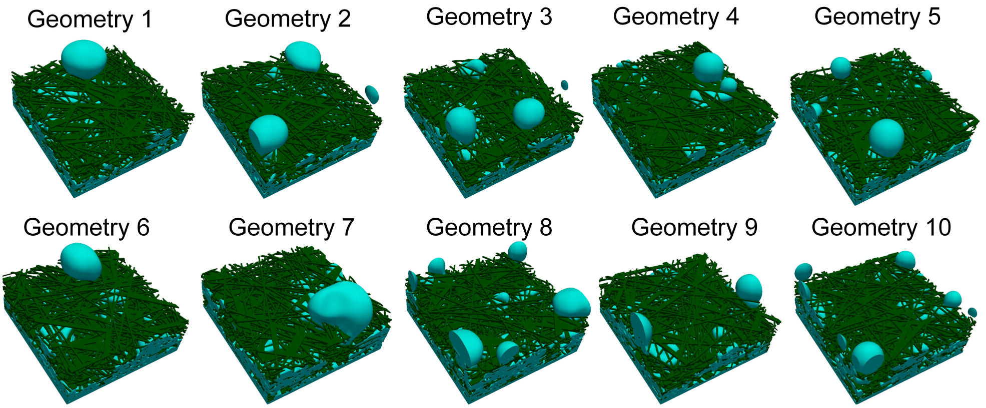

Figure 5.19.: Results of snapshot for 10 different geometries at $t_{\text{snap}} = 14.3$ ms. ($\theta_{\text{PTFE}} \approx 110°$ with $G_{\text{adh},1} = -0.005$)

It can be seen from Fig. 5.19 that different amount of droplets are formed on random positions of GDL. It is caused by the irregular structures even with the similar total porosity (see Fig. 5.17) and the similar pore size distribution (in Thiedmann et al. [171]) of GDL geometries. The breakthrough points are defined with the positions where droplets are formed. The biggest droplet on every geometry has the similar size and their volumes are bigger than the biggest droplet used on the contact angle test in section 4.4. But some droplets are formed near the boundary and touched the boundaries and are so called touching boundary droplets (see geometry 8, 9 and 10 in Fig. 5.19). The touching boundary droplets are intact due to the periodic boundary condition, but the region inside the GDL is not realistic (solid carbon fibers are not periodic) at the boundaries. The droplets which do not touch boundaries are called non-touching boundary droplets. Particularly, droplets on geometries 8 to 10 are all boundary-touching droplets and also some of the droplets touch boundaries on geometries 2 and 3. Therefore, when analyzing the droplet shape (section 6.1) or breakthrough points (6.2), only the non-touching boundary droplets are considered.

- **Flow details analysis**

  The flow details are studied by chosen one of geometries (geometry 5). The local saturation curves along the through-plane direction at different evolution time t are shown in Fig. 5.20

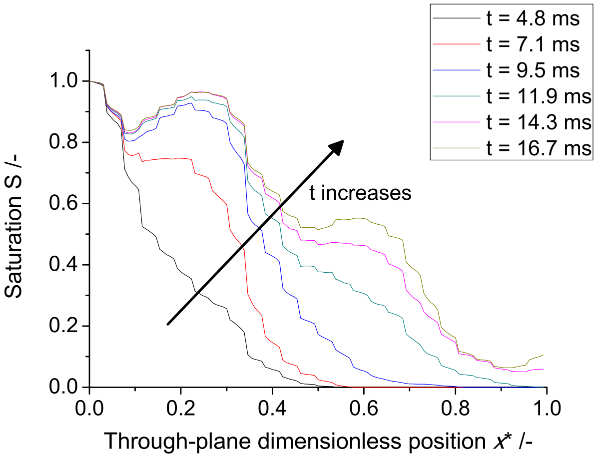

Figure 5.20.: Local saturation along the through-plane direction at different evolution time t ($\theta_{\text{PTFE}} \approx 110°$ with $G_{\text{adh,1}} = -0.005$). (Geometry 5 in Fig. 5.19)

For all evolution time, $S = 1$ when $x^* = 0$ because of the buffer space is fully filled with water. In the region close to the inlet ($0 < x^* < 0.1$), the local saturation is more time independent (saturation does not change too much with time) than other regions along the through-plane direction of GDL. It is also seen at the earlier time ($t = 4.8$ ms) that the saturation decreases along the through-plane direction, but did not break through the GDL. Afterwards, irregular 'S' shape saturation curves are observed because of the random structures inside of the GDL. It means for geometry 5, the flow are highly affect by the GDL structures after $t = 4.8$ ms. Particularly, in the position $x^* \approx 0.25$ and $x^* \approx 0.6$, the local saturation increases. The liquid water breaks through the GDL when $t = 14.3$ ms and $t = 16.7$ ms (saturation $S > 0$ at $X^* = 1$). In the position $x^* \approx 0.9$, S are almost the same between $t = 14.3$ ms and $t = 16.7$ ms but S are more different in the outlet ($x^* = 1$). It means in geometry 5, the 'throat' (also see Fig. 5.21) is most close to the outlet and located near the $x^* \approx 0.9$ position. The more water are injected through the GDL from the 'throat' position and enlarge the formed droplet on the GDL surface [172]. The stream line in geometries 1 and 5 at $t_{\text{snap}} = 14.3$ ms is shown in Fig. 5.21.

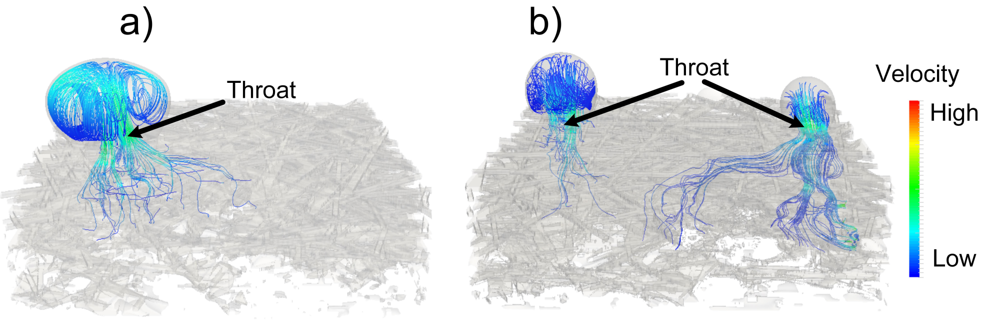

Figure 5.21.: a) Stream line of single formed droplet GDL at $t_{\text{snap}} = 14.3$ ms. (geometry 1). b) Stream line of a multiple formed droplets GDL at $t_{\text{snap}} = 14.3$ ms (geometry 5)

It is seen from Fig. 5.21 a) and b) that whatever for single formed droplet GDL and multiple formed droplet GDL, the 'tree' shapes of flow path are formed which mainly flows from partial region on the bottom of GDL. The observation from Fig. 5.21 a) and b) are consistent with the converging capillary tree water transport mechanism proposed by Nam and Kaviany [170]. The converging capillary tree presented the flow as an 'upside-down tree' that water mainly from different positions on the CL side. With water transporting through the GDL, finally water will flow breakthrough the GDL and water flows converging to a breakthrough area on the GDL surface. It can also be observed that the velocity is increased in some droplets 'throat' positions. These 'throat' positions are near the GDL surface regions, but some are also observed inside of GDL (see Fig. 5.21 b)). The elevation plot of water distribution on geometry 1 at different evolution time t are shown in Fig. 5.22. The water front can be represented with the elevation plot, such as Fig. 5.22 In the elevation plot of Fig. 5.22, the lowest reference point for elevation is the geometry center of the inlet layer and the highest reference point is the geometry center of the GDL surface layer on the outlet side.

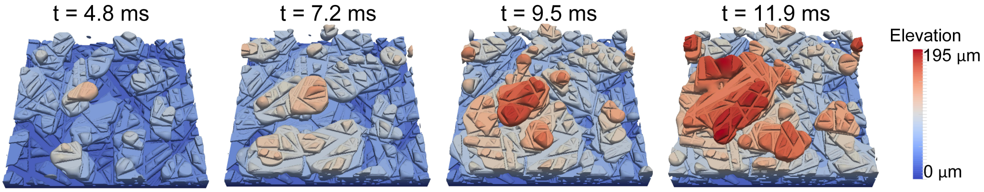

Figure 5.22.: Elevation plot of water distribution at different evolution time t. (Geometry 1)

It is seen from Fig. 5.22 that the water front inside of GDL is irregular. The water flows through some irregular routes. The details of water distribution can be presented on the cross plane I and II (see Fig. 5.2). The situation on cross plane I and II (see Fig. 5.2) of geometry 5 at different evolution time t are shown in Fig. 5.23

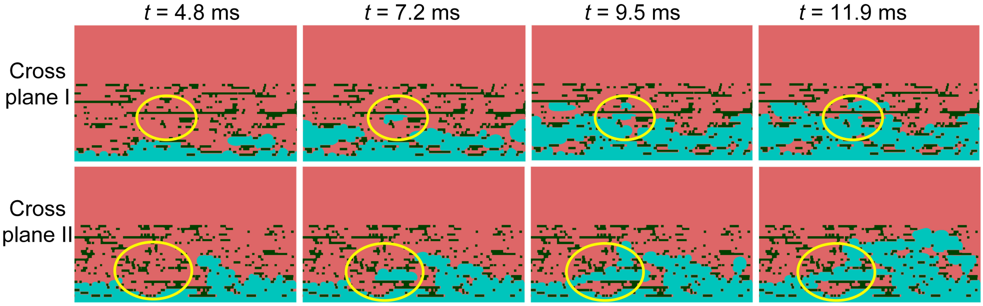

Figure 5.23.: Water distribution on cross plane I and II (see Fig. 5.2) at different evolution time t. (Geometry 1) (yellow frames are the region where create 'empty' (water around the pore) or backward 'finger'). red: air; green: GDL; blue: water

The water distribution on the cross plane I and II (see Fig. 5.2) are randomly and irregular, the dynamic water distributions are consistent with the observations from images taken by the X-Ray from experiments [69]. The 'fingers' grow in all directions, even backward (toward the entrance) (the 'empty' (water around the pore) region may be seen from the 2D cross section) [33]

When comparing the water distribution on R.L.4 (top layer of GDL, see Fig. 5.12) of geometry 4 at two different evolution time in Fig. 5.24

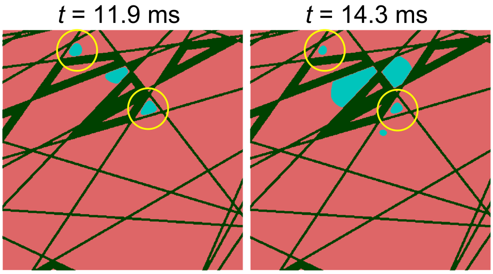

Figure 5.24.: Water distribution on R.L.4 (top layer of GDL, see Fig. 5.12) from $t = 11.9$ ms to $t = 14.3$ ms. (Geometry 4) (yellow frames are the regions where breakthrough areas are smaller). Blue: water; red: air; green: GDL.

It is seen from Fig. 5.24 that saturation on the R.L.4 is bigger and more breakthrough areas are formed as time goes on (three breakthrough areas at $t = 11.9$ ms and five breakthrough areas at $t = 14.3$ ms). However, it is observed that some breakthrough areas (yellow circles in Fig. 5.24) become smaller. The possible reason is that water are partially sucked back to the GDL and support other neighbor breakthrough areas. This 'shrink' phenomenon (comparison of the yellow circle regions between t =11.9 ms and t =14.3 ms in Fig. 5.24) were also observed in other two-phase simulations in GDL by Chen et al. [45].

- **Situation after snapshot time**

  The snapshot time $t_{\text{snap}} = 14.3$ ms is chosen to check the formed droplets on the GDL surface. It determines when the biggest droplet on every geometry is bigger than the biggest droplet (radius = 50 l.u.) used in the contact angle test of section 4.4. The results of geometries after the snapshot time are shown in Fig. 5.25 at $t = 16.3$ ms (2 ms later than the $t_{\text{snap}} = 14.3$ ms).

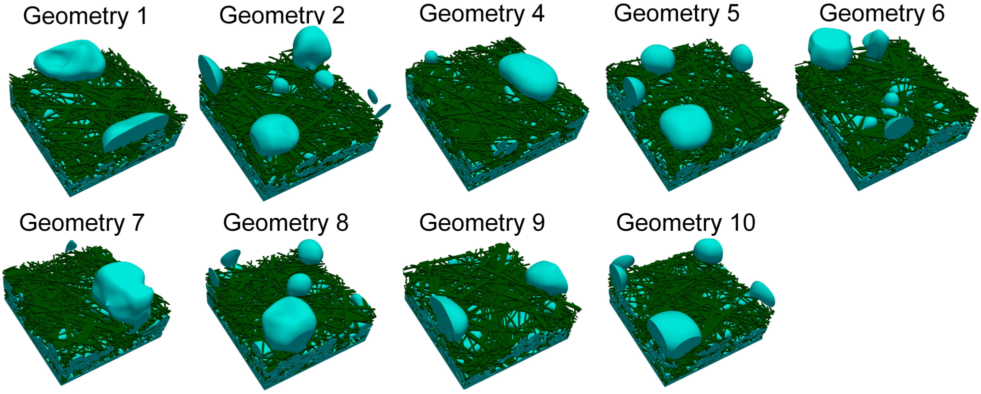

Figure 5.25.: Results of situation after snapshot time for geometries at $t = 16.3$ ms (2 ms later than $t_{\text{snap}} = 14.3$ ms)

Only results of 9 geometries are shown in Fig. 5.25. Geometry 3 is not included because the results are unstable with touching outlet boundary in the snapshot time and extremely irregular structure near the water breakthrough region. In comparison with the results in Fig. 5.19, the formed droplets in snapshot time keeps growing. The bigger droplets touches the randomly distributed carbon fibers near the breakthrough point and cause the irregular shapes. Moreover, the coalescence between quite close neighbor droplets are observed (e.g. in geometry 4, three formed droplets (see Fig. 5.19) coalescence to a bigger droplet). For some cases (like geometries 6 and 7), the biggest droplets touch the outlet boundary and cause the irregular droplets shapes.

- **Situation after switch-off velocity**

In this part, the inlet velocity is switched off to zero after the switch-off time t_{off}, the simulation setup and conditions before t_{off} are the same as description in section 5.1. This analysis is to study the water in GDL and on the GDL surface when shut off the fuel cell. The geometry 1 is chosen on the switch-off velocity analysis and switch-off time $t_{\text{off}} = 14.3$ ms (the same as the snapshot time in Fig. 5.5) is chosen to switch off the inlet velocity. The situation on the GDL surface after the t_{off} are shown in Fig. 5.26.

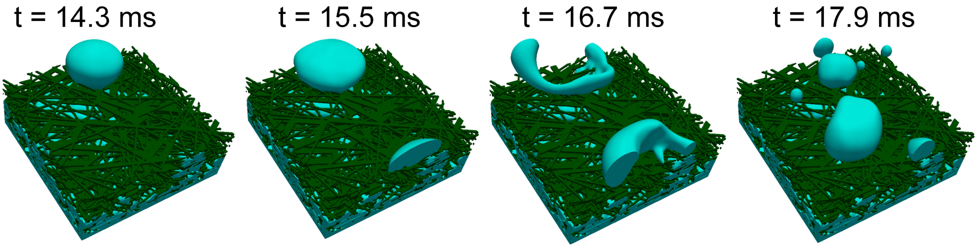

Figure 5.26.: Results of situation on the GDL surface after switching off inlet velocity at $t_{\text{off}} = 14.3$ ms.(Geometry 1) (The result at $t = 14.3$ ms is also shown for the geometry 1 in Fig. 5.19)

It is observed from Fig. 5.26 that the formed droplet keeps growing until an irregular shape after switching off the velocity at $t_{\text{off}} = 14.3$ ms. Then the shape of previously formed droplet on the GDL surface is changed very much (the formed droplet developed to a ring shape in this specific geometry). Three camera directions on viewing the situation at $t = 17.9$ ms are shown in Fig. 5.27

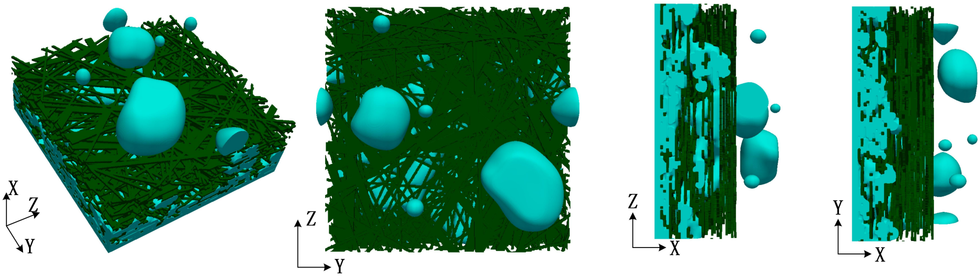

Figure 5.27.: Three camera directions on viewing the situation at $t = 17.9$ ms in Fig. 5.26. (Geometry 1)

It can be seen from the Fig. 5.27 that some irregular droplets leave the GDL surface to somewhere else at $t = 17.9$ ms. Some droplets even touch the outlet boundary. According to the validation of open boundary condition in section 4.5, the simulation results are not accurate when the droplet touches the outlet boundary. In addition, when the water flowing breakthrough the GDL, the dynamic behavior on the GDL surface (in GC) is not reliable because the water flow in GC is not capillary force dominated process and the density ratio and viscosity ratio cannot be negligible [41]. Therefore, the present model is not valid for the dynamic process out of GDL. The dynamic saturation (total saturation) curve of the switch-off velocity test is shown in Fig. 5.28

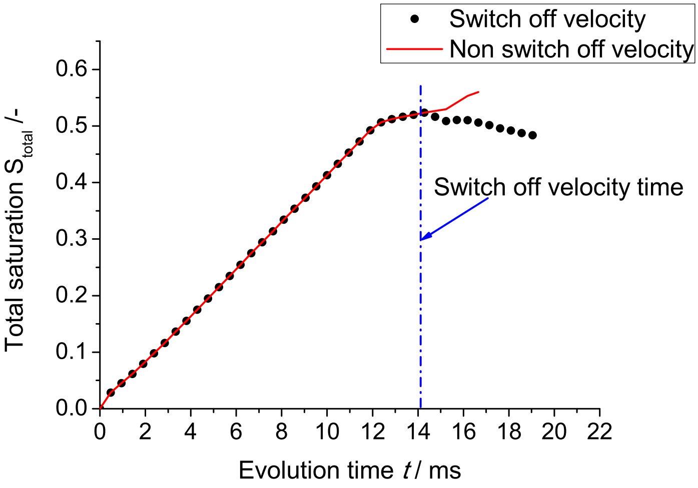

Figure 5.28.: Dynamic saturation curves of switch off velocity case and non switch off velocity case. (Geometry 1) (The switch-off velocity time $t_{\text{off}} = 14.3$ ms (the same as the snapshot time t_{snap} in Fig. 5.5)). Black dot line: inlet velocity is switched to zero after $t_{\text{off}} = 14.3$ ms, like Fig. 5.26. Red solid line: the inlet velocity keeps on, like the geometry 1 in Fig. 5.19 and Fig. 5.25.

It is a clear difference on total dynamic saturation curves between the switch off velocity case and non switch off velocity case after switching off velocity (at $t_{\text{off}} = 14.3$ ms). The S_{total} keeps increasing for the non switch off velocity case, but decreasing for the non switch off velocity. Because in the switch off velocity case, some water inside of GDL is sucked up to the GDL surface and forms the bigger droplet (compare $t = 14.3$ ms and $t = 15.5$ ms in Fig. 5.26). It is consistent with the conclusions from the results in Fig. 5.26. This observation from the simulation is also consistent with the water flow in GDL mechanism proposed by Litster et al.[76]. The local saturation curve along through-plane direction varying with time are shown in Fig. 5.29.

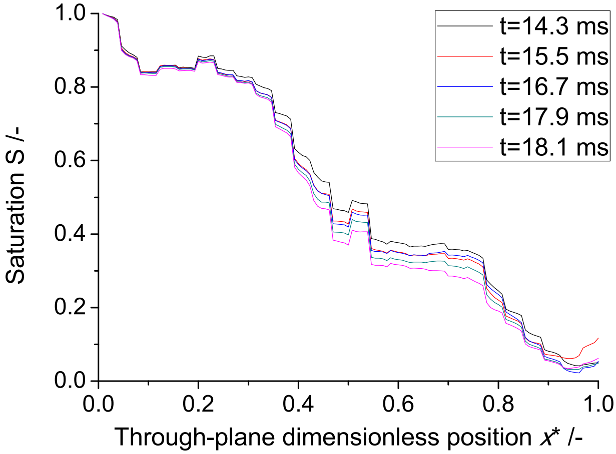

Figure 5.29.: Local saturation along the through-plane direction of switch-off velocity case at different evolution time t. (Geometry 1)

It is seen that the local saturation along the through-plane direction are fluctuated with time. It means the water inside of GDL are reorganized, particularly the region close to the outlet ($0.6 < x^* < 1$), the fluctuation of saturation is not liner (or irregular). The shape of water distribution inside of GDL is different from the situation before switching off velocity and some water in GDL are receding. The elevation plot of situation after the switch-off time ($t_{\text{off}} = 14.3$ ms) are presented on the Fig. 5.30.

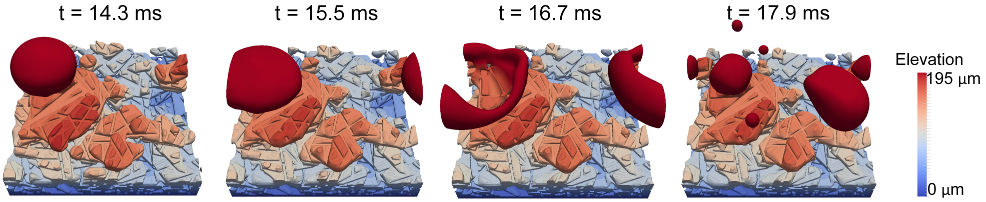

Figure 5.30.: Elevation plots of water distribution at different evolution time t after the switch-off time $t_{\text{off}} = 14.3$ ms. (Geometry 1)

It is observed from Fig. 5.30 that some water is sucked out of the GDL to form the bigger droplets on the GDL. But the main routes inside of GDL does not change very much with evolution time. The water distribution details inside of GDL can be checked on the cross plane I and II (see Fig. 5.2) at different evolution time are shown in Fig. 5.31.

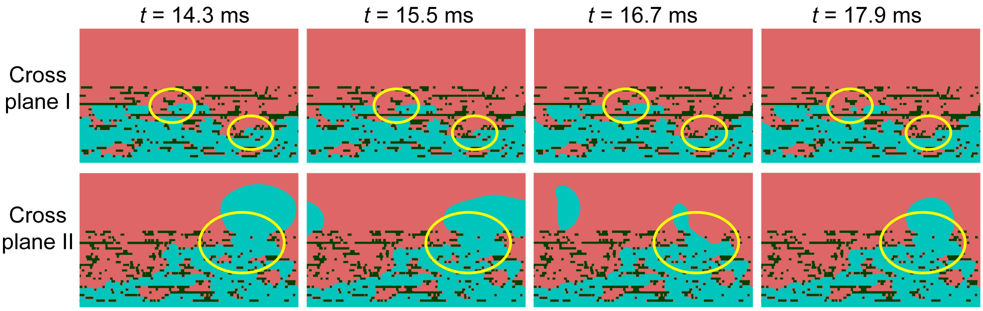

Figure 5.31.: Water distribution on cross plane I and II (see Fig. 5.2) after the switch-off time $t_{\text{off}} = 14.3$ ms at different evolution time t (3D results are in Fig. 5.26). (Geometry 1) (yellow frame region: the main changes area on the cross plane) red: air; green: GDL; blue: water.

This phenomenon were also observed in some experiments and the physical theory behind were analyzed with schematic figures by Litster et al. [76].

- **Conclusion**

  In a summary of geometry effects on liquid water transport through the GDL, the details are analyzed from different aspects and situations including the macro view of formed liquid droplets, the flow details, the droplets keep growing without removing and the situation after switching off input liquid velocity. The saturation curves are different with different GDL geometries. The saturation curves show an average relation to study the physical phenomenon. The 3D details are analyzed for formed droplets and water distribution inside of GDL. Once the liquid water breaks through the GDL, not specific amount of droplets are formed on random positions on the GDL surface. As time goes on, water flow through the GDL and saturation curves are presented dynamically. The water flow routes in GDL are possible to be coalesced each other. When water flowing breakthrough GDL, the saturation of water throat near the GDL interface does not change with evolution time and the suck-back effect are observed on the GDL surface. It is seen from the stream line figures that the droplets on GDL are formed with water from the 'tree' shape routes. The droplets are bigger and their shapes will be irregular as evolution time goes by, because the GC is not considered and the irregular GDL surfaces. In the switch-off velocity analysis, some liquid water are sucked out from GDL to formed the bigger droplets on the GDL surface after switching off the inlet water velocity. The formed bigger and irregular droplets are observed to be randomly distributed on the GDL surface because of the GDL surface roughness.

5.6. Wettability effect

There were some simulation work using different material wettability to study its effects on the flow behaviors in fuel cell components. For example, the contact angle on PTFE up to 140° was used on LBM water through GDL simulations by Mukherjee et al. [29] and Satjaritanun et al. [68]. From the material production side, the material hydrophobicity can be improved by some specific process and produce the super hydrophobic material, the contact angle on these super hydrophobic surface can be up to 170° [148]. So it is worthwhile to study the wettability effect on the water flowing through the GDL process.

In this section, the contact angle on the PTFE materials improves to the 140° ($\theta_{\text{PTFE}} = \theta_{\text{idl}} \approx 140^\circ$ with $G_{\text{adh},1} = -0.01$, see Fig. 4.36). Except the contact angle on the PTFE θ_{PTFE} changes to 140°, other simulation setup and conditions are the same as before and described in section 5.1. 10 GDL geometries which were also used to study geometry effect in section 5.5, are applied on this section. The dynamic saturation curves of 10 geometries with $\theta_{\text{PTFE}} = 140^\circ$ are shown in Fig. 5.32.

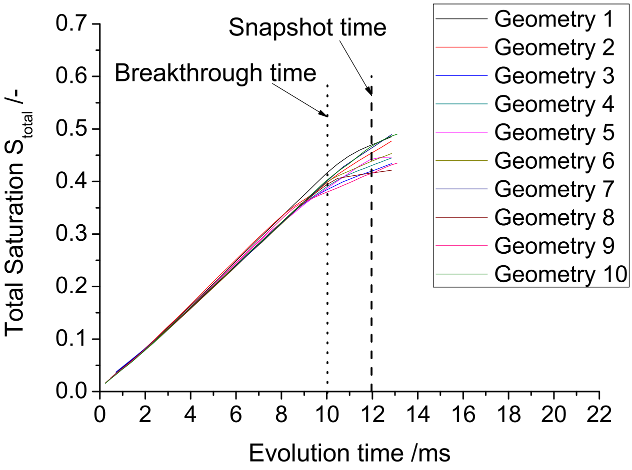

Figure 5.32.: Dynamic saturation curves of 10 different geometries. ($\theta_{\text{PTFE}} \approx 140^\circ$ with $G_{\text{adh},1} = -0.01$)

The definition of breakthrough time t_{break} and snapshot time t_{snap} in geometry effects are the same as that in section 5.5. It is seen from Fig. 5.32 that the breakthrough time is shorter with $\theta_{\text{PTFE}} \approx 140^\circ$ than that with $\theta_{\text{PTFE}} = 110^\circ$ (Fig. 5.18). The snapshot time $t_{\text{snap}} = 11.9$ ms is chosen to analyze the water flow in this dynamic process. The results of 10 geometries with $\theta_{\text{PTFE}} \approx 140^\circ$ at $t_{\text{snap}} = 11.9$ ms are shown in Fig. 5.33

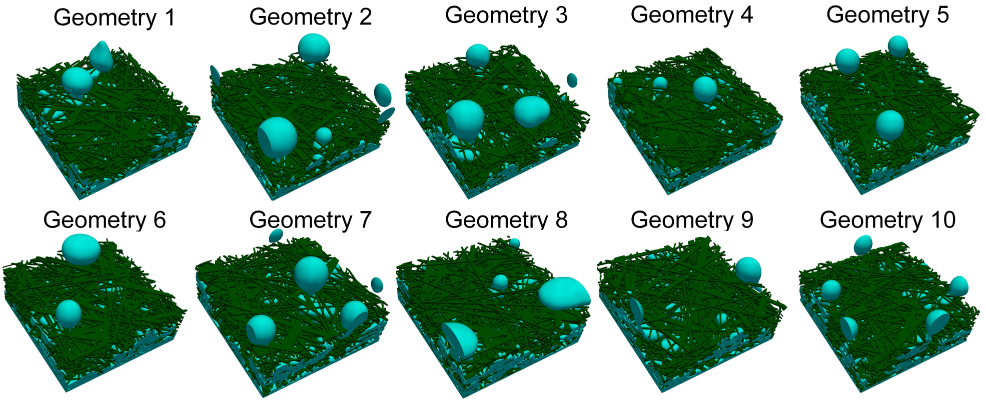

Figure 5.33.: Results of snapshot for 10 different geometries at $t_{\text{snap}} = 11.9$ ms. ($\theta_{\text{PTFE}} \approx 140^\circ$ with $G_{\text{adh},1} = -0.01$)

It is clear from Fig. 5.33 that material wettability have effects on the water flowing through GDL. More breakthrough points are observed on the geometries in comparison with the results in Fig. 5.19. On the snapshot time, some of the formed droplets shapes are irregular (geometry 1 and 8). Some new extra breakthrough points are observed while some same breakthrough points are also observed in the results of $\theta_{\text{PTFE}} = 110°$. The dynamic local saturation along the through-plane direction for geometry 5 is shown in Fig. 5.34.

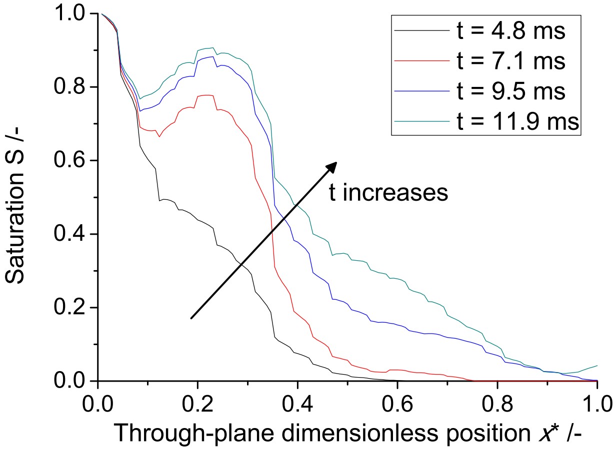

Figure 5.34.: Local saturation along the through-plane direction at different evolution time t ($\theta_{\text{PTFE}} \approx 140°$ with $G_{\text{adh},1} = -0.01$). (Geometry 5 in Fig. 5.33)

In comparison with the Fig. 5.20, it can be concluded the more hydrophobicity can shorten the breakthrough time. In the region close to the inlet $(0 < x^* < 0.1)$, the local saturation in different timesteps are quite similar and is less effected with evolution time. In the region close to the outlet $(0.9 < x^* < 1)$ at $t = 11.9$ ms, the saturation increases because of the droplets are formed on the GDL surface. After the water breaking through the GDL, the position with the lowest local saturation can be 'throat' position and close to the outlet, which is consistent with the observation in Fig. 5.21.

- **Conclusion**

  Some conclusions can be got concerning the wettability effects. With higher hydrophobicity, the water flow is affected and it is more easier to flow breaking through the GDL. The droplets are formed randomly on the GDL surface which are different from that with other hydrophobicity. More breakthrough points are generated with higher hydrophobicity. After flowing breaking through GDL, the total saturation inside of GDL is lower with higher hydrophobicity. It can be concluded the higher hydrophobicity can decrease the risk of flooding in the PEFC.

5.7. Summary

In this section, main conclusions from some fundamental effects analysis above are summarized.

(i) **Buffer space thickness effect.** The small buffer space thickness (such as 5 l.u.) has effect on the water flowing through the GDL and will cause the extra flow route. The buffer space with thickness 10 l.u. is decided to apply on all the afterward water flowing through the GDL simulations.

(ii) **Domain size effect.** The domain sizes have effect on the water flowing through the GDL. In order to observe some phenomenon (such as contact angle and breakthrough point) of two-phase flow in GDL, the domain size is suggested at least 0.45 mm × 0.45 mm (300 l.u. × 300 l.u.). It is decided the domain size with 0.6 mm × 0.6 mm (400 l.u. × 400 l.u.). are applied on all water flowing through the GDL simulations.

(iii) **Capillary number effect.** The capillary number has effect on the water flowing through the GDL. The capillary 'fingers' are more clear with the smaller capillary number. $Ca \approx 10^{-4}$ is decided to applied on the all water flowing through the GDL concerning the operated PEFC.

(iv) **Geometry effect.** The geometry structures have effect on the water flowing through the GDL. 22 different GDL structures, which are based on the stochastic algorithm and equivalent to the real GDL structures, are applied to the all water flowing through the GDL simulations. After water flowing breakthrough the GDL, asymmetric droplets are formed randomly on the GDL surface.

(v) **Wettability effect.** The different wettabilities ($\theta_{\mathrm{PTFE}} \approx 110^{\circ}$ and $\theta_{\mathrm{PTFE}} \approx 140^{\circ}$) have effect on the water flowing through the GDL. The water flowing breakthrough time is shorter with higher hydrophobicity.

6. Statistic analysis of liquid water through GDL

Concerning the application of the simulation results from chapter 5, the irregular droplets will be randomly formed on the GDL surface after water flowing breakthrough the GDL. Therefore, the main random results can be analyzed statistically, such as the apparent contact angle and breakthrough point distance. As one of main motivation summarized in chapter 1.1, some detailed information are expected from the simulation results to bridge the gap in the multi-scale simulations of PEFC . In the multi-scale simulations, the apparent contact angle and breakthrough point distance are output of LBM simulations in GDL, and they are two of main input parameters in the cell-scale simulations (such as volume of fluid (VOF) simulation) in GC. In this chapter, the apparent contact angle and droplets positions (breakthrough point distance are analyzed statistically to describe the droplets shape and positions for application (bridging the gap in multi-scale simulations of PEFC). The simulation setups and conditions are discribed in section 5.1 and the GDL are assumed fully covered with PTFE, the $\theta_{\text{PTFE}} \approx 110^{\circ}$.

6.1. Apparent contact angle

In most cases in Fig. 5.19, the sphere-shape droplets are formed on GDL surface. Therefore, a certain apparent contact based on a specific volume can be formed as well. According to the literature, it is very well known that the roughness or carbon fiber irregularity will cause the irregular droplet local apparent contact angles [173]. Meiron et al. compared different contact angle measurement method for droplets on the rough surface [174]. Moreover, as description in section 1.2.2, contact angle is one of main input parameters in the macro-scale VOF simulations for GC. The contact angle can be obtained from a micro-scale simulation (like LBM) and it will support the macro VOF simulations from the modeling side. In most of VOF in GC cases, the contact angle is usually assumed to be from the ideal droplet on homogeneous GDL surface [72], or based on the sessile droplet experiments [175], while the breakthrough area is set to the regular shape with specific sizes [40]. In the sessile drop experiment, a gravity negligible droplet is put on a sample surface and it is simplified to be a symmetric droplet[176]. The circle method (introduced in section 2.5) is applied to analyze the idealized contact angle (assume an ideal droplet on the ideal smooth solid surface without any other external force) based on the symmetry simplification which is not realistic [145]. The VOF simulations in GC have a certain inaccuracy from mainly two aspects. The one is that the formed droplets on GDL are asymmetric because of their irregular surface. Another one is the droplet contact area is affected by the irregular structures inside of the GDL (liquid droplets are not purely contact GDL surface). Therefore, the apparent contact angles are analyzed in details in this section. The contact angle can also be measured with the dynamic sessile drop method and it is similar to the static sessile drop but the drop to be modified. It determines the largest contact angle possible without increasing the contact area by adding volume dynamically [177]. The maximum angle is the advancing angle and when volume is removed to produce the smallest angle, the receding angle [178]. In this simulation, water droplets are growing and the droplet shape is more likely to be the advancing angle. Therefore, the apparent contact angle can also be understood as the advancing angle and possibly compared with that from the experiments. The apparent contact angle is the contact angle viewed from a certain direction which is vertical to the solid surface.

As the results of geometry effects in Fig. 5.19 of section 5.5, touching and non-touching droplets are observed in some geometries (e.g. touching boundary droplet in geometry 9 and non-touching boundary droplets in geometry 4 of Fig. 5.19). In this section, only the biggest non-touching droplet in every geometry are considered. Therefore, only the geometries 1 to 7 fulfilled this constraint and geometries 8 to 10 are not taken into account. According to the results in Fig. 4.34, the maximum error ϵ_{max} is smaller for the bigger droplet. So only the biggest droplet on every geometry are discussed. The example case of geometry 5 is shown in Fig. 6.1 a), the biggest droplet is extracted from the GDL surface and apparent contact angles are evaluated from view angles (VAs) (0°, 30°, 60° and 90°). The droplet shape of VA=0° on geometry 5 is shown in Fig. 6.1 b). The breakthrough area on the GDL top layer of the studied droplet is shown in Fig. 6.1 c).

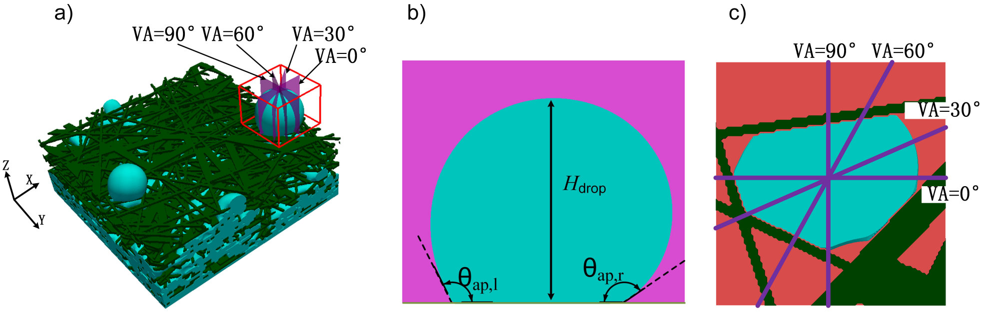

Figure 6.1.: a) Snapshot of result on geometry 5 (Non-touching boundary droplets) [149]; b) Apparent contact angles of subsection when VA=0° in Fig. 6.1 a). c) The breakthrough area on the GDL top layer of the extracted droplet from Fig. 6.1 a). Blue: water; green: carbon fiber; purple: subsection for VA; red: air.

There are two apparent contact angles (on the left hand side $\theta_{\text{ap,l}}$ and on the right hand side $\theta_{\text{ap,r}}$) on a VA in Fig. 6.1 b). The droplet height H_{drop} is shown in Fig. 6.1 b) and the breakthrough area A_{drop} are the water region in Fig. 6.1 c). $\theta_{\text{ap,l}}$ is not equal to $\theta_{\text{ap,r}}$ and it means this droplet is asymmetric when VA=0°. The apparent contact angles θ_{ap} of 7 geometries in different VAs are shown in Fig. 6.2.

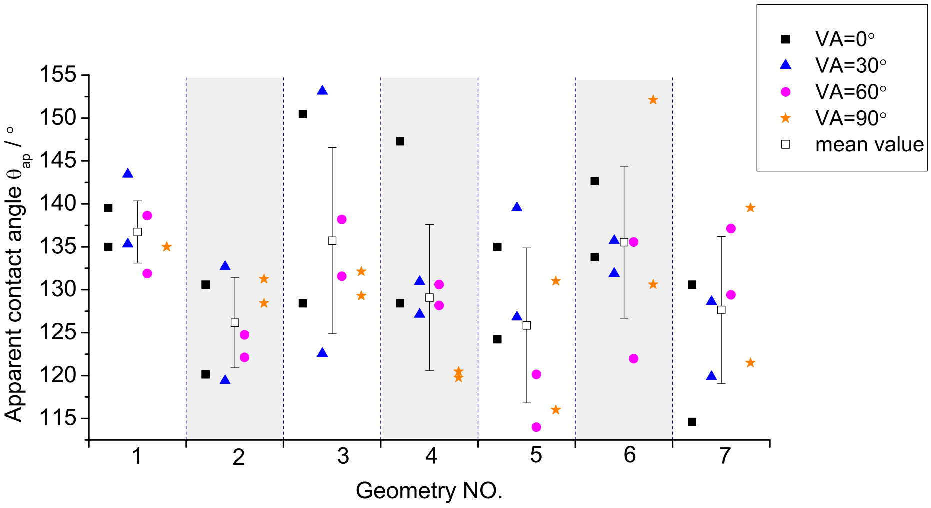

Figure 6.2.: Apparent contact angles θ_{ap} in four VAs of 7 geometries. [149]

It is observed that θ_{ap} are not equal in every geometry and different VAs. In very a few cases, droplet shapes are quite close to the symmetric, like geometry 1 with VA=90° and geometry 4 with VA=90° ($\theta_{\text{ap,l}}$ and $\theta_{\text{ap,r}}$ are overlaping each other and equals θ_{ap} in Fig. 6.2). All θ_{ap} are distributed within a certain range. Therefore, θ_{ap} are analyzed statistically and the variation coefficient c_v is studied in detail. c_v is a dimensionless variable and describes the amount of variability (standard deviation σ_{sd}) relative to the mean value $\bar{\theta}$. The c_v, σ_{sd} and $\bar{\theta}$ can be calculated by the formulas in Eq. (6.1).

$$c_v = \sigma_{sd}/\bar{\theta} \quad ; \quad \sigma_{sd} = \sqrt{\frac{1}{N_s}\sum_{j=1}^{N_s}(\theta_{\text{ap},j} - \bar{\theta})^2} \quad ; \quad \bar{\theta} = \frac{1}{N_s}\sum_{j=1}^{N_s}\theta_{\text{ap},j} \tag{6.1}$$

where $\theta_{\text{ap},j}$ is the apparent contact angle with the sample order j. N_s is the sample amount and equals 8 for every geometry and in total 56 for all 7 geometries. Then the $\bar{\theta}$, σ_{sd} and c_v concerning geometries (subscript with 'geo') and VAs (subscript with 'va') are shown in Table 6.1 and Table 6.2.

Table 6.1.: $\bar{\theta}_{\text{ap,geo}}$, $\sigma_{sd,\text{geo}}$ and $c_{v,\text{geo}}$ concerning geometries [149]

Geometry NO.	$\bar{\theta}_{\text{ap,geo}}$ /°	$\sigma_{sd,\text{geo}}$ /°	$c_{v,\text{geo}}$ /-
1	137	3.6	0.026
2	126	5.3	0.042
3	136	10.9	0.080
4	129	8.5	0.066
5	126	9.0	0.072
6	136	8.9	0.065
7	128	8.6	0.067
Average value	131.0	7.8	0.060

It is seen from Table 6.1 that the $c_{v,\text{geo}}$ are different in geometries. It shows the variation according to different positions on the GDL surface.

Table 6.2.: $\bar{\theta}_{\text{ap,va}}$, $\sigma_{sd,\text{va}}$ and $c_{v,\text{va}}$ concerning VA in all geometries [149]

VA /°	$\bar{\theta}_{\text{ap,va}}$ /°	$\sigma_{sd,\text{va}}$ /°	$c_{v,\text{va}}$ /-
0	133	10.0	0.075
30	132	9.3	0.070
60	129	7.5	0.058
90	130	9.2	0.071
Average value	131.0	9.0	0.069

It is seen from Table 6.2 that $c_{v,\text{va}}$ in different VAs are different. It shows the variation according to the surface roughness at one breakthrough location. In comparison with $c_{v,\text{geo}}$ and $c_{v,\text{va}}$, they fluctuated on different geometries and VAs. But the variance along the VA is in the same order of magnitude as the variance along the geometries. Both geometries and view angles affects the apparent contact angle. The average values of $c_{v,\text{geo}}$ (0.060) and $c_{v,\text{va}}$ (0.069) are in the same range and it means effects mentioned above dominated the apparent contact angles. In order to compare the results with the idealized contact angle θ_{idl} (with the simplified circle method), a dimensionless number η is introduced in Eq. (6.2).

$$\eta = \frac{V_{\text{drop,idl}}}{H_{\text{drop,idl}} A_{\text{drop,idl}}} \tag{6.2}$$

where $V_{\text{drop,idl}}$ and $H_{\text{drop,idl}}$ (see Fig. 6.1 b)) are the idealized volume and height of droplet separately, while $A_{\text{drop,idl}}$ is the idealized breakthrough area (see Fig. 6.1 c)) on the GDL surface). For the idealized droplet (symmetric) on the smooth surface, the droplet shape is an ideal sphere cap shape and the breakthrough region is an ideal circle. The volume $V_{\text{drop,idl}}$ and breakthrough area $A_{\text{drop,idl}}$ of idealized droplet can be calculated by Eq. (6.3).

$$V_{\text{drop,idl}} = \frac{\pi H_{\text{drop,idl}}}{6}\left[3\left(\frac{L_{\text{drop}}}{2}\right)^2 + H^2_{\text{drop,idl}}\right] \quad ; \quad A_{\text{drop,idl}} = \pi\left(\frac{L_{\text{drop}}}{2}\right)^2 \tag{6.3}$$

L_{drop} is the contact length the same as that in Eq. (2.32). Combined with Eq. (6.2), Eq. (6.3) and Eq. (2.32), the dimensionless η of the ideal spherical cap droplet is

$$\begin{aligned}\eta &= \frac{V_{\text{drop,idl}}}{H_{\text{drop,idl}} A_{\text{drop,idl}}}\\ &= \left[\frac{\pi H_{\text{drop,idl}}}{6}\left(3\left(\frac{L_{\text{drop}}}{2}\right)^2 + H^2_{\text{drop,idl}}\right)\right]\Bigg/\left[H_{\text{drop,idl}}\pi\left(\frac{L_{\text{drop}}}{2}\right)^2\right]\\ &= \frac{1}{2} + \frac{2H^2_{\text{drop,idl}}}{3L^2_{\text{drop}}} = \left[3 + \tan\left(\frac{\theta_{\text{idl}}}{2}\right)\right]\Bigg/6\end{aligned} \tag{6.4}$$

Then the relation between the idealized contact angle θ_{idl} and η can be derived from Eq. (6.5).

$$\theta_{\text{idl}} = 2\arctan(6\eta - 3) \tag{6.5}$$

Assume the droplet volume V_{drop} and height H_{drop} in simulation are the same as the idealized droplet volume $V_{\text{drop,idl}}$ and idealized droplet height $H_{\text{drop,idl}}$, the equivalent radius of half sphere

R_{eq} (the same as R_{init} on the contact angle test in section 4.4) follows $L_{\text{drop}}/2 = H_{\text{drop}} = R_{\text{eq}}$. The Eq. (6.3) can be reorganized to Eq. (6.6).

$$R_{\text{eq}} = \left(\frac{3V_{\text{drop,idl}}}{2\pi}\right)^{\frac{1}{3}} = \left(\frac{3V_{\text{drop}}}{2\pi}\right)^{\frac{1}{3}} \tag{6.6}$$

The height H_{drop}, breakthrough area A_{drop}, volume V_{drop} and R_{eq} (equivalent with that in CAT in section 4.4) of the biggest droplet on every geometry is summarized in Table 6.3. The idealized parameters $H_{\text{drop,idl}}$, breakthrough area $A_{\text{drop,idl}}$, volume $V_{\text{drop,idl}}$ are the same as the parameters H_{drop}, A_{drop} and V_{drop} from the simulation.

Table 6.3.: Height H_{drop}, breakthrough area A_{drop}, volume V_{drop}, and R_{eq} of the biggest droplet in seven geometries [149]

Geometry No.	H_{drop} $/10^{-3}$ mm	A_{drop} $/10^{-3}$ mm^2	V_{drop} $/10^{-3}$ mm^3	R_{eq} /l.u.
1	131	19.7	3.51	79
2	126	9.8	1.43	58
3	84	16.8	1.45	59
4	111	9.3	1.15	54
5	83	11.1	0.94	51
6	104	10.0	1.39	58
7	114	11.5	1.36	58
$\bar{\theta}_{ap,geo}$	108	12.6	1.60	-
$\sigma_{sd,geo}$	18.77	4.02	0.86	-
$c_{v,geo}$	0.17	0.319	0.54	-

It is seen that all R_{eq} in Table 6.3 are larger than the largest R_{eq} ($= R_{\text{init}}$=50 l.u. in Fig. 4.34), so these formed biggest droplet on every geometry is large enough to calculate contact angle accurately ($\epsilon \approx 0.5^\circ$ caused by discrete lattice). The $\sigma_{sd,\text{geo}}$ and $\sigma_{sd,\text{va}}$ (in Table 6.1 and Table 6.2) are larger than $\epsilon_{\text{max}} \approx 0.5^\circ$, it means geometries and regular structures dominate the droplet shape. The A are not uniform because of the stochastic GDL structure and different breakthrough time. Concerning the breakthrough area, it is in the range from 9.3×10^{-3} mm^2 to 19.7×10^{-3} mm^2. In the cell-scale VOF simulations of water in GC, the single breakthrough area is one of input parameters [40]. This work gives a breakthrough area in quantity ($(12.60 \pm 4.02) \times 10^{-3}$ mm^2). The H and V are not equal in all geometries due to the same reasons of non-uniform A. It is also found in Table 6.3 that the V cause the maximum $c_{v,\text{geo}}$ $(= 0.17)$, H causes the minimum $c_{v,\text{geo}}$ $(= 0.54)$ while A causes the intermediate $c_{v,\text{geo}}$ (0.319).

Extract some data from Table 6.3, η and θ_{idl} (calculated by Eq. (6.2) and Eq. (6.5)) are reorganized in Table 6.4. Summarize apparent contact angles concerning geometries $\bar{\theta}_{\text{ap,geo}}$, standard deviation $\sigma_{sd,\text{geo}}$, maximum and minimum apparent contact angle $\theta_{\text{ap,max}}$ and $\theta_{\text{ap,min}}$ of every geometry in Table 6.4.

Table 6.4.: η, θ_{idl}, $\bar{\theta}_{\text{ap,geo}}$ with $\sigma_{sd,\text{geo}}$, $\theta_{\text{ap,max}}$ and $\theta_{\text{ap,min}}$ of the geometries [149]

Geometry NO.	η	θ_{idl} /°	$\bar{\theta}_{\text{ap,geo}} \pm \sigma_{sd,\text{geo}}$ /°	$\theta_{\text{ap,max}}$ /°	$\theta_{\text{ap,min}}$ /°
1	1.3784	133	137±4	143	132
2	1.1702	127	126±5	133	119
3	1.0450	122	136±11	153	123
4	1.1328	126	129±8	147	120
5	1.0433	122	126±9	140	114
6	1.3608	133	136±9	152	122
7	1.0495	122	128±9	140	115
Average value	1.1686	126.9	131.0±7.8	144.0	120.6

$\bar{\theta}_{\text{ap,geo}}$ and $\sigma_{sd,\text{geo}}$ are extracted from Table 6.1 while $\theta_{\text{ap,max}}$ and $\theta_{\text{ap,min}}$ are taken from from Fig. 6.2. θ_{idl} and $\bar{\theta}_{\text{ap,geo}}$ are very close and in the same order of magnitude. It observes the relation $\bar{\theta}_{\text{ap,geo}} > \theta_{\text{idl}}$ (except geometry 2 and 3). Especially in geometry 3, the difference between $\bar{\theta}_{\text{ap,geo}}$ and θ_{idl} is bigger than the $\sigma_{sd,\text{geo}}$ while this situation is not observed in other geometries. It can be concluded that the idealized contact angle θ_{idl} can be used in the cell-scale VOF simulations (the most of previous literature did that). However, the apparent contact angle in this work can give more accurate detailed information to cell-scale VOF simulations including the standard deviation. The apparent contact angles are different and the formed droplets are irregular not only with geometries but also with VA, this conclusion can be got by comparing the $\theta_{\text{ap,max}}$, $\theta_{\text{ap,min}}$ with $\bar{\theta}_{\text{ap,geo}}$.

- **Conclusion**

  The slopes of dynamic saturation curves decrease when liquid water broke through the GDL. Irregular liquid water droplets are formed randomly on the GDL surface. The different droplet shapes are proved by the apparent contact angles from different view angles. Due to a series of VAs, there is a distribution of θ_{ap} for one droplet. The droplets have different shapes, they are effected by the irregular GDL structures. The optimum parameters are chosen for the SPPT method to analyze the local apparent contact angle. The θ_{ap} of the biggest droplet in every geometry were investigated statistically. The H_{drop}, A_{drop} and V_{drop} are not equal in terms of geometries. The idealized contact angle θ_{idl} are not fixed but is instead by a distribution in a certain range. The influence from geometries and view angles are in a similar range. The output of θ_{ap} can be the one of the input parameters in the macro-scale two-phase simulations in the GC for PEFC. In this sense, they can bridge the gap between the mesoscale and cell scale simulations of PEFC.

6.2. Breakthrough point distance

In this section, breakthrough point distances (BPD) are analyzed. According to the results in Fig. 5.19, sphere-shape droplets are formed through the breakthrough points (BPs) on the GDL surface. In the theory of multi-scales simulations, the results from micro-scale simulations can be the input of cell-scale simulations [179]. In the cell-scale VOF simulations, the same as the description of contact angle in section 6.1, BPD is one of main simulation setups [39]. In previous literature, the breakthrough point distance was a variable condition and have influence on the water flows on GDL-GC interface [70][71][21]. During the experiments, some certain breakthrough points were also observed. Djilali's group [75][76] did the dynamic experiment to observe water flowing through GDL process under different wettability and compression. Santamaria et al. [78] observed a series of BPs with a series of GDL thickness, water flux and input penetration area. Bazylak et al. [73] observed the dynamic BPs in an ex-situ experiment. Gao et al. [85] and Shahraeeni [83] observed BPs are distributed in different styles of GDL from in-situ experiments by image postprocessing.

In a summary, the water BPs on GDL were observed during in-situ or ex-situ experiments but rare literature study it from the simulation side. The results of LBM simulations in this work is possible to provide the details and support cell-scale VOF simulations. The simulation setups and initialization were described in section 5.1 to ensure $Ca \approx 10^{-4}$. This range of Ca is reasonable (can happen in the operating PEFC, as discussed in section 1.2.1) and it also used in some ex-situ water through GDL experiments setups to guide fuel cell development [53]. In order to ensure a large sample size, 22 realized fully covered PTFE Toray TGP090 GDLs are used to study the BPD. During this dynamic process, the breakthrough time and snapshot time are chosen the same as that in Fig. 5.18. The BP position is evaluated based on a snapshot in a highly dynamic process - as also observed by Bazylak et al. [180]. The results on 10 of 22 geometries were already shown in Fig. 5.19. The breakthrough area are checked in detail for boundary touching droplets, and only the bigger part of breakthrough area on the boundary are considered while the smaller part of droplets which appear on the opposite boundary (due to periodic condition) are not taken into account. Moreover, the BPD is only calculated within the simulation domain, neglecting the distances to mirrored BPs caused by a checker board setup due to the periodic boundary condition.

One of geometries (geometry 15) is chosen to present the details of BPD in Fig. 6.3 a). And the situation on the GC-GDL interface is shown in Fig. 6.3 b) with three BPs (red) and three BPDs (yellow, marked with I to III).

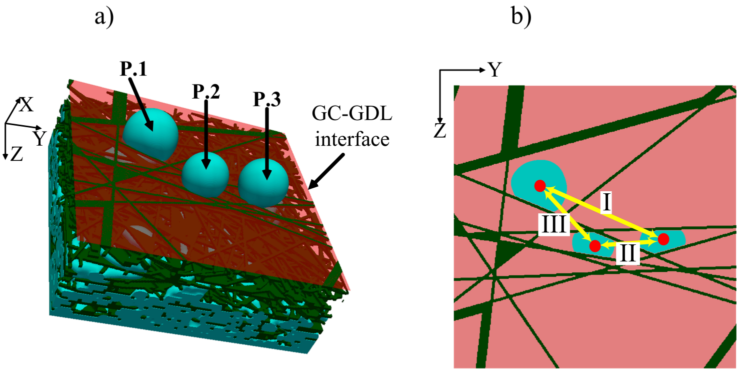

Figure 6.3.: a) Snapshot of result in geometry 15. b)Breakthrough points (P.1, P.2 and P.3 in Fig. 6.3 a)) and BPDs (labeled with I, II and III) on GC-GDL interface (Pink: air; Blue: water; Red: breakthrough points; Yellow: BPD). [181]

BP is on the geometry center (x_{BP}, y_{BP} and z_{BP}) of water region on GC-GDL interface and can be calculated by Eq. (6.7).

$$x_{\mathsf{BP}} = \frac{\sum_{j=1}^{N_p} x_j}{N_p} \quad ; \quad y_{\mathsf{BP}} = \frac{\sum_{j=1}^{N_p} y_j}{N_p} \quad ; \quad z_{\mathsf{BP}} = \frac{\sum_{j=1}^{N_p} z_j}{N_p} \tag{6.7}$$

where N_p is the pixel amount on the breakthrough area, while (x_j, y_j and y_j) is the position of jth grid in the breakthrough area. Two kinds of BPD are studied in this section:

(i) Specific BPD (S-BPD).

It is defined as normal BPD between two breakthrough points without any constraint in a specific domain (e.g. three S-BPD are the BPDs shown in Fig. 6.3 b)). It is affected by the domain size and it will be larger with the bigger domain (more BPs will be formed on a bigger area).

(ii) Shortest neighbor BPD (SN-BPD).

It is a shortest constraint BPD between every neighbor BP. For every droplet, the distance to the nearest neighbor is taken. The SN-BPD can be filtered from data of S-BPD and it is assumed independent of the domain size (e.g. BPD II and III are the two SN-BPDs for three BPs).

BPs are irregularly produced on geometries from Fig. 5.19, so the BPD length L_k and the variation coefficient c_v are analyzed statistically [182]. The subscript k can be replaced by the abbreviate of two kinds BPD ('sbp' for S-BPD and 'snbp' for SN-BPD). $c_{v,k}$ is a dimensionless variable which describes the relative variance to the mean value and can be calculated by the Eq. (6.1), but $\bar{\theta}$ is replaced by $\bar{L}_k$, $\theta_{\text{ap},i}$ and $\bar{\theta}$ are replaced by $L_{k,i}$ and $\bar{L}_k$ (standard deviation $\sigma_{sd,k}$ and mean value $\bar{L}_k$ are summarized in Eq. (6.8)).

$$\sigma_{sd,k} = \sqrt{\frac{1}{Q_k}\sum_{j=1}^{Q_k}(L_{k,j} - \bar{L}_k)^2} \qquad ; \qquad \bar{L}_k = \frac{1}{Q_k}\sum_{j=1}^{Q_k} L_{k,j} \tag{6.8}$$

where Q_k is the amount of sample data. For S-BPD, Q_k follows the combinations and can be calculated by Eq. (6.9)

$$Q_{\text{sbp}} = C(N_{s,\text{geo}}, 2) = \frac{N_{s,\text{geo}}(N_{s,\text{geo}} - 1)}{2} \tag{6.9}$$

where $N_{s,\text{geo}}$ is the number of BP in one geometry and $C(N_{s,\text{geo}}, 2)$ is the number of 2 combinations (because of distance between two BPs) of an $N_{s,\text{geo}}$-set. For the geometries which have only one breakthrough point, there will be no BPD ($Q_{\text{sbp}} = 0$, see Eq. (6.9)). There are 5 of 22 geometries which have only one breakthrough point, therefore the following results are only presented in 17 geometries. The geometry sequence are ordered continuously from 1 to 18 without the touching-boundary geometries. The result of S-BPD and SN-BPD in every geometry are shown in Fig. 6.4 a) and Fig. 6.4 b). the $\bar{L}_k$ and $\sigma_{sd,k}$ are calculated by Eq. (6.8).

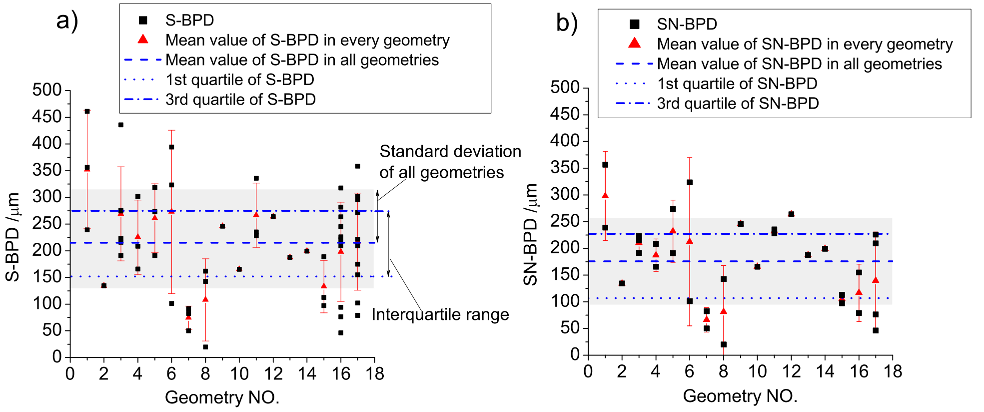

Figure 6.4.: a) The result of S-BPD in geometries. b) The result of SN-BPD in geometries. [181]

It is seen from Fig.6.4 a) and b) that both S-BPD and SN-BPD are randomly arranged. The sample size of SN-BPD is smaller than that of S-BPD because SN-BPD is extracted from S-BPD. Their mean values ($\bar{L}_{\text{sbp}} = 215.1$ µm and $\bar{L}_{\text{snbp}} = 175.6$ µm) are in the same range but with approximate 20% difference. If compare their standard deviation ($\sigma_{sd,\text{sbp}} = 98.6$ µm and $\sigma_{sd,\text{sbp}} = 81.8$ µm), they are also different but in the similar range. But if compare the standard deviation on every geometry with all geometries, they are in the same order of magnitude for most cases except some cases with only one BPD or BPs are very close on the geometry (geometry 7). The 4-quartile are analyzed for all data, the 1st quartile and 3rd quartile are shown as well in Fig. 6.4 a) and Fig. 6.4 b). The 1st quartile and 3rd quartile means 25% and 75% of total amount of samples are less than less than 1st quartile and 3rd quartile separately. The range between 1st and 3rd quartile is called the interquartile range. These statistical properties are summarized in Table 6.5

Table 6.5.: 1st, 3rd quartile and interquartile range of S-BPD and SN-BPD

	1st quartile /µm	3rd quartile /µm	Interquartile range /µm
S-BPD	151.8	274.8	123.0
SN-BPD	106.9	226.9	120.0

It can be seen from Table 6.5 that their 1st quartile and 3rd quartile are different, but the interquartile range are quite similar. It shows that the extreme values for the S-BPD distribution were cut off to get the SN-BPD. The Q_{sbp} and Q_{snbp} of every geometry are shown in Fig. 6.5 a) and the total values are summarized in Table 6.6.

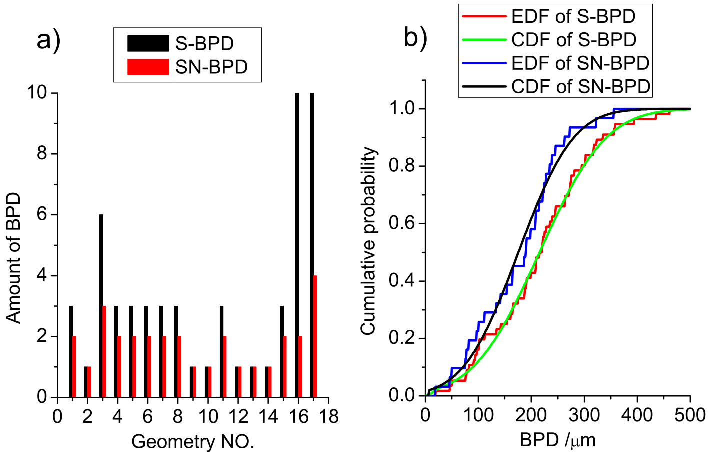

Figure 6.5.: a) Amount of S-BPD (Q_{sbp}) and SN-BPD (Q_{snbp}) in geometries. b) Cumulative probability plot of S-BPD and SN-BPD [181].

It is clear that $Q_{\text{sbp}} \geqslant Q_{\text{snbp}}$ in every geometry. For the geometry with only one S-BPD, they have the relation $Q_{\text{sbp}} \equiv Q_{\text{snbp}}$, $L_{\text{sbp}} \equiv L_{\text{snbp}}$ and $\sigma_{sd,\text{sbp}} \equiv \sigma_{sd,\text{snbp}} \equiv 0$. For the geometries with three S-BPD, they have the general relation $Q_{sd,\text{snbp}} = Q_{sd,\text{sbp}} - 1 = 2$, and it means three BPs are not distributed with a equilateral triangle style ($Q_{sd,\text{snbp}} \equiv 1$) on the GC-GDL interface. For the geometries with more than three S-BPD, the difference between $Q_{sd,\text{sbp}}$ and $Q_{sd,\text{snbp}}$ are not fixed and follow the quite general rule $Q_{sd,\text{snbp}} < Q_{sd,\text{sbp}}$. It tells us that four or five BPs on every geometry are distributed even more complex and irregular than that with three BPs. (see geometries 3, 16 and 17 in Fig. 6.5 a)). It is also seen three geometries with many BPs (geometries 3, 16 and 17) and they have a large impact on the S-BPD than the other geometries. For even large domain size ($\gg 0.6$ mm $\times$ 0.6 mm), the BPs will increase and it will affect the S-BPD but not the SN-BPD.

It can be concluded from Fig. 6.4 a) and Fig. 6.4 b) that S-BPD and SN-BPD are distributed irregularly. Therefore, the Lilliefors test is done to evaluate statistically whether S-BPD and SN-BPD follow a normal distribution or not [183]. It tests the normal distribution that data come from a normal distributed population which the expected value and distribution variance are not specified [184]. The Lilliefors tests are all proceeded by the function '[B_k,φ_k,D_k=lillietest]' in MATLAB2009 [185]. The returned B_k is a binary parameter presenting the test conclusion. $B_k = 0$ indicates that the null hypothesis cannot be rejected at the 5% and $B_k = 1$ means that the null hypothesis can be rejected at the 5% [186]. The φ_k is returned the value in the range (0 1) and presents the probability of observing a test statistic as extreme as (or even more extreme than) the observed value under the null hypothesis [185]. D_k is the maximum discrepancy between the empirical distribution function (EDF) and cumulative distribution function (CDF), which can be defined by the formula in Eq. (6.10)

$$D_k = \max_{1 \leqslant i \leqslant Q_k} |\text{CDF}(i) - \text{EDF}(i)| \tag{6.10}$$

where i is the sample order number. The EDF and CDF of the S-BPD and SN-BPD are shown on the cumulative probability plot in Fig. 6.5 b). It can be seen that both EDF and CDF are fitted very well for both S-BPD and SN-BPD. The results of the Lilliefors test are Summarized in Table 6.6 and it is possible to analyzing whether the D_k is large enough to be statistically significant (5%) and requiring rejection of the normal distribution.

Table 6.6.: Results of the Lilliefors test for S-BPD and SN-BPD [181]

	k	Q_k	$\bar{L}_k$ /µm	$\sigma_{sd,k}$ /µm	$c_{v,k}$	B_k	φ_k	D_k
S-BPD	'sbp'	56	215.1	98.6	0.46	0	0.68	0.07
SN-BPD	'snbp'	36	175.6	81.8	0.47	0	0.49	0.11

S-BPD and SN-BPD have different Q_k. It should be care that in the application on the larger domain or even cell-scale VOF simulations in GC, bigger Q_{sbp} have to be considered because Q_{sbp} will increase with a big order of magnitude ($O(Q^2_{k,\mathsf{geo}})$), see Eq. (6.9). Q_{snbp} may also raise in a bigger domain but the statistic characteristics of SN-BPD is independent of domain size, and SN-BPD can be one of input cell-scale modeling setups. It is also seen from Table 6.6 that S-BPD and SN-BPD have the quite similar relative variability $c_{v,k}$. $\bar{L}_k$ and $\sigma_{sd,k}$ of them have the same order of magnitude but different values (because of different sample sizes and SN-BPD are filtered from S-BPD). Both S-BPD and SN-BPD can be characterized by a normal distribution ($B_k = 0$). S-BPD has the bigger φ_k and smaller D_k than that of SN-BPD because S-BPD has a bigger sample size. But both can be compared with the similar problem with the same sample size from experiments.

- **Conclusions**

  In order to observe the formed droplets or breakthrough points on the geometries used in breakthrough point distance analysis, the domain size is suggested to be at least equal or bigger than the mean SN-BPD with deviation (175.6±81.8 µm). This conclusion explained the reason no droplets or breakthrough points formed in the smaller cut-off domain sizes (see Fig. 5.10 200 l.u.×200 l.u. (300 µm×300 µm) and 100 l.u.×100 l.u. (150 µm×150 µm)) in section 5.3. SN-BPD was identified to be independent for the domain size. The quantities of S-BPD and SN-BPD are different in geometries. The S-BPD which is based on the certain domain size, are randomly distributed on geometries. The SN-BPD usually has less quantity than S-BPD. In comparison with the cumulative probability plot of S-BPD and SN-BPD, their shapes are different but their EDF are fitted with CDF separately. The both distributions of S-BPD and SN-BPD can be described by the normal distribution according to the Lilliefors test. They can be characterized with different mean value and the standard deviations, but they are in the similar order of magnitude. The SN-BPD can provide more useful information on quantity and quality for input simulation setups of cell-scale simulations in GC. From the application and characterization of water flowing through the GDL side, the SN-BPD is preferred because of its independence from the domain size. Simulation on stochastic geometries create results which have statistical variations because of the variation in the geometry data.

7.PTFE effects on water through GDL

In this chapter the PTFE effects on liquid water breaking through GDL are studied. As introduced in section 1, the GDL is usually processed by coating hydrophobic material PTFE on it to improve the hydrophobicity of GDL. The PTFE is assumed to cover with fixed thickness on the carbon fiber surface. In the present geometry model, the cover fraction (c.f.) of PTFE (β_{cover}) can be specified, then the PTFE is randomly cover to the certain region until it reaches the defined cover fraction (explained in section 3.2). It is the definition of how much area of carbon fibers are covered with PTFE. Usually the weight fraction (w.f) is given in literature as well as by the manufactures [5].

7.1. Simulation setups and conditions

In this section, the ShanChen MRT-EDM model is applied on all simulations of water flowing through GDL with different PTFE distributions. One of geometries (geometry 5) is applied on simulations. The simulation setups and boundary conditions are the same as that of dynamic simulation of liquid water through GDL in section 5.1. The graphic representation of simulation setups are shown in Fig. 5.1. The fixed velocity is defined on the inlet to ensure the $Ca\approx 10^{-4}$. The open condition is applied on the outlet of domain. Besides inlet and outlet boundaries, periodic condition are applied on the other boundaries. The GDL properties (domain area is 0.6 mm$\times$ 0.6 mm, GDL thickness is 0.195 mm and porosity is 0.8) are the same as that used in the section 5 of dynamic simulation of liquid water through GDL. On the GDL structure, PTFE are distributed with different styles including :

(i) In-plane PTFE distribution. PTFE are distributed in-plane direction. In the half of GDL in-plane direction is fully covered with PTFE and another half is fully non-PTFE region. Four styles with c.f.50% (called S.1 to S.4) in-plane PTFE distribution are discussed.

(ii) Whole-GDL PTFE distribution. Different content of PTFE are distributed in whole GDL. Five cases are discussed concerning whole GDL including: whole-GDL c.f.0%, whole-GDL c.f.33%, whole-GDL c.f.50%, whole-GDL c.f.66% and whole-GDL c.f.100%.

(iii) Two-sections-through-plane PTFE distribution. The whole GDL is divided into two sections along the through-plane direction. PTFE is fully covered on one of sections.

(iv) Sandwich-through-plane PTFE distribution. The whole GDL is divided into three sections along the through-plane direction to create a 'sandwich' style. The PTFE are distributed on the two outer sections or the inner section.

(v) Quasi-linear-through-plane PTFE distribution. The whole GDL is divided into ten sections to simplify the linear-through-plane PTFE distribution. PTFE on ten sections are distributed with four different gradient (grad.-5%, grad.-2%, grad.2% and grad.5%).

The discussed PTFE distribution cases in this chapter are summarized in the Table. 7.1

Table 7.1.: Summary of discussed PTFE distributions in chapter 7 (Geometry 5)

Sections	Title	PTFE distributions	Short description
7.2	In-plane PTFE distribution	S.1 S.2 S.3 S.4	Half of GDL along in-plane direction are fully covered with PTFE, only total PTFE c.f.50% are discussed. See Fig. 7.2
7.3	Whole-GDL PTFE distribution	whole-GDL c.f.0% whole-GDL c.f.33% whole-GDL c.f.50% whole-GDL c.f.66% whole-GDL c.f.100%	Whole GDL is distributed with different content of PTFE including c.f.0%, c.f.33%, c.f.50%, c.f.66% and c.f.100%. See description in section 7.3
7.4	Two-sections-through-plane PTFE distribution	Inlet-half c.f.50% Outlet-half c.f.50%	Half of GDL along through-plane direction are fully covered with PTFE, only total PTFE c.f.50% are discussed. See Fig. 7.11
7.5	Sandwich-through-plane PTFE distribution	Inner c.f.33% Inner c.f.50% Inner c.f.66% Outer c.f.33% Outer c.f.50% Outer c.f.66%	PTFE distribution with sandwich way including outer (fully PTFE in two outer sections) and inner styles (fully PTFE in one inner section). Total PTFE c.f.33%, 50% and 66% are discussed. See Fig. 7.17
7.6	Quasi-linear-through-plane PTFE distribution	Q-lin Grad.-5% c.f.66% Q-lin Grad.-2% c.f.66% Q-lin Grad.2% c.f.66% Q-lin Grad.5% c.f.66%	Four quasi-linear PTFE distribution on ten section through-plane direction. Four PTFE gradient (grad.-5%, -2%, 2% and 5%) with a fixed total PTFE c.f.66% are discussed. See Fig. 7.26 a) †

The macro average flow behavior and the water distribution are studied in details. It is useful as the standard unit to characterize GDL with certain PTFE, such as weight fraction and cover fraction [93]. In this work, PTFE with a specific cubic volume (30 µm×30µm×30µm) is distributed randomly on the carbon fiber surfaces until it reaches the defined cover fraction.

An algorithm is introduced to convert between weight fraction and cover fraction. The schematic graph of how PTFE is coated on the endless single carbon fiber which is asymptotically equivalent to the fibers of the GDL (all of them are connected each other), is shown in Fig. 7.1 b)

---

† The quasi-linear function of PTFE distribution along the through-plane direction is shown in Fig. 7.26 a)

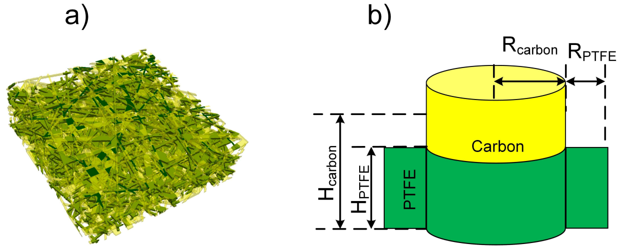

Figure 7.1.: a) 3D realization GDL with 50% PTFE cover fraction. b) Schematic graph of PTFE covered on the single carbon fiber. Green: PTFE; yellow: carbon fiber

It is assumed all carbon fibers in GDL can be mapped to one straight single cylinder carbon fiber and the PTFE is covered on its surface with the uniform thickness. In the present geometry model, the PTFE content does not change the porosity (because the average PTFE thickness (<1 µm) is smaller than the geometry resolution (1.5 µm)) and it is allowed to do this simplification according to experiments observation by Santamaria et al. [78] (the porosity keeps almost constant at around 0.65 when PTFE content increases from w.f.20% to w.f.40%). As shown in Fig. 7.1, single carbon fiber has the radius R_{carbon} and PTFE is covered with thickness R_{PTFE}. According to this simplification, the cover fraction β_{cover} can be calculated by the ratio between PTFE height H_{PTFE} and carbon fiber height H_{carbon} as shown in Eq. (7.1).

$$\beta_{\text{cover}} = \frac{H_{\text{PTFE}}}{H_{\text{carbon}}} \tag{7.1}$$

The weight fraction ζ_{weight} is related with PTFE mass m_{PTFE} and GDL mass m_{GDL} presented as Eq. (7.2).

$$\beta_{\text{weight}} = \frac{m_{\text{PTFE}}}{m_{\text{GDL}}} = \frac{\rho_{\text{PTFE}} V_{\text{PTFE}}}{\rho_{\text{GDL}} V_{\text{GDL}}} \tag{7.2}$$

The PTFE density $\rho_{\text{PTFE}} = 2.2$ g · cm^{-3} and GDL density $\rho_{\text{GDL}} = 0.44$ g · cm^{-3} from the GDL manufactures and literature [187][94]. The ρ_{GDL} is used instead of pure carbon density because usually how much of pure carbon included in GDL is very hard to know, and the carbon content can be estimated by porosity from the GDL [187]. The porosity ζ is usually known and can be computed from the empty pore volume V_{pore} and total GDL volume V_{GDL} according to Eq. (7.3).

$$\zeta = \frac{V_{\text{pore}}}{V_{\text{GDL}}} = \frac{V_{\text{GDL}} - V_{\text{PTFE}} - V_{\text{carbon}}}{V_{\text{GDL}}} \tag{7.3}$$

In combination with Eq. (7.2) and Eq. (7.3), we got the Eq. (7.4).

$$\beta_{\text{weight}} = \frac{m_{\text{PTFE}}}{m_{\text{GDL}}} = \frac{\rho_{\text{PTFE}} V_{\text{PTFE}}}{\rho_{\text{GDL}} \frac{V_{\text{PTFE}} + V_{\text{carbon}}}{1-\zeta}} \tag{7.4}$$

Then the volume of single carbon fiber cylinder V_{carbon} and PTFE annulus V_{PTFE} can be calculated by Eq. (7.5).

$$V_{\text{carbon}} = \pi R_{\text{carbon}}^2 H_{\text{carbon}} \quad ; \quad V_{\text{PTFE}} = \left(\pi (R_{\text{carbon}} + R_{\text{PTFE}})^2 - \pi R_{\text{carbon}}^2\right) H_{\text{PTFE}} \tag{7.5}$$

Subtitute Eq. (7.5) to Eq. (7.4), it is possible to get the relation between β_{weight}, R_{carbon} and

R_{PTFE} as Eq. (7.6).

$$\beta_{\text{weight}} = \frac{\rho_{\text{PTFE}}}{\rho_{\text{GDL}}} \frac{(1-\zeta)(2R_{\text{carbon}}R_{\text{PTFE}} + R_{\text{PTFE}}^2)H_{\text{PTFE}}}{(2R_{\text{carbon}}R_{\text{PTFE}} + R_{\text{PTFE}}^2)H_{\text{PTFE}} + R_{\text{carbon}}^2 H_{\text{carbon}}} \tag{7.6}$$

The ratio $\Gamma = R_{\text{carbon}}/R_{\text{PTFE}}$ is defined, its substitution in Eq. (7.6) and leads to the Eq. (7.7).

$$\beta_{\text{weight}} = \frac{\rho_{\text{PTFE}}}{\rho_{\text{GDL}}} \frac{(1-\zeta)(2\Gamma+1)H_{\text{PTFE}}}{(2\Gamma+1)H_{\text{PTFE}} + \Gamma^2 H_{\text{carbon}}} \tag{7.7}$$

Combine the Eq. (7.7) with Eq. (7.1), the relation between β_{weight} and β_{cover} is shown in Eq. (7.8).

$$\beta_{\text{weight}} = \frac{\rho_{\text{PTFE}}}{\rho_{\text{GDL}}} \frac{(1-\zeta)(2\Gamma+1)\beta_{\text{cover}}}{(2\Gamma+1)\beta_{\text{cover}} + \Gamma^2} \tag{7.8}$$

The β_{weight} and β_{cover} can be freely converted to each other according to Eq. (7.8) when other variables are known. In the literature, the PTFE are inhomogeneously distributed on the carbon fiber surface. Its average thickness is less than 1 μm [188] and it was set $R_{\text{PTFE}} = 0.6$ μm in one of previous LBM simulation done by Chen et al. [153]. The $R_{\text{carbon}} \approx 3.5$ μm of Toray TGP090 GDL [189]. Therefore, the ratio $\Gamma = R_{\text{carbon}}/R_{\text{PTFE}} \approx 5.8$ is defined. The porosity $\zeta \approx 0.8$ is given in this work [32][190]. For example, when $\beta_{\text{cover}} = 50\%$ then $\beta_{\text{weight}} \approx 16\%$ according to Eq. (7.8). For the GDL manufacturers, the up-limit of weight fraction of PTFE is not beyond 35% to compromise the industry (coating process) difficulties and porosity (the bigger weight fraction will highly decrease GDL porosity) [78][91].

In the following parts under this section, five cover fractions of PTFE are mentioned and their corresponding weight fractions are summarized in Table 7.2 according to Eq. (7.8).

Table 7.2.: Summary of cover fraction and weight fraction conversion. ($\zeta \approx 0.8$ and $\Gamma \approx 5.8$)

Cover fraction (c.f.) β_{cover} /%	Weight fraction (w.f.) β_{weight} /%
0	0
33	11
50	16
66	20
100	27

7.2. In-plane PTFE distribution

In this section, the water flow behaviors are studied with different In-plane PTFE distributions with total c.f.50%. The PTFE is fully distributed (c.f.100%) on the half of GDL along the in-plane direction, while another half is no-PTFE region (c.f.0%). The schematic graph of the PTFE distribution on the four different in-plane PTFE distributions (two styles S.1 and S.2 are related with the Z coordinate and another two styles S.3 and S.4 are for Y coordinate) are shown in Fig. 7.2. Then the total PTFE c.f. is 50%. The PTFE transition interface is located on the layer between PTFE and no-PTFE region, which is parallel to the $\mathrm{X}-\mathrm{Y}$ or $\mathrm{X}-\mathrm{Z}$ surfaces. In theory, water flows preferably in the hydrophilic region because of less 'resistance' on the water.

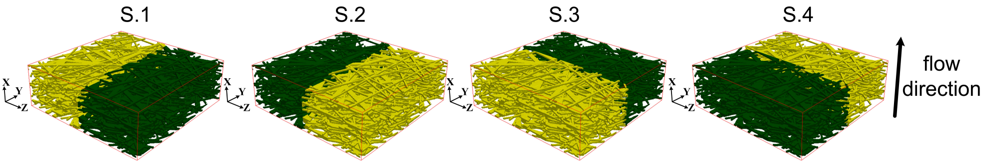

Figure 7.2.: GDL with in-plane c.f.50% PTFE. (Geometry 5) Green: PTFE region; yellow: no-PTFE. (S.1 and S.2: PTFE is covered in-plane along $\mathbb{Z}$ direction; S.3 and S.4: PTFE is covered in-plane along $\mathbb{Y}$ direction.

The dynamic saturation curves of four in-plane PTFE distributions are shown in Fig. 7.3 a) and the zoom of region near the snapshot time are shown in Fig. 7.3 b).

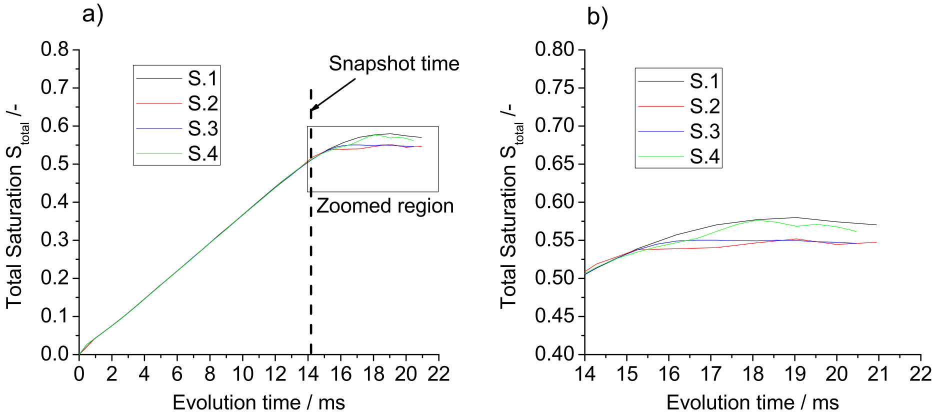

Figure 7.3.: a) Dynamic saturation curves of different in-plane PTFE distributions (c.f.50%). S.1 to S.4 are in-plane PTFE distributions in Fig. 7.2. b) Zoom of frame region in Fig. 7.3 a). (Geometry 5)

It is seen that S_{total} keeps growing with the same speed (slope of the dynamic total saturation curves). The breakthrough times of S.1 to S.4 are evaluated in Fig. 7.3 b), when the slope of total saturation curves decreases and their breakthrough time are quite similar and between 14 ms and 15 ms. The S_{total} after water breaking through the GDL are slightly different ($\Delta S_{\text{total}} \approx 0.1$) because of irregular structures in GDL. The snapshot time $t_{\text{snap}} = 14.4$ ms is chosen to check the water flow details. The results of PTFE c.f.50% along in-plane direction are shown in Fig. 7.4 with a reference cross section which is vertical to the PTFE and non-PTFE interface and passes through the axis of the square GDL geometry. The reference cross section is to check the water distribution details within PTFE and no-PTFE regions.

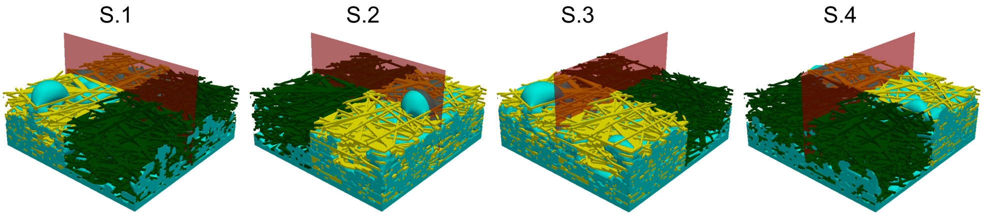

Figure 7.4.: Results of snapshot for four in-plane PTFE distributions (c.f.50%) at $t_{\text{snap}} = 14.4$ ms. (Geometry 5) Green: PTFE; yellow: no-PTFE; blue: water; red: reference cross section (vertical to transition layer between PTFE and no-PTFE region).

From the Fig. 7.4, water flowing breakthrough the GDL are observed on the no-PTFE regions. But the breakthrough point positions are not fixed (in cases S.2 and S.4, they are close to the transition interface between PTFE and no-PTFE regions while S.1 and S.3 are not). The elevation plot of water distribution on the four in-plane PTFE c.f.50% at $t_{\text{snap}} = 14.4$ ms are shown in Fig. 7.5 to check the water flow inside of GDL.

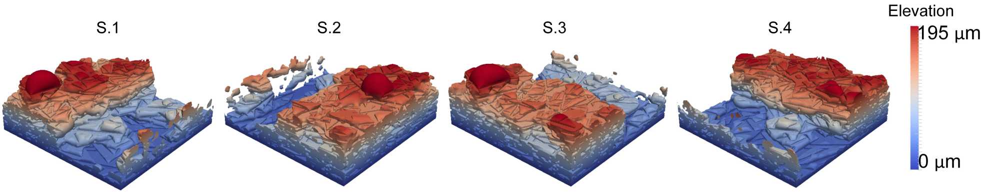

Figure 7.5.: Elevation plot of water distribution on the with four in-plane PTFE distributions (c.f.50%) at $t_{\text{snap}} = 14.4$ ms. (Geometry 5) (S.1 to S.4 are the in-plane PTFE distributions the same as shown in Fig. 7.2)

It is seen that the no-PTFE regions are almost fully flooded (the elevation of water in the no-PTFE region is larger than that in PTFE region). The boundary between PTFE and no-PTFE can be seen from the water elevation plot. But the water flows from PTFE to no-PTFE region are irregular and does not strictly follow the PTFE transition layer position. This irregular water flows on the PTFE transition layer because of the different wettability in the different pores formed by the irregular GDL structures. It can be explained with the critical pressure P_c of pores formed in GDL and it can be defined with formula in Eq. (7.9) [191].

$$P_c = \frac{2\sigma_s \cos\theta}{R_p} \tag{7.9}$$

with σ_s is the surface tension, θ is the contact angle and R_p is the radius of pore. P_c can be positive (hydrophilic and $\cos\theta > 0$), negative (hydrophobic and $\cos\theta < 0$) or zero ($\cos\theta = 0$). P_c is a vector which presents how much pressure is needed to flow through the pore. The imbibition can happen spontaneously when P_c is positive. The drag resistance drives on the fluid flow when P_c is negative. It is seen that the P_c depends on the local wettability (contact angle θ) and pore structures (radius R_p). In hydrophobic situation and $\cos\theta < 0$, it means the surface tension force is driven opposite of the flow direction and it increase the flow resistance. As description in section 3.2 and 7.1, the PTFE does not change the pore size distributions of GDL geometries but only the local wettability are different. Therefore, R_p does not change from the macro-view (average) of the whole GDL, and the flow is only affected by the wettability from the macro-view. For the local flow inside of GDL, it is affected by both local wettability and local pore size (see Eq. (7.9)). In the Fig. 7.5, the total water flows prefer the no-PTFE region (cos$\theta = 0$), so the total water flow is dominated by the wettability. In the PTFE transition position, the pore structure have influence and it cause the water on the PTFE transition position is not exactly fixed with the PTFE transition layer.

The local void fraction along the through-plane direction is shown in Fig. 7.6 a) and the local saturation along the through-plane direction at $t_{\text{snap}} = 14.4$ ms are shown in Fig. 7.6 b).

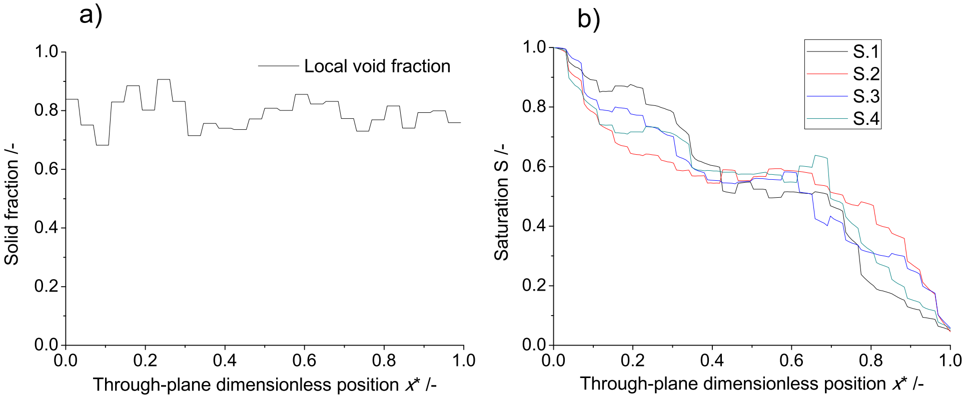

Figure 7.6.: a) Local void fraction along the through-plane direction of geometry 5 (PTFE distribution S.1, S.2, S.3 and S.4 in Fig. 7.2 are based on this geometry). b) Local saturation along the through-plane direction with four in-plane PTFE distribution (c.f.50%) at $t_{\text{snap}} = 14.4$ ms. (Geometry 5) (S.1 to S.4 are the in-plane PTFE distributions the same as shown in Fig. 7.2)

It is seen from the local void fraction distribution in Fig. 7.6 a) that the local void fraction are different due to the irregular structures. The macro porosity of GDL is calculated by the average of local pore fraction. The water distribution in Fig. 7.6 b) decreases along the through-plane direction close to a linear relation but not an exactly linear decreasing. The saturation in the local position does not decrease linear (like case S.4), S increases from $x^* \approx 0.5$ to $x^* \approx 0.7$) because of irregular GDL local structures. It is observed that $S \approx 1$ in the inlet $(x^* = 0)$ due to the simulation setups and the buffer space is initially fully occupied by water (see Fig. 5.1 b)). In the outlet $(x^* = 1)$, saturation of these four cases are the same. It means the in-plane PTFE c.f.50% distribution perform the same breakthrough area on the GDL surface at $t_{\text{snap}} = 14.4$ ms. The water distribution on the cross section (shown in Fig. 7.4) for four in-plane PTFE c.f.50% styles are shown in Fig. 7.7

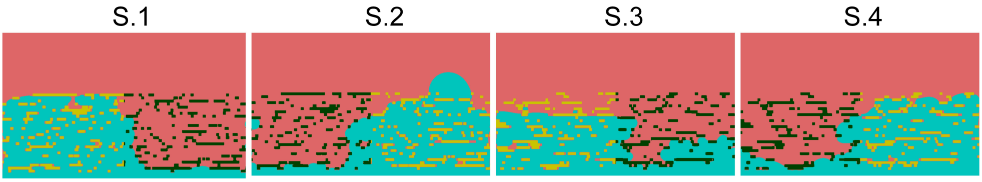

Figure 7.7.: Water distribution on the reference cross section (red surface in Fig. 7.2). (Geometry 5) (S.1 to S.4 are in-plane PTFE distributions the same as shown in Fig. 7.7. Green: PTFE; yellow: no-PTFE; blue: water; red: air.

According to the water distribution shown in Fig. 7.7, water prefers the no-PTFE region and the no-PTFE regions are almost fully flooded on the cross sections. Therefore, there is a higher flood risk in the no-PTFE region. From the stochastic view point, the scenarios S.1 to S.4 (in Fig. 7.7) should show the same result because of the nature of the underlying the same stochastic model. But the in-plane dimension of the uniform PTFE region in S.1 to S.4 is only 200 l.u. (0.3 mm) which is smaller than the minimum size of 300 l.u. suggested in section 5.3. Therefore, the destination in the results of S.1 to S.4 can be influenced by this domain size. The water flows through GDL is a highly dynamic process as described in section 5. So the elevation plot of the water through one of in-plane PTFE c.f.50% GDL (case S.3) in Fig. 7.2) at four different timesteps (4.8, 9.5, 14.4 and 19.2 ms) are shown in Fig. 7.8.

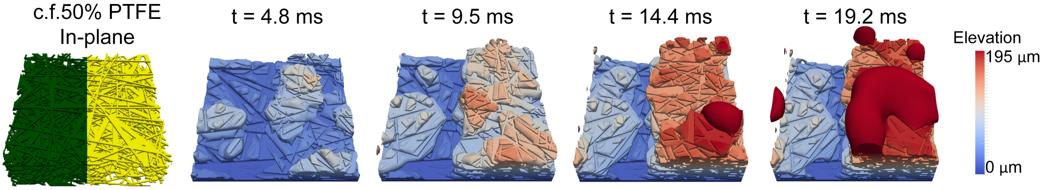

Figure 7.8.: Elevation plot of water distribution with one of in-plane PTFE distributions (S.3 in Fig. 7.2) at different evolution time t (4.8 ms, 9.5 ms, 14.4 ms and 19.2 ms). (Geometry 5) Green: PTFE; yellow: no-PTFE

It is seen from Fig. 7.8 that the water flows preferably in the no-PTFE region. As time goes on, the water flow in the PTFE region is slower than that in the no-PTFE region. According to the Eq. (7.9), the total water flow follows the general physical principle and prefer the hydrophilic region. The PTFE and no-PTFE regions occupied half of whole GDL in-plane direction separately, so it can be assumed that these two regions have the similar porosity (or pore size distribution) and R_p in Eq. (7.9) can be assumed the same. Therefore, two regions have different critical pressure P_c due to different wettability. $P_c = 0$ in no-PTFE region (cosθ=0), so it has less resistance than $P_c < 0$ in PTFE region (cosθ<0) for flowing and water prefer no-PTFE region. Moreover, the irregular water distribution are also observed on the PTFE (hydrophobic) region and this inhomogeneous are caused by the different pore sizes (different R_p according to Eq. (7.9)). After water flowing breakthrough the GDL, the formed droplets coalesce on the GDL surface ($t =$ 19.2 ms in Fig. 7.8). It is consistent with the observation in experiments by Bazylak et al. that the loss of PTFE creates localized hydrophilic routes that became preferable pathways for the water transport in the GDL [75]. In comparison with the results in Fig. 5.15 (same GDL geometry is fully covered with PTFE c.f.100%), the water distribution are different in different timesteps and water is prefer flooded in the no-PTFE region.

- **Conclusion**

  It is concluded from the water flowing through in-plane PTFE c.f.50% distributions, the water prefers flowing through the no-PTFE region. When water flows breakthrough the GDL, the breakthrough point are irregular formed on the GDL surface. The breakthrough points can be formed near the PTFE transition interface and within no-PTFE region. The four in-plane PTFE c.f.50% cases perform the similar dynamic total saturation curves. The water flow inside of GDL are studied on a cross section vertical to the PTFE transition layer with choosing a fixed snapshot. It is observed that some water flowing through the PTFE transition boundary.

7.3. Whole-GDL PTFE distribution

In this section, the PTFE is distributed in the whole GDL with different cover fractions including 33%, 50% and 66% with the process shown in flow chart of Fig. 3.5. And they are compared with two extreme cases that fresh GDL (c.f.0% PTFE) and perfectly processed GDL (c.f.100% PTFE, carbon fibers are fully covered with PTFE). The dynamic saturation curves against the evolution time t are shown in Fig. 7.9 a). The snapshot time $t_{\text{snap}} = 14.4$ ms is chosen before the water flowing breakthrough phenomenon is observed in case whole-GDL c.f.100%. The region after the snapshot time are zoomed and shown in Fig. 7.9 b).

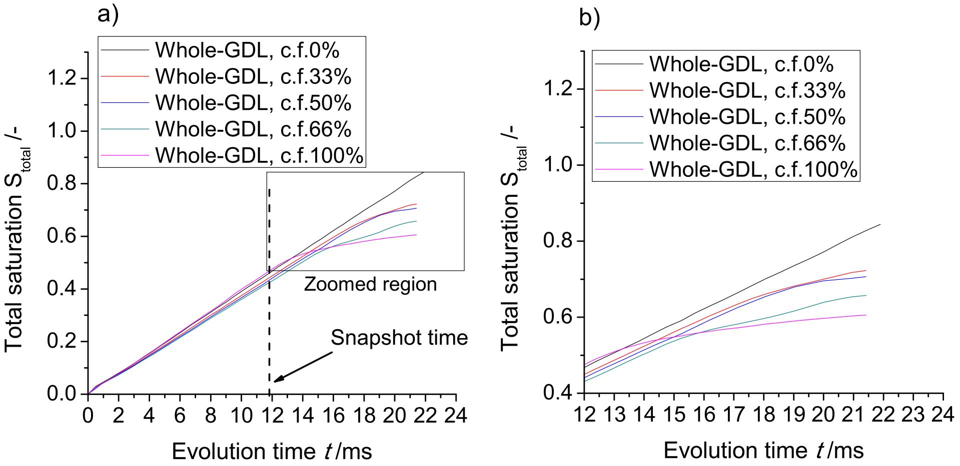

Figure 7.9.: a) Dynamic saturation curves of five whole-GDL PTFE distributions (c.f.0%, c.f.33%, c.f.50%, c.f.66% and c.f.100%). (Geometry 5) b) Zoom of frame region in Fig. 7.9 a).

The PTFE is distributed in the whole GDL with five different contents (c.f.0%, c.f.33%, c.f.50%, c.f.66% and c.f.100%). For the dynamic saturation curves in Fig. 7.9 a), when the hydrophobic case (c.f.100%) flows breakthrough the GDL and the hydrophilic case (c.f.0%) have not broken through the GDL. The total saturation curves of these different PTFE distributions are not exactly the same before $t_{\text{snap}} = 14.4$ in Fig. 7.9 a). According to the theory of mass balance, the total saturation should be the same because of the same mass flux in simulations. But this difference is from the LB algorithm and local structures which can be observed in contact angle test of Fig. 4.37 and coalescence test of Fig. 4.28. There is a two-phase interface with certain lattice (3 l.u. with $G_{\text{coh}} = 0.06$ from Table 4.2) and intermiscible density. The error were also happened on the solid surfaces with different wettability and structures (in Fig. 4.37 and Fig. 5.7). It is also observed from Fig. 7.9 a) that the total dynamic saturation curves of whole-GDL c.f.0% and whole-GDL c.f.100% are very close while other cases are different, it can also be explained by Eq. (7.9). For cases whole-GDL c.f.0% and whole-GDL c.f.100%, the GDL with the same local structures (with the same local wettability) are applied and R_p are the same. The flow only depend on the different wettability and the difference between these two cases are only from the interface thickness between solid and water (see Fig. 4.37). But for other cases whole-GDL 33%, whole-GDL 50% and whole-GDL 66%, the errors are from different local structures (local PTFE distribution are different). So these three intermediate PTFE cases (c.f.33%, 50% and 66%) have the bigger errors than those two extreme PTFE cases (c.f.0% and 100%).

The hydrophobic case has the shorter breakthrough time while the water in hydrophilic case contains water inside of GDL (S_{total} keeps growing with the constant curve slope) [83]. The more PTFE, the more obvious difference between dynamic saturation curves are (such as whole-GDL c.f.66% and whole-GDL c.f.100%). But for the cases with less PTFE (like whole-GDL c.f.33% and whole-GDL c.f.50%), the dynamic saturation curves are very close. The local saturation along the through-plane direction with different whole-GDL PTFE distributions at $t_{\text{snap}} = 14.4$ ms are shown in Fig. 7.10

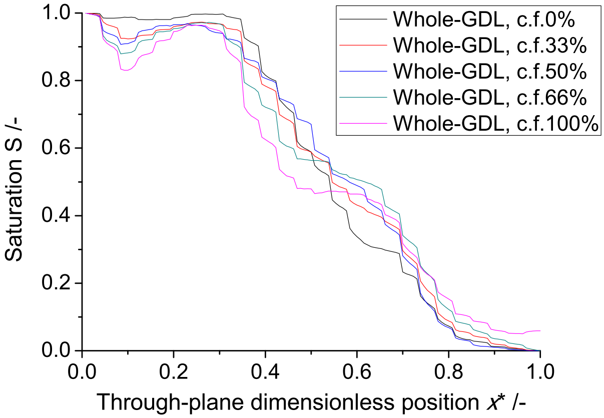

Figure 7.10.: Local saturation along the through-plane direction with five different whole-GDL PTFE distributions (from c.f.0% to c.f.100%) at $t_{\text{snap}} = 14.4$ concerning whole GDL. (Geometry 5)

It is seen from Fig. 7.10, the case whole-GDL c.f.100% is the earliest to achieve the breakthrough time and it already break through the GDL at the snapshot time. On the inlet region ($0 < x^* < 0.1$), the local saturation is lower with higher PTFE content. In the case whole-GDL c.f.0%, almost fully flooded ($S_{\text{total}} \approx 1$) near the inlet region are observed because of the simulation setups on the inlet layer and the hydrophilicity. In the area after the inlet region ($x^* > 0.1$), the tendency of c.f.66% and c.f.100% are close each other, while another three cases (c.f.0%, c.f.33% and c.f.50%) perform the similar local saturation along the through-plane direction at $t_{\text{snap}} = 14.4$ ms. It means when PTFE content beyond c.f.50%, the saturation along the through-plane direction can be systematic characterized (the more PTFE, the lower local saturation). Otherwise, the local saturation along the through-plane direction are affected more by the GDL structures and cannot be systematic characterized. Except the irregular structures effect, the random algorithm of distributing PTFE (in Fig. 3.5) has effect on the local water flow.

- **Conclusion**

  When different content of PTFE is distributed on the whole GDL, the water flows breakthrough the GDL earlier with more PTFE. In the inlet region $(0 < x^* < 0.1)$, the local saturation is lower with more PTFE. The local saturation of case whole-GDL 0% is close to 1 and it has a higher flood risk than other cases. The local saturation for different PTFE content are different because of irregular structures and randomly distributed PTFE.

7.4. Two-sections-through-plane PTFE distribution

It is observed in Fig. 7.7 that the water flow are different on the PTFE transition layers and PTFE content have effect on the water flow as well in section 7.3. Therefore, under this section the c.f.50% PTFE with the same PTFE transition position $(x^* = 0.5)$ are discussed. PTFE is fully distributed on the half of GDL along through-plane direction including the inlet-half and outlet-half two styles. The schematic graph of the inlet-half c.f.50% and outlet-half c.f.50% are shown in Fig. 7.11

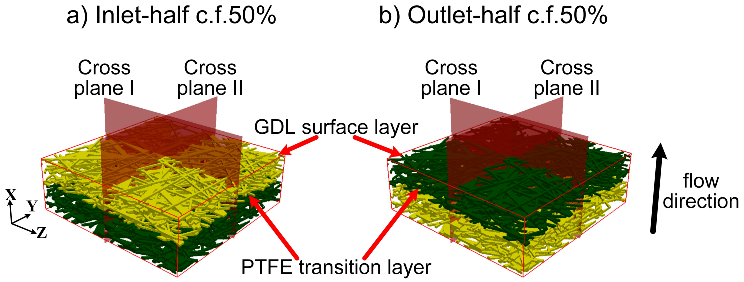

Figure 7.11.: GDL with two two-sections-through-plane PTFE distributions (inlet-half and outlet-half with c.f.50%). (Geometry 5) Green: PTFE; yellow: no-PTFE; red: cross plane I and II.

The PTFE distribution of inlet-half c.f.50% and outlet-half c.f.50% along the through-plane direction are shown in Fig. 7.12 a) and compared with the whole-GDL c.f.50% PTFE style. The inlet-half c.f.50% means the total PTFE cover fraction is 50%, in half of inlet side put 100% PTFE and in outlet half put 0% PTFE. The outlet-half c.f.50% is covered by 100% PTFE on half of outlet side and 0% on half of inlet side and in total it is 50% for whole GDL.

The dynamic total saturation curves of flow through the two-sections-through-plane PTFE distributions (inlet-half c.f.50% and outlet-half c.f.50%) are shown in Fig. 7.12 b) and compared with whole-GDL c.f.50%. The whole-GDL c.f.50% is to put 50% PTFE randomly in whole GDL.

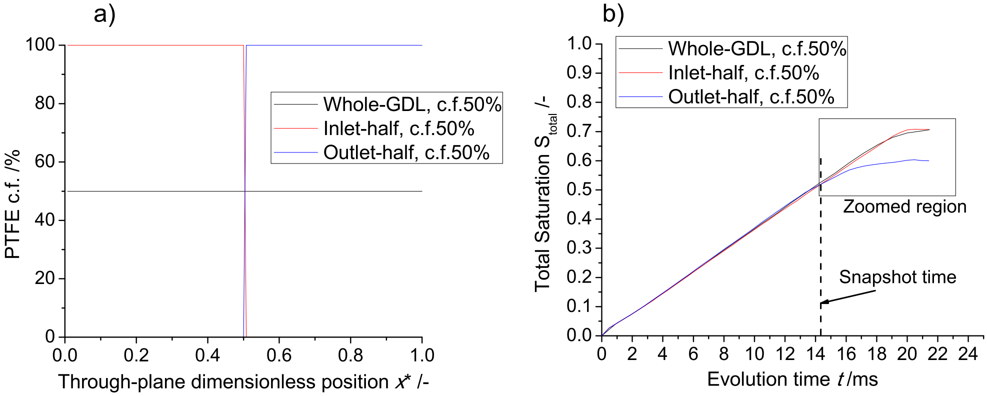

Figure 7.12.: a) Two two-sections-through-plane and whole-GDL PTFE distributions (c.f.50%) along the through-plane direction. (Geometry 5) b) Dynamic saturation curves of two two-sections-through-plane (inlet-half and outlet-half) and whole-GDL PTFE distributions (c.f.50%). (Geometry 5)

It is seen from Fig. 7.12 b) that the total flow behavior of whole-GDL c.f.50% and inlet-half c.f.50% are quite similar. But in different time, their slopes starts to decrease. A snapshot time $t_{\text{snap}} = 14.4$ ms is chosen which is the same that in the section 7.5 to study the water flow in this dynamic process. In order to check the accurate breakthrough time, the total dynamic saturation curves (Fig. 7.12 b)) after the snapshot time are zoomed and presented in Fig. 7.13 a).

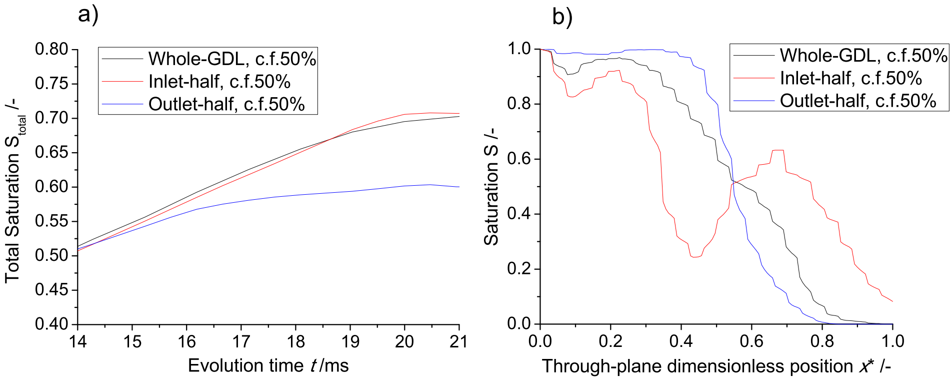

Figure 7.13.: a) Zoom of frame region in Fig. 7.12 b). b) Local saturation along the through-plane direction with two two-sections-through-plane (inlet-half and outlet-half) and whole-GDL PTFE distributions (c.f.50%) at $t_{\text{snap}} = 14.4$ ms. (Geometry 5)

It is seen from Fig. 7.13 a), the slope of dynamic saturation curve for outlet-half c.f.50% starts to decrease earlier than that of whole-GDL c.f.50% and inlet-half c.f.50%. It can be estimated that the breakthrough time for inlet-half c.f.50% is $t \approx 20$ ms, whole-GDL c.f.50% is $t \approx 19$ ms and outlet-half c.f.50% is $t \approx 16$ ms. The inlet-half c.f.50% break through GDL already while the random and outlet-half c.f.50% cases did not break through the GDL yet. It is concluded that the GDL with outlet-half c.f.50% is the easiest case to allow water flowing breakthrough the GDL. The local saturation along the through-plane direction of two-sections-through-plane PTFE distribution (inlet-half c.f.50% and outlet-half c.f.50%) at the snapshot time are shown in Fig. 7.13 b) and in comparison with whole-GDL c.f.50%. The 'S' shape is observed for inlet-half c.f.50% case while the 'ᒣ' shapes are seen for random and outlet-half c.f.50% cases. It is concluded that the 'S' shape can happen on the PTFE transition (from PTFE to no-PTFE) layer in the inlet-half c.f.50% style. The outlet-half c.f.50% has the lowest displacement speed and no water flows over $x^* \approx 0.82$. The whole-GDL c.f.50% has the intermediate displacement speed and no water flows over $x^* \approx 0.95$. In comparison with the water distribution of inner c.f.50% near the PTFE transition layer I ($x^* = 0.25$) in Fig. 7.22 b), the more clear 'S' shape can be seen in the PTFE transition layer I.

The elevation plot of water through two-sections-through-plane PTFE distributions (inlet-half c.f.50% and outlet-half c.f.50%) at different evolution time are shown in Fig. 7.14 to study flow details in a dynamic process.

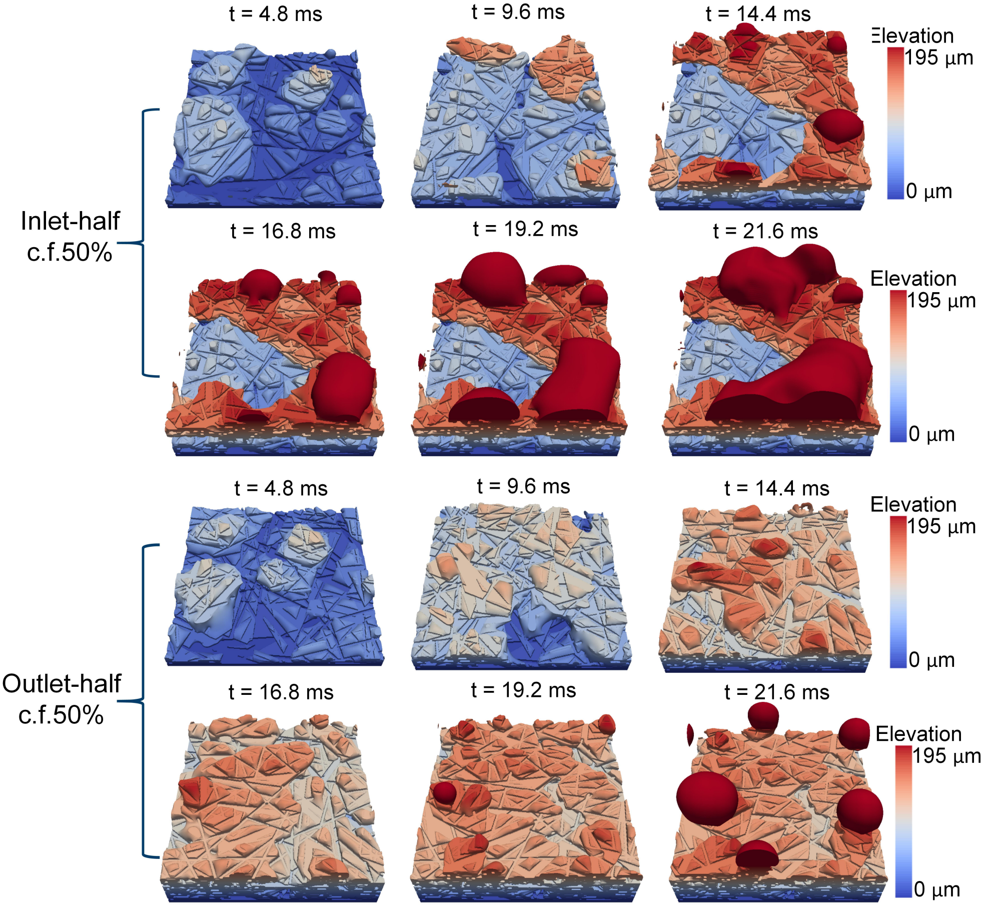

Figure 7.14.: Elevation plot of water distribution with two two-sections-through-plane PTFE distributions (inlet-half and outlet-half (c.f.50%) at different evolution time (4.8 ms, 9.6 ms, 14.4 ms, 16.8 ms, 19.2 ms and 21.6 ms). (Geometry 5)

It is seen from Fig. 7.14 that inlet-half c.f.50% and outlet-half c.f.50% performed the different dynamic water flow behavior. At the beginning period ($t =$ 4.8 ms), the water in both two cases shows the similar flow 'fingers'. For the inlet-half c.f.50%, from $t = 9.6$ ms to $t = 14.4$ ms, water flow breakthrough the GDL and the whole GDL is not fully flooded. Some empty pores are left at $t = 14.4$ ms. From $t = 14.4$ ms to $t = 16.8$ ms, the droplets formed on the breakthrough points keeps growing, but the area of empty pores do not change much. From $t = 19.2$ ms to $t = 21.6$ ms, it is observed the empty pore regions are still left and the area does not change much, but the formed droplets keeps growing and coalesce with neighbor droplets. For the outlet-half c.f.50% from $t = 9.6$ ms to $t = 16.8$ ms, the water flows with 'surface' way and no clear 'finger' are observed. At $t = 19.2$ ms, the water flows breakthrough the GDL. Finally at $t = 21.6$ ms, more than one breakthrough points are observed and sphere shaped droplets are formed on these breakthrough points. Especially at the $t = 14.4$ ms and $t = 16.8$ ms for outlet-half c.f.50%, the elevation the 'fingers' shaped flow route does not increase with time because some water from the 'fingers' are sucked back to other regions. This suck-back observation is consistent with the conclusions from the Fig. 5.24. The dynamic process in Fig. 7.14 can also be compared with the dynamic process in fully covered PTFE (c.f.100%) cases in Fig. 5.22. The water with c.f.100% case already breaking through the GDL at $t = 11.9$ while that with c.f.50% breaking through the GDL later.

In order to see the flow details inside of GDL, the water distribution on the cross plane I and II (see Fig. 7.11) at $t_{\text{snap}} = 14.4$ ms are shown in Fig. 7.15 and compared with the random PTFE 50%.

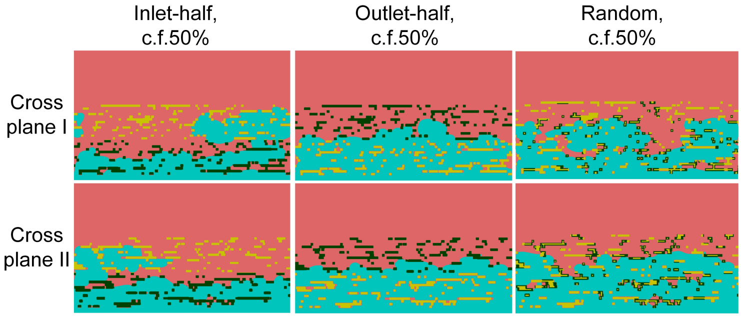

Figure 7.15.: Water distribution on the cross plane I and II (see Fig. 7.11) of two two-sections-through-plane (inlet-half and outlet-half) and whole-GDL PTFE distributions (c.f.50%) at $t_{\text{snap}} = 14.4$ ms. (Geometry 5) Yellow: no-PTFE; green: PTFE; blue: water; red: air

In comparison with inlet-half c.f.50% and whole-GDL c.f.50% cases in Fig. 7.15, the water distribution in the PTFE region lower than PTFE transition layer are similar. But the water near the PTFE transition layer are different. In comparison with all three cases in Fig. 7.15, different breakthrough positions on the PTFE transition layer. The elevation plot of the half GDL along through-plane direction are shown in Fig. 7.16.

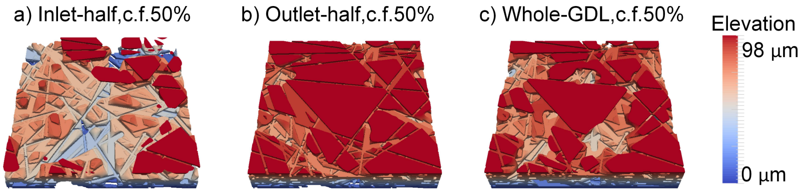

Figure 7.16.: Elevation plot of water distribution within the GDL for two two-sections-through-plane (inlet-half and outlet-half) and whole-GDL PTFE distributions (c.f.50%) at $t_{\text{snap}} = 14.4$ ms. (Geometry 5)

It is seen from Fig.7.16, three cases perform different breakthrough area on the PTFE transition layer. The inlet-half c.f.50% has the least breakthrough area and the outlet-half c.f.50% has the biggest breakthrough area within three cases. The random c.f.50% has the intermediate situation. It means the case inlet-half c.f.50% has the lowest flooding risk in the operating fuel cell. The reactant from the GC has more chance to flow to the catalyst layer and make the reaction continuously happen.

- **Conclusion**

  It is concluded that the inlet-half c.f.50% and outlet-half c.f.50% PTFE distributions have effect on the water flow through GDL. Outer-half c.f.50% shorten the breakthrough time but there is a higher flood risk than inlet-half c.f.50% near the inlet region. The inlet-half c.f.50% has lower flood risk than outlet-half c.f.50%. On the PTFE transition layer, the inlet-half c.f.50% has the lowest flood risk in comparison with outlet-half c.f.50% and whole-GDL c.f.50% PTFE distributions.

7.5. Sandwich-through-plane PTFE distribution

In the processed GDL with PTFE, the PTFE are distributed inhomogeneously along the through-plane direction [90]. The GDL was divided into three sections along the through-plane direction shown in Fig. 7.17 including two outer regions and one inner region with PTFE transition layer I and II. In this section, two extreme cases are discussed including outer styles and inner styles. For the outer style PTFE distribution, the c.f.100% PTFE is distributed on the outer regions of GDL and c.f.0% PTFE is in inner section of GDL as shown in Fig. 7.17 a). The outer style of sandwich-through-plane PTFE distribution is the simplification of the fresh PTFE processed GDL in application [92]. Another extreme case is called inner style that distribute c.f.100% on inner of GDL and c.f.0% on outer of GDL as shown in Fig. 7.17 b). The inner style of sandwich-through-plane PTFE distribution is the simplification of the aged GDL (the GDL is used after fuel cell running a long time), the PTFE on the outer of GDL are easier to lose than that in the inner of GDL [93].

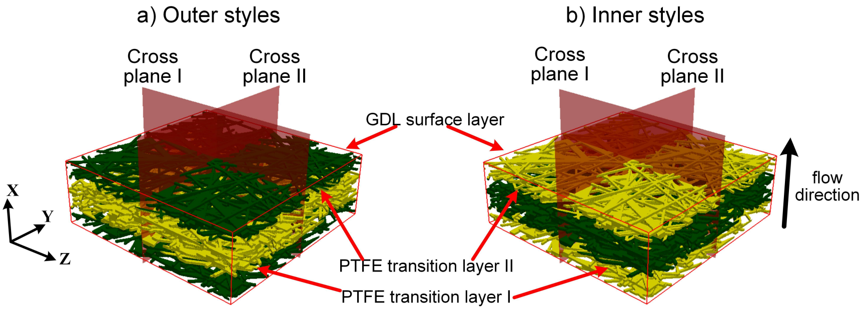

Figure 7.17.: GDL with two sandwich-through-plane PTFE distributions (outer and inner style). (Geometry 5) Green: PTFE; yellow: no-PTFE; red: cross plane I and II.

The positions of PTFE transition layer I and II are not fixed and depend on the PTFE content. The position of PTFE transition layer can be seen from the plot of PTFE content distribution along the through-plane direction shown in Fig. 7.18 a) and Fig. 7.21 a). For example, $x^* = 0.26$ is the position of PTFE transition layer I and $x^* = 0.75$ is the position of PTFE transition layer II of outer c.f.50% style in Fig. 7.18. The details of water flowing through outer and inner styles of sandwich-through-plane PTFE distribution are discussed separately below.

- **Outer styles of PTFE distribution**

  According to the experiments on studying PTFE distribution, the produced GDL with PTFE are inhomogeneously distributed inside and more PTFE are distributed on outer sections (GDL surfaces sides) while the inner region is distributed less PTFE [89][88]. The positions of PTFE transition layers are varied with different PTFE content to ensure the extreme PTFE distributions (outer sections c.f.100% and inner section c.f.0%). The Fig. 7.18 a) shows how the three different outer styles distribute PTFE along the through-plane direction.

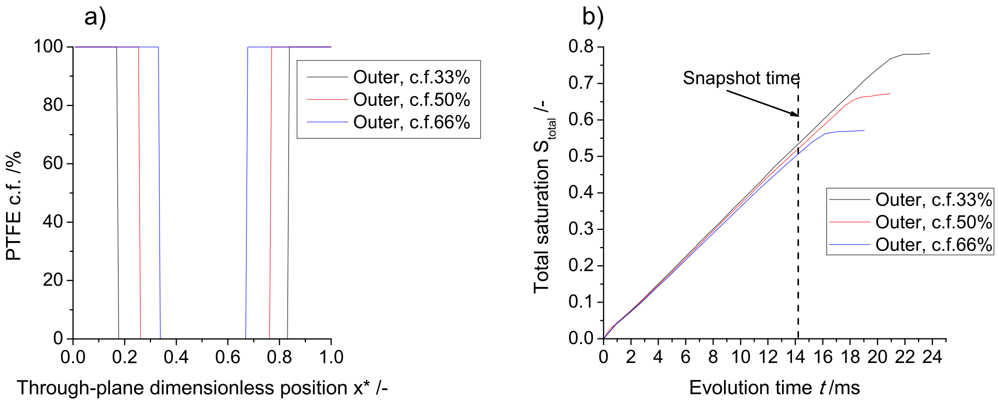

Figure 7.18.: a) Three sandwich-through-plane (outer style) PTFE distributions along the through-plane direction with different content (c.f.33%, c.f.50% and c.f.66%). (Geometry 5) b) Dynamic saturation curves of three sandwich-through-plane (outer style) PTFE distributions with different content (c.f.33%, c.f.50% and c.f.66%). (Geometry 5)

The dynamic saturation curves of three outer styles are shown in Fig. 7.18 b) and they are systematic presented. With more PTFE, the dynamic saturation curve achieve the earlier time when slope of total saturation curves decrease. Then the gradient (slope) of total saturation are shown in Fig. 7.19 a). It is seen that the gradient of three different outer PTFE styles continuously decrease sharply after certain different evolution time which is called breakthrough time. It can be seen from Fig. 7.19 that the more PTFE, the shorter breakthrough time are needed ($t \approx 15$ ms for outer c.f.66%, $t \approx 16.7$ ms for outer c.f.50% and $t \approx 19$ ms for outer c.f.33%).

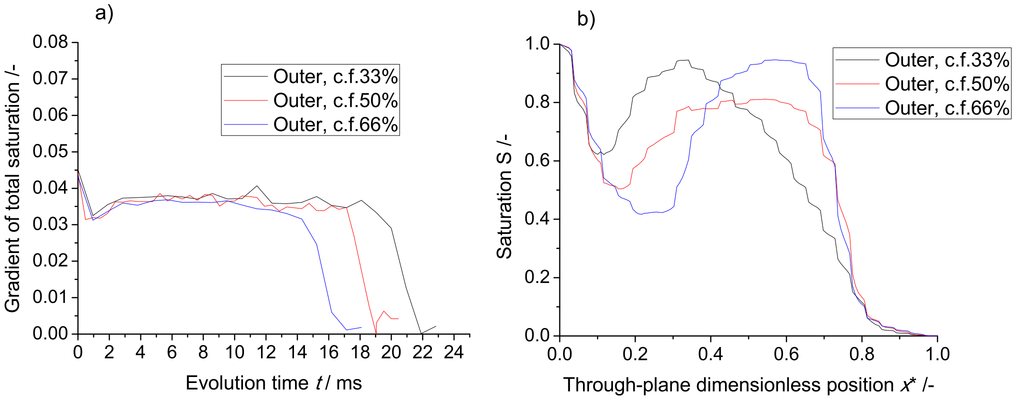

Figure 7.19.: a) Gradient of dynamic saturation curves for three sandwich-through-plane (outer style) PTFE distributions with different content (c.f.33%, c.f.50% and c.f.66%). (Geometry 5) b) Local saturation along the through-plane direction with three sandwich-through-plane (outer style) PTFE distribution with different content (c.f.33%, c.f.50% and c.f.66%) at $t_{\text{snap}} = 14.4$ ms. (Geometry 5)

$t_{\text{snap}} = 14.4$ ms is chosen before all three cases break through GDL to check the local saturation along the through-plane direction. The local saturation curves along the through-plane direction of outer PTFE style cases at $t_{\text{snap}} = 14.4$ ms) are shown in Fig. 7.19 b). Three outer PTFE styles show roughly the 'S' shape water distribution along the through-plane direction. In the outer section of the inlet side, water saturation decrease due to the fully hydrophobic in this region. Different transition positions ($x^* \approx 0.1$ for outer c.f.33%, $x^* \approx 0.15$ for outer c.f.50% and $x^* \approx 0.25$ for outer c.f.66%), where saturation start to increase, are observed because different positions of PTFE transition layer I (see Fig.7.17 and Fig. 7.18 a)). The saturation increase after the positions of PTFE transition layer I and achieve the peak values (close to fully saturated $S = 1$). Positions of the peak saturation are not fixed but locate in the inner hydrophilic region. The peak saturation on the hydrophilic region are not systematically fixed. The peak saturation of outer c.f.50% is lower than those of outer c.f.33% and outer c.f.66% because the local structures of GDL are varied (see Fig. 7.6 a)).

The elevation plot of water flowing through the outer style PTFE distribution (c.f.50%) at different evolution time are shown in Fig. 7.20 to study flow details in the dynamic process.

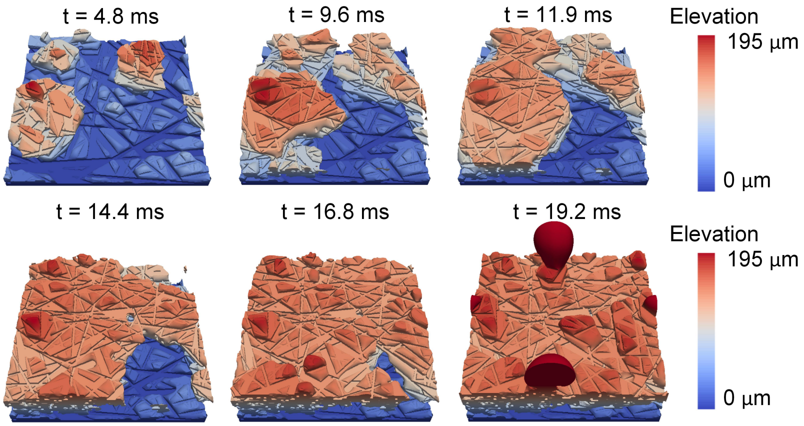

Figure 7.20.: Elevation plot of water distribution with a sandwich-through-plane (outer style, c.f.50%) at different evolution time (4.8 ms, 9.6 ms, 11.9 ms, 14.4 ms, 16.8 ms and 19.2 ms). (Geometry 5)

It is seen from Fig. 7.20, the water flows along some 'finger' routes at the beginning period (t =4.8 ms and 9.6 ms). After that, the water start to flow with a 'surface' way (t = 11.9 ms, 14.4 ms and 16.8 ms). But the GDL inside are still not flooded and some empty pores are left. Finally at t = 19.2 ms, the water flows breakthrough the GDL and one droplet is formed on the GDL surface.

- **Inner styles of PTFE distribution**

The aged GDL loss some PTFE after operating fuel cell several times [36][37]. The PTFE on the GDL surfaces are easier to be lost than those inside of GDL [38]. So the aged GDL can be represented with an extreme sandwich-through-plane PTFE distribution styles in simulations. The extreme sandwich-through-plane PTFE distribution is PTFE is distributed with c.f.100% in the inner section and c.f.0% in the two outer sections. The PTFE distribution along the through-plane direction with different cover fractions are shown in Fig. 7.21 a).

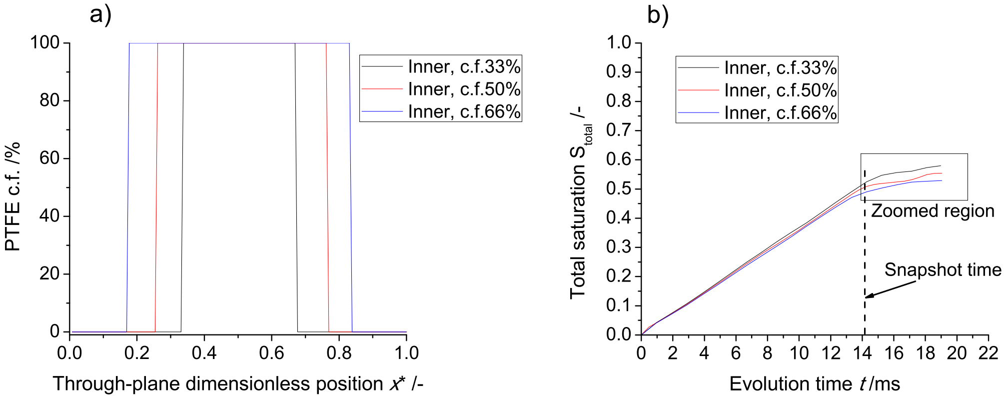

Figure 7.21.: a) Three sandwich-through-plane (inner style) PTFE distributions along the through-plane direction with different content (c.f.33%, c.f.50% and c.f.66%). (Geometry 5) b) Dynamic saturation curves of three sandwich-through-plane (inner style) PTFE distributions with different content (c.f.33%, 50% and 66%). (Geometry 5)

The PTFE transition layer positions of three inner styles can be seen from Fig. 7.21 a). For example, $x^* = 0.18$ is the position of PTFE transition layer I for inner c.f.33%. The total saturation against the evolution time for inner styles PTFE distribution are shown in Fig. 7.21 b). It is seen that they performed the similar macro flow behavior. A fixed snapshot time $t_{\mathsf{snap}} = 14.4$ ms is chosen to study the flow details. The total dynamic saturation curves after the snapshot time are zoomed and shown in Fig. 7.22 a). It is seen that they have quite similar total saturation after flowing breakthrough (the time when the slope of total saturation curves starts to decrease) the GDL (especially inner c.f.50% and inner c.f.66%, see the zoomed region in Fig. 7.22 a), the total saturation curves of inner c.f.50% and inner c.f.66% are very close each other). The difference of total saturation are caused by the PTFE distribution (see Fig. 3.5) and two-phase interface thickness (see Fig. 4.37). The local saturation along the through-plane direction at $t_{\mathsf{snap}} = 14.4$ ms for three inner PTFE cases are shown in Fig. 7.22 b).

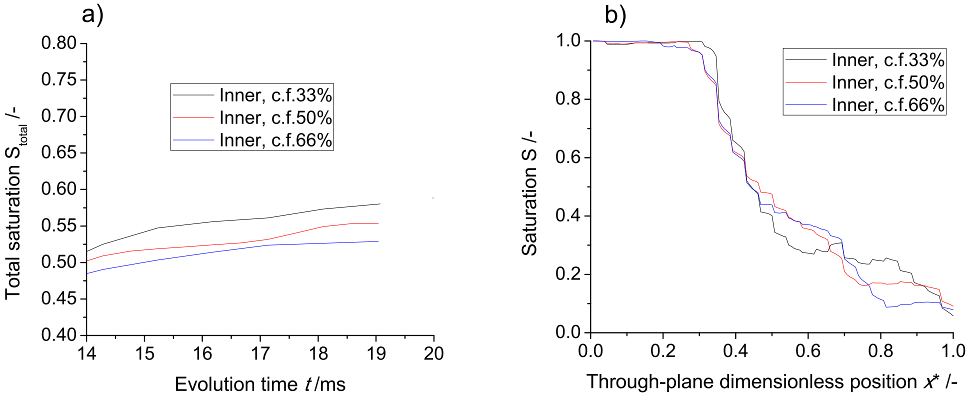

Figure 7.22.: a) Zoom of frame region in Fig. 7.21 b). b) Local saturation along the through-plane direction of three sandwich-through-plane (inner style) PTFE distribution with different content (c.f.33%, c.f.50% and c.f.66%) at $t_{\text{snap}} = 14.4$ ms. (Geometry 5)

It is seen from Fig. 7.22 b), three inner cases show the fully flood $(S \approx 1)$ in the outer hydrophilic region $(0 < x^* < 0.3)$. The water are distributed with a '⅂' shape along the through-plane direction. The saturation decreases sharply at the similar position $(x^* \approx 0.3)$. It can be concluded that the fully saturated area near the inlet is independent of PTFE transition layer I position for inner styles. But after the PTFE transition layer II position, the water saturation decrease slower than that in the inner hydrophobic section because of the transition from hydrophobicity of inner section to the hydrophility of outer section. It can be concluded that the local saturation curve is more sensitive on the PTFE transition layer II positions (see Fig. 7.21 a), $x^* \approx 0.65$ for inner c.f.33%, $x^* \approx 0.78$ for inner c.f.50% and $x^* \approx 0.85$ for inner c.f.66%).

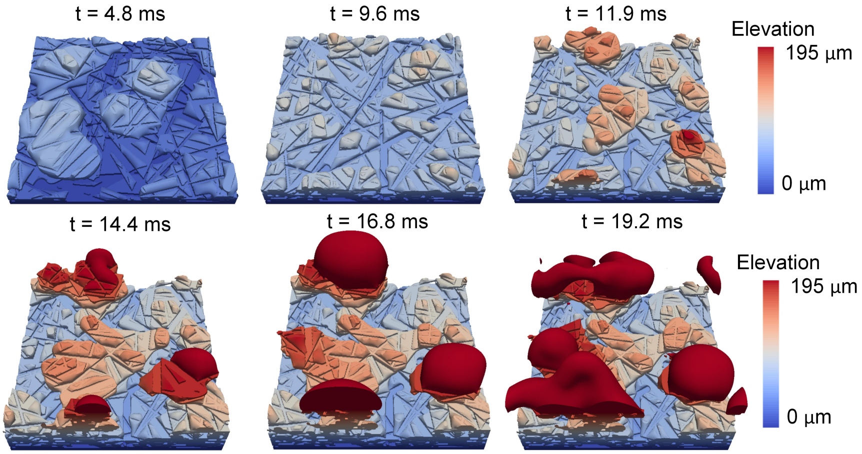

Figure 7.23.: Elevation plot of water distribution with a sandwich-through-plane (inner style) PTFE distribution (c.f.50%) at different evolution time (4.8 ms, 9.6 ms, 11.9 ms, 14.4 ms, 16.8 ms and 19.2 ms). (Geometry 5)

In this dynamic process, the elevation plot of water flowing through the inner style PTFE distribution (c.f.50%) in different timesteps are shown in Fig. 7.23. It is seen from Fig. 7.23, the flow 'surface' and no clear flow 'fingers' are observed at the beginning period (t =4.8 and 9.6 ms). After that at $t = 11.9$ ms and 14.4 ms, some individual breakthrough points are formed and the water flow through the breakthrough points. The droplets on the breakthrough points keep growing. At the time t =16.8 ms, a new breakthrough point is observed. Finally at $t = 19.2$ ms, the bigger droplets are formed with coalesce of neighbor droplets. From $t = 11.9$ ms to $t = 19.2$ ms after water flowing breakthrough the GDL, the water below the GDL surface does not change too much.

- **Comparison of outer and inner styles of PTFE distribution**

In this part, the outer and inner styles of PTFE distributions are compared. An intermediate PTFE content (c.f.50%) is chosen to be discussed. The total dynamic saturation curves of outer c.f.50% and inner c.f.50% are already shown in Fig. 7.18 b) and Fig. 7.21 b) separately. It can be seen their flows are different. In both cases, the same snapshot time $t_{\text{snap}} = 14.4$ ms is chosen to study the water flow on the PTFE transition layers (I and II) and GDL surface (see Fig. 7.17). The elevation plot of outer style (c.f.50%) and inner style (c.f.50%) on the two PTFE transition layers (I and II, see Fig. 7.17) and GDL surface at t_{snap} =14.4 ms are shown in Fig. 7.24

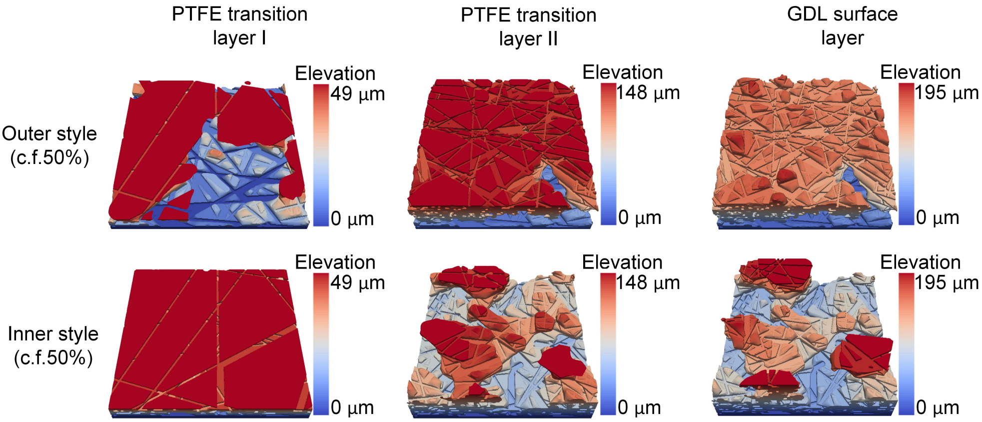

Figure 7.24.: Elevation plot of water distribution within different GDL positions (PTFE transition layer I, II (see Fig. 7.24) and GDL surface layer) of two sandwich-through-plane (outer style and inner style) PTFE distributions (c.f.50%) at t_{snap} =14.4 ms. (Geometry 5)

It is seen from Fig. 7.24 that the situations on the PTFE transition layer I, II and GDL surface layer are different. On the PTFE transition layer I, it is fully flooded with the inner style PTFE distribution, while some empty pores are left with the outer style PTFE distribution. On the PTFE transition layer II, more water are distributed with outer style PTFE distribution. On the GDL surface layer, three individual breakthrough points are observed. For the outer style, the water flows with the 'surface' under the GDL surface layer and does not flow breakthrough the GDL at the snapshot time.

In a further step, the water distribution on the cross plane I and II (see Fig. 7.17) at $t_{\text{snap}} = 14.4$ ms are studied and shown in Fig. 7.25

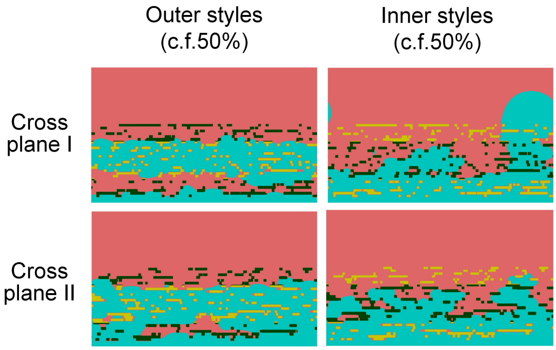

Figure 7.25.: Water distribution on the cross plane I and II (see Fig. 7.17) of two sandwich-through-plane (outer style and inner style) PTFE distributions (c.f.50%) at $t_{\text{snap}} = 14.4$ ms. (Geometry 5) Yellow: no-PTFE; green: PTFE; blue: water; red: air

It is seen from the situation of outer style PTFE distribution in Fig. 7.25 that fully flood are observed on the no-PTFE region of outer styles on both cross plane I and II. In the inner style PTFE distribution, the no-PTFE region near the outlet is not fully flooded, while the no-PTFE region near the inlet is fully flooded.

- **Conclusion**

  It is concluded from the water flows through the sandwich-through-plane PTFE distribution that flows in the outer and inner styles are different. The flow can be analyzed systematically in the outer styles. The more PTFE, the water flows breakthrough GDL faster. The 'S' shape local saturation curves are observed on the outer styles. For the outer styles PTFE distribution, the outlet region is easier to be flooded. For the inner styles PTFE distribution, more droplets are formed on the GDL surface, but it has a high flood risk near the inlet region. In comparison with outer and inner styles, the water distribution on PTFE transition layers and GDL surface layer are different. The water flows in inner style is easier breaking through the GDL and form droplets on the GDL surface. But the inner style has a higher fully flood risk near the inlet region than the outer style.

7.6. Quasi-linear-through-plane PTFE distribution

In this section, four patterned PTFE distribution styles which divide the GDL into ten equal sections along through-plane direction are discussed. The several-sections-through-plane PTFE distribution are the simplification of PTFE is distributed with a linear relation. The total amount of PTFE are the same for the four cases and the PTFE are distributed on ten sections with different gradient. Four PTFE distribution with different PTFE gradient are studied, including gradient 5%, 2%, -2% and 5%. Four different quasi-linear-through-plane PTFE distributions are shown in Fig. 7.26 a). Their dynamic saturation curves are shown in Fig. 7.26 b).

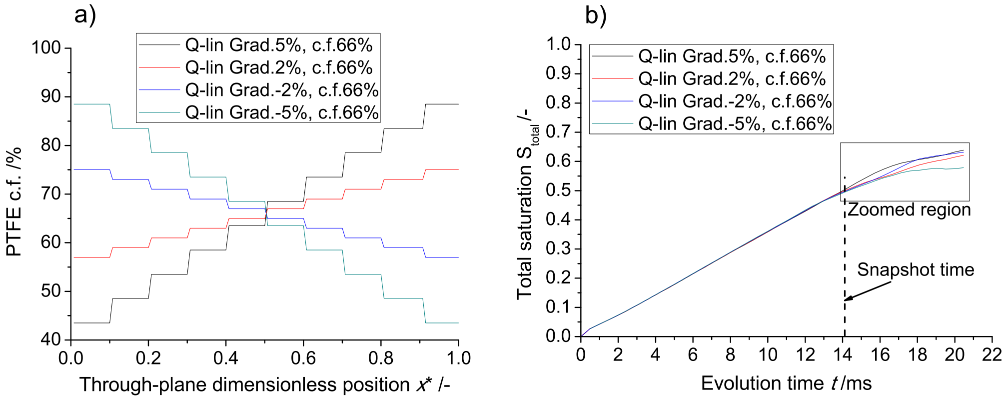

Figure 7.26.: a) Four quasi-linear-through-plane PTFE distributions along the through-plane direction (c.f.66%) of different gradient (grad.-5%, grad.-2%, grad.2% and grad.5%,). (Geometry 5) b) Dynamic saturation curves of four quasi-linear-through-plane PTFE distributions (c.f.66%). (Geometry 5)

It is seen from Fig. 7.26 b), four quasi-linear-through-plane cases performed the similar flow behaviors. The flow behavior are different after water flowing breakthrough the GDL. $t_{\text{snap}} =$ 14.4 ms is the same as that in Fig. 7.12 b) to study the flow details. The region after the snapshot time in the total dynamic saturation curves in Fig. 7.26 b) are zoomed and presented in Fig. 7.27 a). It is seen from Fig. 7.26 b), the dynamic total saturation curves are quite close but have different breakthrough time. The detailed breakthrough times can be checked from the Fig. 7.27 a), the breakthrough time cannot be not systematically analyzed. It is concluded that the gradient of quasi-linear-through-plane PTFE distribution have no systematic effects on the macro flow behaviors (total saturation). In order to analyze the water situation locally along the through-plane direction, the local saturation along the through-plane direction of four quasi-linear-through-plane PTFE distributions at the snapshot time are shown in Fig. 7.27 a).

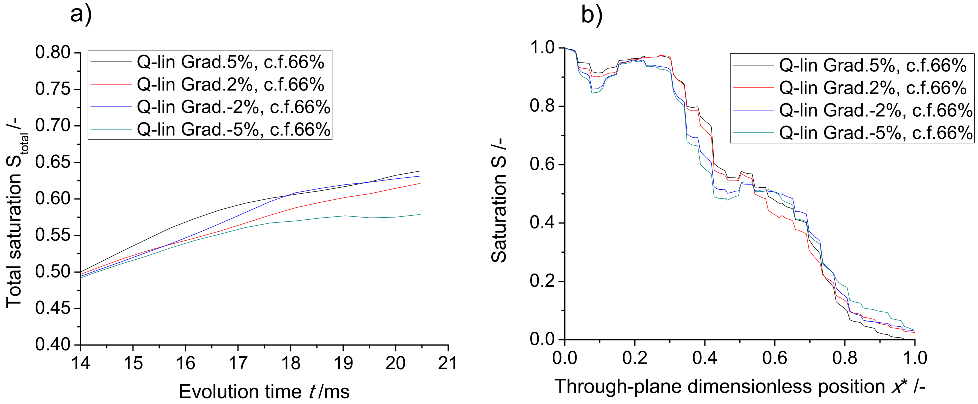

Figure 7.27.: a) Zoom of frame region in Fig. 7.26 b). b) Local saturation along the through-plane direction with four quasi-linear-through-plane PTFE distributions (c.f.66%) of different gradient (grad.-5%, grad.-2%, grad.2% and grad.5%) at $t_{\text{snap}} = 14.4$ ms. (Geometry 5)

It is seen from Fig. 7.27 b) that the water in all cases already break through (the saturation at $x^* = 1$ are larger than 0) the GDL except the case with grad.5% at the snapshot time. It is concluded that more water are accumulated in GDL and harder to break through the GDL for Q-lin Grad.5% PTFE distribution. Therefore, the quasi-linear-through-plane PTFE distribution with grad.5% has the highest flooding risk within four PTFE distributions in this section. It is also systematically observed from Fig. 7.27 b) that the more PTFE perform the lower saturation when $x^* < 0.5$. In the half of GDL to the outlet side ($x^* > 0.5$), no regular relations between four curves are observed because of irregular GDL structures and randomly PTFE distributions.

- **Conclusion**

  It is concluded that the quasi-linear-through-plane PTFE distributions with different gradient have no systematic effects on the water flow behavior. When checking the local water saturation along through-plane direction, the more PTFE distribution cause the lower water saturation in the half of GDL to the inlet side ($x^* < 0.5$). The PTFE distribution with grad.5% has the highest flooding risk within four discussed cases in this section. The water flowing through the GDL is a dynamic process, therefore the local variation in the breakthrough time is to be expected.

8. Discussion

In the motivation of section 1.1, some goals of this work are declared including suitable model development to better understand water flowing through the GDL, bridging the gap in multi-scale simulations of PEFC and a first sight of PTFE effect on water flow. These goals are all achieved in this dissertation with certain accuracy or limitations.

The LB ShanChen MCMP model is chosen due to some intrinsic benefits on the simulation in porous media and parallel computing from the algorithm side. The present ShanChen MCMP model has two main limitations (viscosity ratio and density ratio are one) which are allowed for the water flow through the GDL process. According to the analysis of *Ca* for water through the GDL, it is found this process is a capillary force dominated process with $Ca \approx 10^{-8}$ (the operating conditions are in Table 1.2). In the capillary force dominated process, the density ratio and viscosity ratio between two phases can be neglected.

The LBM is a discritized simulation method, so it is well known to discuss the lattice dependence and a particular issue - the relaxation time (viscosity) dependence. Results are converged and the absolute error are less with the finer lattices. It is consistent with the principle of discritized method that the result with certain accuracy can be achieved with specific lattice amount. For the relaxation time dependence, the MRT approach is more independent of relaxation time in comparison with that with SRT approach, particularly on the main algorithm error sources like spurious velocity and intermiscible density. The LB ShanChen model are also affected with different forces schemes. In comparison with different force schemes, the results highlight the strong recommendation of MRT with EDM scheme in model. Therefore, the MRT-EDM ShanChen MCMP model is applied on the water flowing through the GDL.

In the selected model, some model parameters (G_{coh} and $G_{\text{adh},1}$) are chosen to achieve the phase separation and wettability. The phase separation is controlled by G_{coh}. But with larger G_{coh}, two main algorithm errors have different effects that spurious velocity is bigger and intermiscible density is smaller. A suitable value has to be chosen to balance the spurious velocity and intermiscible density. According to the literature from Mohamad et al. [119], G_{coh} is in different range with different fluids and we determined G_{coh} based on one of LBM PEFC work done by Chen et al. [45]. The G_{coh} must be re-evaluated from the spurious velocity and intermiscible density sides when applying different fluids. The different wettability (contact angles) can be simulated with adjusting $G_{\text{adh},1}$. It is similar with the determination of G_{coh} and is also related with fluid. Therefore, $G_{\text{adh},1}$ must be re-calculated for different fluids. When simulating water through the GDL with PTFE or without PTFE, two different specific $G_{\text{adh},1}$ are needed. As development of the GDL industry, GDL may be produced with other materials or other coating materials on the original GDL surface. Then the different $G_{\text{adh},1}$ can be chosen from Fig. 4.36 for different material wettability (material properties can be obtained from the textbooks).

For the water through the GDL, the dominated physical behaviors behind can be analyzed by checking the *Ca*. With the definition of *Ca* in Eq. (1.8), the flow velocity can be achieved with defining the velocity boundary condition, and the viscosity can be derived from the input relaxation time by Eq. (2.20). Within the present model, the surface tension σ_s can only be obtained from the single ideal droplet test. Therefore, for different fluids, the correlated σ_s must be re-calculated by the single ideal droplet test. For the GDL geometries, different styles of GDL (not limited to the Toray090 GDL carbon paper) can be applied and only the binary images of the structures are needed. The buffer space thickness and domain size effects should be discussed to check the influence from boundary conditions (inlet boundary and circumjacent boundary). The buffer space in simulations is to solve the conflict between velocity boundary condition and the bounce back condition of the first solid layer on the inlet side. The simulation results are independent of buffer space thickness. The buffer space thickness is suggested not too large to save computation time. For the domain size effects, a suitable domain size should be chosen to ensure some main flow phenomenon (e.g. water breakthrough location) can be observed. The domain size can be any big size but the CPU memories will be proportional to the domain size.

Then some preliminary work were done to discuss the capillary number, the geometry and the wettability effects. Different capillary numbers are achieved with different water inlet velocities. It is observed the capillary numbers affect the water flow in GDL. In the PEFC, the local water produced velocity is inhomogeneous and the local water flow behavior is different, and they can be one of reasons for inhomogeneous local current distribution. The water flow breakthrough the GDL and formed droplets on breakthrough locations. The droplets shapes and breakthrough locations are influenced by the geometry structures. With irregular GDL structures, the breakthrough location are randomly distributed on the simulated GDL domain and droplet shape are asymmetric from different sight camera directions. With the development of GDL manufacture, the GDL may be coated with another more hydrophobic material than PTFE to improve the wettability. The GDL wettability affect the water flow and the higher wettability (bigger contact angle) cause more breakthrough locations. Concerning the application to the PEFC, the higher wettability is helpful to generate more breakthrough locations and form droplets on the GDL/GC interface. Concerning the application of the simulation results, some stochastic created GDL structures are applied on the simulation. Because one geometry may not be representative but a series of geometries which are all stochastic equivalent. It can create results which can be relevant for material characteristics.

In the results, droplets are formed on the breakthrough locations after water flowing breakthrough the GDL. The breakthrough locations are randomly distributed on the GDL and droplet shape are irregular due to the stochastic GDL structures. Therefore, the contact angle and breakthrough locations can be analyzed statistically. For the asymmetric (irregular) droplet, the SPPF method is used to calculate the local apparent contact angle. The irregular droplets and random breakthrough locations are from the stochastic geometries. In the multi-scale simulation of PEFC, the output of LBM two-phase simulations in GDL can be the input of the cell-scale simulations in GC. Particularly, the apparent contact angle and breakthrough location distances are two main characteristics which can bridge the gap in multi-scale simulations of PEFC. The apparent contact angle is compared with the idealized case, they are in the similar range but the apparent contact angle is more accurate. Therefore, it can be proved the assumption of symmetric droplet shape is reasonable in the two-phase cell-scale simulations in GC. This dissertation gives the future GC two-phase cell-scale simulation a more realistic range of contact angle. The contact angle in cell-scale simulation can use a range value instead of a fixed idealized value.

It is similar with the apparent contact angle, the breakthrough location distance is another output which can bridge the gap in multi-scale simulations of PEFC. The breakthrough location distance are randomly distributed on the GDL geometries. Particularly, the shortest neighbor breakthrough point distance (SN-BPD) is more valuable than the specific breakthrough point distance (S-BPD). According to the definition of SN-BPD and S-BPD, SN-BPD is geometry size independent but the S-BPD is not. The SN-BPD distribution is analyzed by the Lilliefors test and it is proved that SN-BPD is distributed with normal distribution. This result is due to the irregular GDL structures and is consistent with the stochastic GDL model. Concerning the application of GDL, different styles of GDL can be used except carbon paper, such as carbon cloth. Therefore, the water through the carbon cloth can be simulated as well and the

SN-BPD can be the characterization of different porous media. Moreover, the breakthrough point distances on stochastic geometries have statistical variations because of the variation in the geometry data. In the future, the experiments of water invasion through GDL can be done and evaluate the SN-BPD from the experiment side. In one way, the experiments results may be compared with the results in this dissertation. In another way, the SN-BPD on different types of GDL can be a characterization of porous material property.

Finally, the PTFE effects on the water flowing through the GDL are discussed. Water flow is affected by the PTFE content (cover fraction) and its distribution (in-plane and through-plane). (i): For the PTFE content, the water flowing breakthrough GDL time is shorter with higher content PTFE. The total water saturation in GDL before flowing breakthrough the GDL is bigger with less PTFE content and have a higher flooding risk. Therefore, the fully covered PTFE style is encouraged to minimize the flooding risk in GDL concerning the application of PTFE. In no-fully covered PTFE cases, the distribution styles (mainly include in-plane, through-plane and whole GDL random distribution) have impact on the water flow. (ii): For the in-plane PTFE distribution, it is not preferred because it will cause fully flood in the specific no-PTFE region and water distribution in GDL is inhomogeneous which is not benefit for the chemical reaction. (iii): For the through-plane PTFE distribution, we discussed two styles including two-sections-through-plane, sandwich-through-plane and quasi-linear-through-plane PTFE distributions. In the two-sections-through-plane case, it is observed that the PTFE content on the GC side does not affect too much on the water flow behavior. So it is suggested to put more PTFE on the CL side than that on the GC side. In the actual manufacture process of GDL, more PTFE is distributed on external of GDL (outer style) and forms the sandwich-through-plane style. This style causes the higher flood risk in the center region of GDL. In comparison with the ideal aged GDL that PTFE is fully distributed in the center along the through-plane direction of GDL (inner style). When checking the water distribution in outer and inner PTFE styles in a snapshot time, water is distributed along the through-plane direction with the 'S' shape and the 'ד' shape in the outer and inner PTFE styles separately. Moreover, the GDLs of PTFE distribution along through-plane direction with quasi-linear functions (different gradient) are applied on simulation. The PTFE distribution with grad.5% has the highest flooding risk within four quasi-linear-through-plane cases. The local water saturation are similar under the different quasi-linear-through-plane styles (with different gradient of the quasi-linear functions). They are slightly different because of the different local PTFE distribution. Therefore, in the future work the dependence of PTFE distribution algorithm can be studied. In this dissertation, the PTFE effect on water flow behaviors are only studied in one GDL geometry and the results are analyzed in quantity. Due to the stochastic GDL structure, the PTFE effect on the water flowing through the GDL with different PTFE distribution can be analyzed from the statistical way. Several stochastic equivalent GDL geometries can be applied with the same PTFE distribution style and the results have chance to be analyzed statistically in quality.

9. Conclusion

According to the discussions above, it is seen the work in this thesis concentrate on the LB two-phase model development and model applications on the PEFC. Some main conclusions concerning the four achievements are summarized below:
Model development: In this work, the LB MRT-EDM ShanChen two-phase model is developed. Some conclusions concerning model development are below:

(i) The ShanChen two-phase model with MRT approach is more independent of fluid viscosity (relaxation time) than SRT approach. The finer grids can decrease the lattice errors.

(ii) The force schemes (SV scheme, Guo scheme and EDM scheme) can be implemented in the LB single-phase model and they are equivalent with the same accuracy. But the EDM scheme is more accurate and independent of fluid viscosity than SV scheme in the two-phase model.

(iii) The spurious velocity, the intermiscible density and the two-phase interface thickness are the error sources from the algorithm. The algorithm errors can be decreased with an optimum model parameter G_{coh}.

(iv) The density ratio and viscosity ratio between two phases are limited to 1. The present MRD-EDM ShanChen two-phase model is only valid on the capillary force dominated process (like water transport in GDL), which the density ratio and viscosity ratio can be negligible.

(v) The model can simulate different wettabilities (contact angles from 30° to 150°) by varying model parameter $G_{\mathrm{adh},1} (= -G_{\mathrm{adh},2})$. The SPPF method is valid to compare with the circle method for the symmetric droplet. The contact angle on PTFE material $\theta_{\mathrm{PTFE}} = 110^\circ$ with $G_{\mathrm{adh},1} = -0.005$ and the contact angle on carbon material $\theta_{\mathrm{carbon}} = 90^\circ$ with $G_{\mathrm{adh},1} = 0$.

Effects of water flowing through GDL: The developed LB-MRT-EDM ShanChen two-phase model is applied on simulating the water flowing through GDL with fully covered with PTFE ($\theta_{\mathrm{PTFE}} \approx 110^\circ$). Some fundamental effects are studied and get some main conclusions:

(i) Buffer space thickness effect. The buffer space with thickness 10 l.u. is applied on simulations to balance the accuracy and computation consumption.

(ii) Domain size effect. Flow behaviors are affected by domain sizes. The simulation domain size is necessary to be larger than 300 l.u. × 300 l.u to catch the main output information (such as apparent contact angle and breakthrough point distance).

(iii) Capillary number effect. The bigger capillary number leads the more breakthrough points.

(iv) Geometry effect. The water flow are affected by different stochastic GDL geometries. When water flowing breakthrough the GDL, droplets are randomly formed on the GDL surface.

(v) Wettability effect. The more hydrophobic GDL lead the more breakthrough points and shorter breakthrough time.

Statistical analysis of results: After water flowing breakthrough the GDL, the contact angles of the formed droplets on GDL and the breakthrough point distances are analyzed statistically. Some conclusions are below:

(i) The water flowing through GDL is a capillary force dominated process which the density ratio and viscosity ratio between water and air can be negligible and equal to one.

(ii) When water flowing breakthrough the GDL, droplets are formed randomly in different positions.

(iii) Formed droplets on the GDL surface are irregular and asymmetric because of irregular GDL structures. The local apparent contact angles are analyzed by SPPF method from different view directions.

(iv) The local apparent contact angles can be one of input parameters in the cell-scale two-phase flow simulations in GC. The apparent contact angle can bridge the gap in the multi-scale simulations of PEFC.

(v) In comparison with the idealized contact angle, the local apparent contact angle is more accurate but both contact angles are in the same order of magnitude.

(vi) The shortest neighbor breakthrough point distance (SN-BPD) follow the normal distribution according to the Lilliefors test. It is independent of domain size and more useful than S-BPD for the cell-scale two-phase simulations in GC. The information of SN-BPD bridges the gap in the multi-scale simulations of PEFC.

PTFE effect: The GDL with different PTFE distributions are applied on simulations with two material properties $\theta_{\text{PTFE}} = 110^\circ$ and $\theta_{\text{carbon}} = 90^\circ$. Some main conclusions are below:

(i) The PTFE cover fraction and weight fraction can be converted with a simplified model.

(ii) The water flows prefer the hydrophilic (no-PTFE) regions inside of GDL. The water flows with the 'finger' style in the fully PTFE region and the 'surface' style in the completely no-PTFE region.

(iii) More PTFE cause more breakthrough points and shorter breakthrough time.

(iv) Distribute more PTFE on the inlet region can decrease the flood risk in the PEFC.

(v) The water are distributed with the 'S' shape on the PTFE to no-PTFE transition layer, while the 'ד' shape on the no-PTFE to PTFE transition layer inside of GDL.

(vi) The gradient of quasi-linear-through-plane PTFE distribution have small effect on the water flow through the GDL.

In a summary, the following highlights are main contribution to the PEFC development.

- A LB ShanChen MRT-EDM two-phase model is developed to simulate water flowing through the stochastic GDL geometries.
- The statistical information of droplet apparent contact angle and water breakthrough point distance can bridge the gap in multi-scale simulations of PEFC
- The effects of PTFE with different content and distribution styles on the water through GDL are analyzed in quality.

Bibliography

[1] Srinivasan, Supramaniam: *Fuel cells: from fundamentals to applications*. Springer Science & Business media, 2006 (208–212)

[2] Kirubakaran, A ; Jain, Shailendra ; Nema, RK: A review on fuel cell technologies and power electronic interface. In: *Renewable Sustainable Energy Rev.* 13 (2009), Nr. 9, 2430–2440

[3] Wang, Yun ; Chen, Ken S. ; Mishler, Jeffrey ; Cho, Sung C. ; Adroher, Xavier C.: A review of polymer electrolyte membrane fuel cells: technology, applications, and needs on fundamental research. In: *Appl. Energy* 88 (2011), Nr. 4, 981–1007

[4] Arvay, A ; Yli-Rantala, E ; Liu, C-H ; Peng, X-H ; Koski, P ; Cindrella, L ; Kauranen, P ; Wilde, PM ; Kannan, AM: Characterization techniques for gas diffusion layers for proton exchange membrane fuel cells–A review. In: *J. Power Sources* 213 (2012), 317–337

[5] PLASTECH: www.plastechcoatings.com. (12/03/2018)

[6] TEST, ACCU D.: www.accudynetest.com. (10/04/2017)

[7] Energy, EERE. U.S. D.: http://www1.eere.energy.gov/hydrogenandfuelcells/mypp/. (March 2017)

[8] O'Hayre, Ryan ; Cha, Suk-Won ; Prinz, Fritz B. ; Colella, Whitney: *Fuel cell fundamentals*. John Wiley & Sons, 2016

[9] Papageorgopoulos, D: An Introduction to the 2010 Fuel Cell Pre-Solicitation Workshop in DOE fuel cell pre-solicitation workshop. In: *http://www.eere.energy.gov/hydrogenandfuelcells* (10/03/2010)

[10] Owejan, Jon P. ; Owejan, Jeanette E. ; Gu, Wenbin: Impact of platinum loading and catalyst layer structure on PEMFC performance. In: *J. Electrochem. Soc.* 160 (2013), Nr. 8, F824–F833

[11] Chen, Li ; Feng, Yong-Liang ; Song, Chen-Xi ; Chen, Lei ; He, Ya-Ling ; Tao, Wen-Quan: Multi-scale modeling of proton exchange membrane fuel cell by coupling finite volume method and lattice Boltzmann method. In: *International Journal of Heat and Mass Transfer* 63 (2013), 268–283

[12] Baschuk, JJ ; Li, Xianguo: Carbon monoxide poisoning of proton exchange membrane fuel cells. In: *Int. J. Energy Res.* 25 (2001), Nr. 8, 695–713

[13] Bhattacharya, PK: Water flooding in the proton exchange membrane fuel cell / Department of Chemical Engineering, IIT Kanpur. Directions, 2015. – Technical report

[14] Paulino, André LR ; Robalinho, Eric ; Cunha, Edgar F. ; Passos, Raimundo R. ; Santiago, Elisabete I. ; others: Current Distribution on PEM Fuel Cells with Different Flow Channel Patterns. In: *Proceedings of the 2013 COMSOL Conference*, 2013, 1–5

[15] Zhang, Guobin ; Jiao, Kui: Multi-phase models for water and thermal management of proton exchange membrane fuel cell: A review. In: *Journal of Power Sources* 391 (2018), 120–133

[16] Li, Hui ; Tang, Yanghua ; Wang, Zhenwei ; Shi, Zheng ; Wu, Shaohong ; Song, Datong ; Zhang, Jianlu ; Fatih, Khalid ; Zhang, Jiujun ; Wang, Haijiang ; others: A review of water flooding issues in the proton exchange membrane fuel cell. In: *J. Power Sources* 178 (2008), Nr. 1, 103–117

[17] Pasaogullari, Ugur ; Wang, CY: Liquid water transport in gas diffusion layer of polymer electrolyte fuel cells. In: *J. Electrochem. Soc.* 151 (2004), Nr. 3, A399–A406

[18] Lucia, Umberto: Overview on fuel cells. In: *Renewable Sustainable Energy Rev.* 30 (2014), 164–169

[19] Han, M ; Xu, JH ; Chan, SH ; Jiang, San P.: Characterization of gas diffusion layers for PEMFC. In: *Electrochim. Acta* 53 (2008), Nr. 16, 5361–5367

[20] Brinkmann, Jan P.: *Lattice-Boltzmann-Simulation in faserbasierten Mikrostrukturen*, RWTH Aachen University, Diss., 2014

[21] Ding, Y ; Bi, HT ; Wilkinson, DP: Three dimensional numerical simulation of gas–liquid two-phase flow patterns in a polymer–electrolyte membrane fuel cells gas flow channel. In: *J. Power Sources* 196 (2011), Nr. 15, 6284–6292

[22] Chen, Shiyi ; Doolen, Gary D.: Lattice Boltzmann method for fluid flows. In: *Annu. Rev. Fluid Mech.* 30 (1998), Nr. 1, 329–364

[23] Li, Qing ; Luo, KH ; Kang, QJ ; He, YL ; Chen, Q ; Liu, Q: Lattice Boltzmann methods for multiphase flow and phase-change heat transfer. In: *Prog. Energy Combust. Sci.* 52 (2016), 62–105

[24] Barbir, Frano: PEM fuel cells. In: *Fuel Cell Technology*. Springer, 2006, 27–51

[25] Cengel, Yunus A. ; others: *Introduction to thermodynamics and heat transfer*. McGraw-Hill New York, 1997

[26] H., Lienhard IV J. ; H., Lienhard V J.: *A Heat Transfer Textbook, 4th edition*. Phlogiston Press, 2017

[27] Lide, DR: *CRC handbook of chemistry and physics: a ready-reference book of chemical and physics data*. CRC Press, 2002

[28] Dixon, John C.: *The Shock Absorber Handbook: Appendix B: Properties of Air*. Wiley Online Library, 2013. – 375–378

[29] Mukherjee, Partha P. ; Wang, Chao-Yang ; Kang, Qinjun: Mesoscopic modeling of two-phase behavior and flooding phenomena in polymer electrolyte fuel cells. In: *Electrochim. Acta* 54 (2009), Nr. 27, 6861–6875

[30] Liley, Peter E. ; Buck, Evan ; Ch, M S E.: *Physical and Chemical Data* . Springer, 1999. – 2–86

[31] Nam, Jin H. ; Lee, Kyu-Jin ; Hwang, Gi-Suk ; Kim, Charn-Jung ; Kaviany, Massoud: Microporous layer for water morphology control in PEMFC. In: *Int. J. Heat Mass Transfer* 52 (2009), Nr. 11, 2779–2791

[32] Thiedmann, Ralf ; Fleischer, Frank ; Hartnig, Christoph ; Lehnert, Werner ; Schmidt, Volker: Stochastic 3D modeling of the GDL structure in PEMFCs based on thin section detection. In: *J. Electrochem. Soc.* 155 (2008), Nr. 4, B391–B399

[33] Lenormand, Roland ; Touboul, Eric ; Zarcone, Cesar: Numerical models and experiments on immiscible displacements in porous media. In: *J. Fluid Mech.* 189 (1988), 165–187

[34] Ewing, Robert P. ; Berkowitz, Brian: Stochastic pore-scale growth models of DNAPL migration in porous media. In: *Adv. Water Resour.* 24 (2001), Nr. 3, 309–323

[35] Weber, Adam Z. ; Borup, Rodney L. ; Darling, Robert M. ; Das, Prodip K. ; Dursch, Thomas J. ; Gu, Wenbin ; Harvey, David ; Kusoglu, Ahmet ; Litster, Shawn ; Mench, Matthew M. ; others: A critical review of modeling transport phenomena in polymer-electrolyte fuel cells. In: *Journal of The Electrochemical Society* 161 (2014), Nr. 12, F1254–F1299

[36] Park, Jaeman ; Oh, Hwanyeong ; Ha, Taehun ; Lee, Yoo I. ; Min, Kyoungdoug: A review of the gas diffusion layer in proton exchange membrane fuel cells: durability and degradation. In: *Appl. Energy* 155 (2015), 866–880

[37] Park, Sehkyu ; Lee, Jong-Won ; Popov, Branko N.: A review of gas diffusion layer in PEM fuel cells: materials and designs. In: *Int. J. Hydrogen Energy* 37 (2012), Nr. 7, 5850–5865

[38] Bazylak, A: Liquid water visualization in PEM fuel cells: A review. In: *Int. J. Hydrogen Energy* 34 (2009), Nr. 9, 3845–3857

[39] Anderson, Ryan ; Zhang, Lifeng ; Ding, Yulong ; Blanco, Mauricio ; Bi, Xiaotao ; Wilkinson, David P.: A critical review of two-phase flow in gas flow channels of proton exchange membrane fuel cells. In: *J. Power Sources* 195 (2010), Nr. 15, 4531–4553

[40] Andersson, Martin ; Beale, SB ; Espinoza, M ; Wu, Z ; Lehnert, W: A review of cell-scale multiphase flow modeling, including water management, in polymer electrolyte fuel cells. In: *Appl. Energy* 180 (2016), 757–778

[41] Chen, Li ; Kang, Qinjun ; Mu, Yutong ; He, Ya-Ling ; Tao, Wen-Quan: A critical review of the pseudopotential multiphase lattice Boltzmann model: Methods and applications. In: *Int. J. Heat Mass Transfer* 76 (2014), 210–236

[42] Wood, David L. ; Rulison, Christopher ; Borup, Rodney L.: Surface properties of PEMFC gas diffusion layers. In: *J. Electrochem. Soc.* 157 (2010), Nr. 2, B195–B206

[43] Park, J ; Li, X: Multi-phase micro-scale flow simulation in the electrodes of a PEM fuel cell by lattice Boltzmann method. In: *J. Power Sources* 178 (2008), Nr. 1, 248–257

[44] Park, J ; Matsubara, M ; Li, X: Application of lattice Boltzmann method to a micro-scale flow simulation in the porous electrode of a PEM fuel cell. In: *J. Power Sources* 173 (2007), Nr. 1, 404–414

[45] Chen, Li ; Luan, Hui-Bao ; He, Ya-Ling ; Tao, Wen-Quan: Numerical investigation of liquid water transport and distribution in porous gas diffusion layer of a proton exchange membrane fuel cell using lattice Boltzmann method. In: *Russ. J. Electrochem.* 48 (2012), Nr. 7, 712–726

[46] Chen, Li ; Luan, Hui-Bao ; He, Ya-Ling ; Tao, Wen-Quan: Pore-scale flow and mass transport in gas diffusion layer of proton exchange membrane fuel cell with interdigitated flow fields. In: *Int. J. Therm. Sci.* 51 (2012), 132–144

[47] Niu, Xiaodong ; Munekata, Toshihisa ; Hyodo, Shi-Aki ; Suga, Kazuhiko: An investigation of water-gas transport processes in the gas-diffusion-layer of a PEM fuel cell by a multiphase multiple-relaxation-time lattice Boltzmann model. In: *J. Power Sources* 172 (2007), Nr. 2, 542–552

[48] Zhou, P ; Wu, CW: Liquid water transport mechanism in the gas diffusion layer. In: *J. Power Sources* 195 (2010), Nr. 5, 1408–1415

[49] Kim, Kwang N. ; Kang, Jung H. ; Lee, Sang G. ; Nam, Jin H. ; Kim, Charn-Jung: Lattice Boltzmann simulation of liquid water transport in microporous and gas diffusion layers of polymer electrolyte membrane fuel cells. In: *J. Power Sources* 278 (2015), 703–717

[50] Molaeimanesh, GR ; Akbari, MH: A three-dimensional pore-scale model of the cathode electrode in polymer-electrolyte membrane fuel cell by lattice Boltzmann method. In: *J. Power Sources* 258 (2014), 89–97

[51] Hao, Liang ; Cheng, Ping: Lattice Boltzmann simulations of water transport in gas diffusion layer of a polymer electrolyte membrane fuel cell. In: *J. Power Sources* 195 (2010), Nr. 12, 3870–3881

[52] Hao, Liang ; Cheng, Ping: Lattice Boltzmann simulations of liquid droplet dynamic behavior on a hydrophobic surface of a gas flow channel. In: *J. Power Sources* 190 (2009), Nr. 2, 435–446

[53] Tabe, Yutaka ; Lee, Yongju ; Chikahisa, Takemi ; Kozakai, Masaya: Numerical simulation of liquid water and gas flow in a channel and a simplified gas diffusion layer model of polymer electrolyte membrane fuel cells using the lattice Boltzmann method. In: *J. Power Sources* 193 (2009), Nr. 1, 24–31

[54] Koido, Tetsuya ; Furusawa, Toru ; Moriyama, Koji: An approach to modeling two-phase transport in the gas diffusion layer of a proton exchange membrane fuel cell. In: *J. Power Sources* 175 (2008), Nr. 1, 127–136

[55] Gao, Yuan ; Zhang, Xiaoxian ; Rama, Pratp ; Chen, Rui ; Ostadi, Hossein ; Jiang, Kyle: Lattice Boltzmann simulation of water and gas flow in porous gas diffusion layers in fuel cells reconstructed from micro-tomography. In: *Computers & Mathematics with Applications* 65 (2012), Nr. 6, 891–900

[56] Jeon, Dong H. ; Kim, Hansang: Effect of compression on water transport in gas diffusion layer of polymer electrolyte membrane fuel cell using lattice Boltzmann method. In: *J. Power Sources* 294 (2015), 393–405

[57] Han, Bo ; Meng, Hua: Numerical studies of interfacial phenomena in liquid water transport in polymer electrolyte membrane fuel cells using the lattice Boltzmann method. In: *Int. J. Hydrogen Energy* 38 (2013), Nr. 12, 5053–5059

[58] Molaeimanesh, Golamreza ; Akbari, Mohammad H.: Water droplet dynamic behavior during removal from a proton exchange membrane fuel cell gas diffusion layer by Lattice-Boltzmann method. In: *Korean J. Chem. Eng.* 31 (2014), Nr. 4, 598–610

[59] Molaeimanesh, GR ; Akbari, MH: Impact of PTFE distribution on the removal of liquid water from a PEMFC electrode by lattice Boltzmann method. In: *Int. J. Hydrogen Energy* 39 (2014), Nr. 16, 8401–8409

[60] Gaiselmann, Gerd ; Thiedmann, Ralf ; Manke, Ingo ; Lehnert, Werner ; Schmidt, Volker: Stochastic 3D modeling of fiber-based materials. In: *Computational Materials Science* 59 (2012), 75–86

[61] Gaiselmann, Gerd ; Froning, Dieter ; Tötzke, Christian ; Quick, Christian ; Manke, Ingo ; Lehnert, Werner ; Schmidt, Volker: Stochastic 3D modeling of non-woven materials with wet-proofing agent. In: *Int. J. Hydrogen Energy* 38 (2013), Nr. 20, 8448–8460

[62] Brinkmann, Jan P. ; Froning, Dieter ; Reimer, Uwe ; Schmidt, Volker ; Lehnert, Werner ; Stolten, Detlef: 3D modeling of one and two component gas flow in fibrous microstructures in fuel cells by using the Lattice-Boltzmann method. In: *ECS Trans.* 50 (2013), Nr. 2, 207–219

[63] Froning, Dieter ; Yu, Junliang ; Gaiselmann, Gerd ; Reimer, Uwe ; Manke, Ingo ; Schmidt, Volker ; Lehnert, Werner: Impact of compression on gas transport in non-woven gas diffusion layers of high temperature polymer electrolyte fuel cells. In: *J. Power Sources* 318 (2016), 26–34

[64] Froning, Dieter ; Gaiselmann, Gerd ; Reimer, Uwe ; Brinkmann, Jan ; Schmidt, Volker ; Lehnert, Werner ; others: Stochastic aspects of mass transport in gas diffusion layers. In: *Transp. Porous Media* 103 (2014), Nr. 3, 469–495

[65] Froning, Dieter ; Brinkmann, Jan ; Reimer, Uwe ; Schmidt, Volker ; Lehnert, Werner ; Stolten, Detlef: 3D analysis, modeling and simulation of transport processes in compressed fibrous microstructures, using the Lattice Boltzmann method. In: *Electrochim. Acta* 110 (2013), 325–334

[66] Zamel, Nada ; Li, Xianguo ; Becker, Jürgen ; Wiegmann, Andreas: Effect of liquid water on transport properties of the gas diffusion layer of polymer electrolyte membrane fuel cells. In: *International Journal of Hydrogen Energy* 36 (2011), Nr. 9, 5466–5478

[67] Hyman, Jeffrey D. ; Smolarkiewicz, Piotr K. ; Winter, C L.: Heterogeneities of flow in stochastically generated porous media. In: *Physical Review E* 86 (2012), Nr. 5, 056701

[68] Satjaritanun, P ; Weidner, JW ; Hirano, S ; Lu, Z ; Khunatorn, Y ; Ogawa, S ; Litster, SE ; Shum, AD ; Zenyuk, IV ; Shimpalee, S: Micro-Scale Analysis of Liquid Water Breakthrough inside Gas Diffusion Layer for PEMFC Using X-ray Computed Tomography and Lattice Boltzmann Method. In: *J. Electrochem. Soc.* 164 (2017), Nr. 11, E3359–E3371

[69] García-Salaberri, Pablo A. ; Hwang, Gisuk ; Vera, Marcos ; Weber, Adam Z. ; Gostick, Jeff T.: Effective diffusivity in partially-saturated carbon-fiber gas diffusion layers: Effect of through-plane saturation distribution. In: *Int. J. Heat Mass Transfer* 86 (2015), 319–333

[70] Qin, CZ: *Numerical investigations on two-phase flow in polymer electrolyte fuel cells*, Utrecht University, Diss., 2012

[71] Zhu, Xun ; Sui, PC ; Djilali, Ned: Three-dimensional numerical simulations of water droplet dynamics in a PEMFC gas channel. In: *J. Power Sources* 181 (2008), Nr. 1, 101–115

[72] Polverino, Pierpaolo ; Esposito, Angelo ; Pianese, Cesare: Experimental validation of a lumped model of single droplet deformation, oscillation and detachment on the GDL surface of a PEM fuel cell. In: *Int. J. Hydrogen Energy* 38 (2013), Nr. 21, 8934–8953

[73] Bazylak, Aimy ; Sinton, David ; Djilali, Ned: Dynamic water transport and droplet emergence in PEMFC gas diffusion layers. In: *J. Power Sources* 176 (2008), Nr. 1, 240–246

[74] Markötter, H ; Manke, I ; Krüger, Ph ; Arlt, T ; Haussmann, J ; Klages, M ; Riesemeier, Heinrich ; Hartnig, Ch ; Scholta, J ; Banhart, J: Investigation of 3D water transport paths in gas diffusion layers by combined in-situ synchrotron X-ray radiography and tomography. In: *Electrochem. Commun.* 13 (2011), Nr. 9, 1001–1004

[75] Bazylak, A ; Sinton, D ; Liu, Z-S ; Djilali, N: Effect of compression on liquid water transport and microstructure of PEMFC gas diffusion layers. In: *J. Power Sources* 163 (2007), Nr. 2, 784–792

[76] Litster, S ; Sinton, D ; Djilali, N: Ex situ visualization of liquid water transport in PEM fuel cell gas diffusion layers. In: *J. Power Sources* 154 (2006), Nr. 1, 95–105

[77] Benziger, Jay ; Nehlsen, James ; Blackwell, David ; Brennan, Tom ; Itescu, Johannah: Water flow in the gas diffusion layer of PEM fuel cells. In: *J. Membr. Sci.* 261 (2005), Nr. 1, 98–106

[78] Santamaria, Anthony D. ; Das, Prodip K. ; MacDonald, James C. ; Weber, Adam Z.: Liquid-water interactions with gas-diffusion-layer surfaces. In: *J. Electrochem. Soc.* 161 (2014), Nr. 12, F1184–F1193

[79] Lamibrac, A ; Roth, J ; Toulec, M ; Marone, F ; Stampanoni, M ; Büchi, FN: Characterization of liquid water saturation in gas diffusion layers by X-ray tomographic microscopy. In: *J. Electrochem. Soc.* 163 (2016), Nr. 3, F202–F209

[80] Eberhardt, SH ; Marone, F ; Stampanoni, M ; Büchi, FN ; Schmidt, TJ: Operando X-ray Tomographic Microscopy Imaging of HT-PEFC: A Comparative Study of Phosphoric Acid Electrolyte Migration. In: *J. Electrochem. Soc.* 163 (2016), Nr. 8, F842–F847

[81] Zenyuk, Iryna V. ; Lamibrac, Adrien ; Eller, Jens ; Parkinson, Dilworth Y. ; Marone, Federica ; Büchi, Felix N. ; Weber, Adam Z.: Investigating evaporation in gas diffusion layers for fuel cells with x-ray computed tomography. In: *The Journal of Physical Chemistry C* 120 (2016), Nr. 50, 28701–28711

[82] Deevanhxay, Phengxay ; Sasabe, Takashi ; Tsushima, Shohji ; Hirai, Shuichiro: Observation of dynamic liquid water transport in the microporous layer and gas diffusion layer of an operating PEM fuel cell by high-resolution soft X-ray radiography. In: *J. Power Sources* 230 (2013), 38–43

[83] Shahraeeni, Mehdi: *Study of fluid flow in the porous media of gas diffusion layers in proton exchange membrane fuel cells*, University of British Columbia, Diss., 2013

[84] Kitahara, Tatsumi ; Nakajima, Hironori ; Mori, Kyohei: Hydrophilic and hydrophobic double microporous layer coated gas diffusion layer for enhancing performance of polymer electrolyte fuel cells under no-humidification at the cathode. In: *J. Power Sources* 199 (2012), 29–36

[85] Gao, Bin ; Steenhuis, Tammo S. ; Zevi, Yunati ; Parlange, J-Yves ; Carter, Robert N. ; Trabold, Thomas A.: Visualization of unstable water flow in a fuel cell gas diffusion layer. In: *J. Power Sources* 190 (2009), Nr. 2, 493–498

[86] Fu, Richard S. ; Pasaogullari, Ugur ; Shiomi, Takeshi ; Tabuchi, Yuichiro ; Hussey, Daniel S. ; Jacobson, David L.: High-resolution neutron radiography of through-plane liquid water distribution in polymer electrolyte membrane and gas diffusion layer. In: *J. Electrochem. Soc.* 159 (2012), Nr. 9, F545–F553

[87] Sabharwal, Mayank ; Gostick, Jeff T. ; Secanell, Marc: Virtual Liquid Water Intrusion in Fuel Cell Gas Diffusion Media. In: *Journal of The Electrochemical Society* 165 (2018), Nr. 7, F553–F563

[88] Mendoza, AJ ; Hickner, MA ; Morgan, J ; Rutter, K ; Legzdins, C: Raman spectroscopic mapping of the carbon and PTFE distribution in gas diffusion layers. In: *Fuel Cells* 11 (2011), Nr. 2, 248–254

[89] Song, Wei ; Yu, Hongmei ; Shao, Zhigang ; Yi, Baolian ; Lin, Jin ; Liu, Na: Effect of polytetrafluoroethylene distribution in the gas diffusion layer on water flooding in proton exchange membrane fuel cells. In: *Chin. J. Catal.* 35 (2014), Nr. 4, 468–473

[90] Rofaiel, A ; Ellis, JS ; Challa, PR ; Bazylak, A: Heterogeneous through-plane distributions of polytetrafluoroethylene in polymer electrolyte membrane fuel cell gas diffusion layers. In: *J. Power Sources* 201 (2012), 219–225

[91] Reshetenko, Tatyana V. ; St-Pierre, Jean ; Artyushkova, Kateryna ; Rocheleau, Richard ; Atanassov, Plamen ; Bender, Guido ; Ulsh, Michael: Multianalytical study of the PTFE content local variation of the PEMFC gas diffusion layer. In: *J. Electrochem. Soc.* 160 (2013), Nr. 11, F1305–F1315

[92] Tötzke, C ; Gaiselmann, G ; Osenberg, M ; Arlt, T ; Markötter, H ; Hilger, A ; Kupsch, Andreas ; Müller, Bernd R. ; Schmidt, V ; Lehnert, W ; others: Influence of hydrophobic treatment on the structure of compressed gas diffusion layers. In: *J. Power Sources* 324 (2016), 625–636

[93] Mortazavi, Mehdi ; Tajiri, Kazuya: Effect of the PTFE content in the gas diffusion layer on water transport in polymer electrolyte fuel cells (PEFCs). In: *J. Power Sources* 245 (2014), 236–244

[94] Antolini, E ; Pozio, A ; Giorgi, L ; Passalacqua, E: Morphological characteristics of carbon/polytetrafluoroethylene films deposited on porous carbon support. In: *J. Mater. Sci.* 33 (1998), Nr. 7, 1837–1843

[95] Friess, BR ; Hoorfar, M: Measurement of average contact angles of gas diffusion layers using a novel fluorescence microscopy method. In: *J. Fuel Cell Sci. Technol.* 8 (2011), Nr. 2, 021006

[96] Kozbial, Andrew ; Zhou, Feng ; Li, Zhiting ; Liu, Haitao ; Li, Lei: Are graphitic surfaces hydrophobic? In: *Acc. Chem. Res.* 49 (2016), Nr. 12, 2765–2773

[97] Pike, Carolyn M. ; Grabner, Chad P. ; Harkins, Amy B.: Fabrication of amperometric electrodes. In: *J. of Visualized Experiments* (2009), Nr. 27, e1040–e1040

[98] Taherian, Fereshte ; Marcon, Valentina ; Vegt, Nico F. d. ; Leroy, Frederic: What is the contact angle of water on graphene? In: *Langmuir* 29 (2013), Nr. 5, 1457–1465

[99] Wang, Shiren ; Zhang, Yue ; Abidi, Noureddine ; Cabrales, Luis: Wettability and surface free energy of graphene films. In: *Langmuir* 25 (2009), Nr. 18, 11078–11081

[100] Rafiee, Javad ; Mi, Xi ; Gullapalli, Hemtej ; Thomas, Abhay V. ; Yavari, Fazel ; Shi, Yunfeng ; Ajayan, Pulickel M. ; Koratkar, Nikhil A.: Wetting transparency of graphene. In: *Nat. Mater.* 11 (2012), Nr. 3, 217–222

[101] Luo, L.-S.: *Lattice-Gas Automata and Lattice Boltzmann Equations for Two-Dimensional Hydrodynamics*, Georgia Institute of Technology, Diss., 1993

[102] Ziegler, Donald P.: Boundary conditions for lattice Boltzmann simulations. In: *J. Stat. Phys.* 71 (1993), Nr. 5, 1171–1177

[103] Molaeimanesh, GR ; Googarchin, H S. ; Moqaddam, A Q.: Lattice Boltzmann simulation of proton exchange membrane fuel cells–A review on opportunities and challenges. In: *Int. J. Hydrogen Energy* 41 (2016), Nr. 47, 22221–22245

[104] Chen, Shiyi ; Wang, Zheng ; Shan, Xiaowen ; Doolen, Gary D.: Lattice Boltzmann computational fluid dynamics in three dimensions. In: *J. Stat. Phys.* 68 (1992), Nr. 3, 379–400

[105] Pennycuick, Colin J.: *Newton rules biology*. Oxford University Press, 1992

[106] Ablitt, Justin: Technical Guides–Speed of Sound in Pure Water / National Physical Laboratory, Teddington, UK. 2000. – Technical report

[107] Succi, Sauro: *The lattice Boltzmann equation: for fluid dynamics and beyond*. Oxford university press, 2001 (11–13)

[108] Tsien, Hsue S.: *Problems in motion of compressible fluids and reaction propulsion*, California Institute of Technology, Diss., 1939

[109] Rothman, Daniel H. ; Keller, Jeffrey M.: Immiscible cellular-automaton fluids. In: *J. Stat. Phys.* 52 (1988), Nr. 3-4, 1119–1127

[110] Shan, Xiaowen ; Chen, Hudong: Lattice Boltzmann model for simulating flows with multiple phases and components. In: *Physical Review E* 47 (1993), Nr. 3, 1815

[111] Swift, Michael R. ; Orlandini, E ; Osborn, WR ; Yeomans, JM: Lattice Boltzmann simulations of liquid-gas and binary fluid systems. In: *Physical Review E* 54 (1996), Nr. 5, 5041

[112] He, Xiaoyi ; Chen, Shiyi ; Zhang, Raoyang: A lattice Boltzmann scheme for incompressible multiphase flow and its application in simulation of Rayleigh–Taylor instability. In: *J. Comput. Phys.* 152 (1999), Nr. 2, 642–663

[113] Huang, Haibo ; Sukop, Michael ; Lu, Xiyun: *Multiphase lattice Boltzmann methods: Theory and application*. John Wiley & Sons, 2015 (7–8)

[114] Guo Zhaoli, Zheng C.: *Theory and Application of Lattice Boltzmann Method (In Chinese)*. Science Publisher, 2009

[115] Frisch, Uriel ; Hasslacher, Brosl ; Pomeau, Yves: Lattice-gas automata for the Navier-Stokes equation. In: *Phys. Rev. Lett.* 56 (1986), Nr. 14, 1505

[116] Qian, YH ; d'Humières, Dominique ; Lallemand, Pierre: Lattice BGK models for Navier-Stokes equation. In: *EPL (Europhysics Letters)* 17 (1992), Nr. 6, 479

[117] Wolf-Gladrow, Dieter A.: *Lattice-gas cellular automata and lattice Boltzmann models: an introduction*. Springer, 2004

[118] Sukop, Michael C. ; Thorne, DT: *Lattice Boltzmann modeling. An introduction for geoscientists and engineers.* Springer, 2007

[119] Mohamad, Abdulmajeed A.: *Lattice Boltzmann method: fundamentals and engineering applications with computer codes*. Springer Science & Business Media, 2011

[120] Shan, Xiaowen ; Chen, Hudong: Lattice Boltzmann model for simulating flows with multiple phases and components. In: *Physical Review E* 47 (1993), Nr. 3, 1815

[121] d'Humières, Dominique: Multiple–relaxation–time lattice Boltzmann models in three dimensions. In: *Philosophical Transactions of the Royal Society of London A: Mathematical, Physical and Engineering Sciences* 360 (2002), Nr. 1792, 437–451

[122] He, Xiaoyi ; Luo, Li-Shi: Theory of the lattice Boltzmann method: From the Boltzmann equation to the lattice Boltzmann equation. In: *Physical Review E* 56 (1997), Nr. 6, 6811

[123] Martys, Nicos S. ; Chen, Hudong: Simulation of multicomponent fluids in complex three-dimensional geometries by the lattice Boltzmann method. In: *Physical Review E* 53 (1996), Nr. 1, 743

[124] Shan, Xiaowen ; Chen, Hudong: Simulation of nonideal gases and liquid-gas phase transitions by the lattice Boltzmann equation. In: *Physical Review E* 49 (1994), Nr. 4, 2941

[125] He, Xiaoyi ; Doolen, Gary D.: Thermodynamic foundations of kinetic theory and lattice Boltzmann models for multiphase flows. In: *J. Stat. Phys.* 107 (2002), Nr. 1, 309–328

[126] Pan, C ; Hilpert, M ; Miller, Cass T.: Lattice-Boltzmann simulation of two-phase flow in porous media. In: *Water Resour. Res.* 40 (2004), Nr. 1

[127] Yuan, Peng ; Schaefer, Laura: Equations of state in a lattice Boltzmann model. In: *Phys. Fluids* 18 (2006), Nr. 4, 42101

[128] Shan, Xiaowen ; Doolen, Gary: Diffusion in a multicomponent lattice Boltzmann equation model. In: *Physical Review E* 54 (1996), Nr. 4, 3614

[129] Huang, Haibo ; Thorne Jr, Daniel T. ; Schaap, Marcel G. ; Sukop, Michael C.: Proposed approximation for contact angles in Shan-and-Chen-type multicomponent multiphase lattice Boltzmann models. In: *Physical Review E* 76 (2007), Nr. 6, 066701

[130] Hirt, Christian ; Claessens, Sten ; Fecher, Thomas ; Kuhn, Michael ; Pail, Roland ; Rexer, Moritz: New ultrahigh-resolution picture of Earth's gravity field. In: *Geophys. Res. Lett.* 40 (2013), Nr. 16, 4279–4283

[131] Lallemand, Pierre ; Luo, Li-Shi: Theory of the lattice Boltzmann Method: Dispersion, Dissipation, Isotropy, Galilean Invariance, and Stability. In: *Physical Review E* 61 (2000), Nr. 6, 6546–6562

[132] Higuera, FJ ; Succi, S ; Benzi, R: Lattice gas dynamics with enhanced collisions. In: *EPL (Europhysics Letters)* 9 (1989), Nr. 4, 345

[133] d'Humieres, Dominique: Generalized lattice-Boltzmann equations. In: *Progress in Astronautics and Aeronautics* 159 (1994), 450–450

[134] McCracken, Michael E. ; Abraham, John: Multiple-relaxation-time lattice-Boltzmann model for multiphase flow. In: *Physical Review E* 71 (2005), Nr. 3, 036701

[135] Yu, Zhao ; Fan, Liang-Shih: Multirelaxation-time interaction-potential-based lattice Boltzmann model for two-phase flow. In: *Physical Review E* 82 (2010), Nr. 4, 046708

[136] Succi, Sauro: Lattice boltzmann 2038. In: *EPL (Europhysics Letters)* 109 (2015), Nr. 5, 50001

[137] Guo, Zhaoli ; Zheng, Chuguang ; Shi, Baochang: Discrete lattice effects on the forcing term in the lattice Boltzmann method. In: *Physical Review E* 65 (2002), Nr. 4, 046308

[138] Kupershtokh, AL ; Medvedev, DA ; Karpov, DI: On equations of state in a lattice Boltzmann method. In: *Computers & Mathematics with Applications* 58 (2009), Nr. 5, 965–974

[139] Li, Q ; Luo, KH ; Li, XJ: Forcing scheme in pseudopotential lattice Boltzmann model for multiphase flows. In: *Physical Review E* 86 (2012), Nr. 1, 016709

[140] Mattila, K ; Hyväluoma, J ; Rossi, T: Mass-flux-based outlet boundary conditions for the lattice Boltzmann method. In: *Journal of Statistical Mechanics: theory and experiment* 2009 (2009), Nr. 06, P06015

[141] Chen, Shiyi ; Martinez, Daniel ; Mei, Renwei: On boundary conditions in lattice Boltzmann methods. In: *Phys. Fluids* 8 (1996), Nr. 9, 2527–2536

[142] Vega, C ; De Miguel, E: Surface tension of the most popular models of water by using the test-area simulation method. In: *J. of Chemical Physics* 126 (2007), Nr. 15, 154707

[143] Wenzel, Robert N.: Resistance of solid surfaces to wetting by water. In: *Industrial & Engineering Chemistry* 28 (1936), Nr. 8, 988–994

[144] Stacy, Russell: *Contact angle measurement technique for rough surfaces*, Michigan Technological University, Bachelor Thesis, 2009

[145] Law, Kock-Yee ; Zhao, Hong: *Surface wetting: characterization, contact angle, and fundamentals*. Springer, 2015

[146] Flückiger, Reto ; Marone, Federica ; Stampanoni, Marco ; Wokaun, Alexander ; Büchi, Felix N.: Investigation of liquid water in gas diffusion layers of polymer electrolyte fuel cells using X-ray tomographic microscopy. In: *Electrochim. Acta* 56 (2011), Nr. 5, 2254–2262

[147] Chini, S F. ; Amirfazli, A: A method for measuring contact angle of asymmetric and symmetric drops. In: *Colloids Surf., A* 388 (2011), Nr. 1, 29–37

[148] Zimmermann, Jan ; Seeger, Stefan ; Reifler, Felix A.: Water shedding angle: a new technique to evaluate the water-repellent properties of superhydrophobic surfaces. In: *Text. Res. J.* 79 (2009), Nr. 17, 1565–1570

[149] Yu, Junliang ; Froning, Dieter ; Reimer, Uwe ; Lehnert, Werner: Apparent contact angles of liquid water droplet breaking through a gas diffusion layer of polymer electrolyte membrane fuel cell. In: *Int. J. Hydrogen Energy* 43 (2018), Nr. 12, 6318 - 6330

[150] Zou, Qisu ; He, Xiaoyi: On pressure and velocity boundary conditions for the lattice Boltzmann BGK model. In: *Phys. Fluids* 9 (1997), Nr. 6, 1591–1598

[151] Liu, Haihu ; Kang, Qinjun ; Leonardi, Christopher R. ; Schmieschek, Sebastian ; Narváez, Ariel ; Jones, Bruce D. ; Williams, John R. ; Valocchi, Albert J. ; Harting, Jens: Multiphase lattice Boltzmann simulations for porous media applications. In: *Comput. Geosci.* 20 (2016), Nr. 4, 777–805

[152] Keuler, S: *Parallele implementierung einer lattice boltzmann simulation von gas diffusion layern fuer brennstoffzellen, Aachen University of Applied Sciences*, Bachelor Thesis, 2011

[153] Chen, Wang ; Jiang, Fangming: Impact of PTFE content and distribution on liquid–gas flow in PEMFC carbon paper gas distribution layer: 3D lattice Boltzmann simulations. In: *Int. J. Hydrogen Energy* 41 (2016), Nr. 20, 8550–8562

[154] Jiao, Kui ; Li, Xianguo: Water transport in polymer electrolyte membrane fuel cells. In: *Prog. Energy Combust. Sci.* 37 (2011), Nr. 3, 221–291

[155] Albernaz, Daniel ; Do-Quang, Minh ; Amberg, Gustav: Multirelaxation-time lattice Boltzmann model for droplet heating and evaporation under forced convection. In: *Physical Review E* 91 (2015), Nr. 4, 043012

[156] Chaplin, Martin: Water structure and science / London South Bank University. 2011. – Technical report

[157] Sun, Kai ; Wang, Tianyou ; Jia, Ming ; Xiao, Gang: Evaluation of force implementation in pseudopotential-based multiphase lattice Boltzmann models. In: *Physica A* 391 (2012), Nr. 15, 3895–3907

[158] Tadros, Tharwat: *Encyclopedia of Colloid and Interface Science.* Springer, 2013

[159] Yiotis, Andreas G. ; Psihogios, John ; Kainourgiakis, Michael E. ; Papaioannou, Aggelos ; Stubos, Athanassios K.: A lattice Boltzmann study of viscous coupling effects in immiscible two-phase flow in porous media. In: *Colloids Surf., A* 300 (2007), Nr. 1, 35–49

[160] Hou, Shuling ; Shan, Xiaowen ; Zou, Qisu ; Doolen, Gary D. ; Soll, Wendy E.: Evaluation of two lattice Boltzmann models for multiphase flows. In: *J. Comput. Phys.* 138 (1997), Nr. 2, 695–713

[161] Young, T.: An essay on the cohesion of fluids. In: *Phil. Trans.* (1805), 65

[162] Siqveland, Leiv M. ; Skjæveland, Svein M.: Derivations of the Young-Laplace equation / University of Stavanger. 2014. – Technical report

[163] Li, Qing ; Luo, KH ; Kang, QJ ; Chen, Q: Contact angles in the pseudopotential lattice Boltzmann modeling of wetting. In: *Physical Review E* 90 (2014), Nr. 5, 053301

[164] Osborne, Kenneth L.: *Temperature dependence of the contact angle of water on graphite, silicon, and gold*, Worcester Polytechnic Institute, Diss., 2009

[165] Zhang, Feng-Yuan ; Spernjak, Dusan ; Prasad, Ajay K. ; Advani, Suresh G.: In situ characterization of the catalyst layer in a polymer electrolyte membrane fuel cell. In: *J. Electrochem. Soc.* 154 (2007), Nr. 11, B1152–B1157

[166] Liu, J ; Gazzarri, J ; Eikerling, M: Model-Based Ex Situ Diagnostics of Water Fluxes in Catalyst Layers of Polymer Electrolyte Fuel Cells. In: *Fuel Cells* 13 (2013), Nr. 2, 134–142

[167] Nouri-Khorasani, Amin ; Malek, Kourosh ; Malek, Ali ; Mashio, Tetsuya ; Wilkinson, David P. ; Eikerling, Michael H.: Molecular modeling of the proton density distribution in a water-filled slab-like nanopore bounded by Pt oxide and ionomer. In: *Catal. Today* 262 (2016), 133–140

[168] Thiedmann, Ralf ; Hartnig, Christoph ; Manke, Ingo ; Schmidt, Volker ; Lehnert, Werner: Local structural characteristics of pore space in GDLs of PEM fuel cells based on geometric 3D graphs. In: *J. Electrochem. Soc.* 156 (2009), Nr. 11, B1339–B1347

[169] Sinha, Puneet K. ; Wang, Chao-Yang: Pore-network modeling of liquid water transport in gas diffusion layer of a polymer electrolyte fuel cell. In: *Electrochim. Acta* 52 (2007), Nr. 28, 7936–7945

[170] Nam, Jin H. ; Kaviany, Massoud: Effective diffusivity and water-saturation distribution in single-and two-layer PEMFC diffusion medium. In: *Int. J. Heat Mass Transfer* 46 (2003), Nr. 24, 4595–4611

[171] Hinebaugh, James ; Fishman, Zachary ; Bazylak, A: Unstructured pore network modeling with heterogeneous PEMFC GDL porosity distributions. In: *J. Electrochem. Soc.* 157 (2010), Nr. 11, B1651–B1657

[172] Wu, J ; Huang, JJ ; Yan, WW: Lattice Boltzmann investigation of droplets impact behaviors onto a solid substrate. In: *Colloids Surf., A* 484 (2015), 318–328

[173] Wolansky, Gershon ; Marmur, Abraham: The actual contact angle on a heterogeneous rough surface in three dimensions. In: *Langmuir* 14 (1998), Nr. 18, 5292–5297

[174] Meiron, Tammar S. ; Marmur, Abraham ; Saguy, I S.: Contact angle measurement on rough surfaces. In: *J. Colloid Interface Sci.* 274 (2004), Nr. 2, 637–644

[175] Qin, Chaozhong ; Rensink, Dirk ; Hassanizadeh, S M. ; Fell, Stephan: Direct simulation of liquid water dynamics in the gas channel of a polymer electrolyte fuel cell. In: *J. Electrochem. Soc.* 159 (2012), Nr. 4, B434–B443

[176] SK: Effect of drop volume on static contact angles / KRUSS. 2004. – Technical report

[177] Yuan, Yuehua ; Lee, T R.: *Contact angle and wetting properties*. Springer, 2013. – 3–34

[178] KRUSS: https://www.kruss-scientific.com/services. (08/05/2018)

[179] Weinan, E: *Principles of multiscale modeling*. Cambridge University Press, 2011

[180] Bazylak, A ; Berejnov, V ; Markicevic, B ; Sinton, D ; Djilali, N: A microfluidic pore network approach to investigate water transport in fuel cell porous transport layers. In: *Proceedings of the sixth International ASME Conference on Nanochannels, Microchannels and Minichannels ICNMM2008-62349 (June 23-25, 2008)*, 2008

[181] Yu, Junliang ; Froning, Dieter ; Reimer, Uwe ; Lehnert, Werner: Liquid water breakthrough location distances on a gas diffusion layer of polymer electrolyte membrane fuel cells. In: *J. Power Sources* 389 (2018), 56 - 60

[182] Abebe, A ; Daniels, J ; McKean, JW ; Kapenga, J: *Statistics and data analysis*. Western Michigan University Publisher, 2001

[183] Lilliefors, Hubert W.: On the Kolmogorov-Smirnov test for normality with mean and variance unknown. In: *J. Am. Stat. Assoc.* 62 (1967), Nr. 318, 399–402

[184] Dallal, Gerard E. ; Wilkinson, Leland: An analytic approximation to the distribution of Lilliefors's test statistic for normality. In: *The American Statistician* 40 (1986), Nr. 4, 294–296

[185] https://de.mathworks.com/help/stats/lillietest.html 10/09/2017.

[186] Abdi, Hervé ; Molin, Paul: Lilliefors/Van Soestâs test of normality. In: *Encyclopedia of Measurement and Statistics* (2007), 540–544

[187] http://fuelcellsetc.com/helpful-tools/gas-diffusion-layer-gdl-comparison-chart/. (2017/11/02)

[188] Park, Sung B. ; Park, Yong-il: Fabrication of gas diffusion layer (GDL) containing microporous layer using flourinated ethylene prophylene (FEP) for proton exchange membrane fuel cell (PEMFC). In: *Int. J. Precis. Eng. Manuf.* 13 (2012), Nr. 7, 1145–1151

[189] Mathias, MF ; Roth, Joerg ; Fleming, Jerry ; Lehnert, Werner: *Diffusion media materials and characterisation*. Wiley Online Library, 2003

[190] Store, Fuel C.: www.fuelcellstore.com/. (12/03/2018)

[191] Clover, P: Petrophysics MSc Course Note. In: *Imperial College, London* (2008), 10–20

[192] https://de.mathworks.com/help/symbolic/atan.html/stid=srchtitle. (10/04/2018)

A. Appendix

A.1. Transformation matrix in MRT

$$
\mathbf{M} = \begin{bmatrix}
1 & 1 & 1 & 1 & 1 & 1 & 1 & 1 & 1 & 1 & 1 & 1 & 1 & 1 & 1 & 1 & 1 & 1 & 1 \\
-30 & -11 & 8 & -11 & 8 & -11 & 8 & -11 & 8 & -11 & 8 & 8 & 8 & 8 & -11 & 8 & 8 & 8 & 8 \\
12 & -4 & 1 & -4 & 1 & -4 & 1 & -4 & 1 & -4 & 1 & 1 & 1 & 1 & -4 & 1 & 1 & 1 & 1 \\
0 & 1 & 1 & 0 & -1 & -1 & -1 & 0 & 1 & 0 & 1 & 0 & -1 & 0 & 0 & 1 & 0 & -1 & 0 \\
0 & -4 & 1 & 0 & -1 & 4 & -1 & 0 & 1 & 0 & 1 & 0 & -1 & 0 & 0 & 1 & 0 & -1 & 0 \\
0 & 0 & 1 & 1 & 1 & 0 & -1 & -1 & -1 & 0 & 0 & 1 & 0 & -1 & 0 & 0 & 1 & 0 & -1 \\
0 & 0 & 1 & -4 & 1 & 0 & -1 & 4 & -1 & 0 & 0 & 1 & 0 & -1 & 0 & 0 & 1 & 0 & -1 \\
0 & 0 & 0 & 0 & 0 & 0 & 0 & 0 & 0 & -1 & -1 & -1 & -1 & -1 & 1 & 1 & 1 & 1 & 1 \\
0 & 0 & 0 & 0 & 0 & 0 & 0 & 0 & 0 & 4 & -1 & -1 & -1 & -1 & -4 & 1 & 1 & 1 & 1 \\
0 & 2 & 1 & -1 & 1 & 2 & 1 & -1 & 1 & -1 & 1 & -2 & 1 & -2 & -1 & 1 & -2 & 1 & -2 \\
0 & -4 & 1 & 2 & 1 & -4 & 1 & 2 & 1 & 2 & 1 & -2 & 1 & -2 & 2 & 1 & -2 & 1 & -2 \\
0 & 0 & 1 & 1 & 1 & 0 & 1 & 1 & 1 & -1 & -1 & 0 & -1 & 0 & -1 & -1 & 0 & -1 & 0 \\
0 & 0 & 1 & -2 & 1 & 0 & 1 & -2 & 1 & 2 & -1 & 0 & -1 & 0 & 2 & -1 & 0 & -1 & 0 \\
0 & 0 & 1 & 0 & -1 & 0 & 1 & 0 & -1 & 0 & 0 & 0 & 0 & 0 & 0 & 0 & 0 & 0 & 0 \\
0 & 0 & 0 & 0 & 0 & 0 & 0 & 0 & 0 & 0 & 0 & -1 & 0 & 1 & 0 & 0 & 1 & 0 & -1 \\
0 & 0 & 0 & 0 & 0 & 0 & 0 & 0 & 0 & 0 & -1 & 0 & 1 & 0 & 0 & 1 & 0 & -1 & 0 \\
0 & 0 & 1 & 0 & -1 & 0 & -1 & 0 & 1 & 0 & -1 & 0 & 1 & 0 & 0 & -1 & 0 & 1 & 0 \\
0 & 0 & -1 & 0 & -1 & 0 & 1 & 0 & 1 & 0 & 0 & 1 & 0 & -1 & 0 & 0 & 1 & 0 & -1 \\
0 & 0 & 0 & 0 & 0 & 0 & 0 & 0 & 0 & 0 & -1 & 1 & -1 & 1 & 0 & 1 & -1 & 1 & -1
\end{bmatrix}
$$

$$
\mathbf{M}^{-1} = \begin{bmatrix}
\frac{1}{19} & -\frac{5}{399} & \frac{1}{21} & 0 & 0 & 0 & 0 & 0 & 0 & 0 & 0 & 0 & 0 & 0 & 0 & 0 & 0 & 0 & 0 \\
\frac{1}{19} & -\frac{11}{2394} & -\frac{1}{63} & \frac{1}{10} & -\frac{1}{10} & 0 & 0 & 0 & 0 & \frac{1}{18} & -\frac{1}{18} & 0 & 0 & 0 & 0 & 0 & 0 & 0 & 0 \\
\frac{1}{19} & \frac{4}{1197} & \frac{1}{252} & \frac{1}{10} & \frac{1}{40} & \frac{1}{10} & \frac{1}{40} & 0 & 0 & \frac{1}{36} & \frac{1}{72} & \frac{1}{12} & \frac{1}{24} & \frac{1}{4} & 0 & 0 & \frac{1}{8} & -\frac{1}{8} & 0 \\
\frac{1}{19} & -\frac{11}{2394} & \frac{1}{63} & 0 & 0 & \frac{1}{10} & -\frac{1}{10} & 0 & 0 & -\frac{1}{36} & \frac{1}{36} & \frac{1}{12} & -\frac{1}{12} & 0 & 0 & 0 & 0 & 0 & 0 \\
\frac{1}{19} & \frac{4}{1197} & \frac{1}{252} & -\frac{1}{10} & -\frac{1}{40} & \frac{1}{10} & \frac{1}{40} & 0 & 0 & \frac{1}{36} & \frac{1}{72} & \frac{1}{12} & \frac{1}{24} & -\frac{1}{4} & 0 & 0 & -\frac{1}{8} & -\frac{1}{8} & 0 \\
\frac{1}{19} & -\frac{11}{2394} & -\frac{1}{63} & -\frac{1}{10} & \frac{1}{10} & 0 & 0 & 0 & 0 & 0 & \frac{1}{18} & -\frac{1}{18} & 0 & 0 & 0 & 0 & 0 & 0 & 0 \\
\frac{1}{19} & \frac{4}{1197} & \frac{1}{252} & -\frac{1}{10} & -\frac{1}{40} & -\frac{1}{10} & -\frac{1}{40} & 0 & 0 & \frac{1}{36} & \frac{1}{72} & \frac{1}{12} & \frac{1}{24} & \frac{1}{4} & 0 & 0 & -\frac{1}{8} & \frac{1}{8} & 0 \\
\frac{1}{19} & -\frac{11}{2394} & -\frac{1}{63} & 0 & 0 & -\frac{1}{10} & \frac{1}{10} & 0 & 0 & -\frac{1}{36} & \frac{1}{36} & \frac{1}{12} & -\frac{1}{12} & 0 & 0 & 0 & 0 & 0 & 0 \\
\frac{1}{19} & \frac{4}{1197} & \frac{1}{252} & \frac{1}{10} & \frac{1}{40} & -\frac{1}{10} & -\frac{1}{40} & 0 & 0 & \frac{1}{36} & \frac{1}{72} & \frac{1}{12} & \frac{1}{24} & -\frac{1}{4} & 0 & 0 & \frac{1}{8} & \frac{1}{8} & 0 \\
\frac{1}{19} & -\frac{11}{2394} & -\frac{1}{63} & 0 & 0 & 0 & 0 & -\frac{1}{10} & \frac{1}{10} & -\frac{1}{36} & \frac{1}{36} & -\frac{1}{12} & \frac{1}{12} & 0 & 0 & 0 & 0 & 0 & 0 \\
\frac{1}{19} & \frac{4}{1197} & \frac{1}{252} & \frac{1}{10} & \frac{1}{40} & 0 & 0 & -\frac{1}{10} & -\frac{1}{40} & \frac{1}{36} & \frac{1}{72} & -\frac{1}{12} & -\frac{1}{24} & 0 & 0 & -\frac{1}{4} & -\frac{1}{8} & 0 & -\frac{1}{8} \\
\frac{1}{19} & \frac{4}{1197} & \frac{1}{252} & 0 & 0 & \frac{1}{10} & \frac{1}{40} & -\frac{1}{10} & -\frac{1}{40} & -\frac{1}{18} & -\frac{1}{36} & 0 & 0 & 0 & -\frac{1}{4} & 0 & 0 & \frac{1}{8} & \frac{1}{8} \\
\frac{1}{19} & \frac{4}{1197} & \frac{1}{252} & -\frac{1}{10} & -\frac{1}{40} & 0 & 0 & -\frac{1}{10} & -\frac{1}{40} & \frac{1}{36} & \frac{1}{72} & -\frac{1}{12} & -\frac{1}{24} & 0 & 0 & \frac{1}{4} & \frac{1}{8} & 0 & -\frac{1}{8} \\
\frac{1}{19} & \frac{4}{1197} & \frac{1}{252} & 0 & 0 & -\frac{1}{10} & -\frac{1}{40} & -\frac{1}{10} & -\frac{1}{40} & -\frac{1}{18} & -\frac{1}{36} & 0 & 0 & 0 & \frac{1}{4} & 0 & 0 & -\frac{1}{8} & \frac{1}{8} \\
\frac{1}{19} & -\frac{11}{2394} & -\frac{1}{63} & 0 & 0 & 0 & 0 & \frac{1}{10} & -\frac{1}{10} & -\frac{1}{36} & \frac{1}{36} & -\frac{1}{12} & \frac{1}{12} & 0 & 0 & 0 & 0 & 0 & 0 \\
\frac{1}{19} & \frac{4}{1197} & \frac{1}{252} & \frac{1}{10} & \frac{1}{40} & 0 & 0 & \frac{1}{10} & \frac{1}{40} & \frac{1}{36} & \frac{1}{72} & -\frac{1}{12} & -\frac{1}{24} & 0 & 0 & \frac{1}{4} & -\frac{1}{8} & 0 & \frac{1}{8} \\
\frac{1}{19} & \frac{4}{1197} & \frac{1}{252} & 0 & 0 & \frac{1}{10} & \frac{1}{40} & \frac{1}{10} & \frac{1}{40} & -\frac{1}{18} & -\frac{1}{36} & 0 & 0 & 0 & \frac{1}{4} & 0 & 0 & \frac{1}{8} & -\frac{1}{8} \\
\frac{1}{19} & \frac{4}{1197} & \frac{1}{252} & -\frac{1}{10} & -\frac{1}{40} & 0 & 0 & \frac{1}{10} & \frac{1}{40} & \frac{1}{36} & \frac{1}{72} & -\frac{1}{12} & -\frac{1}{24} & 0 & 0 & -\frac{1}{4} & \frac{1}{8} & 0 & \frac{1}{8} \\
\frac{1}{19} & \frac{4}{1197} & \frac{1}{252} & 0 & 0 & -\frac{1}{10} & -\frac{1}{40} & \frac{1}{10} & -\frac{1}{40} & -\frac{1}{18} & -\frac{1}{36} & 0 & 0 & 0 & -\frac{1}{4} & 00 & -\frac{1}{8} & -\frac{1}{8}
\end{bmatrix}
$$

A.2. Example of unit conversion

According to the theory description of LBM in section 2.4, the parameters with SI and LU can be converted each other. In this section, a detailed example of unit conversion is explained. The following explaination are for the simulations in section 5 and 7.1 concerning water transport through GDL.
The reference parameters l_r, t_r and m_r are calculated according to the following steps:

1. Calculate reference length l_r. The resolution of images are given and equals the reference lenght. So the refernce length $l_r = 1.5$ µm $= 1.5 \times 10^{-6}$ m.

2. Calculate reference time t_r. The relaxation time τ_α is defined in MRT-EDM ShanChen model. According to the relaxation time dependence discussions in section 4. The MRT-EDM is relaxation time independent and $\tau_1 = \tau_2 = 0.6$ (the subscript 1 is for water and 2 is for air) is choosen for water through GDL simulations. According to the Eq. (2.5), the kinematic viscosity of water with LU can be calculated and $\nu_{l,1} = 0.033$ l.u.. The kinematic viscosity of water in SI unit is known and $\nu_{p,1} = 3.6 \times 10^{-7}$ m$^2 \cdot$ s^{-1} (see Table 1.1). Then the reference time t_r for water is calculated according to Eq. (2.29) and reorganized in Eq. (A.1).
$$t_r = \frac{\boldsymbol{\nu}_l l_r^2}{\boldsymbol{\nu}_p} = \frac{\boldsymbol{\nu}_{l,1} l_r^2}{\boldsymbol{\nu}_{p,1}} = \frac{0.033 \times (1.5 \times 10^{-6})^2}{3.6 \times 10^{-7}} = 2.06 \times 10^{-7} \text{ s} \tag{A.1}$$

3. Calculate reference mass m_r. The reference mass m_r is calculate from Eq. (2.30). The surface tension with SI unit is given and $\sigma_{\text{s,p}} = 0.072$ kg $\cdot$ s^{-2} (see Table 1.2). The surface tension with LU is obtained from the SIDT in section 4.3.1 and $\sigma_{s,l} = 0.1883$ l.u. (see Fig. 4.23). The m_r is calculated according to Eq. (2.30) and reorganized as Eq. (A.2).
$$m_r = \frac{\boldsymbol{\sigma}_{s,p} \cdot t_r^2}{\boldsymbol{\sigma}_{s,l}} = \frac{0.072 \times (1.5 \times 10^{-6})^2}{0.1883} = 8.6 \times 10^{-13} \text{ kg} \tag{A.2}$$

Finally, other parameters with SI unit and LU can be converted according to the relations listed in the Table 2.3.

A.3. SPPF method in MATLAB

For the SPPF method calculating the local contact angle introduced in section 2.5, the method can be achieved by the commercial software MATLAB. Three steps of SPPF including dectecting the droplet boundary, finding the contact point and contact angle calculation can be achieved by Paraview 5.0 and MATLAB R2009b.
In the first step, the droplet boundary has to be selected. This step was done in Paraview. The output results of simulation including density and velocity fields, are import to the Paraview. The data of all fields on a 2D cross section from a specific view direction are extracted by the 'Slice' function and exported to the '.csv' files in Paraview. The data of density field in '.csv' files are read by MATLAB and a threshold value is defined to detect the droplet boundary points positions (see Fig. 2.4 a)). In the second step, the 1st order polynomial curve fitting is done by function 'polyfit(x, y, c)' in MATLAB. The function 'polyfit' is to fit polynomial to data and the commend line in MATLAB can be shown as f=polyfit(x, y, c). It finds the coefficient of a polynomial $f(x)$ of degree c that fits the data y best in a least-squares sense.

(x, y) shows the data positions on the rectangular coordinate. f is a row vector of length $c + 1$ containing the polynomial coefficients in descending powers [192]. In the third step, the constrained polynomial curve fitting is done by the '$\hat{f}$=polyfix$(x, y, c, \hat{x}, \hat{y})$'. The parameters of curve fitting are found in the least-squares sense the same as 'polyfit' and a constraint of fitted curve pass through point $(\hat{x}, \hat{y})$ [192]. Afterward, the slope of the constraint fitted curve $\hat{f}$ is calculated by 'polyder$(\hat{f})$' command that returns the derivative of the polynomial whose coefficients are the elements of vector a. Finally, the contact angle in degree is converted from slope by arc-tangent with command 'atan' [192].

B. Abbreviate

B.1. Acronyms

ADSA	Axisymmetric drop shape analysis
BiP	Bipolar plate
BP	Breakthrough point
BPD	Breakthrough point distance
BGK	Bhatnagar-Gross-Krook
Bo	Bond number
CFD	Computational fluid dynamics
CDF	Cumulative distribution
CAT	Contact angle test
Ca	Capillary number
C-S	Carnahan-Starling
CL	Catalyst layer
c.f.	Cover fraction
EDF	Empirical distribution function
EDM	Exact difference method
EOS	Equation of state
GDL	Gas diffusion layer
GC	Gas channel
grad.	Gradient
HOR	Hydrogen oxidation reaction
HCZ	He-Chen-Zhang
HT	High temperature
IEK	Institute of energy and climate research
Kn	Knudsen number
LBE	Lattice Boltzmann equation
LBM	Lattice Boltzmann method

LB	Lattice Boltzmann
LU	Lattice unit
l.u.	Lattice unit (dimension)
MPL	Microporous layer
MCMP	Multi-component multi-phase
MRT	Multi-relaxation time
NS	Navier-Stokes
ORR	Oxygen reduction reaction
PLT	Poisson line tessellations
PTFE	Polytetrafluoroethylene
PNM	Pore net-work model
PEFC	Polymer Electrolyte fuel cell
P-R	Peng-Robinson
Q-lin	Quasi-linear-through-plane PTFE distribution
Re	Reynolds number
RK	Rothman-Keller
R.L.	Reference layer
S-BPD	Specific breakthrough point distance (BPD)
SN-BPD	Shortest neighbor breakthrough point distance (BPD)
SA	Sample angle
SI	International system of units
SPPF	Sub-pixel polynomial fitting
SCMP	Single component multi-phase
SRT	Single-relaxation-time
SV	Shift velocity
SEM	Scanning electron microscopy
SIDT	Single ideal droplet test
SFIT	Steady flat interface test
S.	Style

VA	View angle
VOF	Volume of fluid
We	Webber number
w.f.	Weight fraction
XTM	X-ray tomographic microscopy

Greek symbols

α	Component number
α_g	Angle of single fiber in the stochastic geometry model
$\beta_{\textbf{cover}}$	Cover fraction of PTFE
$\beta_{\textbf{weight}}$	Weight fraction of PTFE
ω_i	Weight factor on ith discrete velocity direction
τ_α	Relaxation time of αth component
$\tau_{\alpha,\textbf{upl}}$	up limit of the αth component relaxation time
$\tau_{\alpha,\textbf{lowl}}$	low limit of the αth component relaxation time
ν	Kinematic viscosity
ν_α	Kinematic viscosity of αth component
Δt	Time difference
ΔP	Pressure difference
λ	Stoichiometry number
λ_f	Mean free path length
ρ	Total density
ρ_α	Density of αth component
$\rho_{\alpha,\textbf{init}}$	Initial density of αth component
$\rho_{\textbf{itm}}$	Intermiscible density
$\rho^*_{\textbf{itm}}$	Scaled intermiscible density
ρ_0	Reference density concerning EOS
$\rho_{\textbf{GDL}}$	Density of GDL
$\rho_{\textbf{PTFE}}$	Density of PTFE

ψ_α	Effective number density of αth component
ψ_0	Reference effective number density concerning EOS
Λ_α	Diagonal matrix of αth component
ζ	Porosity
ζ_α	Bulk viscosity of αth component
σ_s	Surface tension
$\sigma_{s,p}$	Surface tension in SI unit
$\sigma_{s,l}$	Surface tension in lattice unit
σ_{sd}	Standard deviation
$\sigma_{sd,k}$	Standard deviation of k in BPD (k is 'sbp' or 'snbp')
$\sigma_{sd,\textbf{sbp}}$	Standard deviation of specific breakthrough point distance
$\sigma_{sd,\textbf{snbp}}$	Standard deviation of shortest neighbor breakthrough point distance
$\sigma_{sd,\textbf{geo}}$	Standard deviation concerning geometry effects
θ	Contact angle
$\bar{\theta}$	Mean value of contact angle
$\theta_{\textbf{idl}}$	Idealized contact angle
$\theta_{\textbf{idl,max}}$	Maximum idealized contact angle
$\theta_{\textbf{idl,min}}$	Minimum idealized contact angle
$\theta_{\textbf{ap}}$	Apparent contact angle
$\theta_{\textbf{ap,max}}$	Maximum apparent contact angle
$\theta_{\textbf{ap,min}}$	Minimum apparent contact angle
$\bar{\theta}_{\textbf{ap,geo}}$	Average apparent contact angle concerning geometry effects
$\bar{\theta}_{\textbf{ap,av}}$	Average apparent contact angle concerning view angles
$\theta_{\textbf{ap,l}}$	Apparent contact angle on the left hand side
$\theta_{\textbf{ap,r}}$	Apparent contact angle on the right hand side
$\theta_{\textbf{ap},j}$	jth apparent contact angle
$\theta_{\textbf{PTFE}}$	Contact angle on the PTFE material
$\theta_{\textbf{carbon}}$	Contact angle on the carbon material
μ	Dynamic viscosity

$\mu_{\mathbf{H_2O}}$	Dynamic viscosity of water
$\mu_{\mathbf{O_2}}$	Dynamic viscosity of oxygen
ε_r	Relative error
$\varepsilon_{\text{limit}}$	Limited error
ϵ_{max}	Maximum absolute error
γ_{LG}	Interfacial energy between liquid and gas phase
γ_{SG}	Interfacial energy between solid and gas phase
γ_{SL}	Interfacial energy between solid and liquid phase
Γ	The ratio between single fiber radius R_{carbon} and PTFE thickness R_{PTFE}
η	Dimensionless number to convert to idealized contact angle θ_{idl}
φ_k	Parameter of Lilliefors text function for k BPD in MATLAB (k is 'sbp' or 'snbp')

B.2. Latin symbols

A_{inlet}	Inlet area
A_{drop}	Breakthrough area on the GDL surface
$A_{\text{drop,idl}}$	Idealized breakthrough area on the GDL surface
A_{sim}	Simulation GDL area
A_{eff}	Effective reaction area
$A_{\text{trans, GC}}$	Transport area in gas channel
$A_{\text{trans,GDL}}$	Transport area in GDL
B_k	Binary parameter of the Lilliefors test function in MATLAB
c_s	Sound velocity
c_v	Variation coefficient
$c_{v,\text{va}}$	Variation coefficient concerning view angles
$c_{v,\text{geo}}$	Variation coefficient concerning geometry effects
D_k	Maximum discrepancy between EDF and CDF of k in BPD (k is 'sbp' or 'snbp')
d_g	Distance for single fiber on one layer in the geometry model
$\mathbf{e}_i$	Discrete velocity on ith discrete velocity direction
f	Single particle distribution function

f_{α}^{eq}	Equilibrium distribution function of αth component
$f_{\alpha,i}$	Distribution function of αth component in ith discrete velocity direction
$f_{\alpha,i,\textbf{out}}$	Distribution function of αth component in ith discrete velocity direction on the outlet layer
$f_{\alpha,i,\textbf{out-1}}$	Distribution function of αth component in ith discrete velocity direction on the layer next to the outlet
F	Faraday’s constant
$\mathbf{F}_{\alpha}$	Total Body force acting on αth component
$\mathbf{F}_{\textbf{coh},\alpha}$	Cohesive body force acting on αth component
$\mathbf{F}_{\textbf{adh},\alpha}$	Adhesive body force acting on αth component
$\mathbf{F}_{\textbf{ext},\alpha}$	External body force acting on αth component
$\mathbf{g}_{\alpha}$	Gravity acceleration of αth component
g	Range of values along iteration steps
$G_{\textbf{coh}}$	Parameter to control cohesive body force
$G_{\textbf{coh,crit}}$	Critical value of G_{coh}
$G_{\textbf{adh}}$	Parameter to control adhesive body force
H	Height
$H_{\textbf{drop}}$	Height of droplet
$H_{\textbf{PTFE}}$	Height of PTFE for PTFE content conversion
$H_{\textbf{carbon}}$	Height of single carbon fiber for PTFE content conversion
i	Discrete velocity direction
it	Iteration steps
I	Electric current
$\dot{I}$	Current density
j	Sample order
k	Kind of BPD (’sbp’ for S-BPD and ’snbp’ for SN-BPD)
l	Length
l_r	Reference length
$\bar{L}_k$	Breakthrough point distance of kind k of BPD
$\bar{L}_{\textbf{sbp}}$	Mean value of specific breakthrough point distance

$\bar{L}_{\mathbf{snbp}}$	Mean value of shortest neighbor breakthrough point distance
L	Representative physical length scale (characteristic length)
$L_{\mathbf{GC}}$	Characteristic length of gas channel
$L_{\mathbf{GDL}}$	Characteristic length of gas diffusion layer
L_b	Base length
$L_{\mathbf{buffer}}$	Buffer length (thickness of buffer region)
$L_{\mathbf{sim,GDL}}$	Simulated GDL thickness
$L_{\mathbf{drop}}$	Droplet base length
$L_{\mathbf{plate}}$	Half distance between two parallel plates
$L_{\mathbf{wet}}$	Half distance of wet phase region
$L_{k,j}$	Breakthrough point distance k of the jth sample
m	Pixel number for the 2nd order polynomial curve fitting in SPPF method
$m_{\mathbf{PTFE}}$	Mass of PTFE
$m_{\mathbf{GDL}}$	Mass of GDL
$\mathbf{m}_{\alpha}$	Distribution function in the momentum space of αth component
$\mathbf{m}_{\alpha}^{eq}$	Equilibrium distribution function in the momentum space of αth component
$\dot{m}$	Mass flux
$\dot{m}_r$	Mass flux of component r (r is 'H_2O' for water and 'O_2' for oxygen)
$\boldsymbol{M}$	Dynamic viscosity ratio
$\mathbf{M}$	Transformation matrix for D3Q19
$\mathbf{M}^{-1}$	Inverse transformation matrix for D3Q19
M	Molar mass
n	Pixel number for the 1st order polynomial curve fitting in SPPF method
N	Amount of exchanged electrons
N_s	Sample amount
$N-p$	Pixel amount on the breakthrough area
$N_{s,\mathbf{geo}}$	Amount of breakthrough point on one geometry
O	Order of magnitude
P	Pressure

P_c	Critical pressure
$P_{\textbf{inlet}}$	Pressure in inlet
$P_{\textbf{inside}}$	Pressure inside of droplet
$P_{\textbf{outlet}}$	Pressure in outlet
$P_{\textbf{outside}}$	Pressure outside of droplet
Q_k	Sample amount of kth kind of BPD (k is 'sbp' for S-BPD and 'snbp' for SN-BPD)
$Q_{\textbf{sbp}}$	Amount of specific breakthrough point distances
R	Radius of sphere droplet
R_p	Radius of pore
$R_{\textbf{eq}}$	Equivalent radius of droplet
$R_{\textbf{init}}$	Initial radius of droplet
$R_{\textbf{carbon}}$	Radius of carbon fiber
$R_{\textbf{PTFE}}$	PTFE thickness on the single carbon fiber
S	Saturation
$S_{\textbf{total}}$	Total saturation
$S_{\textbf{total,anal}}$	Analytical solution of total saturation
$S_{\textbf{local}}$	Local saturation
S_α	Source term of αth component
$S_{\textbf{anal}}$	Analytical saturation (analytical water fraction)
$s_{i,\alpha}$	ith element in the diagonal matrix of αth component
T	Temperature
t	Time
t_l	Time in lattice unit
$t_{\textbf{off}}$	Switch-off time
$t_{\textbf{snap}}$	Snapshot time
$t_{\textbf{break}}$	Breakthrough time
t_r	Reference time
t^*	Dimensionless time
$t_{\textbf{cal}}$	Calculation time

$t_{\textsf{cal,min}}$	Minimum calculation time
$\mathbf{u}$	Velocity
$\mathbf{u}_\alpha$	Velocity of αth component
$\mathbf{u}_{it}$	Velocity in the iteration step it
$\mathbf{u}_{it-g}$	Velocity in the iteration step $it-g$
$\mathbf{u}^*$	Dimensionless velocity
$\mathbf{u}_{\textsf{anal}}$	Analytical solution of velocity
$\mathbf{u}^*_{\textsf{anal}}$	Dimensionless analytical solution of velocity
$\mathbf{u}_{\textsf{anal,aver}}$	Average analytical solution of velocity
$\mathbf{u}_{\textsf{anal,max}}$	Maximum analytical solution of velocity
$\mathbf{u}^{eq}_\alpha$	Equilibrium velocity of αth component
$\mathbf{u}_{\textsf{spu}}$	Spurious velocity
$\mathbf{u}_{\textsf{spu,max}}$	Maximum spurious velocity
$\mathbf{u}_{\alpha,\textsf{spu,max}}$	Maximum spurious velocity of α component
$\mathbf{u}'$	Velocity common to the various components
$\bar{\mathbf{u}}$	Average velocity
$\bar{\mathbf{u}}_r$	Average velocity of component r (r is 'H_2O' for water and 'O_2' for oxygen)
$\mathbf{u}_{\textsf{inlet}}$	Inlet velocity
$\mathbf{u}_{\textsf{inlet},l}$	Inlet velocity in lattice unit
$\mathbf{u}_{\textsf{inlet},p}$	Inlet velocity in SI unit
$\dot{V}$	Volume flux
$\dot{V}_r$	Volume flux of component r (r is 'H_2O' for water and 'O_2' for oxygen)
$V_{\textsf{tot}}$	Total volume
$V_{\textsf{drop}}$	Droplet volume
$V_{\textsf{drop,idl}}$	Idealized droplet volume
$V_{\textsf{liquid}}$	Volume of liquid
$V_{\textsf{liquid,init}}$	Initial volume of liquid
$V_{\textsf{PTFE}}$	Volume of PTFE
$V_{\textsf{GDL}}$	Volume of GDL

$V_{\textsf{\textbf{carbon}}}$	Volume of carbon
$\mathrm{X}_{\textsf{\textbf{flow}}}$	Channel distance along the flow direction
$\mathrm{X}_{\textsf{\textbf{max}}}$	Maximum position along the X direction
x	Position in X direction
x^*	Dimensionless position in X direction (flow direction)
x_j	Position of jth sample in X coordinate
$x_{\textsf{\textbf{BP}}}$	Breakthrough point position in X direction
y	Position in Y direction
y_j	Position of jth sample in Y coordinate
$y_{\textsf{\textbf{BP}}}$	Breakthrough point position in Y direction
y^*	Dimensionless position in Y direction
z	Position in Z direction
z_j	Position of jth sample in Z coordinate
$z_{\textsf{\textbf{BP}}}$	Breakthrough point position in Z direction

List of Figures

List of Tables

C. Acknowledgments

I would like to acknowledge a number of people who have encouraged and helped me to fulfill my doctoral research over the past few years.

First of all, I would like to thank my professor, Prof. Werner Lehnert, to give me the opportunity to work in the institute of energy and climate research (IEK-3) in Forschungszentrum Jülich. I really appreciate for your support not only on academic but also on the living. Through our numerous discussions, I gained a lot of knowledge on fuel cells and multi-phase flow in porous media. Particularly, he taught me how to motivate and conduct scientific studies. I believe it will be benefit for my whole life.

I would say thanks to my co-supervisor Dieter Froning for his constructive comments and very patient discussions on my research. He helped every where from the work to the daily life. For the work, we discussed a lot for fuel cells, modeling and supported me with his lattice Boltzmann experiences. For the life, I will never forget the small gifts he gave me and it makes me have a deeper understanding of enjoying life. Without his precious support and guidance, it would be not possible to conduct this work. My sincere thanks go to the rest of my thesis committee: Prof. Wolfgang Schröder, Prof. Dirk Müller and Prof. Dirk Abel, for their valuable time and insightful comments.

I would also like to thank the master students, Niklas Adams, Niklas Selke and Laura Hofer, who supported me during the development of Julabos. Under your technical support, the Julabos became more powerful and helped me to finish all my simulations fluently.

It's a pleasure to thank my colleagues from HPB group: Dr. Qing Cao, Dr. Uwe Reimer, Prof. Martin Andersson, Prof. Steven Beale, Dr. Yu Lin, Shidong Zhang, Shuai Liu, Ruiyu Li, Yun Cai, Wei Zou, Yan Shi, who all helped me in numerous ways during different stages of my PhD. I would also thank to the Chinese colleagues from other groups, Chang Liu, Yanpeng Suo, Yuan Wang, Yulin Yan, Jingjing Lin, who helped me a lot after work. I will remember all the fun we have in the past years. The friendship will be forever. Particularly, Dr. Yasser Rahim and Dr. Diankai Qiu, I will never forget the happy time that we spent together in the same office.

In addition, I am grateful to the Chinese Scholarship Council (CSC) who funding my study in Germany. This undoubtedly opened a door for me, and changed my life completely.

At last, my sincere and deep gratitude to my father Jianqing Yu, mother Qingying Liang, paternal grandmother Guilan Zhang, maternal grandfather Tiezhu Liang, maternal grandmother Fenglan Wang, my mother's younger brother Yanguo Liang, my mother's younger sister Yanhui Liang, other relatives and friends in China, for their love and support to all my decisions all the time. This work would not be possible without them, and I dedicate this milestone to them.

Band / Volume 425
Herstellung und Charakterisierung von Lithiumlanthanzirkonat-Funktionsschichten für Lithium-Festkörperbatterien
T. Reppert (2018), vii, 187 pp
ISBN: 978-3-95806-331-0

Band / Volume 426
Proton Conduction and Gas Permeation through Polymer Electrolyte Membranes during Water Electrolysis
M. Schalenbach (2018), VI, 212 pp
ISBN: 978-3-95806-333-4

Band / Volume 427
Improved characterization of root zone soil moisture by assimilating groundwater level and surface soil moisture data in an integrated terrestrial system model
H. Zhang (2018), x, 125 pp
ISBN: 978-3-95806-335-8

Band / Volume 428
Manipulation of magnetism in iron oxide nanoparticle / $BaTiO_3$ composites and low-dimensional iron oxide nanoparticle arrays
L. Wang (2018), VI, 151 pp
ISBN: 978-3-95806-338-9
Band wurde nicht veröffentlicht. Erscheint als Schlüsseltechnologieband 180

Band / Volume 429
Characterization of spatial-temporal varying riverbed hydraulic conductivity and its role on the estimation of river-aquifer exchange fluxes with data assimilation
Q. Tang (2018), xv, 117 pp
ISBN: 978-3-95806-339-6

Band / Volume 430
Der Einfluss von Wasserdampf auf den Sauerstofftransport in keramischen Hochtemperaturmembranen
F. Thaler (2018), ii, 93, XXXI pp
ISBN: 978-3-95806-340-2

Band / Volume 431
Analysis & modeling of metastable photovoltaic technologies: towards dynamic photovoltaic performance models
M. Görig (2018), 246 pp
ISBN: 978-3-95806-342-6

Schriften des Forschungszentrums Jülich
Reihe Energie & Umwelt / Energy & Environment

Band / Volume 432
Laser Treatment of Silicon Thin-Films for Photovoltaic Applications
C. Maurer (2018), vii, 165 pp
ISBN: 978-3-95806-347-1

Band / Volume 433
Mentalitäten und Verhaltensmuster im Kontext der Energiewende in NRW
K. Schürmann & D. Schumann (Hrsg.) (2018), 236 pp
ISBN: 978-3-95806-349-5

Band / Volume 434
Adhäsionsverhalten von wässrigen Nafion-Lösungen an dispersen Phasengrenzen
A. Schulz (2018), xii, 129 pp
ISBN: 978-3-95806-354-9

Band / Volume 435
Alterungs- und fehlertolerante optimale Betriebsführung eines Direktmethanol-Brennstoffzellensystems
R. Keller (2018), XX, 175 pp
ISBN: 978-3-95806-355-6

Band / Volume 436
Chamber study of biogenic volatile organic compounds: plant emission, oxidation products and their OH reactivity
Y. Zhujun (2018), ix, 139 pp
ISBN: 978-3-95806-356-3

Band / Volume 437
Characterization of High Temperature Polymer Electrolyte Fuel Cells
Y. Rahim (2018), iii, 162 pp
ISBN: 978-3-95806-359-4

Band / Volume 438
Lattice Boltzmann Simulation in Components of Polymer Electrolyte Fuel Cell
J. Yu (2018), ii, 173 pp
ISBN: 978-3-95806-360-0

Weitere ***Schriften des Verlags im Forschungszentrum Jülich*** unter
http://wwwzb1.fz-juelich.de/verlagextern1/index.asp

Energie & Umwelt / Energy & Environment
Band / Volume 438
ISBN 978-3-95806-360-0

Mitglied der Helmholtz-Gemeinschaft

JÜLICH
Forschungszentrum